# CONTENTS

## Vol. 16, No. 4, December 2023

This journal has the permission number 87/5265 from Research Deputy of Islamic Azad University.

*Int. J. Advanced Design and Manufacturing Technology, 2023, Vol. 16, No. 4, pp. 1-7*

*DOI: 10.30486/admt.2024.1966579.1377* *ISSN: 2252-0406* *https://admt.isfahan.iau.ir*

# Investigation of Compressive Stresses of Stainless Steel 316L Diamond Lattice Structures Under the Effect of Spherical Connections Produced by SLM Additive Manufacturing

**Behnam Ahmadi Roozbahani**
Mapna Group, TUGA, Tehran, Iran
E-mail: Roozbahani.behnam@Mapnaturbine.com

**Ali Akbar Lotfi Neyestanak***
Department of Mechanical Engineering, Yadegar-e-Imam Khomeini (RAH), Shahr-e-Ray Branch. Islamic Azad University, Tehran, Iran
E-mail: Aklotfi@gmail.com
*Corresponding author

**Received: 29 August 2022, Revised: 26 January 2023, Accepted: 10 July 2023**

**Abstract:** In this study, the compressive stresses of dodecahedron diamond lattice structures have been investigated. The finite element method has been used for Stress analysis. After the simulation, it was found that more stresses are applied at the junction of the struts of this structure due to the application of compressive force. For this purpose, the connection point of the structure's struts was strengthened by spherical connections, and a new type of dodecahedron structure was created. The validation and effect of spherical connections in compressive stresses have been evaluated experimentally. Two types of diamond lattice structures are made of stainless steel 316L by the SLM method. The results show that in the same condition, the use of spherical connections with twice the diameter of the structure's struts helps to strengthen the structure and increase its compressive strength by 18% compared to the simple structure.

**Keywords:** Additive Manufacturing, Compressive Stresses, Lattice structures, Spherical Connections, Stainless steel 316L

**Biographical notes: Behnam Ahmadi Roozbahani** is an additive manufacturing engineer in Mapna Group, TUGA, Tehran, Iran. He received his MSc in Mechanical Engineering from Islamic Azad University, Shahr-e-Qods Branch in 2022. His current research interest is Design for Additive Manufacturing (DFAM) and optimisation of products. **Ali Akbar Lotfi Neyestanak** is an Assistant Professor at the Department of Mechanical Engineering, Yadegar-e-Imam Khomeini (RAH), Shahr-e-Rey Branch, Islamic Azad University, Tehran, Iran. His current research interests include WEDM, Conductive polymers, Mechanical behavior of a material, and Damage Analysis of Composite.

Research paper

## 1 INTRODUCTION AND LITERATURE REVIEW

Additive manufacturing technologies are known for their ability to fabricate parts with complex geometries. Lattice structures use this ability to create parts with a high strength-to-weight ratio and other desirable structural qualities [1-2]. These structures have the potential to reduce the weight of components in the aerospace and biomedical industries with a new approach to incremental fabrication [3]. Using these structures more effectively reduces the time and cost required to make additive metals.

Numerical and experimental studies have been carried out in this field. In previous research, the properties of foam and lattice structures have been investigated, and by analyzing the mechanical properties of cellular solids, a wide range of properties for alternative structures have been presented [4]. This research has been used to investigate Maxwell's stability criterion and the bending behavior of the structure in the current research. A comprehensive summary of experimental data on mechanical response is presented by examining the design, construction, and performance of SLM lattice structures, a source of experimental and design data for AM tools has been provided to designers [1]. In addition, research with the design of 9 lattice structures with relative density, the geometric quality of stainless steel 316L construction, and the manufacturing capability of the SLM technique have been examined, and reasons for the deviation of the dimensions of the lattice struts with the designed struts have been determined [5]. The use of a series of experimental tests on the mechanical properties of random metal foams and regular lattices with titanium grade 5 number 3 has been evaluated by the EBM technique according to the unit cells of the lattices to ensure that the mechanical properties under what type of conditions have measured independently of the size [6]. In the current study, to obtain the desired mechanical properties from the experience of the aforementioned research, select the appropriate number of unit cells in the structure used. In a doctoral thesis, a wide range of mechanical properties of titanium grade 5 diamond structure made by the EBM technique has been analyzed, and its working method is a suitable reference for the current study [7]. An early study reported an article that was presented at the 13th International Conference, which investigated the lattice structures made of nickel-based superalloy by SLM, and various mechanical tests were performed on them, and their anisotropy was also investigated [8]. Since stainless steel 316L has been used in the current study using the SLM method, the compression test results presented in the mentioned research have been reviewed and taken into consideration in the current study. In previous research, the effect of construction direction and strut length on 4 compressive mechanical characteristics of BCC structure under quasi-static axial compressive loading was investigated using finite element analysis, and two types of lattices were created and analyzed [9]. The effect of strut length mentioned in the previous research was used and the compatibility of the length of the strut with its diameter was considered. The application of the lattice structure, according to the selected material, will have the ability to be used in an environment with high temperatures. It should also be noted that due to the presence of chromium, this alloy has acceptable corrosion resistance [10-11].

In the previous studies and works of researchers, structures have been studied from the point of view of product stylization. In this research, in addition to maintaining the above advantage, the effect of compressive stresses on this structure was investigated and the critical places where the stress is high were identified, with the results obtained in the places where the struts of the structure are connected, spherical connections were added to the structure to strengthen and optimize, this operation created a new dodecahedron structure that is stronger than the previous structure. Therefore, a piece made with a structure is expected, it is suggested that it can be used in places where the applied stress level is equal to the experimentally measured resistance of this structure. Apart from industrial use, this structure may also have the possibility of being used in medical applications due to its good corrosion resistance. The analyses performed and the computational approach of this study can be used for materials that have better medical applications. For example, making the same structure and using it for medical implants made with titanium will be practical [3].

## 2 MATERALS AND METHODS

### 2.1. Material Properties

In this study, non-standard tensile tests were used to evaluate the material properties. This not only saves material and time of tests considerably but also helps to consider the effects of position and build rate in the case of the metal additive manufacturing process. Miniature test specimens similar to the standard ASTM E8 were designed and used for testing. The test was mainly conducted on the baseline material stainless steel 316L, while designing the miniature specimen, the standard architecture of the specimen was retained [12].

ASTM E8 provides test methods for tension testing of metallic materials [12]. Considering these guidelines and the previous work in the field, a sheet-type specimen with a square cross-section was designed for a miniature tensile test. These specimens could either have wedgeshaped shoulder ends for gripping. The design miniature specimen had a gage length of 5.7 mm and a width of 1.2 mm. The overall length of the specimen was 17 mm with a thickness of 0.5 mm. The gage area was nominally 1.2 mm by 1 mm. The test set-up was designed for 2000 KN ratings and grips were designed for this rating [12]. The miniature specimen follows the same architecture as the ASTM E8 standard, square cross-section test specimen. The dimensions of the miniature specimen are shown in “Fig 1”.

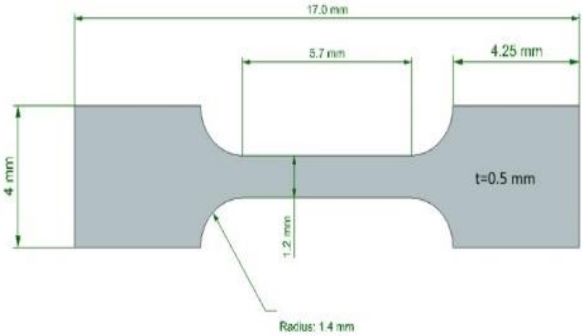

**Fig. 1** ASTM E8 – Sheet type tensile test specimen [12-13].

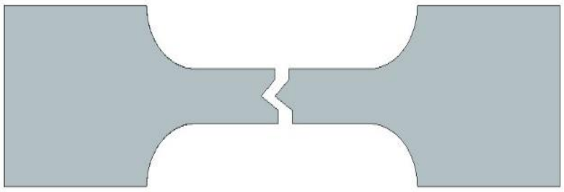

**Fig. 2** Expected post failure conduction of designed miniature tensile specimen showing the failure in the gage section.

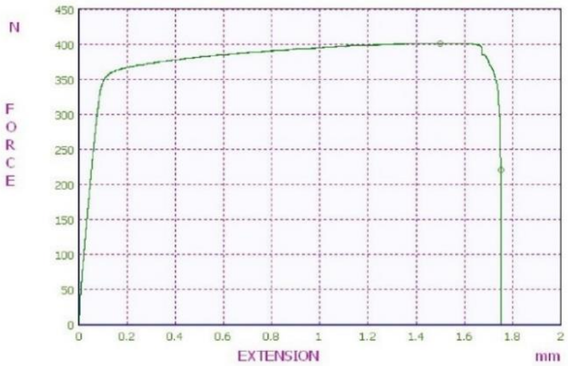

**Fig. 3** Force-displacement diagram of stainless steel 316L material.

To validate the test, tensile failure should be in the design gage section. Figure 2 shows the expected post-failure condition of the tensile test specimen that would confirm the validity of the test. Tests were conducted on the ASTM E8 standard. The tensile tests were conducted with a constant speed of 0.15 mm/s on 3 Specimens. Force-displacement data was acquired from the test frame according to the diagram as shown in “Fig. 3”. According to this figure, the properties obtained for the Stainless steel 316L material are listed in “Table 1”.

**Table 1** Stainless steel 316L material properties

| | |
|---|---|
| Yield Strength, MPa | 595±9 |
| Ultimate tensile strength, MPa | 671 |
| Elongation [%] | 23.8±0.5 |
| Density, $g/cm^3$ | 7.99 |
| Composition | 10.34Ni-16.1Cr-2.62Mo-0.8Mn-0.25Si-0.06C |

## 2.2. Hypotheses and Experimental Work

The studied structure is a simple dodecahedron diamond lattice structure shown in “Fig. 4”. Each node was connected to four struts with an angle of 109.5 degrees to each other. The struts were designed with a circular cross-section with a fixed diameter of 0.3 mm in single cells with dimensions of 3x3x3 mm and the overall dimensions of the structure are 12x12x12 mm. The periodic structure consisting of a dodecahedron structure creates a single diamond cell. The number of unit cells in each direction is 4 and a total of 64 unit cells in the structure have been used.

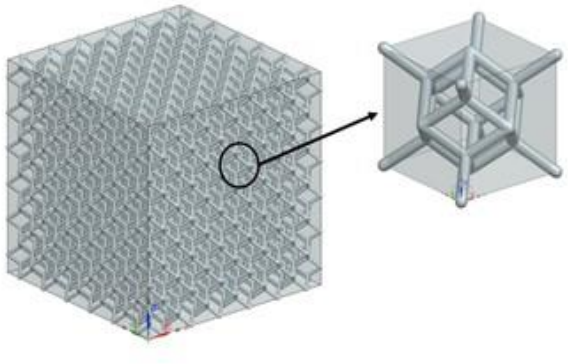

**Fig. 4** Simple diamond lattice structure.

For preliminary investigation, a unit cell of the structure with the boundary conditions shown in “Fig. 5” was subjected to a compressive test simulation in the software. In the numerical solution to apply the boundary conditions and accurate loading, the constraint boundary conditions were used in which the grid is placed between two plates so that the upper and lower levels are tied to completely rigid plates while all the other four sides of the grid are unrestricted [14]. These plates are considered representative of the jaws of the compression testing machine.

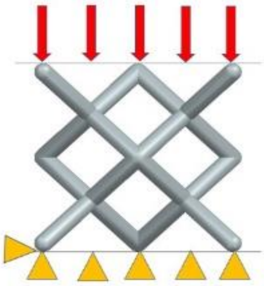

**Fig. 5** Constraint boundary conditions.

The vertical behavior of contact between the lattice structure and the indicated plates is rigid (Hard) and the tangential behavior is also defined without friction. The isotropic material is considered and the effects of strain rate are ignored. For the numerical solution, the relationship between the deformation and stress of the material is considered in the form of the entire plastic range. The relevant diagram and data points defined in the software are given in “Fig. 3”.

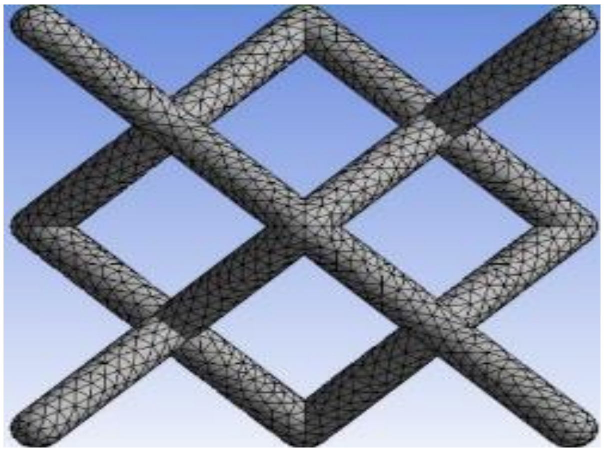

**Fig. 6** 4 Nodes rigid 3D shell mesh.

A meshing is shown in “Fig. 6”, the used element type is a 4-node rigid 3D shell element. This type of element provides high performance in terms of computing time and accuracy of results which fulfils the purpose of this study, which is to investigate axial compressive stresses. As shown in “Fig. 7” in the numerical solution of the simulation of the unit cell compressive test, it was found that more stresses are applied to the structure at the connections of the struts.

So, knowing this, the connection between the struts was strengthened by spherical balls and a new structure was created which is shown in “Fig. 8”. In the structure with spherical connections, the radius of the spheres was considered 0.6 mm.

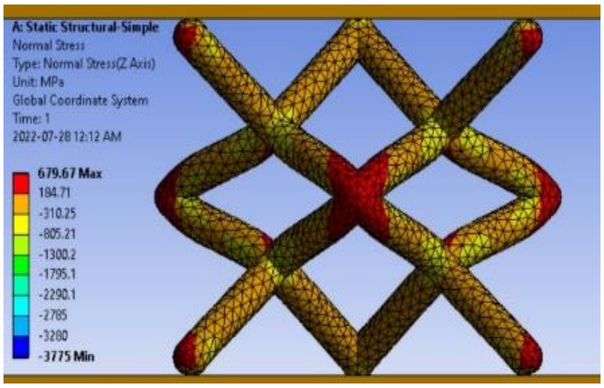

**Fig. 7** Normal Stress in the simple diamond lattice structure.

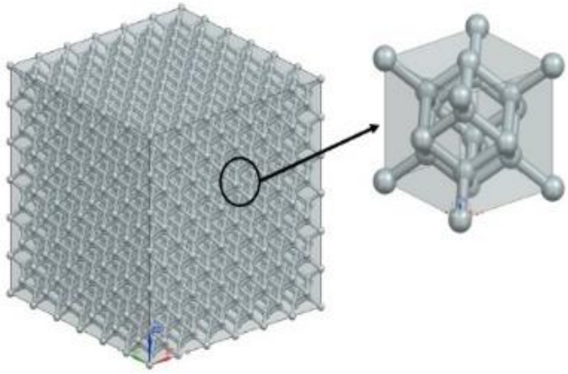

**Fig. 8** Reinforced dodecahedron lattice structure.

The meshes and boundary conditions in the reinforced structure unit cell were considered exactly like the simple structure unit cell. As shown in “Fig. 9”, in the numerical simulation, a unit cell of the new reinforced structure was investigated and it was found that by performing this operation, the stresses at the connections of the struts are reduced.

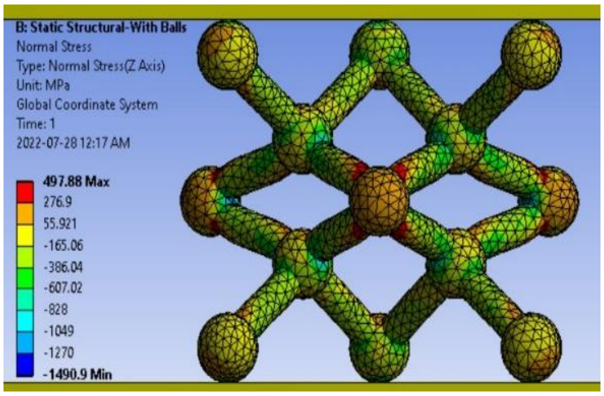

**Fig. 9** Normal Stress in reinforced lattice structure.

As shown in “Figs. 10 and 11” two samples of each structure have been fabricated using SLM additive manufacturing technology. Selective Laser Melting (SLM) is an additive manufacturing method that is used to fabricate different types of complex components using a layer-by-layer approach. The parts are produced directly from three-dimensional computer-aided design data by melting the powdered material layer-by-layer with the aid of laser power. The characteristics and performance of the process are given in ISO/ASTM 52904 standard.

Compressive mechanical testing of both the simple structure and the structure with spherical connections was done experimentally. All lattice models were selected based on a preliminary investigation of the effect of spherical connections between struts.

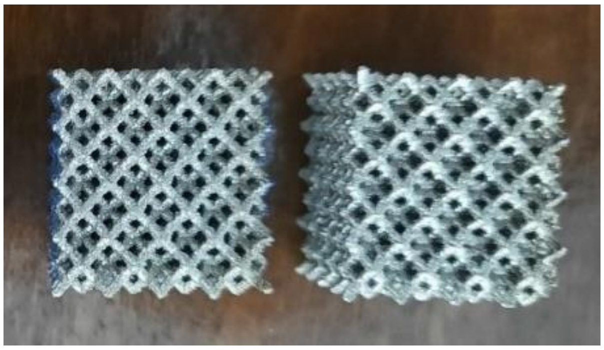

**Fig. 10** Simple diamond lattice structure.

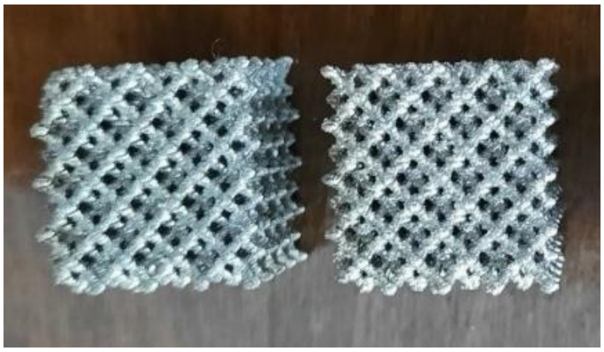

**Fig. 11** Lattice structure with spherical connections.

After the experimental test and analysis, the final bearing force of the part is considered with two criteria: The end limit of linear deformation and the ultimate limit of tolerable force can be derived by dividing the force number by the equivalent area of the structure, the tolerable nominal stress in this structure.

To validate the simulation, the experimental validation of the simple structure and reinforced structures with SLM additive manufacturing technology was made with the Noura-M100P machine in MAPNA Turbine Engineering and Manufacturing Company (TUGA). Optimized manufacturing process parameters are used to obtain the desired structure of stainless steel 316L with the highest quality [15]. The experimental results of the compressive test of the simple structure were compared with the experimental results of the reinforced structure with spherical connections. It should be noted that the compressive test of the manufactured samples is by ISO/IEC17025 standard.

## 3 RESULTS AND DISCUSSION

The experimental test piece has experienced failure in many places. For better clarification, the crushed parts after the experimental tests are shown in “Figs. 12 and 13”.

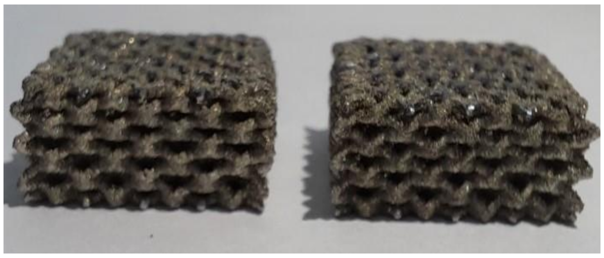

**Fig. 12** Simple lattice structure after compressive test.

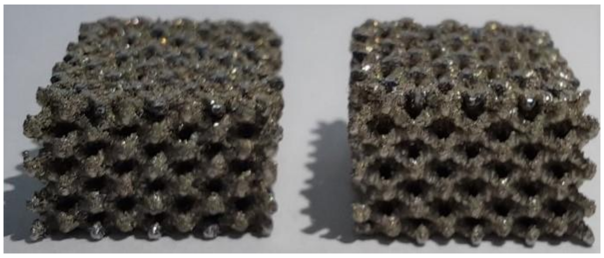

**Fig. 13** Reinforced lattice structure after compressive test.

The graph obtained is the experimental comparison of the compressive test of the simple lattice structure and the reinforced lattice structure with spherical connections, which is shown in “Fig. 14”.

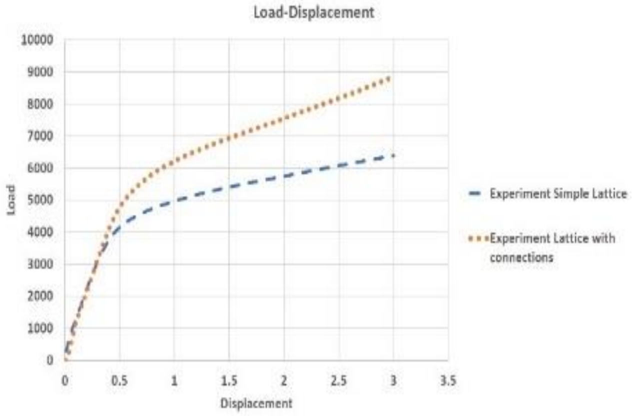

**Fig. 14** Load-displacement comparison diagram of simple structure and reinforced structure with spherical connections.

The remarkable note about this figure is the improvement of the maximum force that the structure can tolerate using reinforced connections. This study shows the improvement of mechanical resistance by adding reinforcement (balls) at the junction between the struts.

In line with the application of this structure, the nominal tolerable stress obtained from the experimental test for the ultimate force-bearing limit of the simple structure is equal to 42 MPa and for the linear end limit is 27 MPa. In this situation, the proposed structure can be used for applications that have temperature tolerance, corrosion, and stress levels equivalent to the above values. In addition, due to the very high porosity, high solid-to-fluid heat transfer capability is expected for this structure. Therefore, in cases where it is necessary to cool a hard surface resistant to corrosion, this structure can be used.

## 4 CONCLUSIONS

The purpose of this study is to investigate the compressive stresses of the diamond lattice structure under the effect of spherical connections. Increasing the compressive strength of the structure can be an effective step in making it more practical. The results of the simple lattice structure showed that the most compressive stress occurs at the connection point of the struts, therefore, spherical connections have been used to strengthen the strut. Under the same conditions, the use of spherical connections with a diameter of 0.6 mm in the structure increases the compressive strength compared to a simple diamond structure by about 18%.

According to the experimental results and obtaining the maximum nominal stress of 42 MPa, the use of this structure is applicable for parts whose stress is equivalent to this value. It is important to note that the weight of this type of lattice structure has decreased by about 10 times compared to the weight of a solid structure with the same dimensions.

## 5 ACKNOWLEDGEMENTS

This research was done under the support of the material and additive laboratory of MAPNA Turbine Engineering and Manufacturing Company (TUGA) for the fabrication of the lattice structures. The authors wish to thank the other members of the material and additive lab at MAPNA group (TUGA) for their help throughout this work; in particular, engineer Hossein Davarzani for many useful discussions.

## REFERENCES

[1] Tobias, M., Martin, L., Bill, L., Xuezhe, Zh., Ma, Q., Omar, F., and Milan, B., SLM Lattice Structures: Properties, Performance, Applications and Challenges, 10.1016/J.MATDES.2019.108137, 2019.

[2] Long, B., Junfang, Zh., Xiaohong, Ch., Changyan, Y, Rui, Ch., and Zixiang, Zh.,. Configuration Optimization Design of Ti6Al4V Lattice Structure Formed by SLM, 10.3390/ma11101856, 2018.

[3] Doruk, G., Binnur, S., Additive Manufactured Ti6Al4V Lattice Structures for Biomedical Applications, Vol. 5, No. 2, 2021, pp. 155-163, 31.08.2021.

[4] M. Ashby., The Properties of Foams and Lattices, Philosophical Transactions of the Royal Society, Vol. 364, 2005, pp. 15.

[5] Paweł, P., Judyta, S., Jacek, J., and Fengchun, J., Investigations on Mechanical Properties of Lattice Structures with Different Values of Relative Density Made from 316L by Selective Laser Melting (SLM), Materials, Vol. 13, No. 9, 2020, pp. 2204.

[6] Morrish, S. J. N., Pedersen. M., Wong, K. F. W., Todd, I., and Goodall, R., Size Effects in Compression in Electron Beam Melted Ti6Al4V Diamond Structure Lattices, Mater. Lett., Vol. 190, 2017, pp. 138–142.

[7] Sarah, N. M. J., Mechanical Properties and Structural Evaluation of Diamond Structure Ti6Al4V Lattices Made by Electron Beam Melting, A Thesis Presented for The Degree of Doctor of Philosophy, Department of Materials Science and Engineering the University of Sheffield, 2017

[8] Hakan, B., Jonas, S., Mechanical Properties of Lattice Truss Structures Made of a Selective Laser Melted Superalloy, 13th International Conference on Fracture, Beijing, China., 2013.

[9] Hasanain, A., Designing New Generations of BCC Lattice Structures and Developing Scaling Laws to Predict Compressive Mechanical Characteristics and Geometrical Parameters, A thesis presented for the degree of degree of Doctor of Philosophy in Wright State University, 2020.

[10] V. Salarvand, V., SohrabpoorH., Mohammadi, M. A., Nazai, M., Raghavendra, R., Mostafaei, A., and Brabazon, D., Microstructure and Corrosion Evaluation of As-Built and Heat-Treated 316l Stainless Steel Manufactured by Laser Powder Bed Fusion, 10.1016/j.jmrt.2022.03.156, 2022.

[11] Manuel, G., Lizangela, G., Barbara, B., Roberto, C., and Luis, R., Characterization of Sio2-Tio2 Coatings on 316L Stainless Steel Substrates, L. Reyes et al, Journal of Advanced Materials and Processing, Vol. 6, No. 1, 2018, pp. 3-13

[12] ASTM, Standard E-8, Standard Test Methods for Tension Testing of Metallic Materials.

[13] Pengfei, Zh., Ran, Ch., Haiting, L., Jiming, Ch., Zhijie, Zh., Xing, L., and Yao, Sh., On the Standard and

Practices for Miniaturized Tensile Test-A Review, 10.1016/j.fusengdes.2020.112006.

[14] Ushijima, K., Cantwell, W., Mines, R., Tsopanos, S., and Smith, M., An Investigation into The Compressive Properties of Stainless-Steel Micro-Lattice Structures, Journal of Sandwich Structures and Materials, Vol. 13, No. 3, 2011, pp. 303-329.

[15] TUGA Technical Review, First MGT-30 Gas Turbine Additively Manufactured Parts Set to Render Conventional Manufacturing Process of The Part Obsolete, No. 16, 2021.

*Int. J. Advanced Design and Manufacturing Technology, 2023, Vol. 16, No. 4, pp. 9-22*

*DOI: 10.30486/admt.2024.1980467.1402 ISSN: 2252-0406 https://admt.isfahan.iau.ir*

# Simulation and Dynamic-Thermal Analysis of Ceramic Disc and Brake Pad for Optimization by Finite Element Method

**Navvab Gholami, Ahmad Afsari *, Seyed Mohammad Reza Nazemosadat**

Department of Mechanical Engineering, Shiraz
Branch, Islamic Azad University, Shiraz, Iran
E-mail: Ah.Afsari1338@iau.ac.ir
*Corresponding author

**Mohammad Javad Afsari**

Department of Computer Engineering,
University of Tehran, Tehran, Iran

**Received: 17 February 2023, Revised: 14 December 2023, Accepted: 17 December 2023**

**Abstract:** The braking system in automotives directly deals with the issue of safety, and as a result, it is essential to pay attention to this matter. One of the materials used to make disc and brake pads in disc brakes is ceramic material. This research aims to simulate and analyze the dynamic-thermal ceramic brake disc during the braking operation using the finite element method. Currently, the conventional brake disc is used in the Peugeot 206 automotive (domestic production), which has low efficiency in terms of life, wear, etc. Therefore, in this research, considering the significant production of Peugeot 206 automotive in the country, the disc and brake pads of this automotive have been selected, which were first modelled by Catia software, and after transferring the model to Abaqus software and defining the types of ceramics, Cast iron was analyzed by finite element method. The results of the Peugeot 206 ceramic brake disc and pad analysis were compared with the results of the standard (cast iron) discs in this automotive. The results showed that the maximum Von-Mises stress in the ceramic disc was 260.7 MPa, while the maximum Von-Mises stress in the cast iron disc was 293.3 MPa. The amount of heat produced in the ceramic disc during the braking action in 4 seconds was almost 84% less than the cast iron disc in the same period. Also, the results showed that the ceramic disc has a higher safety factor (1.98) than the cast iron disc (1.45).

**Keywords:** Brake Disc, Ceramic Materials, Finite Elements, Modeling, Pads

**Biographical notes: Navvab Gholami** graduated with a MSc degree in Mechanical Engineering from Islamic Azad University, Shiraz branch in 2022. **Ahmad Afsari** is an associate professor of Mechanical Engineering at Islamic Azad University, Shiraz branch. He received his PhD from the Indian Institute of Technology - Delhi, India in 1998. His speciality is in manufacturing and production methods (welding, casting, shaping and machining) and also precision measurement systems. **Seyed Mohammad Reza Nazemosadat** is an assistant professor of Mechanical Engineering at Islamic Azad University, Shiraz branch. He received his PhD in Mechanical Engineering of Biosystems from Shahrekord University in 2022. His current research is in the field of agricultural machinery and automotive design, FEM, chassis reliability analysis and optimization. **Mohammad Javad Afsari** is a computer engineering undergraduate student at the University of Tehran. His expertise is in the field of artificial intelligence and he cooperates with knowledge-based companies in this field.

Research paper

## 1 INTRODUCTION

As the most vital safety system in automotive, the brake has an important task; that's why from the past until now, it has witnessed the progress, evolution, and emergence of various innovations in automotive brake systems. Today, unlike in the past, brakes are responsible for slowing down and stopping the automotive and play a vital role in the automotive's steering. Now the question arises of how to improve the braking system in automotives and whether the materials that make up the parts of the braking system in automotives affect their improvement. Innovation in producing components such as pads and brake discs improved the braking and thus increased the automotive's safety. Ceramics are among the materials used in the production of brake pads and discs for modern automotives, which improve the braking power of automotives and increase their lifespan due to better heat transfer than cast iron and a higher friction coefficient [1].

Structurally, the brake system installed in the automotive can be divided into three general categories: wire brakes, hydraulic brakes, and pneumatic brakes. The handbrake, also known as the parking brake, is one of the wire brakes. A hand brake is used to keep a stopped automotive stable. In this case, the engine may be on or off. The handbrake must have the necessary power to keep the automotive stationary and be able to keep the automotive stationary on an incline of 30 degrees. A hydraulic brake is a type of hydraulic system that transfers the force of the brake pedal to the wheels. The components of the hydraulic brake system include the main cylinder, booster, combination valve, wheel cylinders, and mechanisms acting on the wheels. Pneumatic brake systems were first introduced in the railway industry of the United States of America by George Westinghouse in 1869 [2]. Later, trucks, buses, and even light trucks were used. The operation of the pneumatic brake is such that the ends of the brake shoes are connected to an S-shaped part. During braking, compressed air enters the air chamber and moves the transmission rod, causing the S-shaped part to rotate, and the shoes move and come into contact with the wheel bowl. It reduces the speed and eventually stops the wheels [3].

Based on the mechanisms acting on the wheel, the brake is divided into two categories, the drum, and the disc mechanism. In drum brakes, the brake drum is connected to the wheel and rotates with it, and two crescent-shaped iron shoes on which the brake pads are pressed are installed on the floor. In the typical case, when the automotive does not need to brake, they are adjusted so that there is a small distance between the brake drum and the pads of the shoes. When the driver presses the brake pedal, the oil pressure in the master cylinder increases. The internal pistons of the wheel cylinder move away from each other due to the oil pressure and move the brake shoes towards the brake drum. As a result of the force coming from the pad on the brake drum, the friction force between the drum and the pad is created, resulting in negative acceleration in the wheels and stopping them. An example of a brake with a drum mechanism can be seen in Fig. 1-b.

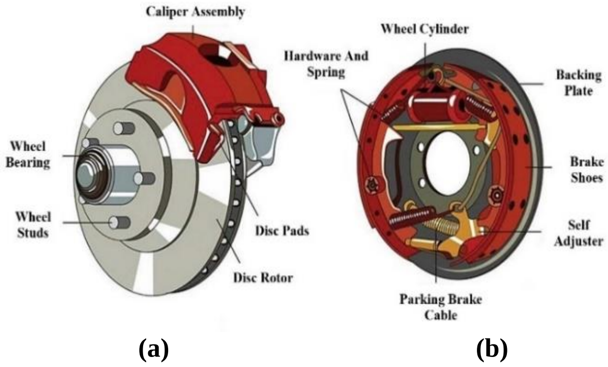

**Fig. 1** (a): Disc brake, and (b): Drum brake.

In an automotive disc brake, when the brake pedal is depressed, the push rod applies pressure to the master cylinder piston, allowing the return spring to push into the master cylinder bore, which creates pressure in the reservoir. A pellet of the oil fluid inside the reservoir allows it to enter the brake pipes, and a secondary bead ensures that oil does not flow back the other way. The oil enters the cylinder hole of the caliper set through the brake hoses and pushes the pistons of the caliper set that are connected to the pad forward causing the pad to contact the disc, which slows down the speed of the disc due to the friction between the disc and the pad. And finally, the disc stops [4]. One of the advantages of disc brakes compared to drum brakes is easier cooling, lighter weight, and easy placement. Fig. 1-a shows the components of a disc brake.

Brake discs are made of different materials, but the important point that gives an advantage to each of these alloys is to increase the thermal coefficient of the disc and reduce its depreciation against high contact and wear. Materials used in brake discs include stainless steel, gray cast iron, carbon ceramic composites, titanium alloys, and aluminum matrix composites. Ceramic composites have received much attention due to their high thermal and mechanical properties. These properties include thermal conductivity, mechanical strength, hardness, and high-temperature resistance. The improvement of their performance is due to the use of ceramic materials in the matrix and reinforcement, and ceramic composites are also used in various applications, including automotive brake discs. It should be noted that the way of processing and manufacturing directly affects the properties of composites. Common manufacturing methods of ceramic composites include powder infiltration processing and slurry impregnation, polymer infiltration and thermal decomposition (PIP), chemical vapor infiltration (CVI), direct metal oxidation (DMO), and liquid silicon infiltration (LSI). Choosing the right method to produce a ceramic composite depends on various factors, such as the type of user, construction cost, and availability of raw materials, tools, and equipment [5].

Heydar Khalil et al. [6] analyzed the automotive disc brake. This article compared temperature distribution, deformation, and Von-Mises stress of gray cast iron and carbon ceramic brake discs. The results showed that carbon ceramic could show more resistance against thermal stress, and there is almost no deformation for it. In addition, carbon ceramic was preferred to achieve better brake performance. Venkatraman et al. [7] investigated and analyzed the brake disc using Ansys software. In this research work, they proposed the design of a disc brake with a copper lining, and its purpose was thermal analysis and temperature distribution in the brake disc. The results showed that the maximum heat produced in the brake disc made of gray cast iron without copper lining is 603.5 °C., while the maximum temperature produced in the brake disc with copper lining is 335.98 °C. Therefore, it is concluded that copper lining can be used in the brake disc at high temperatures.

Manavlan et al. [8] analyzed gray cast iron and ceramic brake disc using the finite element method in Ansys software. Their goal was to predict the temperature distribution in brake discs. This article used ceramic composites with carbon materials instead of traditional ceramic brake discs. The results showed that heat production decreases by adding carbon to ceramic materials because their thermal conductivity coefficient increases. Therefore, this increases the life of the brake and also improves its performance of the brake. Belhousin Ali [9] analyzed brake discs and automotive pads using the finite element method. This research aimed to study the thermodynamic behavior of automotive disc brakes in the braking phase and then a completely mechanical study of the dry contact between the disc and the pads. The results of this research showed that the tension on the surface of the disc increases during braking. In addition, the friction path between the disc and the pads, causes mechanical (radial) phenomena such as cracks, wear, and tears. Also, the presence of grooves in the pads adversely affects the brake's mechanical behavior. The important point here is that disc deformation increases significantly when thermal and mechanical stresses are combined.

Limpert [10] investigated the thermal characteristics of cast iron discs, which led to the rupture and cracking of the disc surface. Thermal stress analysis showed that disc surface rupture occurs when the induced compressive stress exceeds the compressive yield strength of a brake disc, which is an important factor that causes disc cracking during repeated braking. Soderberg et al. [11] investigated and analyzed the contact between the pad and the brake disc to determine the amount of wear with the help of Ansys software. In this research, they performed two wear simulations, one with disc displacement and the other without displacement. The approximate sliding distance is 75 meters, and the analysis solution time is three minutes. The analysis results showed that the deepest wear occurs in the high-pressure area; while there is almost no wear at the edge, after 1600 rotations, the wear process remains in a constant state, where all points on the surfaces have the same wear rate.

Mojavar et al. [12] investigated and thermally analyzed the automotive brake disc with the aim of temperature distribution in the disc during operation using Ansys software. The results of the thermal analysis showed that the temperature increases from 300 to 800°C during braking and also showed that the thermal conductivity of the brake pad material is smaller than that of the brake disc. In a study, Sridevi et al. [13] modelled and analyzed the structural and thermal disc brakes of the Honda Civic with three different materials, including steel, cast iron, and aluminium alloy, all of which are stainless. Because the real disc is without holes, they created holes in the design to dissipate more heat. Thermal analysis was performed by Ansys software. The results showed that the Von-Mises stress values of the disc with aluminum alloy are lower than steel and cast iron, and thermal analysis showed that the thermal gradient in the aluminum alloy is higher than in steel and cast iron, while the lowest thermal gradient was observed in steel. Pranta et al. [14] performed a computational study on modified disc brake rotors' structural and thermal behavior. They developed the disc brake rotor as a modified ventilated disc with curved cross-section valves with holes and slots. They analyzed the stress and temperature distribution using the finite element method with the help of Ansys software. They compared the results with the structural and thermal characteristics of the reference disc brake rotor. The analysis showed that the proposed disc brake rotors perform better than conventional disc brake rotors in terms of stress generation, temperature distribution, and safety factors.

Suval et al. [15], in their research, investigated the problems in Yamaha FZ_25 disc brakes. In this research, they presented four different models of the ventilated disc, the first model has equal and symmetrical holes, the second model has equal and asymmetrical holes, the third model has smooth and straight grooves, and the fourth model has curved grooves. They performed the analysis using the finite element method with the help of

Ansys software and compared the obtained results with the reference brake disc. The main goal of this research was to choose the best design to solve the problems in the reference disc and improve it, such as reducing the disc's weight, reducing the disc's deformation, and reducing the stress and temperature in the disc. The analysis results of four disc models indicate that the fourth model has managed to provide better performance than the original disc by increasing the stable stress by 2.05 MPa and reducing the deformation by 0.0002 mm. Also, this model performs better than the original disc and other models by increasing the stable temperature up to 15.73 °C, reducing the weight by 0.05 kg, and reducing the production cost by 9.26 rupees. In their research, Raj Kamal et al. [16] investigated and analyzed the structure of automotive disc brakes. The main goal of this research is to reduce the failure of the brake disc by using a material that has positive effects compared to the current brake disc manufacturing materials; that is why they replace the brake disc with materials including stainless steel, cast iron, and carbon-carbon composite in terms of deformability and thermally. They were analyzed using the finite element method to determine the temperature coefficient. The results obtained with the disc made of vanadium steel were investigated and compared. Completing this analysis proved that vanadium steel has better resistance and temperature distribution factors than the other three materials.

The innovation of ceramic brake discs and pads in automotives, compared to conventional brake discs and pads, is the reduction of brake dust, reduction of heat loss, reduction of noise, high durability and longevity, and corrosion resistance. Ceramic disc plates are easily able to perform their tasks at 800 °C, and this is thanks to the process of processing carbon fibers, and due to the low specific weight of the materials used, the amount of heat that is generated is less. Since such a structure is resistant to rust and erosion, its performance is at least 300,000 km. Also, ceramic discs have a 50% weight reduction compared to conventional metal discs, which significantly increases the automotive's controllability. The conducted studies show that little research has been done in the field of finite element analysis of ceramic disc type; Therefore, in this research, finite element analysis is performed on Peugeot 206 brake disc and pad by defining the characteristics of two types of ceramic and cast iron and comparing them in dynamic-thermal terms.

## 2 MATERIALS AND METHODS

### 2.1. Materials Used to Make Discs and Pads

This research uses materials such as gray cast iron and ceramic composites to make the brake disc. In this research, ceramic composite is considered for making brake discs made of c/c/sic composites by liquid silicon infiltration method (LSI) and brake pads made of gray cast iron. The mechanical and thermal properties of the brake disc (composite c/c/sic) and brake pad (gray cast iron GG25), as well as the characteristics of the brake disc (cast iron), are presented in “Tables 1 and 2”.

**Table 1** Mechanical properties of brake disc and pad [17]

| Specification | Pad (gray cast iron GG25) | Disc (ceramic composite c/c/sic) | Cast iron disc |
|---|---|---|---|
| Density kg/m$^3$ | 1400 | 1900 | 7250 |
| Modulus of elasticity (E) Gpa | 103 | 140 | 130 |
| Porosity | -- | 0.3% | -- |
| Poisson's ratio (ν) | 0.25 | 0.34 | 0.28 |
| Friction coefficient between disc and brake pads (μ) | 0.35 | | |

**Table 2** Thermal properties of brake disc and pad [17]

| Specification | Pad (gray cast iron GG25) | Disc (ceramic composite c/c/sic) | Cast iron disc |
|---|---|---|---|
| heat transfer coefficient k (w/m$^2$.$^o$C) | 5 | 20 | 11 |
| specific heat c (J/kg.$^o$C) | 1000 | 1200 | 460 |
| Thermal expansion coefficient α, 10$^{-6}$/$^o$C | 10 | 5 | 8 |

### 2.2. Geometry and Dimensions of Brake Disc and Pad

The brake disc and pad dimensions were measured for 3D modeling in Catia software by calipers (“Fig. 2”), and the radius and thickness of the disc and pad were measured as input for finite element analysis in Abaqus software. Figures 3 and 4 show the Peugeot 206 brake disc and caliper and the measured brake disc and pad symbols, respectively. The measured dimensions can be seen in “Table 3”.

**Fig. 2** Measurement of Peugeot 206 brake disc by caliper.

**Fig. 3** Peugeot 206 brake disc and caliper.

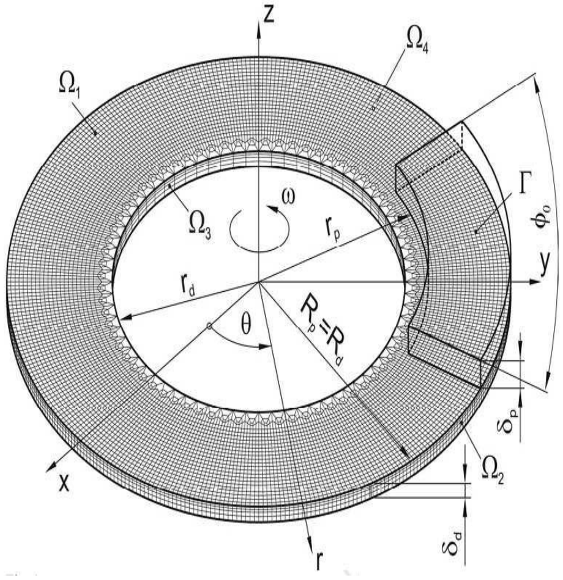

**Fig. 4** Measured brake disc and pad symbols.

**Table 3** Measured dimensions of brake disc and pad

| Dimensions | Concept | Symbol |
|---|---|---|
| 91 mm | Brake pad inner radius (mm) | $r_p$ |
| 133 mm | The outer radius of the brake pad (mm) | $R_p$ |
| 78 mm | Brake disc inner radius (mm) | $r_d$ |
| 133 mm | The outer radius of the brake disc (mm) | $R_d$ |
| 6.70 mm | Brake disc thickness (mm) | $\delta_d$ |
| 13.6 mm | Brake pad thickness (mm) | $\delta_p$ |

## 2.3. Brake Disc and Pad Modeling

A three-dimensional brake disc and pad model was modeled for dynamic analysis using Catia software (“Fig. 5”).

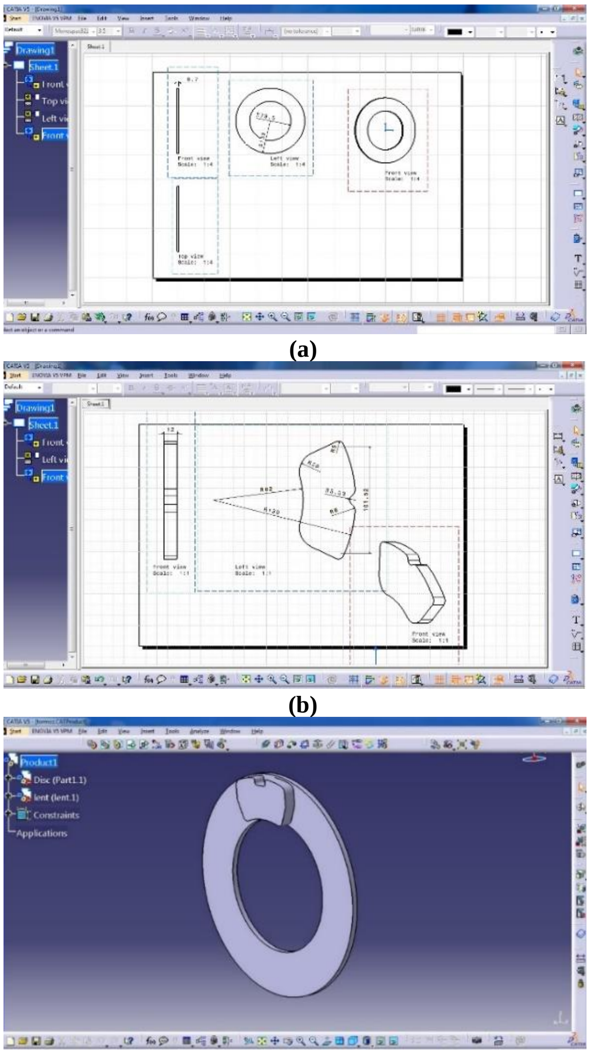

(a)

(b)

(c)

**Fig. 5** Modeling of Peugeot 206 brake disc and pad in Catia: (a): Disc map, (b): Pad map, and (c): 3D model of disc and pad.

## 2.4. Dynamic-Thermal Analysis and Safety Factor Calculation

The main goal of this research is the thermomechanical analysis and investigation of temperature and pressure distribution between pads and discs in disc brakes. Therefore, the goal is to obtain a suitable model to identify hot spots between them through simulation to optimize and upgrade the disc brake system.

### 2.4.1. Dynamic Analysis

In inelastic stress analysis, a mathematical Equation includes three main stresses known as the yield function. If the calculated yield function is greater than the initial value, yield strength of the material, plastic strain, and softening or hardening will occur. In general, there are several yield functions to investigate the state of stress beyond the elastic region, including the Von-Mises stress criterion and the maximum shear stress. If a material is subjected to pressure beyond that, a change in the yield surface occurs in the elastic region. There are two basic types of change in the yield surface. One is based on the assumption that the center of the yield surface remains constant while, at the same time, the yield surface expands without deformation, known as isotropic hardening. The other, known as kinematic hardening, is based on the assumption that the yield surface is visible in the stress space but does not change its size or shape. Both shear stress and Von-Mises stress are criteria used to predict the yield levels of flexible materials.

In contrast, the maximum normal stress criterion is usually used to predict the failure of brittle materials because the yield stress occurs at low strain levels and is difficult to define. Shear and Von-Mises stress are generally used when structural materials are flexible. Von-Mises theory predicts failure more accurately, but Tresca theory is often used in the design because it is simple and more consistent. Von-Mises theory relates the distortion energy of a point under the general state of stress. A state of hydrostatic stress occurs when all three main stresses are equal. In this condition, normal strains are equal in all directions, and there is no shear stress due to symmetry.

### 2.4.2. Thermal Analysis

When an automotive is moving at speed, it has kinetic energy. By applying the brakes, the pads pressing on the brake disc convert this energy into thermal energy. All of this is related to the first law of thermodynamics, known as the law of conservation of energy, which states that energy is neither created nor destroyed but is transformed from one form to another. In the case of brakes, it is converted from kinetic energy to thermal energy; which is equal to:

$$E_c = {}^{1}\!/_{2}\, mV_0{}^2 \tag{1}$$

In Equation 1, m is the automotive's total mass, and $V_0$ is its initial speed. To obtain the amount of heat released by each brake, one must extract the automotive's weight distribution. Therefore, the amount of heat released from each disc is equal to the following:

$$Q = 0.5 \times {}^{1}\!/_{2}\, mV_0{}^2 = 0.25\, V_0{}^2 \tag{2}$$

The heat energy generated by brake friction can be transferred to the brake disc and pads. This distribution of thermal energy depends on the relative thermal resistances of the pad and brake disc, which is a function of the density of the respective materials, their thermal capacities and thermal conductivity, as well as the presence of any transfer film or third layer of the body at the interface. In theory, the thermal resistance of the pad should be higher than the thermal resistance of the disc to protect the brake fluid from high temperatures. Still, the amount of thermal resistance varies from one pad material to another. In this analysis, the following relations and calculations are performed to calculate the heat distribution coefficient between pad and disc (γ) for thermal input to the brake disc. The thermal penetration of the disc ξd and the thermal penetration of the pad ξp are obtained from the following relationships [17]:

$$\xi_d = \sqrt{K\rho_d c_d} \tag{3}$$

$$\xi_p = \sqrt{K\rho_p c_p} \tag{4}$$

Where, K is the heat transfer coefficient, ρ is the density, and c is the specific heat of the disc and pad. Sd and Sp, which are the disc and pad frictional contact surfaces, respectively, are obtained from the following relations:

$$S_d = 2\pi \int_{r_2}^{r_3} rdr \tag{5}$$

$$S_p = \varphi_0 \int_{r_2}^{r_3} rdr \tag{6}$$

Where, $\varphi_0$ is the central angle of the pad and $r_2$, and $r_3$ are the internal and external radii of the disc, respectively ("Fig. 6").

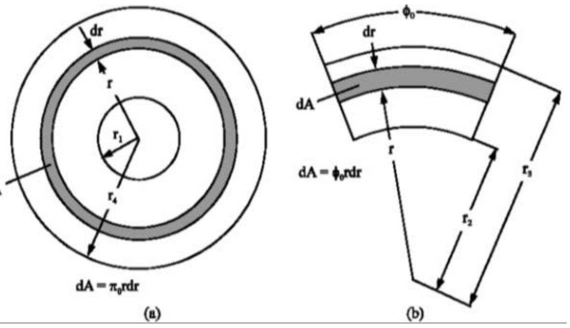

**Fig. 6** Elements of contact of two surfaces of disc and pad.

The relative braking energy (γ), which is called the heat distribution coefficient, is obtained by the following Equation:

$$\gamma = \frac{\xi_d S_d}{\xi_d S_d + \xi_p S_p} \tag{7}$$

The ratio of heat generated for friction between this surface is calculated from the following Equation:

$$d\dot{E} = r\omega\mu p\varphi_0 rdr \tag{8}$$

Where, $\varphi_0$ is the central angle of the pad, μ is the friction coefficient, ω is the angular velocity, and p is the surface contact pressure.

The heat flux in the disc for uniform pressure is a function of time and the change of the distance r, the reduction of the angular velocity during the braking time, and the work done by the friction force. This phenomenon often happens when the pads are new. The heat flux in the disc is obtained from the Equations (9-a and b) [17]:

$$q_d(r,t) = \frac{d\dot{E}_d}{dS_d} = \frac{\gamma\omega\mu p\varphi_0 r^2 dr}{2\pi r dr} = \frac{\varphi_0}{2\pi}\gamma\mu p r\omega_t \tag{9-a}$$

$$q_{0d}(r,0) = \frac{d\dot{E}_d}{dS_d} = \frac{\gamma\omega\mu p\varphi_0 r^2 dr}{2\pi r dr} = \frac{\varphi_0}{2\pi}\gamma\mu p r\omega_0 \tag{9-b}$$

Where, $\gamma$ is the heat distribution coefficient between the pad and disc, $\varphi_0$ is the central angle of the pad, $\mu$ is the friction coefficient, $\omega$ is the angular velocity, $d\dot{E}$ is the rate of heat produced due to friction between two surfaces and r is the radius of the disc.

The heat flux in the pad is also obtained from the Equations (10-a and b):

$$q_p(r,t) = \frac{d\dot{E}_p}{dS_p} = \frac{(1-\gamma)\omega\mu p\varphi_0 r^2 dr}{\varphi_0 r dr} = (1-\gamma)\mu p r\omega_t \tag{10-a}$$

$$q_{0p}(r,0) = \frac{d\dot{E}_p}{dS_p} = \frac{(1-\gamma)\omega\mu p\varphi_0 r^2 dr}{\varphi_0 r dr} = (1-\gamma)\mu p r\omega_0 \tag{10-b}$$

### 2.4.3. Calculation of Safety Factor

The conventional design method in mechanical engineering, which is sometimes called the classical method or deterministic design method, is based on the concept of the safety factor. This means that the design of different parts is done in such a way that the maximum applied stress is smaller than the minimum resistance of the materials used in the structure or part. In this research, the safety factor was determined using the theory of energy and torsion. According to the DE theory, material destruction due to yielding occurs when the torsional strain energy (or distortion energy) per unit volume is equal to or greater than the strain energy, such as its tensile or compressive yield strength. The theory of torsional energy is widely used in the case of deformable materials, and this theory should be used in problems where the type of theory is not mentioned [18]. In the DE theory, the Von-Mises stress component is calculated from Equation (11):

$$\sigma' = \left[\frac{(\sigma_1-\sigma_2)^2+(\sigma_2-\sigma_3)^2+(\sigma_3-\sigma_1)^2}{2}\right]^{1/2} \tag{11}$$

Where, $\sigma_1$, $\sigma_2$ and $\sigma_3$ are the main stresses in the part and $\sigma'$ is the component of Von-Mises stress. The safety factor is also determined from Equation (12):

$$\sigma' = \frac{S_y}{n} \tag{12}$$

In this relation, $S_y$ is the yield strength of the material used in the construction of the part and n is its safety factor.

Since the elastic stresses and strains are fully reversible and non-cumulative, the brake disc model is only considered for one braking period. The range of elastic strain with the range of stress $\sigma_a$ is by Hooke's law in the form of Equation (13):

$$\varepsilon_e = \frac{\sigma_a}{E} \tag{13}$$

Where, $\sigma_a$ is stress, $\varepsilon_e$ is elastic strain and E is modulus of elasticity.

### 2.5. Dynamic and Thermal Analysis of Finite Element Using Abaqus Software

After 3D modeling of disc and brake pad in Catia software; for dynamic analysis using the finite element method, the 3D model was transferred to Abaqus software.

#### 2.5.1. Determining the Properties of Ingredients in The Property Module

The mechanical properties of ceramic and gray cast iron were defined for disc and brake pad, respectively, according to “Table 1” in the property module of the Abaqus program, which included density, Poisson's ratio, thermal conductivity coefficient, specific heat, and modulus of elasticity (“Fig. 7”).

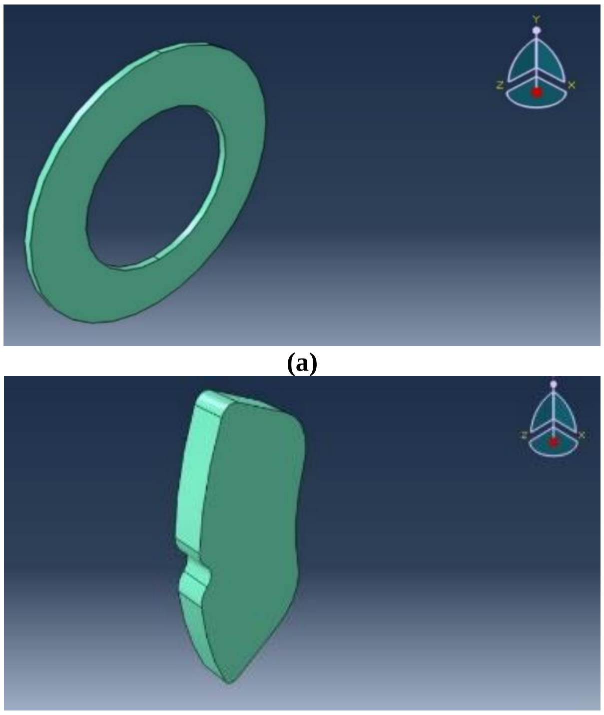

**(a)**

**(b)**

**Fig. 7** (a): Determining the properties of disc materials, and (b): Determining the properties of brake pad materials.

### 2.5.2. Assembling the Disc and Pad

Each model in Abaqus may consist of different parts, which are used to put these parts together and form a final system and apply geometric constraints between them using the Assembly module. This module's disc and brake pads form an integrated brake system after assembly ("Fig. 8"). Since each of these parts is designed in the same coordinates, when they are called in this part, they may overlap with each other, so to move them, the option Translate instance is used to move the vector.

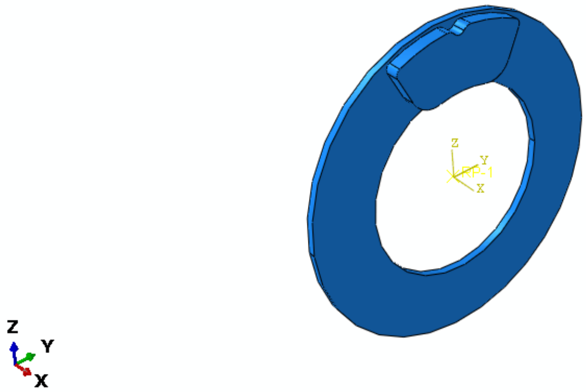

**Fig. 8** Disc and pad assembly.

### 2.5.3. Problem-Solving and the Type of Analysis in The Step Module

Each physical phenomenon has its differential Equations. Due to the dynamic nature of brake disc and pad analysis, a suitable solver is used to analyze the heat of folding from the friction between the disc and the brake pad. For this purpose, the Dynamic Explicit option, i.e., dynamic analysis with a braking time of 4 seconds, is considered in the Step module. Also, the purpose of doing a project in Abaqus software is to get a series of output data and analyze and check them. For this purpose, it is determined in the Step module that at the end of the work, dynamic stresses are delivered as output.

### 2.2.4. Contact Between the Disc and The Pad in The Interaction Module

Undoubtedly, the importance of collision and contact for analyzing a set in Abaqus is very high; therefore, in this study, we must specify the type of contact between the pads and the brake disc in the Interaction module ("Fig. 9"). Also, in this section, the contribution of the heat input to the disc and pad during braking should be determined, which is calculated using Equation (14). After calculating it, you should enter the obtained numbers in the Interaction module:

$$\frac{Q_d}{Q_p} = \frac{\sqrt{\rho_{d*}\lambda_{d*}C_d}}{\sqrt{\rho_{p*}\lambda_{p*}C_p}} \tag{14}$$

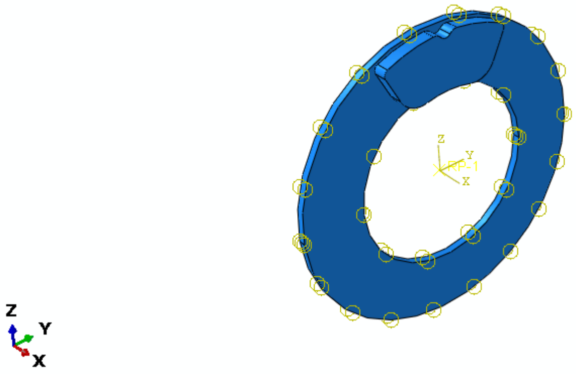

**Fig. 9** Determination of the type of disc and pad contact.

Where, $Q_d$ is the heat input to the disc, $Q_p$ is the heat input to the pad, ρ is the density, λ is the heat transfer coefficient, and c is the specific heat capacity.

### 2.5.5. Boundary Conditions and Application of Forces in The Load Module

In this section, the initial temperature of the disc and pad is assumed to be 30 °C, at time t=0, while the constant heat flux produced by pressing the pad on the friction surface of the disc is the only input heat source of the model. The boundary conditions in the symmetry state for the disc should only have rotation around the X axis ($U_1$) and no rotation along the Y and Z axes. It should also specify the same stages of boundary conditions for the pad that has freedom of movement only in the direction of the X-axis. The initial speed of the disc in this section should be specified as VR1, i.e., the speed around the X-axis, which is 260 radians/second here. The force applied to the pad during braking is a compressive force equal to one MPa. ("Fig. 10").

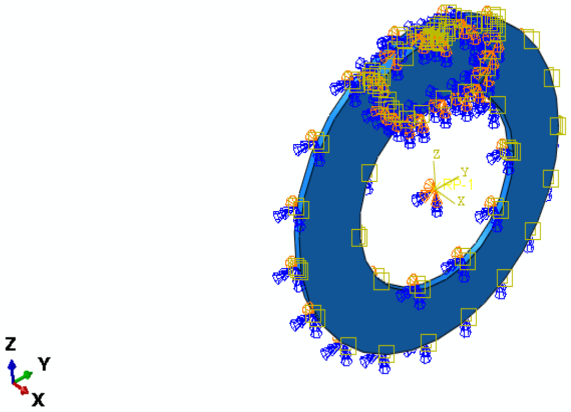

**Fig. 10** Determination of the boundary conditions and applying force on the disc and pad.

### 2-5-6- Meshing and Loading Conditions of Disc and Pad

In this research, the elements used for meshing, due to the symmetry of half of the disc and one number of brake pads, hexahedral (C3D8T) meshing with eight nodes, was used and created a regular network of elements in it. (“Figs. 11 and 12”). The number and size of the elements are inversely proportional to each other; that is, the more the number of elements in the mesh created on geometry, the smaller the size of the elements [19]. According to “Fig. 13”, with the increase in the number of elements (the elements become smaller), the stress has converged to a fixed limit.

**Fig. 11** Brake disc meshing.

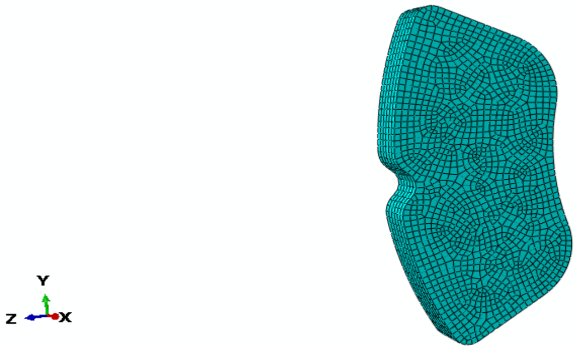

**Fig. 12** Brake pad meshing.

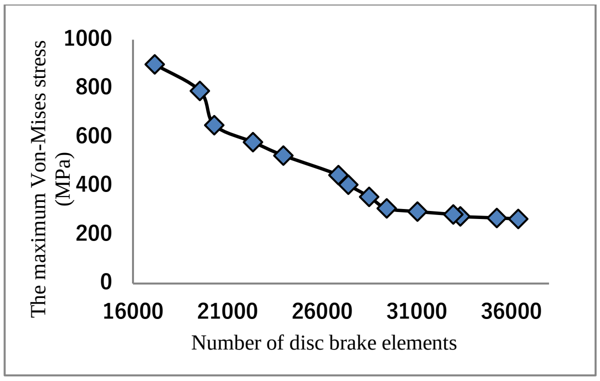

**Fig. 13** Brake disc meshing validation diagram.

## 3 RESULTS AND DISCUSSION

### 3.1. Von-Mises Stress of Disc

Figure 14 shows the Von-Mises stress contour of the ceramic disc. According to this Figure, the maximum Von-Mises stress in the contact area between the pad and the disc is equal to 260.7 MPa; meanwhile, in the cast iron disc (“Fig. 15”), the maximum Von-Mises stress is equal to 293.3 MPa. Figure 16 also shows the Von-Mises stress contour of an element of a ceramic disc.

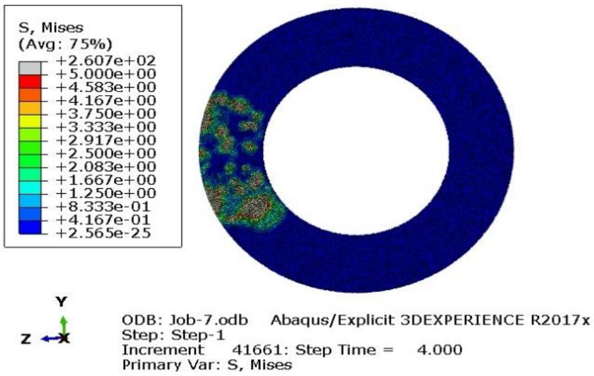

**Fig. 14** Von-Mises stress contour of ceramic disc.

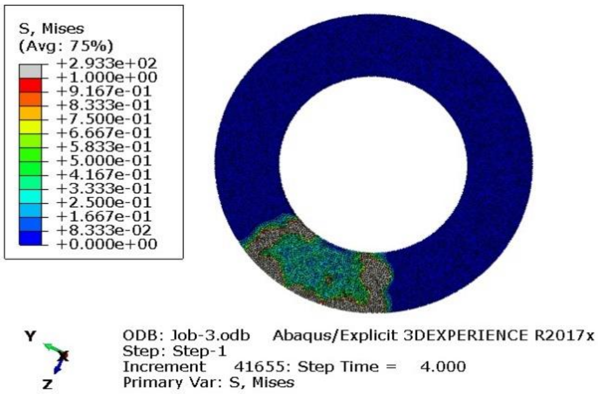

**Fig. 15** Von-Mises contour tension of cast iron disc.

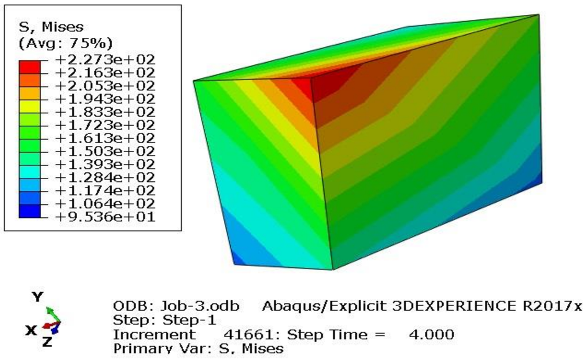

**Fig. 16** Von-Mises stress contour of a ceramic disc element.

### 3.1.1 Von-Mises Stress in The Peripheral Path of The Disc

This analysis analyzed three different paths of Von-Mises stress on the surface of ceramic and cast iron discs. Figure 17 shows a path marked on the surface of the ceramic disc and close to the hub for the Von-Mises stress.

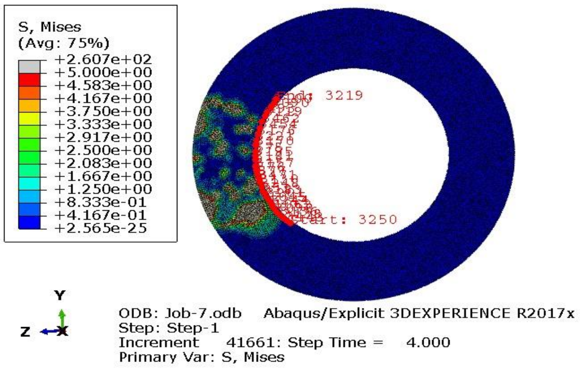

**Fig. 17** Von-Mises stress of the path on the surface of the inner diameter of the ceramic disc.

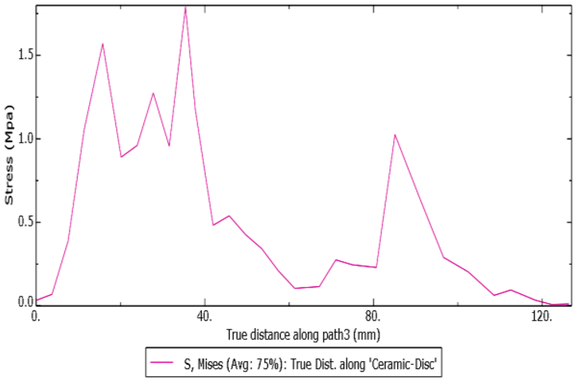

**Fig. 18** Von-Mises stress diagram of the path on the surface of the inner diameter of the ceramic disc.

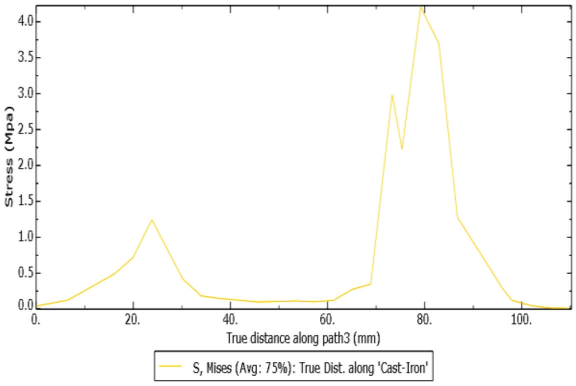

**Fig. 19** Von-Mises stress diagram of the path on the surface of the inner diameter of the cast iron disc.

The Von-Mises stress diagram related to this path ("Fig. 18") shows that the Von-Mises stress in the ceramic disc is between 0 and 1.75 MPa, while the value of Von-Mises stress in the same direction on the surface of the cast iron disc ("Fig. 19") fluctuates between 0 and 4 MPa.

### 3.1.2. Von-Mises Stress in The Disc Thickness

Figure 20 shows the Von-Mises stress diagram in the thickness of the ceramic disc. According to this figure, the stress is linear, and from the beginning of the path to the thickness of 2.3 mm, its value is nearly 20 MPa, and after that, this stress increases until the end, and its value reaches 75 MPa. Compared to the Von-Mises stress diagram in the thickness of the cast iron disc ("Fig. 21"), the stress along the path of the disc thickness increases from the beginning and reaches 14.5 MPa.

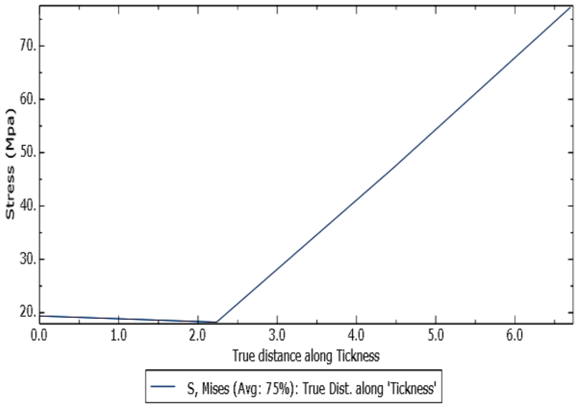

**Fig. 20** Von-Mises stress diagram in the thickness of the ceramic disc.

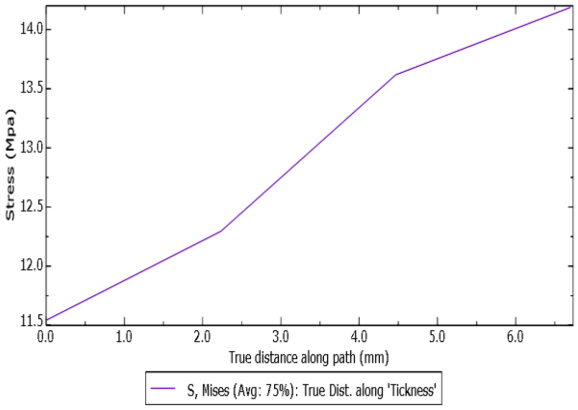

**Fig. 21** Von Mises stress diagram in the thickness of cast iron disc.

### 3.1.3. Comparison of Safety Factor of The Ceramic Disc and Cast-Iron Disc

It was considered that the yield strength of the ceramic disc is 498 MPa, and the yield stress of the cast iron disc is 425 MPa. Therefore, by placing these numbers and the maximum Von-Mises stress value obtained from the finite element analysis in Equation (12) and solving it, the coefficient Confidence is calculated. Comparing the safety factor values of the ceramic and cast iron disc shows that the ceramic disc has a higher safety factor ("Table 4").

**Table 4** Safety factor of ceramic and cast-iron disc

| Safety factor of ceramic disc | Safety factor of cast iron disc |
|---|---|
| 1.98 | 1.45 |

### 3.1.4. Shear Stress in Ceramic Disc

The shear stress contour ($\tau_{xy}$) is shown in "Fig. 22". The lowest shear stress in the xy direction equals -25.62 MPa, and the highest shear stress in the xy direction is +42.01 MPa. Also, the shear stress contour ($\tau_{xz}$) is shown in "Fig. 23". The lowest shear stress in the xz direction equals -36.97 MPa, and the highest stress in the xz direction is +99 MPa. "Table 5" compares shear stress values in ceramic and cast-iron discs.

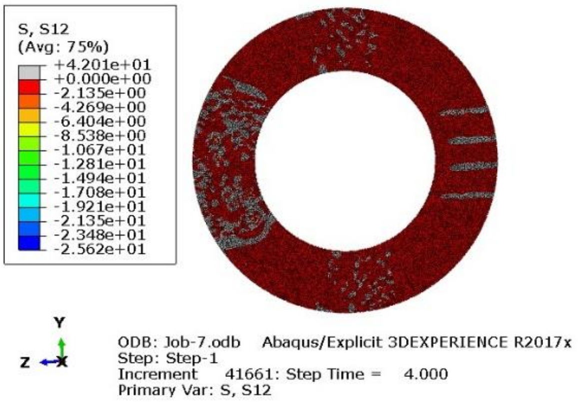

**Fig. 22** Shear stress contour ($\tau_{xy}$) in ceramic disc.

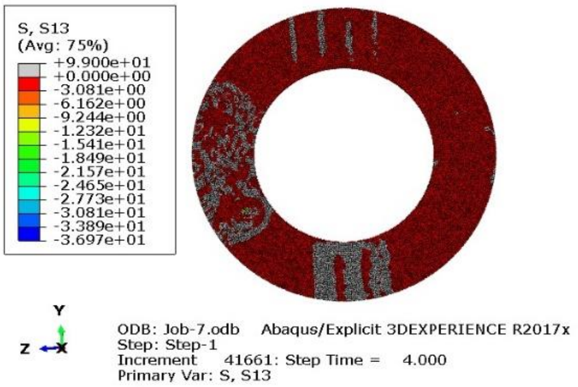

**Fig. 23** Shear stress contour ($\tau_{xz}$) in ceramic disc.

**Table 5** Comparison of shear stress values in ceramic and cast-iron discs

| shear stress | The lowest shear stress (MPa) | | The highest shear stress (MPa) | |
|---|---|---|---|---|
| | cast iron disc | Ceramic disc, | cast iron disc | Ceramic disc, |
| $\tau_{xy}$ (S12) | -43.27 | -25.62 | +44.45 | +42.01 |
| $\tau_{xz}$ (S13) | -43.87 | -36.97 | +130.5 | +99 |
| $\tau_{yz}$ (S23) | -80.15 | -79.53 | +90.04 | +70.78 |

### 3.1.5. Movement in Ceramic Disc

The displacement contour in Fig. 24 shows that the amount of displacement after the braking action is between 0 and +0.00002 mm.

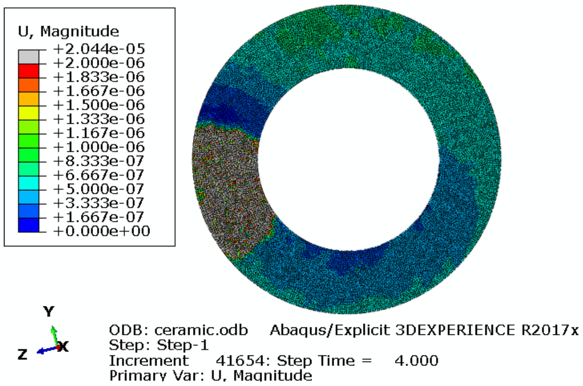

**Fig. 24** Displacement contour in ceramic disc.

### 2.3. Estimating the Temperature on The Surface of The Ceramic Disc and Comparing It with The Cast Iron Disc

Figure 25 shows the surface temperature contour of the ceramic disc, which is predicted by the finite element method by Abaqus software at the end of the braking operation for 4 seconds.

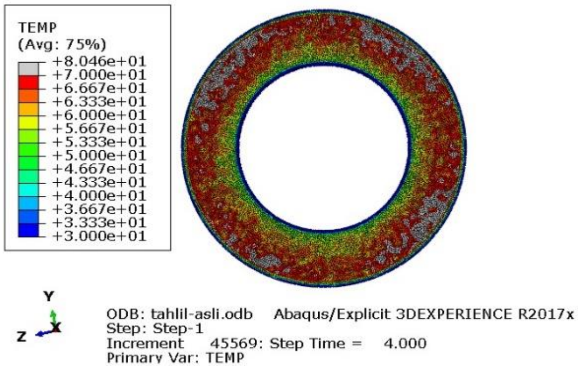

**Fig. 25** Ceramic disc surface temperature contour.

As can be seen, the maximum surface temperature of the ceramic disc is 80.46 °C, which is 148.1 °C, which is 84% lower than the cast iron discs (“Fig. 26”). Therefore, it can play a significant role in braking performance and ability. This analysis considers gray cast iron brake pads for both ceramic and cast iron discs.

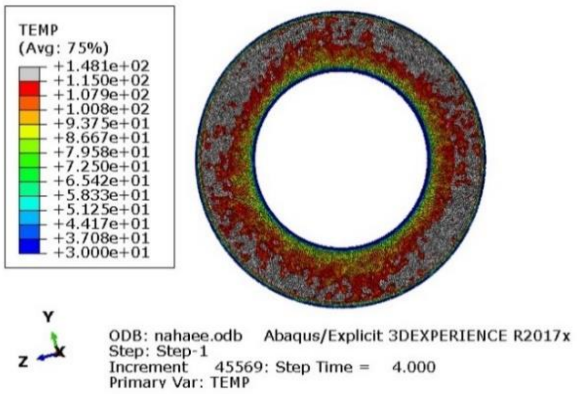

**Fig. 26** Cast iron disc surface temperature contour.

Figure 27 shows the contour of an element of a ceramic disc where the highest temperature is on its surface. Also, Fig. 28 shows the temperature versus time graph that shows a sudden increase in temperature from the initial moment of braking to the first second. In another 3 seconds from the time of full braking, the temperature is in the maximum range due to the equal rate of heat generation and heat exit from the contact area.

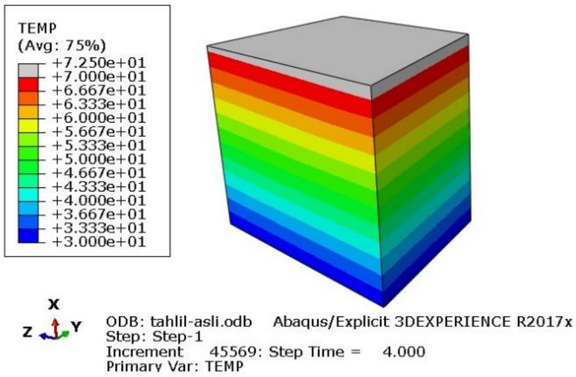

**Fig. 27** Ceramic disc surface temperature contour. Temperature contour of a ceramic disc element.

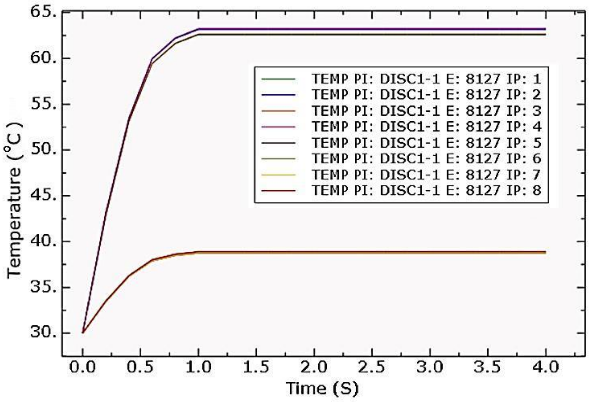

**Fig. 28** Ceramic disc surface temperature contour. Temperature-time diagram of an element of ceramic disc.

### 3.2.1. Temperature Distribution in The Peripheral Path of The Ceramic Disc

This analysis analyzed three environmental paths (external, middle, and internal) of the surface of the ceramic disc. Figure 29 shows the temperature contour in the second path (average environment) as an example. The temperature distribution diagram related to this path in “Fig. 30” shows that the temperature distribution in this path is mainly in the temperature range between 65 and 75 °C. Compared to the temperature distribution in the same route on the surface of the cast iron disc (“Fig. 31”), the temperature is mainly in the range between 100 and 130 °C.

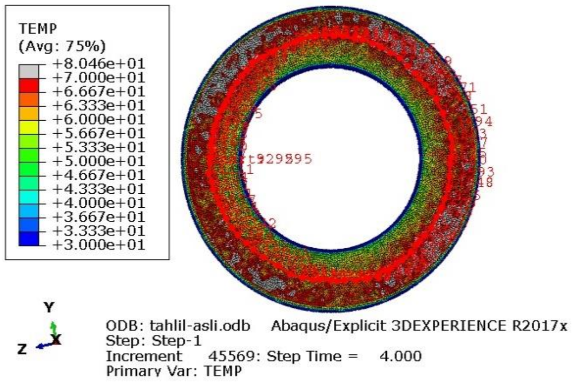

**Fig. 29** Ceramic disc surface temperature contour. Temperature distribution (average path) on the ceramic disc surface.

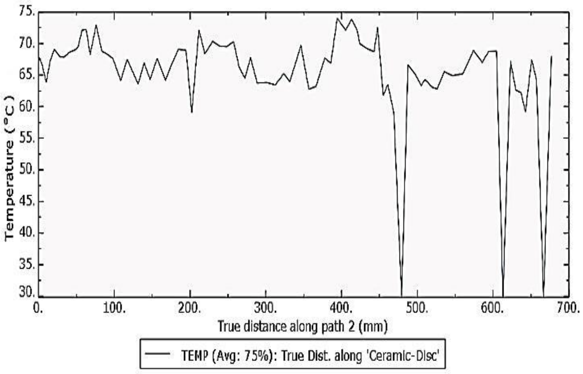

**Fig. 30** Ceramic disc surface temperature contour. Temperature distribution diagram in the medium path (ceramic disc).

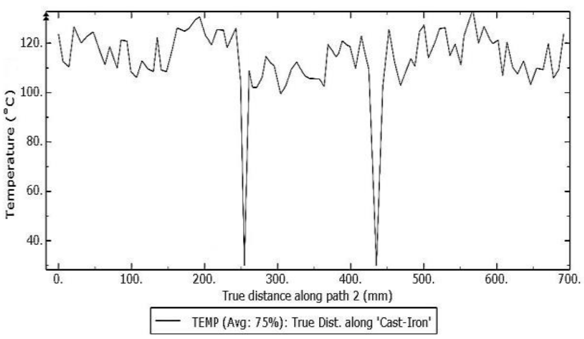

**Fig. 31** Ceramic disc surface temperature contour. Temperature distribution diagram (average path) of cast iron disc.

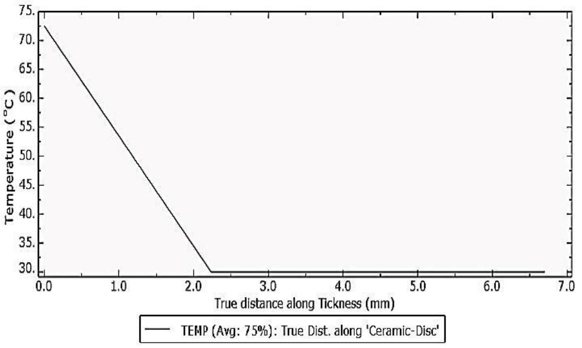

**Fig. 32** Temperature distribution diagram in the thickness of the ceramic disc.

### 3.2.2. Temperature Distribution in The Thickness of The Ceramic Disc

As “Fig.32” shows, the temperature distribution in the disc's thickness started from the pad's surface and the disc with a temperature of 72.5 °C. It penetrated to a depth of 2 mm from the disc's thickness. The rest of the way, the temperature of the disc thickness remains constant in the ambient temperature range; this is due to the contact of the back surface of the disc with air and its cooling.

### 3.2.3. The Effect of Temperature on The Reduction of Braking and Friction Coefficient

Brake discs are forced to absorb a significant amount of heat during braking. Decreasing braking creates a situation where heat is generated faster than it can transfer to the surrounding environment. The normal temperature of the disc in everyday driving is less than 135°C; during frequent braking, excessive heat may be generated, which reduces the brake's ability and even breaks it down. High temperature in disc brakes reduces the coefficient of friction and thus reduces friction, and high temperature also increases wear. The same things mentioned affect the performance of disc brakes and reduce the amount of braking power. Considering that the maximum temperature produced in the ceramic disc is 80.46°C (“Fig. 25”), it is concluded that even in frequent braking, the temperature of the ceramic disc is lower than usual. It shows that the ceramic disc does not lose its ability in regular braking.

### 3.2.4. The Effect of Temperature on The Formation of Tribo Layer, Wear, And Cracking

Pad and disc surfaces change their characteristics due to friction, wear, and other mechanical interactions related to increased frequent braking and increased temperature. The temperature created in the contact between the pad and the disc is a significant influencing factor on friction. It can be explained from the perspective that temperature affects the formation of the so-called tribo layer. Surfactant additives are present in the contact line of the pad and disc contact surfaces and control friction. The speed of production of this layer is influenced by surface activity dependent on temperature. Due to thermomechanical stresses caused by interactions resulting from friction, the ingredients of the disc and pad are gradually removed from its surface (wear occurs). Since the wear on the contact surface is high, the brake assembly's risk of failure and inefficiency increases. One of the explanations for this phenomenon is that metal wear debris fills the open area on the disc surface and increases the tendency for more friction between the two contact surfaces. It makes it easier for the two contacting surfaces to form an adhesive-like bond (welded joint).

The increase in disc temperature and the resulting thermal stress is the main cause of disc cracking, especially on the disc surface. This cracking can be caused by the thermal energy entering the friction surfaces. The occurrence of surface tearing and cracking that occurs in a brake depends on the induced temperature. During repeated braking, fatigue characteristics can be an important factor in determining the initiation of the disc cracking. The result of the analysis of the ceramic disc shows that due to the low temperature, wear, and cracking factors do not occur due to the high temperature.

## 4 CONCLUSIONS

This research used finite element analysis to study stress and temperature in ceramic disc brakes. By comparing the analysis of stress and temperature in ceramic discs compared to cast iron discs, the following results were obtained.

- The maximum Von-Mises stress in the ceramic disc is 260.7 MPa. This maximum tension is created in the contact area between the pad and the disc. While the maximum Von-Mises stress in the cast iron disc is 293.3 MPa.
- Comparison of shear stress values in ceramic and cast iron discs shows that cast iron disc has more shear stress in xy, xz and yz directions (respectively +44.45, +130.5 and +90.04 MPa) than ceramic disc. It is entered in xy, xz and yz directions (+42.01, +99 and +70.78 MPa, respectively).
- The comparison of calculated safety factor values of ceramic and cast iron disc showed that ceramic disc has a higher safety factor (1.98) than cast iron disc (1.45).
- Comparison of analysis of ceramic and cast iron brake discs during braking by finite element method showed that the amount of heat produced in the ceramic disc during braking action in 4 seconds is almost 84% less than the cast iron disc in the same period.
- The low temperature in the ceramic disc reduces wear and cracking and ultimately improves the braking performance of the brake disc.

## REFERENCES

[1] Amrollahi Beyuki, H., Mahmoudi Kleiber, M., Chassis and Body Technology, In Persian, SAD Publications, 2019.

[2] Turner, W.V., The Air Brake as Related to Progress in Locomotion. Pittsburg, Pennsylvania: Westinghouse Air Brake Company, 1910.

[3] Buckman, L. C., Commercial Vehicle Braking Systems: Air Brakes, ABS and Beyond, Society of Automotive Engineers, Indianapolis, The 43rd L. Ray Buckendale Lecture, International Truck and Bus Meeting and Exposition, Indianapolis, Society of Automotive Engineers, 1998.

[4] Sowjanya, K., Suresh, S., Structural Analysis of Disc Brake Rotor, International Journal of Computer Trends and Technology (IJCTT), Vol. 4, No. 7, 2013.

[5] Jahdi, R., Shakiba Jahormi, S., A Study on The Production and Application of Ceramic Matrix Composites in Macro and Micro Scale, In Persian, The First National Conference on Fundamental Research in Mechanical Engineering, Tehran, 2017.

[6] Khaleel, H. H., Khashan, M. K., and Baqir, A. SH., Modeling and Analysis of Disc Brake in Automobiles, Journal of Mechanical Engineering Research & Developments (JMERD), 2018.

[7] Venkatramanan, R., Kumaragurubaran, S. B., Vishnu Kumar, C., Sivakumar, S., and Saravanan, B., Design and Analysis of Disc Brake Rotor, International Journal of Applied Engineering Research, ISSN: 0973-4562, Vol. 10, No. 19, 2015.

[8] Manavalan, S., Aswin Gopi, J., Arivarasu, A., and Abishek, A. HI., Chandru, S., Review on Ceramic Disc Brake System, International Journal of Recent Technology and Engineering (IJRTE), ISSN: 2277-3878, Vol. 7, No, 6S2, 2019.

[9] Belhocine. A., Finite Element Analysis of Automotive Disc Brake and Pad in Frictional Model Contact, International Journal of Manufacturing, Materials, and Mechanical Engineering, Vol. 5, No. 4, 2015, pp. 32-62.

[10] Limpert, R., An Investigation of Thermal Conditions Leading to Surface Rupture of Cast Iron Rotors, SAE Technical Paper Series, , 1972, 720447.

[11] Söderberg, A., Andersson, S., Simulation of Wear and Contact Pressure Distribution at The Pad-To-Rotor Interface in A Disc Brake Using General Purpose Finite Element Analysis Software, International Journal of Wear, 2009.

[12] Mujawar, L., Savatekar, P., Korade, A., Naidu, A., Ekal, O., and Nalawade, S., Design and Thermal analysis of Disc Brake, International Research Journal of Engineering and Technology (IRJET), Vol. 05, No. 08, 2018.

[13] Sreedevi, K. N. V., Radha Krisha Prasad, P., Murali Krishna, M. V. S., and Gangireddy, J. N., Modeling and Analysis of a Disc Brake, International Journal of Science and Research (IJSR), ISSN: 2319-7064, 2018.

[14] Pranta, M. H., Rabbi, M. S., Banik, M. C., Hafez, M. G., and Ming Chu, Y. U., A Computational Study on Structural and Thermal Behavior of Modified Disc Brake Rotors, Alexandria Engineering Journal, 2022.

[15] Suwal, B., Maharjan, S., Design of Rotor Disc Brake using Structural & Thermal Analysis, IOE Graduate Conference, 2021.

[16] Rajkamal, M. D., Dylan Abraham Samson, T., Dhinesh Kumar, P., and Chithambaravishnu, S., Structural Analysis of Disc Brake, International Journal of Mechanical Engineering and Technology (IJMET), Vol. 9, No. 3, 2018.

[17] Deressa, K. T., Tilahun, D., Thermal Stress Analysis of Disc Brake Rotor by Finite Element Method, A Thesis Submitted to the Graduate School of Addis Ababa University in Mechanical Engineering, 2013.

[18] Budynas, R. G., Nisbett, J. K., Shigley's Mechanical Engineering Design (8th ed), McGraw-Hill's, 2008.

[19] Nazemosadat, S. M. R., Ghanbarian, D., Naderi-Boldaji, M., and Nematollahi, M. A., Structural Analysis of a Mounted Mouldboard Plough using Finite Element Simulation Method, Spanish Journal of Agricultural Research, Vol. 20 No. 2, 2022, pp. 1-14, https://doi.org/10.5424/sjar/2022202-18157.

*Int. J. Advanced Design and Manufacturing Technology, 2023, Vol. 16, No. 4, pp. 23-35*

*DOI: 10.30486/admt.2024.1983665.1405 ISSN: 2252-0406 https://admt.isfahan.iau.ir*

# Evaluation and Comparison of Different Artificial Neural Networks and Genetic Algorithm in Analyzing a 60 MW Combined Heat and Power Cycle

**Parisa Ghorbani**
Department of Mechanical Engineering, Najafabad Branch, Islamic Azad University, Najafabad, Iran
Email: parisaghorbani.71@gmail.com

**Arash Karimipour ***
Department of Mechanical Engineering, Najafabad Branch, Islamic Azad University, Najafabad, Iran
Email: arashkarimipour@gmail.com
*Corresponding author

**Received: 9 April 2023, Revised: 29 October 2023, Accepted: 4 November 2023**

**Abstract:** The constant growth of energy consumption, increased fuel costs, non-renewable fossil fuel sources, and environmental pollution caused by increased emission of greenhouse gases, and global warming highlight the need for the analysis and optimization of main energy generation bases, i.e. power plants. The Artificial Neural Network (ANN) is a useful novel method for better processing information and controlling, and optimizing and modeling industrial processes. For the first time in this study, an ANN was designed and applied to data extracted from modeling and analyzing a 60 MW combined heat and power generation power plant. To this end, the error backpropagation network was selected as the optimal network, and the generator load or capacity, condenser pressure, and Feedwater temperature were considered inputs to the ANN. The energy and exergy efficiencies of the power plant and the overall energy and exergy losses of the cycle were considered outputs of the ANN. The ANN was coded and designed with the help of MATLAB. The Genetic Algorithm (GA) was used to obtain the optimal values of input parameters and the minimum losses and maximum efficiencies based on the first and second laws of thermodynamics.

**Keywords:** Energy Efficiency, Genetic Algorithm, Irreversibility, Neural Network, Steam Power Plant

**Biographical notes: Parisa Ghorbani** received her MSc in Mechanical Engineering from the Department of Mechanical Engineering, Najafabad Branch, Islamic Azad University, Najafabad, Iran in 2021. Her current research interest includes the optimization of energy generation stations and turbo machines. **Arash Karimipour** is an Associate Professor of Energy Conversion at the Department of Mechanical Engineering, Najafabad Branch, Islamic Azad University, Najafabad, Iran. He received his PhD in Mechanical Engineering from Sistan & Baluchestan University of Iran. His current research focuses on fluid flow, thermodynamics, heat transfer and energy.

Research paper

## 1 INTRODUCTION

The vital role of electricity in the industrial and economic infrastructure and the huge amounts of investment in this sector makes proper utilization and efforts necessary for optimizing the power industry. Most thermal power plants are old but play a key role in supplying the required electricity. Identifying the minimum and maximum energy losses in different parts of power plants and estimating the optimal first- and second-law efficiencies with the maximum values for components and the power plant greatly help the proper design and improvement of thermal power plants bringing useful environmental and economic outcomes. Different methods are used for repowering and optimizing to achieve better performance in power plants. The ANN and GA are useful methods for this purpose and have been extensively used in the literature. Jack *et al.* used an ANN based on the simulation results of a physical model for optimizing and minimizing the costs of a CHP plant. According to their results, the ANN reduced the time required for analyzing the system by more than 7000 times. The optimization results also confirmed the role of exact prediction of the performance of each piece of equipment using a physical model. The computational time decreased in this study while improving the optimization accuracy [1]. In another study, after modelling and obtaining the results for different modes in Bandar Abbas Steam Power Plant, Nikbakht *et al.* optimized the power cycle by the GA using the exergy efficiency and power generation cost functions. The Pareto diagram displaying cost variations versus the exergy efficiency plays a key role in selecting the proper investment mode [2]. The GA and the feedforward ANN with multiple hidden layers were considered for the optimal estimation of daily power consumption in a real university building in the UK. Considering the significant relationship between the influential factors and power consumption in the real world, the use of multiple hidden layers improves the prediction accuracy of the ANN. The optimal architecture of the model is generally determined by a very complex time-consuming trial-and-error process. To cope with this problem, the GA was used for the automatic design of an optimal architecture with improved generalizability. Data measured during 1.5 years was used for training and testing the proposed model [3]. An intelligent GA-based ANN was employed to deal with the estimation error, long delays, high inertia, and the nonlinear nature of the steam temperature controlled in the power plant. The GA allows optimization, global searching, rapid convergence, and improvement of the network weights. The simulation results confirmed the superiority of the intelligent ANN control system over the conventional control system in terms of control and robustness [4].

Full repowering methods can be used as efficient, previously experienced, and generalizable techniques considering the large number of old power plants and the need to rebuild the vital power generation sector. This method is usually used for repowering power plants at the end of their useful life. In such cases, the initial capital costs significantly decrease as compared to the construction of a combined cycle with the same specifications. Taking into account the unit price of electricity and the exergy efficiency of Besat Power Plant as objective functions, Hosseinalipour *et al.* obtained the most optimal technical-economic specifications of the repowering cycle of Baset Power Plant using the GA optimization technique in single- and two-objective optimization scenarios. Using the full repowering method and GA optimization, a 12-17% increase was obtained in the thermal efficiency [5]. Adding a gas turbine to the steam power plants is also known as a repowering method to enhance the specifications of the steam cycle and heat recovery from additional cycles. Repowering methods can be divided into partial and overall repowering techniques. Parallel Feedwater heating is considered a novel partial repowering method. Mehrpanahi *et al.* applied this method to Shahid Rajaei Power Plant. The electricity price and exergy efficiency were considered objective functions in the single- and two-objective optimizations. The use of the GA led to reasonable results for improved performance of the cycle [6].

In this study, an ANN is used for processing data extracted from analyzing and modeling the considered power plant. The GA [7-12] is used to obtain the optimal values for the variable thermodynamic parameters of the cycle, the minimum losses, the maximum first- and second-law efficiencies, and the power generation conditions with the maximum efficiency.

## 2 PROBLEM STATEMENT

For the first time in this study, an ANN is designed and applied to data extracted from modeling and analyzing the considered power plant. The error backpropagation network was selected as the optimal network, and the generator load or capacity, the condenser pressure, and the Feedwater temperature were considered inputs to the ANN. Power plant energy and exergy analysis (first and second laws of thermodynamics), and the overall energy and exergy losses of the cycle were considered the ANN outputs. The generator loads and capacities were 15, 30, 45, and 60 MW, and the Feedwater temperatures were 200, 210, 220, and 230˚C. The condenser pressure ranged from 0.050 to 0.175 bar. These values were considered inputs to the designed ANN. Considering these inputs, 96 data were extracted from thermodynamic modelling of the cycle for each output.

## 3 ANN ARCHITECTURE AND TRAINING

Neural networks can be regarded as information processing systems. By training the ANN with the learning algorithms, the neural network makes the output vector closer to the target by changing and modifying the weight vector and biases.

This study aims to achieve optimal conditions for a power plant with maximum efficiency and minimum energy and exergy losses. The results are analyzed by the error backpropagation ANN in which the output error is computed by comparing the output rate with the desired value or the experimental value. The network has a feedforward architecture in which input data to the network are processed feedforward, and the output of each layer barely affects the next layer. Figure 1 schematically displays the architecture of the designed ANN.

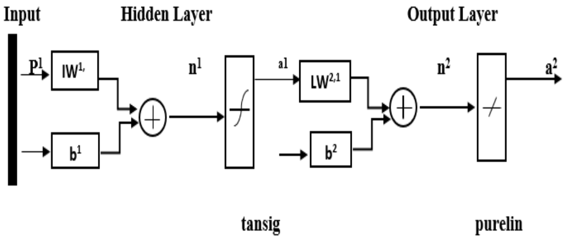

**Fig. 1** The architecture of the error backpropagation network [11].

To analyze the results using the error backpropagation network, the generator load or capacity, the condenser pressure, and the Feedwater temperature were considered inputs to the ANN. The energy and exergy efficiencies of the power plant and the overall energy and exergy losses of the cycle, were considered the ANN outputs. The ANN was coded and designed with the help of MATLAB.

Considering the role of ANN training and architecture in the output of the improved network performance, the network architecture was examined by varying the number of neurons in the hidden layer (10, 15, and 20 neurons). Various training methods were considered for the error backpropagation networks, and the best training method and network architecture were selected for outputs. The results are given in “Tables 1 to 4”.

After multiple tests and comparison of the performance of the ANN with different architectures and training methods, the error backpropagation network via a single secret layer and 10 neurons trained by the Levenberg-Marquardt algorithm was considered the best network with a good performance for analyzing the study results. “Tables 1 to 4” show a significant decrease in the mean squared error (MSE) of all four outputs in the Levenberg-Marquardt algorithm. The learning rules of the Levenberg-Marquardt algorithm are as follows:

$$\boldsymbol{x}_{k+1} = \boldsymbol{x}_k - [\boldsymbol{J}_k{}^T\boldsymbol{J}_k + \mu_k\boldsymbol{I}]^{-1}\boldsymbol{J}_k{}^T\boldsymbol{e}_k \qquad (1)$$

$$\boldsymbol{J}_k = \begin{bmatrix} \frac{\partial e_1}{\partial x_1} & \frac{\partial e_1}{\partial x_2} & \cdots & \frac{\partial e_1}{\partial x_n} \\ \frac{\partial e_2}{\partial x_1} & \frac{\partial e_2}{\partial x_2} & \cdots & \frac{\partial e_2}{\partial x_n} \\ \vdots & \vdots & \ddots & \vdots \\ \frac{\partial e_N}{\partial x_1} & \frac{\partial e_N}{\partial x_2} & \cdots & \frac{\partial e_N}{\partial x_n} \end{bmatrix} \qquad (2)$$

Where, $\boldsymbol{e}^T = [e_1 \quad e_2 \quad \cdots \quad e_N]$ and $e$ shows the error (difference) between the existing output and the desired worth. $\mu_k$ checks the convergence quickness so that it increases to accelerate training as the error increases. In contrast, it decreases to guarantee convergence of the algorithm when the error decreases.

**Table 1** Contrast of network architectures and training styles for the initial output

| Training type | Neurons numbers in the hidden layer | Mean square error (MSE) |
|---|---|---|
| MATLAB default | 20 | 0.00094 |
| MATLAB default | 15 | 0.0000092 |
| MATLAB default | 10 | 0.000000514 |
| Gradient descent training (traingd) | 10 | 0.45 |
| Gradient descent with momentum training (traingdm) | 10 | 0.88 |
| Variable learning rate (traingda) | 10 | 0.22 |
| Variable learning rate (traindgx) | 10 | 0.058 |
| Resilient back propagation (trainrp) | 10 | 0.008 |
| Conjugate gradient (traincgf) | 10 | 0.046 |
| Conjugate gradient (traincgp) | 10 | 0.028 |
| Conjugate gradient (traincgb) | 10 | 0.017 |
| Conjugate gradient (trainscg) | 10 | 0.013 |
| Quasi-Newtonian (trainbfg) | 10 | 0.0024 |
| Quasi-Newtonian (trainoss) | 10 | 0.17 |
| Levenberg Marquardt (trainlm) | 10 | 0.00000215 |

**Table 2** Contrast of network architectures and training styles for the second output

| Training type | Neurons numbers in the hidden layer | Mean square error (MSE) |
|---|---|---|
| MATLAB default | 20 | 0.000266 |
| MATLAB default | 15 | 0.00000677 |
| MATLAB default | 10 | 0.000000136 |
| Gradient descent training (traingd) | 10 | 0.163 |
| Gradient descent with momentum training (traingdm) | 10 | 5.06 |
| Variable learning rate (traingda) | 10 | 1.27 |
| Variable learning rate (traindgx) | 10 | 0.16 |
| Resilient back propagation (trainrp) | 10 | 0.095 |
| Conjugate gradient (traincgf) | 10 | 0.015 |
| Conjugate gradient (traincgp) | 10 | 0.146 |
| Conjugate gradient (traincgb) | 10 | 0.084 |
| Conjugate gradient (trainscg) | 10 | 0.015 |
| Quasi-Newtonian (trainbfg) | 10 | 0.003 |
| Quasi-Newtonian (trainoss) | 10 | 0.2 |
| Levenberg Marquardt (trainlm) | 10 | 0.00000154 |

**Table 3** Contrast of network architectures and training styles for the third output

| Training type | Neurons numbers in the hidden layer | Mean square error (MSE) |
|---|---|---|
| MATLAB default | 20 | 1202.84 |
| MATLAB default | 15 | 544.68 |
| MATLAB default | 10 | 252.31 |
| Gradient descent training (traingd) | 10 | 584698785.16 |
| Gradient descent with momentum training (traingdm) | 10 | 3602804076.61 |
| Variable learning rate (traingda) | 10 | 10315158.62 |
| Variable learning rate (traindgx) | 10 | 3701847.85 |
| Resilient back propagation (trainrp) | 10 | 280775.64 |
| Conjugate gradient (traincgf) | 10 | 1832222.88 |
| Conjugate gradient (traincgp) | 10 | 389779.9 |
| Conjugate gradient (traincgb) | 10 | 362442.54 |
| Conjugate gradient (trainscg) | 10 | 337732.16 |
| Quasi-Newtonian (trainbfg) | 10 | 3865188.29 |
| Quasi-Newtonian (trainoss) | 10 | 4846449.38 |
| Levenberg Marquardt (trainlm) | 10 | 574.16 |

**Table 4** Contrast of network architectures and training styles for the fourth output

| Training type | Neurons numbers in the hidden layer | Mean square error (MSE) |
|---|---|---|
| MATLAB default | 20 | 1584.15 |
| MATLAB default | 15 | 489.62 |
| MATLAB default | 10 | 171.93 |
| Gradient descent training (traingd) | 10 | 24445553224.9 |
| Gradient descent with momentum training (traingdm) | 10 | 5819427709.58 |
| Variable learning rate (traingda) | 10 | 50957217.11 |
| Variable learning rate (traindgx) | 10 | 47142966.22 |
| Resilient back propagation (trainrp) | 10 | 3551275.95 |
| Conjugate gradient (traincgf) | 10 | 2304328.88 |
| Conjugate gradient (traincgp) | 10 | 49396333.66 |
| Conjugate gradient (traincgb) | 10 | 66943211.48 |
| Conjugate gradient (trainscg) | 10 | 6070721.82 |
| Quasi-Newtonian (trainbfg) | 10 | 5272623.91 |
| Quasi-Newtonian (trainoss) | 10 | 40014703.3 |
| Levenberg Marquardt (trainlm) | 10 | 64.295 |

## 4 GENETIC ALGORITHMS

Influenced by the evolutionary manner in nature, the Genetic Algorithm (GA) solves problems. Like in nature, the GA makes a population of creatures and obtains an optimum set or an optimum creature through certain operations. According to the GA structure, after recognizing and modeling the problem, and forming the initial population to achieve the final solution, namely the optimal values for the problem parameters, an iterative process should be repeated to meet the end conditions. Given the problem geometry, a multi-objective optimization problem is solved in this study by the GA with specifications in “Table 5”. The GA forms an elementary population of $N$ random arrangements [7-9]:

$$\bar{w}_{ij} \in [-\omega, +\omega]\ \omega > 0, \tag{3}$$

$$w_{ijk} \in\ [-\omega, +\omega]\ \omega > 0, \tag{4}$$

$$F_s^g = \frac{1}{E_s^g} S = 1,2, \dots, N, \tag{5}$$

$$E_s^g = \frac{1}{2P} \sum_{p=1}^{P} \sum_{i=1}^{K} (y_{spi}^g - d_{pi})^2 \ \ y_{spi}^g = \Gamma\left(\bar{w}_s^g, w_s^g, x_p\right) \tag{6}$$

$$P(Z, t+1) = P(Z, t) \frac{f(Z)}{\bar{f}} (1 - \{P_c losses\}) + \{P_c gains\} \tag{7}$$

This is moreover part of an idealized model of a rudimentary GA. The potentiality of “losses” and “gains” for the string $Z$ = 000 is calculated below, while $P$I0 = 1 signifies the possibility of crossover [10].

$$\begin{aligned} \text{Losses} = {} & P_{\text{I0}} f(111) \bar{f} P(111, t) + \\ & P_{\text{I0}} f(101) \bar{f} P(101, t) + P_{\text{I1}} f(110) \bar{f} P(110, t) + \\ & P_{\text{I2}} f(011) \bar{f} P(011, t), \end{aligned} \tag{8}$$

$$\begin{aligned} & Gains \\ & = P_{\text{I0}} f(001) \bar{f} P(001, t) f(100) \bar{f} P(100, t) \\ & + P_{\text{I1}} f(010) \bar{f} P(010, t) f(100) \bar{f} P(100, t) \\ & + P_{\text{I1}} f(011) \bar{f} P(011, t) f(100) \bar{f} P(100, t) \\ & P_{\text{I2}} f(001) \bar{f} P(001, t) f(110) \bar{f} P(110, t) \ + \\ & P_{\text{I2}} f(001) \bar{f} P(001, t) f(010) \bar{f} P(010, t) \end{aligned} \tag{9}$$

**Table 5** The GA specifications

| Specifications | Factor |
|---|---|
| Number of variables | 3 |
| The upper limit of variations | 60, 0.175, 230 |
| The lower limit of variations | 15, 0.05, 200 |
| Population size | 50 |
| Display level | ‘iter’ |
| Plot function (plotFcn) | ‘gaplotparet’ |
| Pareto fraction | 0.6 |

## 5 RESULTS AND DISCUSSION

As previously mentioned, this study aimed to design and apply an ANN on data extracted from modeling and analyzing the 60 MW combined heat and power generation power plant. The error backpropagation network was selected as the optimal network for this purpose. The generator load or capacity, the condenser pressure, and the Feedwater temperature were considered inputs to the neural network. The energy and exergy efficiencies of the power plant and the overall exergy and energy losses of the cycle were considered the ANN outputs. The results obtained from the selected network are analyzed in the following sections.

### 5.1. The Performance Diagram of The Optimal Network

To ensure the accuracy of the designed neural network, besides the training dataset for the network, a dataset is automatically used for validation and some data in the test dataset to examine error variations. When a network is well trained, the error decreases in both the test and validation datasets and error propagation ends. The performance or efficiency diagrams versus the epoch show error variations in datasets. As shown in “Figs. 2 to 5”, the most excellent network appearance for the first output, *i.e.*, the energy efficiency, is obtained at epoch 724 with an MSE of 0.00000215.

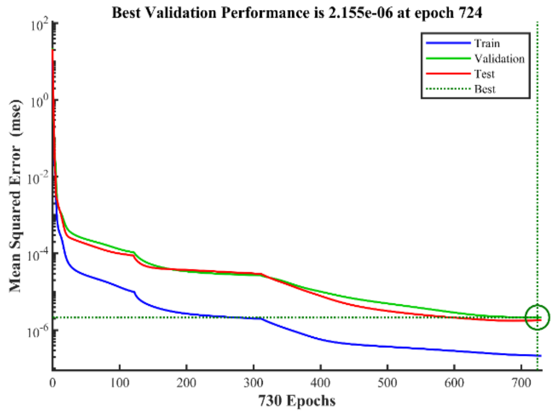

**Fig. 2** The optimal performance of the network for the first output.

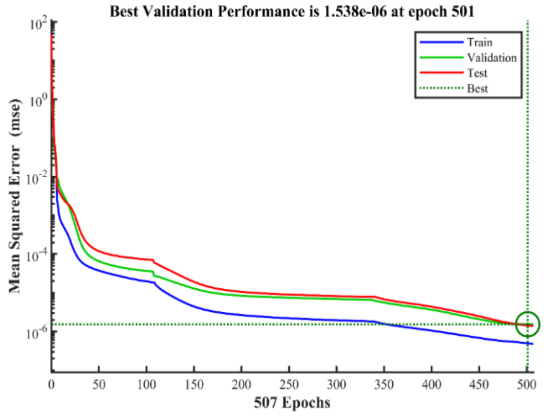

**Fig. 3** The optimal performance of the network for the second output.

It was seen that the best network performance for the second (exergy efficiency), third (energy losses), and fourth outputs is obtained at epochs 501, 92, and 466 with an MSE of 0.00000154, 574.16, and 64.295.

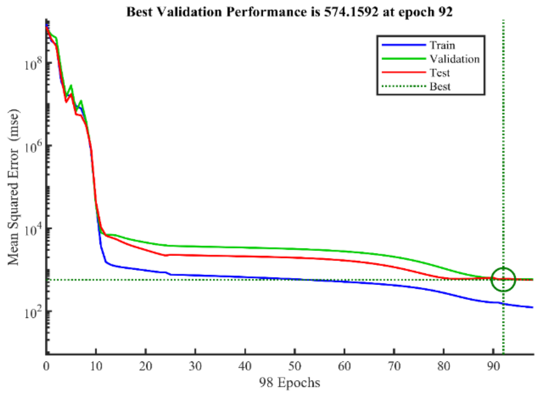

**Fig. 4** The optimal performance of the network for the third output.

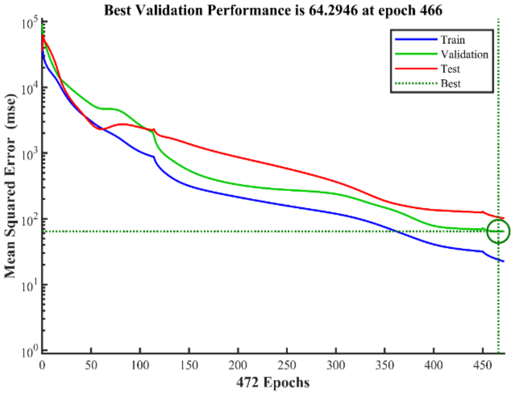

**Fig. 5** The optimal performance of the network for the fourth output.

## 5.2. The Regression Diagram for The Optimal Network

A major challenge facing linear regression is to reduce diversity among the predicted & observed values in existing data. A lower difference indicates better consistency between the predicted and observed values so that the regression approaches a desired value of unity. Figures 6 to 9 show the regression diagrams of the optimal network for the first to fourth outputs. As shown in "Figs. 6 to 9", three regression diagrams are plotted to separately analyze the accuracy. The 4th diagram tests the three datasets together to plot the accuracy diagram. For all four outputs, any dataset with a regression value of 1 shows a very good accuracy suggesting that the designed neural network was well and adequately trained and well predicted all untrained points. Consequently, the network is reliable with sufficient accuracy to analyze the study results.

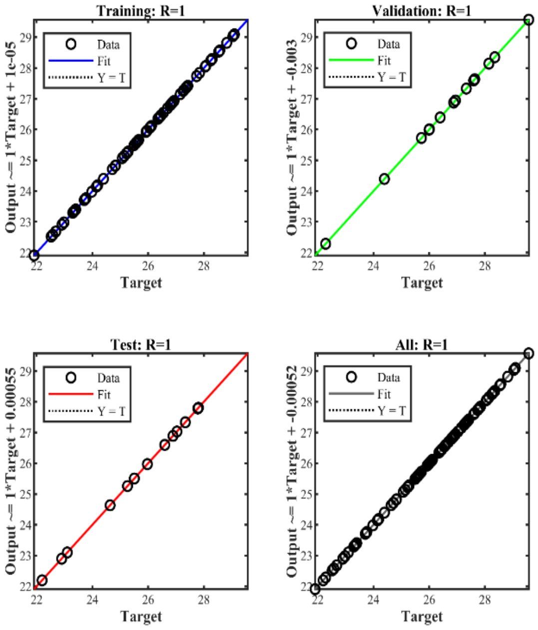

**Fig. 6** Regression chart at first output of the optimum network.

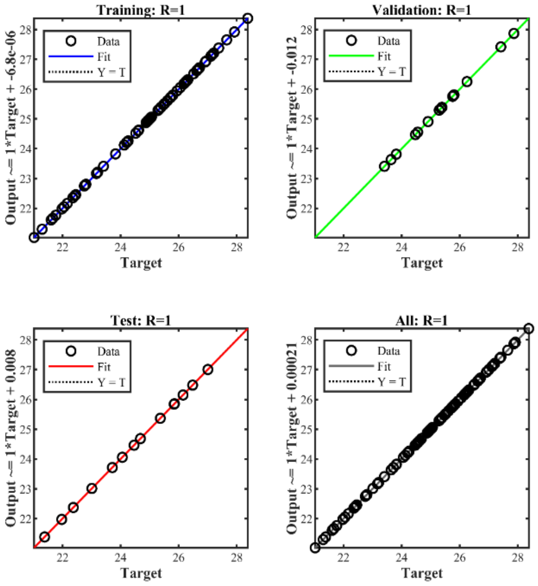

**Fig. 7** Regression chart at the second output of the optimum network

## 5.3. The Network Consequences at Trained Points

Figures 10 and 11 display the results for the optimal neural network. As shown, the power plant efficiency increases with increasing the generator load as it approaches the production capacity of the power plant

(60 MW). The maximum exergy and energy efficiencies are obtained at full loading of the cycle when the generator is at a maximum capacity of 60 MW. Peaks appear with increasing the Feedwater temperature.

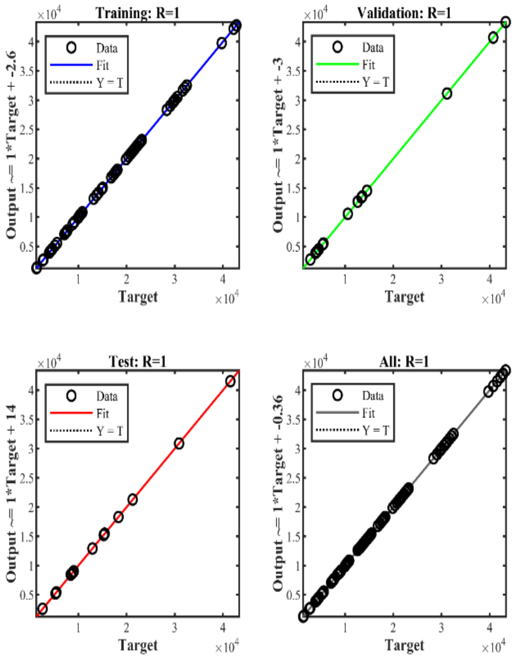

**Fig. 8** Regression chart at the third output of the optimum network.

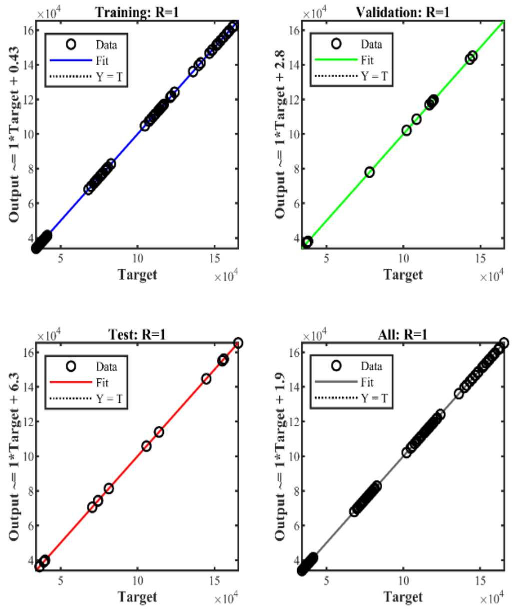

**Fig. 9** Regression chart at the fourth output of the optimum network.

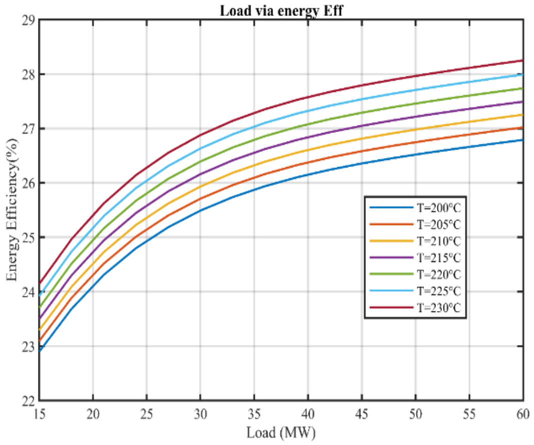

**Fig. 10** Energy efficiency against the load at various Feedwater temperatures.

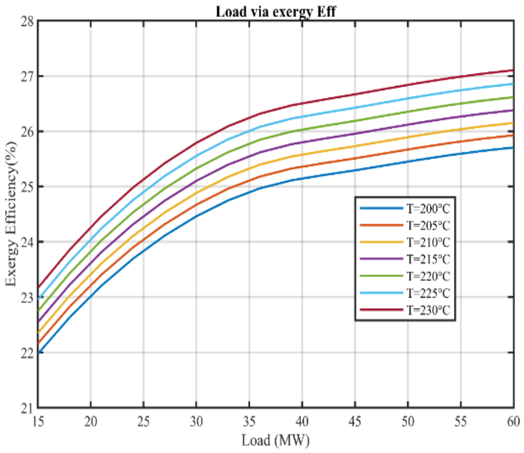

**Fig. 11** Exergy efficiency against load at various Feedwater temperatures.

The observed increase in the exergy and energy efficiencies can be justified considering the design of the power plant cycle at full load. The increased efficiency seems logical with increasing the power plant output relative to the required input of the cycle. Figures 10 and 11 show the uptrend of the power plant efficiency by increasing the generator capacity. The peaks in the diagrams decrease with decreasing the Feedwater temperature. Fuel consumption by the boiler decreases with increasing the water temperature in the boiler as it requires less thermal energy for vaporizing water in the turbine. As a result, energy consumption and thermal exergy of the boiler decrease leading to an increase in the exergy and energy efficiencies of the boiler. This in turn positively affects the overall performance of the cycle causing an increase in the overall energy and exergy efficiencies of the power plant.

As expected, the exergy and energy losses of the cycle increase with increasing the production load of the power plant. Figures 12 and 13 show an uptrend for both energy and exergy losses with increasing the generator capacity. The peaks decrease with increasing the Feedwater temperature. Fuel consumption by the boiler decreases with increasing the water temperature in the boiler improving the cycle performance while reducing the energy and exergy losses.

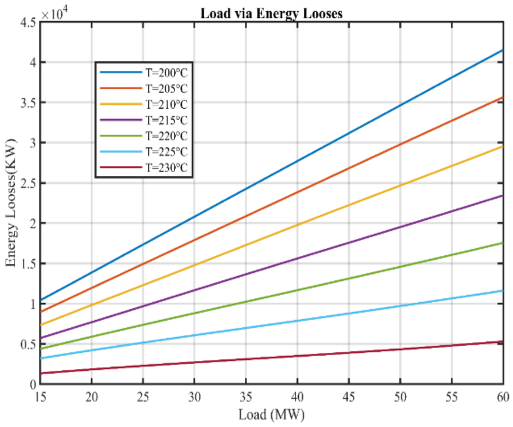

**Fig. 12** Total energy losses against the load at various Feedwater temperatures.

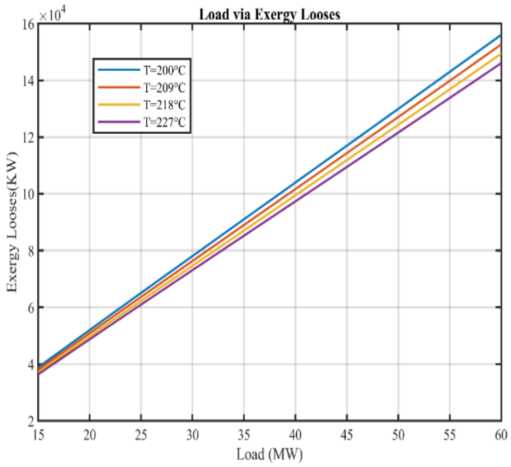

**Fig. 13** Total exergy losses against load at various Feedwater temperatures.

Energy losses also increase despite an increase in the energy and exergy efficiencies at the maximum load of the power plant equipment and the generator. The energy and exergy losses could be decreased up to a certain limit by increasing the Feedwater temperature using specific equipment under certain conditions.

## 5.4. Application of the Designed Neural Network at New Points

In addition to the optimal performance at trained points, an optimal neural network must also show an acceptable performance at untrained points. To this end, the network was tested at new points and the results are displayed for the four outputs respectively in "Figs. 14 to 17". These results are consistent with those obtained for the trained points in "Figs. 10 to 13". According to "Figs. 14 and 15", the peaks for the first and second outputs occur at the maximum load and Feedwater temperature. The energy and exergy efficiencies increase as the Feedwater temperature and the production load increase.

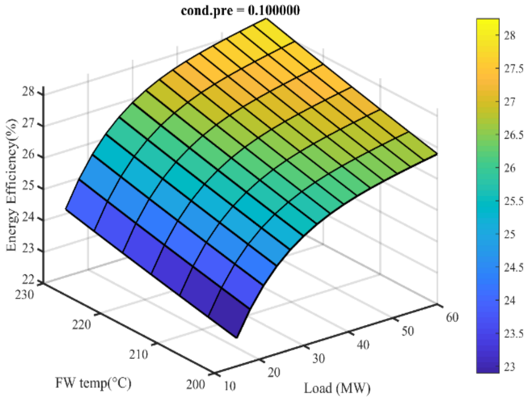

**Fig. 14** Effect of load and Feedwater temperature on the first output.

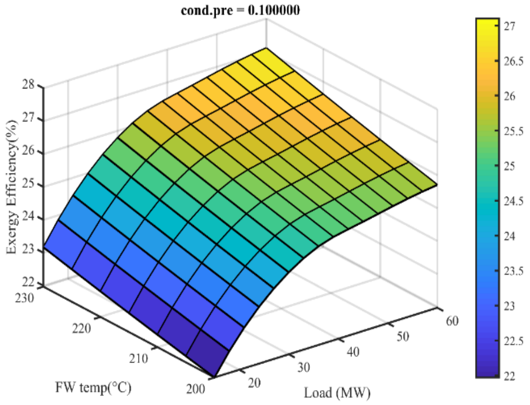

**Fig. 15** Effect of load and Feedwater temperature on the second output.

As shown in "Figs. 16 and 17", the peaks for the third and fourth outputs occur at the maximum load factor and minimum Feedwater temperature. Thus, more energy and exergy are lost at lower Feedwater temperatures, because more fuel is consumed or more energy and exergy are consumed from the thermodynamic point of view when low-temperature water enters the boiler. Certainly, the consumed energy and exergy are not totally useful and losses increase with increasing fuel consumption. Notably, with increasing the Feedwater temperature, energy losses sharply decline even at the maximum generator capacity. However, the exergy losses slowly decrease with increasing the Feedwater temperature at the full load of the power plant.

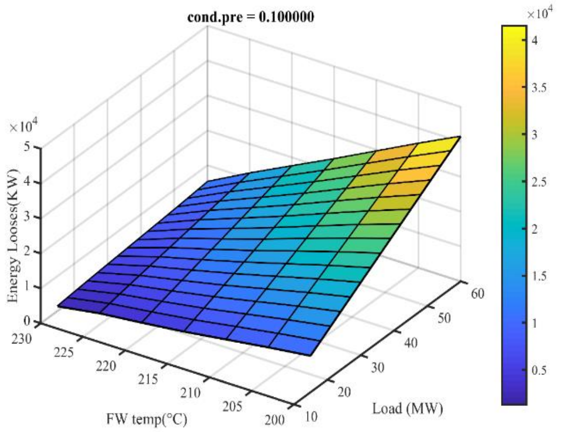

**Fig. 16** Effect of load and Feedwater temperature on the third output.

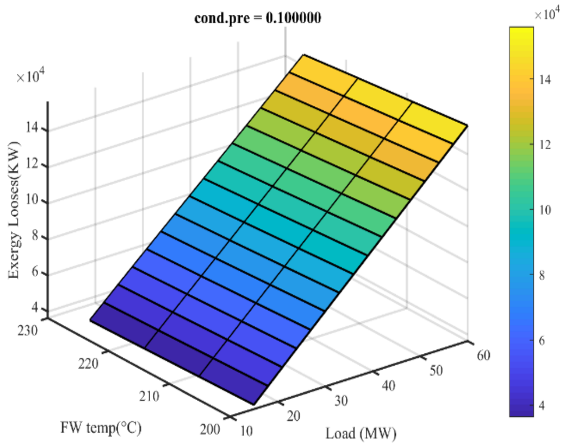

**Fig. 17** Effect of load and Feedwater temperature on the fourth output.

Figures 18 to 21 display the effect of the condenser pressure and generator capacity at a constant Feedwater temperature on the energy and exergy efficiencies and the total energy and exergy losses. As shown in “Figs. 18 and 19”, the utmost energy and exergy efficiencies are achieved by decreasing the condenser pressure and increasing the generator capacity. As the condenser pressure decreases, the vacuum at the end of the turbine increases and end-stage vapors are sucked into the condenser. This process facilitates the movement of steam along the turbine and reduces the resistance to steam movement. Also, a larger share of steam energy is converted into electrical energy. As shown in “Figs. 20 and 21”, the energy and exergy losses decrease with a relatively same slope with decreasing the pressure condenser and load factor. In other words, the energy lost at higher condenser pressures can be converted into useful work, and the energy and exergy losses can be minimized by reducing the condenser pressure.

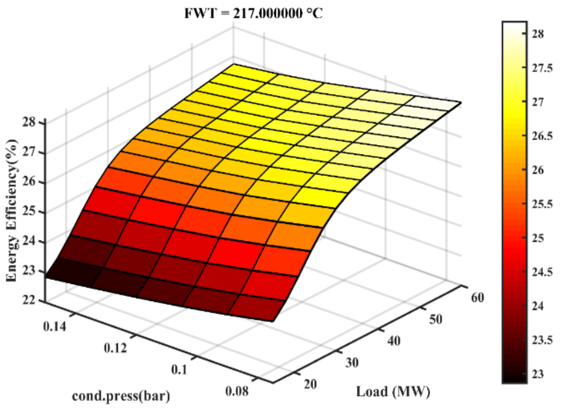

**Fig. 18** Effect of load and condenser pressure on the first output.

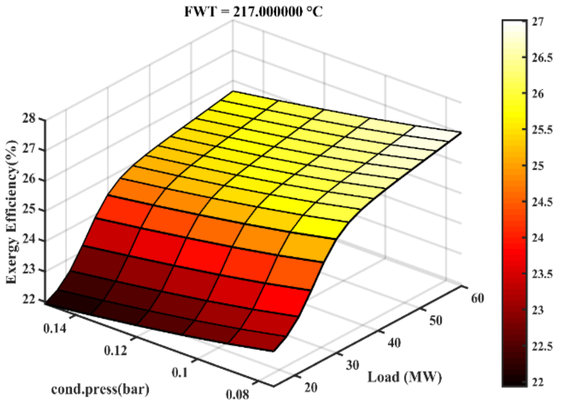

**Fig. 19** Effect of load and condenser pressure on the second output.

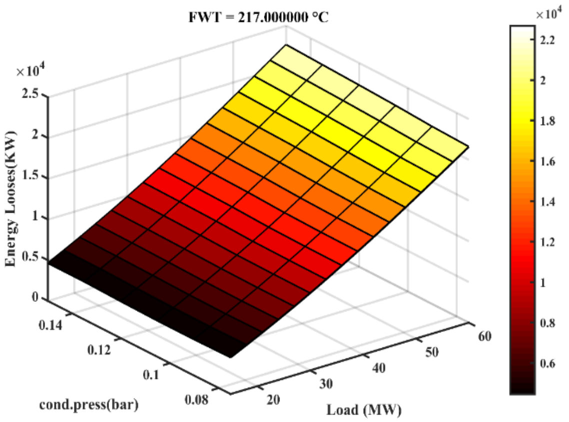

**Fig. 20** Effect of load and condenser pressure on the third output.

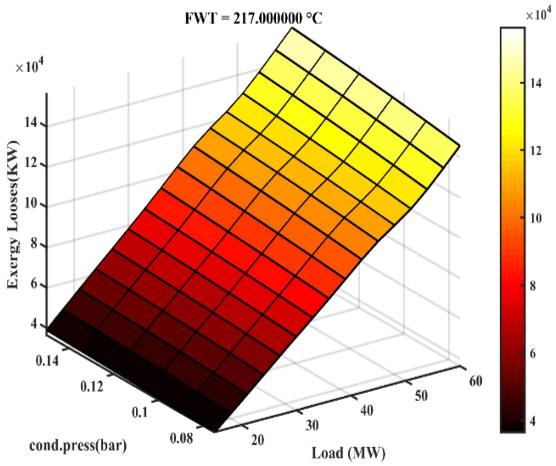

**Fig. 21** Effect of load and condenser pressure on the fourth output.

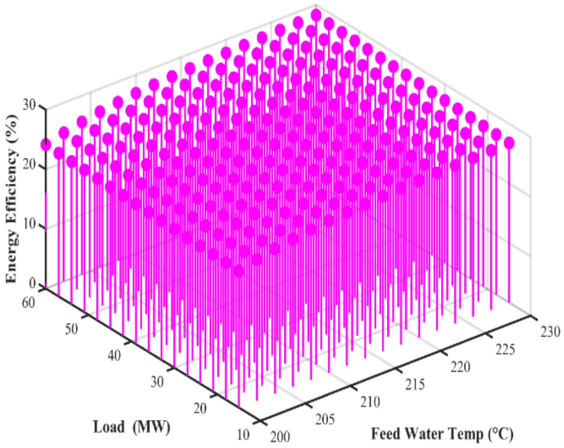

**Fig. 22** The error chart for the initial output

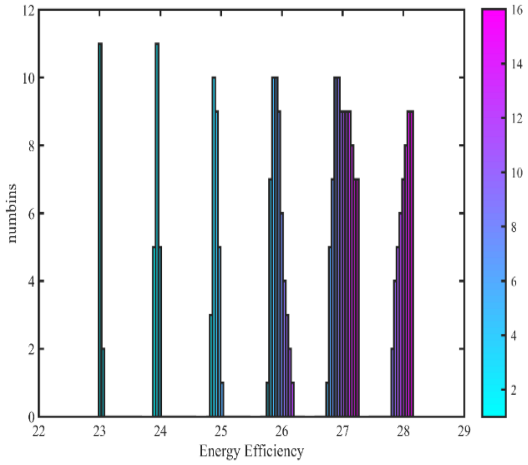

**Fig. 23** The histogram for the initial output.

## 5.5. Network Error

As mentioned in the network accomplishment part, the MSE of the network varies with the network architecture and training method. Moreover, the number of data, data scattering, and classification affect the network error and the study results. Figures 22 to 29 show the error and histogram diagrams for all four outputs of the network.

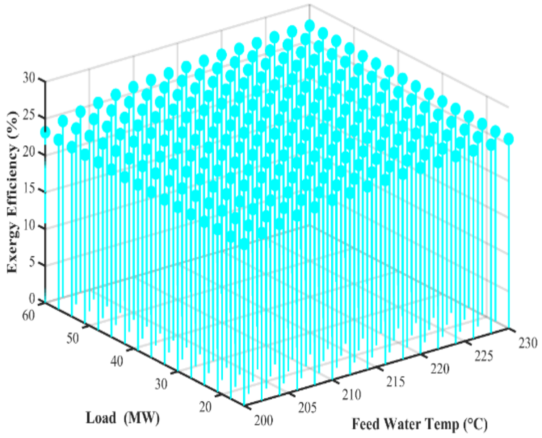

**Fig. 24** The error chart for the second output.

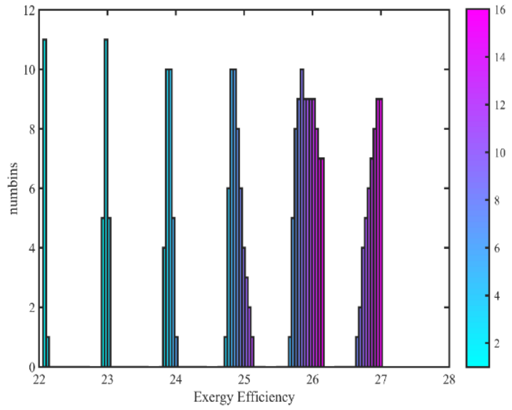

**Fig. 25** The histogram for the second output.

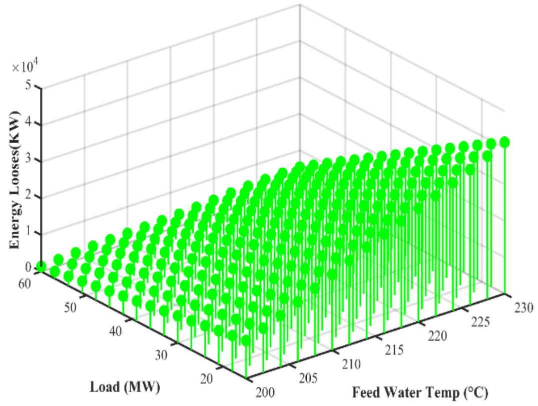

**Fig. 26** The error chart for the third output.

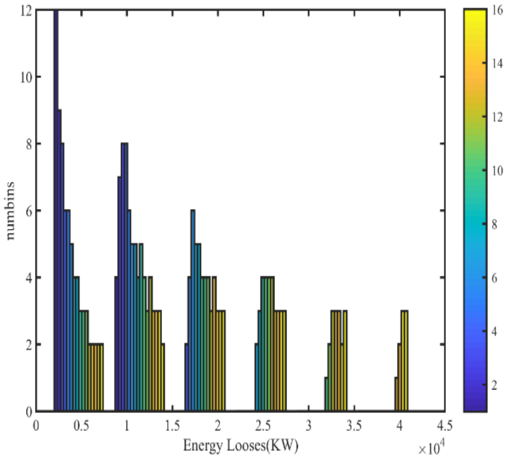

**Fig. 27** The histogram for the third output.

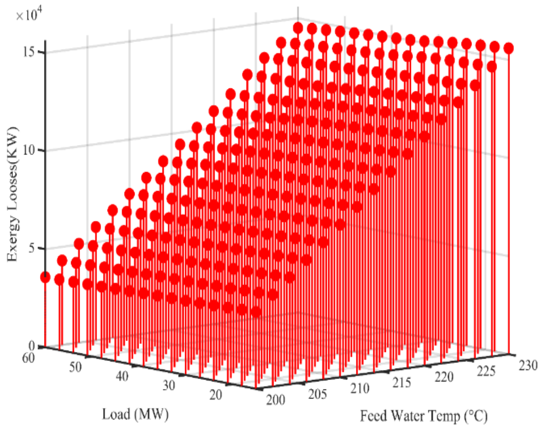

**Fig. 28** The error chart for the fourth output.

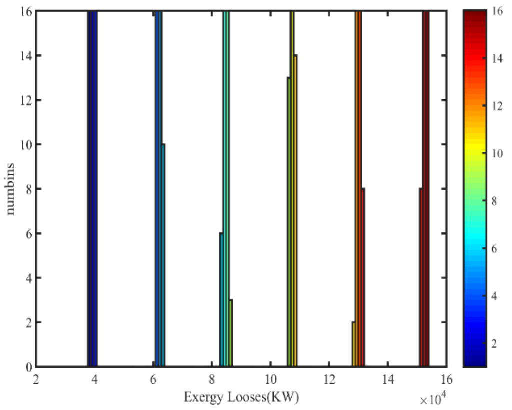

**Fig. 29** The histogram for the fourth output.

As shown in the error diagrams, data discretization and scattering have good density and accuracy in the designed neural network. However, the histograms show that the gaps where data are not available cause an error in the network.

## 5.6. Optimization of Results by The Genetic Algorithm

The GA aims to discover the optimum benefits for the problem outputs. In multi-objective optimization when the outputs are competing, by overcoming some points over other ones, an optimum curve named the Pareto front is obtained by the GA. This diagram is a set of optimal solutions from which the best solution can be selected according to the problem geometry and limitations. Figures 30 and 31 show the optimal solutions for the first and second, and the third and fourth outputs, respectively.

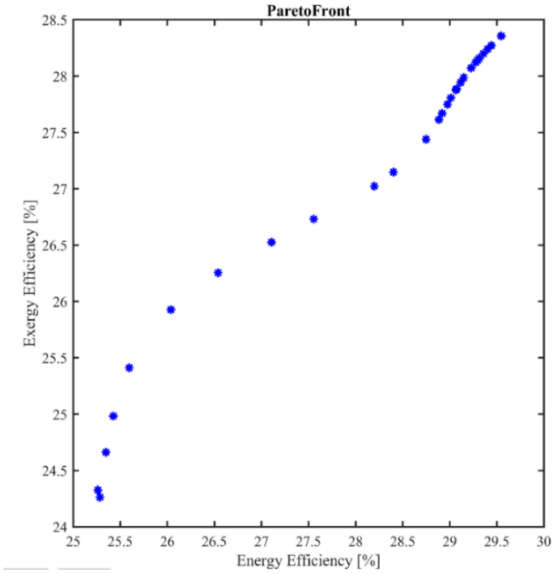

**Fig. 30** The Pareto front diagram for the first and second outputs.

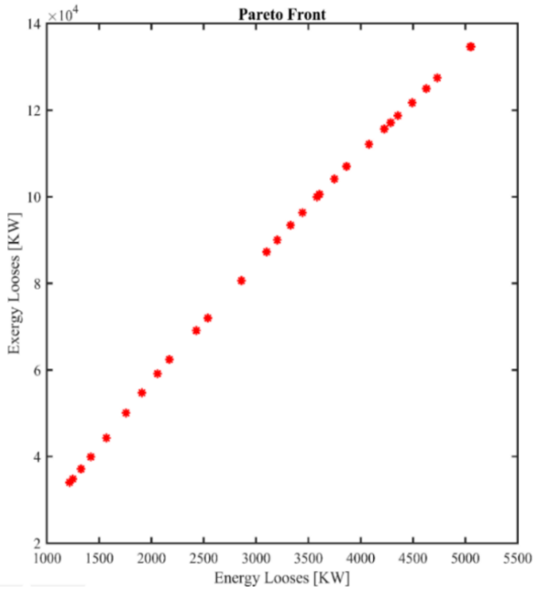

**Fig. 31** The Pareto front diagram for the third and fourth outputs.

This study aims to achieve the maximum efficiency and the minimum energy and exergy losses. Accordingly, from the optimal solutions obtained by the GA, the best solutions in the output space were obtained in the 23rd Pareto where the energy efficiency, exergy efficiency, energy losses, and exergy losses are 28.4%, 27.2%, 2539.2 kW, and 71963.7 kW, respectively. The best solutions in the input space are 229.99˚C, 0.0502 bar, and 31.67 MW, respectively for the Feedwater temperature, the condenser pressure, and the optimal generator capacity. The optimal solutions are listed in “Table 6”.

**Table 6** The optimal points in the input and output spaces obtained from the GA

| Number | Load [MW] | Energy Efficiency [%] | Exergy Efficiency [%] | Energy Losses [KW] | Exergy Losses [KW] |
|---|---|---|---|---|---|
| 1 | 59.305 | 29.547 | 28.357 | 5048.292 | 134664.984 |
| 2 | 30.405 | 28.197 | 27.023 | 2428.674 | 69109.436 |
| 3 | 59.295 | 29.546 | 28.356 | 5054.429 | 134647.379 |
| 4 | 16.395 | 25.346 | 24.662 | 1327.448 | 37166.334 |
| 5 | 24.117 | 26.539 | 26.254 | 1909.838 | 54732.801 |
| 6 | 35.468 | 28.748 | 27.439 | 2860.485 | 80605.337 |
| 7 | 17.621 | 25.426 | 24.983 | 1421.203 | 39926.466 |
| 8 | 55.038 | 29.404 | 28.241 | 4627.773 | 124975.984 |
| 9 | 27.499 | 27.554 | 26.732 | 2171.399 | 62410.855 |
| 10 | 59.305 | 29.546 | 28.357 | 5047.985 | 134667.348 |
| 11 | 15.001 | 25.283 | 24.263 | 1217.345 | 34044.880 |
| 12 | 42.403 | 29.013 | 27.806 | 3444.052 | 96351.277 |
| 13 | 50.942 | 29.275 | 28.122 | 4224.772 | 115679.178 |
| 14 | 45.827 | 29.115 | 27.945 | 3747.631 | 104104.766 |
| 15 | 47.097 | 29.148 | 27.986 | 3865.241 | 107009.842 |
| 16 | 15.328 | 25.262 | 24.327 | 1248.711 | 34824.533 |
| 17 | 26.042 | 27.107 | 26.526 | 2058.240 | 59149.330 |
| 18 | 44.266 | 29.071 | 27.887 | 3605.605 | 100558.348 |
| 19 | 56.132 | 29.441 | 28.272 | 4732.199 | 127454.901 |
| 20 | 41.113 | 28.975 | 27.750 | 3331.074 | 93422.115 |
| 21 | 22.088 | 26.037 | 25.927 | 1756.52 | 50074.815 |
| 22 | 43.992 | 29.065 | 27.878 | 3581.557 | 99930.933 |
| 23 | 31.669 | 28.401 | 27.147 | 2539.171 | 71963.704 |
| 24 | 38.394 | 28.884 | 27.614 | 3101.342 | 87255.786 |
| 25 | 19.544 | 25.595 | 25.412 | 1569.709 | 44315.255 |
| 26 | 51.583 | 29.295 | 28.141 | 4286.518 | 117135.385 |
| 27 | 49.379 | 29.227 | 28.073 | 4078.969 | 112133.979 |
| 28 | 53.608 | 29.358 | 28.199 | 4492.298 | 121733.563 |
| 29 | 39.590 | 28.910 | 27.670 | 3202.974 | 90016.555 |
| 30 | 52.287 | 29.312 | 28.157 | 4355.397 | 118752.508 |

## 6 CONCLUSIONS

An ANN was used for better processing the simulation results of a 60 MW combined heat and power generation power plant. The optimum network with proper performance was selected. Through multiple tests, the optimal architecture and training method were determined to ensure the accurate performance of the designed neural network. The results are summarized below:

1. Despite an increase in the energy and exergy efficiencies of the power plant at the maximum load of equipment and generator, the energy and exergy losses also increased. By heating the Feedwater and raising its temperature, the energy and exergy losses can be reduced up to a certain value.
2. With increasing the Feedwater temperature, energy losses sharply declined even at the maximum generator capacity. However, the exergy losses slowly decreased with increasing the Feedwater temperature at the full load of the power plant. Huge amounts of energy and exergy are lost in the boiler when low-temperature water entered the boiler. By raising the Feedwater temperature, energy losses could be compensated even at full load. However, the exergy losses significantly decreased by increasing the Feedwater temperature and decreasing the produced load.
3. Maximum energy and exergy efficiencies were obtained by decreasing the condenser pressure and increasing the generator capacity. On the other hand, the energy and exergy losses decreased with a relatively same slope by decreasing the pressure condenser and load. In other words, the energy losses at higher condenser pressures can be converted into useful work,

and the energy and exergy losses can be minimized by reducing the condenser pressure.

4. From the optimal solutions obtained from the GA, the best solutions in the output space were 28.4%, 27.2%, 2539.2 kW, and 71963.7 kW, respectively for the first-law efficiency (energy), second-law efficiency (exergy), energy losses, and exergy losses. The best solutions in the input space were 229.99˚C, 0.0502 bar, and 31.67 MW, respectively for the Feedwater temperature, the condenser pressure, and optimal generator capacity.

## REFERENCES

[1] Kim, M. J., Kim, T. S., Flores R. J., and Brouwer, J., Neural-Network-Based Optimization for Economic Dispatch of Combined Heat and Power Systems, Applied Energy, Vol. 256, 2020.

[2] Nikbakht Naserabad, S., Mehrpanahi, A., and Ahmadi, G., Multi-Objective Optimization of HRSG Configurations on The Steam Power Plant Repowering Specifications, Energy, Vol. 159, 2018, pp. 277-293.

[3] Luo, X. J., Juan Manuel Davila Delgado, A. O., Owolabi, H. A., and Ahmed, A., Genetic Algorithm-Determined Deep Feedforward Neural Network Architecture for Predicting Electricity Consumption in Real Buildings, Energy and AI, Vol. 2, 2020.

[4] Li, H., Zhen-yu, Zh., The Application of The Immune Genetic Algorithm in Main Steam Temperature of PID Control of BP Network, Physics Procedia, Vol. 24A, 2012, pp. 80-86.

[5] Hosseinalipour, S. M., Mehrpanahi, A., and Mobini, K., Full Repowering to Enhance the Technical-Economic Specifications of a Steam Power Plant, Mechanical Engineering Journal, Tarbiat Modarres University, Vol. 11, No. 1, 2011, pp. 1-18.

[6] Mehrpanahi, A., Hosseinalipour, S. M., and Seijanivandi, S., Multi-Objective Optimization of Parallel Feedwater Heating Repowering of a Steam Power Plant by The Genetic Algorithm, Amir Kabir Journal (Mechanical Engineering), Vol. 45, No. 1, 2013, pp. 93-108.

[7] Holland, J. H., Adaptation in Natural and Artificial Systems, Ann Arbor, MI: University of Michigan Press, 1975.

[8] Goldberg, D. E., Genetic Algorithms in Search, Optimization, and Machine Learning. Reading, MA: Addison-Wesley, 1989.

[9] Montana, D. J., Davis, L., Training Feedforward Neural Networks Using Genetic Algorithms, In Proceedings of the 11th International Joint Conference on Artificial Intelligence, Morgan Kaufmann, San Mateo, CA, Vol. 1, 1989, pp. 762–767.

[10] Whitley, D. A., Genetic Algorithm Tutorial, Stat Comput., Vol. 4, No. 2, 1994, pp. 65-85.

[11] Nguyen Q., et al., Performance of Joined Artificial Neural Network and Genetic Algorithm to Study the Effect of Temperature and Mass Fraction of Nanoparticles Dispersed in Ethanol. Mathematical Methods in the Applied Sciences, 2020, DOI: 10.1002/mma.6688.

[12] Ghorbani, P., Smida, K., Razzaghi, M. M., Yazd, M. J., Sajadi, S. M., Bagherzadeh, S. A. and Inc, M., Modeling and Thermoeconomic Analysis of a 60 MW Combined Heat and Power Cycle Via Feedwater Heating Compared to A Solar Power Tower, Sustainable Energy Technologies and Assessments, Vol. 54, 2022, pp. 102861.

*Int. J. Advanced Design and Manufacturing Technology, 2023, Vol. 16, No. 4, pp. 37-48*

*DOI: 10.30486/ADMT.2021.1920150.1239 ISSN: 2252-0406 https://admt.isfahan.iau.ir*

# Dynamic Response of FGM Plates Under Blast Load

**Reza Azarafza [*], Puya Pirali, Ali Davar, Majid Ghadimi**
Faculty of Materials and Manufacturing Technologies,
Malek Ashtar University of Technology, Tehran, Iran
E-mail: azarmut@mut.ac.ir, ppirali@mut.ac.ir, davar78@gmail.com,
ghadimi_m2@yahoo.com
*Corresponding author

**Received: 9 January 2021, Revised: 2 April 2021, Accepted: 9 April 2021**

**Abstract:** The present study investigates the deformation of FGM plates under blast load. Hamilton's principle is used to obtain the dynamic Equations. The two constituent phases, ceramic and metal, vary across the wall thickness according to a prescribed power law. Boundary conditions are assumed to be Simply Supported (SS). The type of explosive loading considered is a free in-air spherical air burst and creates a spherical shock wave that travels radially outward in all directions. For the pressure time of the explosion loading, Friedlander's exponential relation has been used. In order to determine the response analytically, the stress potential field function is considered. Using the Galerkin method, the final Equations are obtained as nonlinear and nonhomogeneous second-order differential Equations. The effect of temperature including thermal stress resultants and different parameters on the dynamic response have been investigated. Results have been compared with references and validated. Results showed that the amplitude of the center point deflection of the FGM plate is less than the pure metal plates when exposed to blast load, by increasing the volumetric index percentage of FGM, center point deflection is increased and in the FGM plates, deformation of symmetrical plates is smaller than the asymmetric plates. Also by applying the damping coefficient of the FGM plates, the amplitude of center point deflection is reduced, and by increasing the aspect ratio of the FGM plate, its center point deflection against explosion waves is reduced and by considering the effects of thermal resultant forces and moments, center point deflection is increased.

**Keywords:** Dynamic Response, Explosive Loading, Functional Graded Materials, Rectangular FGM Plates

**Biographical notes: Reza Azarafza** is an Associate Professor of Mechanical Engineering at Malek Ashtar University of Technology, Tehran, Iran. His current research focuses on composite structures, plates and shell analysis, and vibrations. **Puya Pirali** is an Assistant Professor at the Department of Mechanical Engineering, at Malek Ashtar University of Technology, Tehran, Iran. His current research focuses on plates and shell analysis. **Ali Davar** is currently an Assistant Professor at the Department of Mechanical Engineering, at Malek Ashtar University, Tehran, Iran. His current research interest includes composite structures. **Majid Ghadimi** is currently a PhD student at Malek Ashtar University and his main research interests are composite structures and Modal Analysis.

Research paper

## 1 INTRODUCTION

Increasing the knowledge of scientific and industrial communities always has been a factor in improving technology and achieving superior technology. In this regard, the use of new materials to achieve specific functional properties always have been a consideration of engineering researchers. Functionally graded Material (FGM) is a kind of modern material that has been widely used in recent years. Extensive research has been conducted to produce the FGM in order to resist high temperature and thermal shock for use in the body of spacecraft and nuclear power plants. FGMs are a kind of composite materials that are heterogeneous in terms of infrastructure, and the volume fraction of its constituent material is a function of the spatial position in each body, so that, in accordance with volume fraction, the other mechanical properties are also exhibiting continually gradual changes along the thickness from one plane to another. This feature of these materials not only increases their resistance to mechanical loadings but also makes them tolerable in extreme temperature gradient environments. The common type of this material is the combination of ceramic and metal, in which case it has a metal face and the other face is ceramic, and mechanical properties change continually from metal to ceramic through the thickness [1].

Recently, more attention has been paid to the design and development of explosion-resistant structures. As in most countries, extensive studies have been done on the reaction of structures, buildings, facilities, and equipment against explosions caused by explosive materials. Therefore, considering the remarkable characteristics of FGM materials of ceramic-metal based combination, in carrying loads such as explosion and penetration, investigating and understanding the behavior and response of these materials under various dynamic loads such as the explosion wave has been attractive to the researchers.

So far, extensive research has been done to study the mechanical effects of explosion on plates made of FGM materials, which can be mentioned below. Turkmen and Mecitoglu [2] compared the results of experimental tests and numerical solutions with the finite element method for a composite plate with reinforced layers under explosive load, and the effect of reinforcements and applied load on the dynamic response of the plate has been studied. Chi and Chung [3] have studied the mechanical behaviour of an elastic rectangular plate supported on the FGM bed exposed to transversal loading with SS boundary conditions. Alibeigloo [4] has studied the three-dimensional thermoelastic analysis of FGM rectangular plates with small deformation on SS boundary conditions. In this study, the thermoelastic properties of the plate change with exponential function in the thickness direction. Tung and Duc [5] studied the nonlinear analysis of stability for functionally graded plates under mechanical and thermal loads. Hause [6] has investigated the deflection of the functionally graded plates under the influence of the explosion theoretically. The theory of classic plates (CPT) has been used and plates have been exposed to a Friedlander exponential explosive loading. Aksoylar et al. [7] investigated the nonlinear transient analysis of FGM and FML composite plates under non-destructive explosive loads using experimental and FE methods.

Sreenivas et al. [8] studied and investigated the transient dynamic response of functionally graded materials. Goudarzi and Zamani [9] have investigated the maximum deflection of circular plates under the effect of uniform and nonuniform shock waves due to explosion by experimental and numerical analysis. Duong and Duc [10] considered the evaluation of the elastic properties and thermal expansion coefficient of composites reinforced by randomly distributed spherical particles with negative Poisson ratios. Duc et al. [11] presented the nonlinear dynamic response and vibration of imperfect shear deformable functionally graded plates subjected to blast and thermal loads. Duc et al. [12] presented the nonlinear dynamic and vibration of the S-FGM shallow spherical shells resting on elastic foundations including temperature effects. Cong et al. [13] investigated the nonlinear vibration and dynamic response of ES-FGM plates using third-order shear deformation theory (TSDT).

Hajlaoui et al. [14] presented the nonlinear dynamics analysis of FGM shell structures with a higher order shear strain enhanced solid-shell element. Tong et al. [15] studied the thermo-mechanical buckling and post-buckling of cylindrical shells with functionally graded coatings reinforced by stringers. Duc et al. [16] presented the nonlinear dynamic response of functionally graded porous plates on elastic foundations subjected to thermal and mechanical loads. Cong and Duc [17] studied analytical solutions for the nonlinear dynamic response of ES-FGM plates under blast load. Kim et al. [18] studied the nonlinear vibration and dynamic buckling of eccentrically oblique stiffened FGM plates resting on elastic foundations in a thermal environment. Duc et al. [19] presented the free vibration and nonlinear dynamic response of imperfect nanocomposite FG-CNTRC double-curved shallow shells in a thermal environment.

The main goal of this paper is to calculate the dynamic response of FGM plates under explosive load by considering the thermal forces and moments. Studying the effect of thermal forces and moments on the response of FGM plate is one of the innovations and advantages of this research that less has been studied in the previous research and the literature. Also, the effect of the damping coefficient, power law index of FGM plate, aspect ratio (L1/L2) of FGM plate, and symmetric and asymmetric FGM plate on dynamic response have been investigated.

## 2 GOVERNING EQUATIONS

### 2.1. Mechanical Properties of FGM Material

As shown in “Fig. 1”, a rectangular FGM plate with dimensions L1 and, L2 and thickness h is in Cartesian coordinates, so that the origin of the coordinate system (x, y, z) is located at the middle surface of the plate.

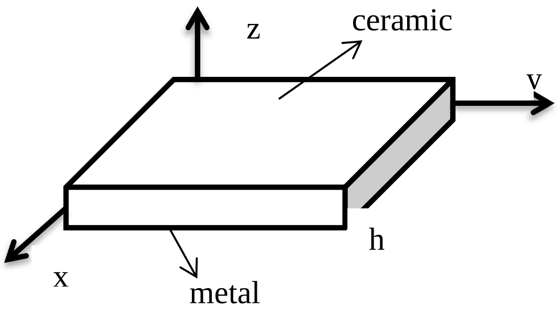

**Fig. 1** Geometric characteristic of FG plate.

If $V_m$ and $V_c$ are the volume fractions of ceramic and metal in the FGM, respectively, then the relation of each mechanical property related to the volume fractions will be as follows [20]:

$$P_f(z) = P_m V_m(z) + P_c V_c(z) \qquad (1)$$

As $P_m$ and $P_c$ are, respectively, metal and ceramic properties in the FGM, therefore, with respect to the above relations, the properties of a FGM material such as modulus of elasticity, linear coefficient of expansion, shear modulus, or density can be obtained as:

$$P_f(z) = \left(P_c - P_m\right) V_c(z) + P_m \qquad (2)$$

Two cases for grading and gradual changes of ceramic and metal phases along the thickness of FG plates can be considered:

**Symmetrical case**: The ceramic and metal phase elements are changed symmetrically in the thickness direction of plate, so that both outer surfaces of the plate are completely ceramic and the middle surface of the plate is full metal. In this case, the volume fractions of ceramic $V_C(z)$ is expressed in the form of Equation (3) [6]:

$$V_c(z) = \left(\frac{z}{h/2}\right)^N \left(\frac{1+\operatorname{sgn}(z)}{2}\right) + \left(\frac{-z}{h/2}\right)^N \left(\frac{1-\operatorname{sgn}(z)}{2}\right) \qquad (3)$$

In the above Equation, N is the volumetric percentage index of the material FGM, h is the thickness of the plate and z is the coordinates perpendicular to the middle surface along the thickness direction.

**Asymmetrical case**: Ceramic and metal phase elements change asymmetrically in the thickness direction of the plate, the upper surface of the plate is full ceramic and the bottom surface of the plate is full metal. In this case, as in “Fig. 1”, the bottom of the plate is completely metallic and its upper surface is completely ceramic and between these two surfaces will be a combination of ceramic and metal. In this case, the volume fraction of ceramic $V_C(z)$ is expressed in the form of Equation (4) [6]:

$$V_c(Z) = \left(\frac{2z+h}{2h}\right)^N \qquad (4)$$

Regarding the function of FGM materials in high-temperature environments, according to Reddy [1], the mechanical properties of its constituents have significant changes with temperature. Therefore, according to Equation 6, properties such as the $E_f$ modulus of elasticity, the Poisson ratio $\upsilon_f$ , the thermal expansion coefficient $\alpha_f$ , and the thermal conductivity coefficient $K_f$ could be related to the temperature [1].

$$P_f(Z,T) = \left[P_c(T) - P_m(T)\right]\left(\frac{2Z+h}{2h}\right)^N + P_m(T) \qquad (5)$$

### 2.2.The Fundamental Equation of FGM Plate

### 2.2.1. Displacement components

According to the classical theory of plates, the displacement field is as follows [21]:

$$\begin{aligned} &u = u_0(x,y,t) - z\bar{\psi}_x(x,y,t) \\ &v = v_0(x,y,t) - z\bar{\psi}_y(x,y,t) \quad , \quad w = w_0(x,y,t) \end{aligned} \qquad (6)$$

In the above relations $u_0$ and $v_0$, respectively, represent the displacements of the middle surface in thex and y directions, and $w_0$ is the transverse displacement along the z direction. Also, the functions $\psi_x$ and $\psi_y$ are rotations of the middle surface around x and y axes, respectively, and are as follows:

$$\psi_x = \frac{\partial w_0}{\partial x} \quad , \quad \psi_y = \frac{\partial w_0}{\partial y} \qquad (7)$$

### 2.2.2. Nonlinear strain- displacement relations

The nonlinear relations of Von-Karman between strain and displacement at any point in the thickness of the plate at distance z from the middle surface according to the strains and curvatures of the middle surface are as follows [22]:

$$\begin{aligned} &\varepsilon_{xx} = \varepsilon_{xx}^{0} + z\kappa_{x} \quad , \qquad \varepsilon_{yy} = \varepsilon_{yy}^{0} + z\kappa_{y} \\ &\gamma_{xy} = \gamma_{xy}^{0} + z\kappa_{xy} \quad , \qquad \varepsilon_{zz} = \varepsilon_{xz} = \varepsilon_{yz} = 0 \end{aligned} \tag{8}$$

In the above relations $\varepsilon_{xx}^{0}$ , $\varepsilon_{yy}^{0}$ and $\gamma_{xy}^{0}$ , are the strain of the middle surface and $\kappa_x$, $\kappa_y$ and $\kappa_{xy}$ are the curvatures of the middle surface, which are related to the displacement components u, v, w as follows:

$$\begin{aligned} &\varepsilon_{xx}^{0} = \frac{\partial u}{\partial x} + \frac{1}{2}\left(\frac{\partial w}{\partial x}\right)^{2} \quad , \qquad \varepsilon_{yy}^{0} = \frac{\partial v}{\partial y} + \frac{1}{2}\left(\frac{\partial w}{\partial y}\right)^{2} \\ &\gamma_{xy}^{0} = \frac{\partial u}{\partial y} + \frac{\partial v}{\partial x} + \frac{\partial w}{\partial x}\frac{\partial w}{\partial y} \quad , \qquad \kappa_{x} = -\frac{\partial \psi_{x}}{\partial x} = -\frac{\partial^{2} w}{\partial x^{2}} \\ &\kappa_{y} = -\frac{\partial \psi_{y}}{\partial y} = -\frac{\partial^{2} w}{\partial y^{2}} \quad , \qquad \kappa_{xy} = -\frac{\partial \psi_{x}}{\partial y} - \frac{\partial \psi_{y}}{\partial x} = -2\frac{\partial^{2} w}{\partial x \partial y} \end{aligned} \tag{9}$$

According to Hooke's law, the stress-strain relations are defined by the following Equation:

$$\begin{bmatrix} \sigma_{xx} \\ \sigma_{yy} \\ \sigma_{xy} \end{bmatrix} = \begin{bmatrix} Q_{11} & Q_{12} & 0 \\ Q_{12} & Q_{22} & 0 \\ 0 & 0 & Q_{66} \end{bmatrix} \begin{Bmatrix} \varepsilon_{xx} - \alpha(z,T)\Delta T \\ \varepsilon_{yy} - \alpha(z,T)\Delta T \\ \gamma_{xy} \end{Bmatrix} \\ \sigma_{zz} = \sigma_{xz} = \sigma_{yz} = 0 \tag{10}$$

In the above relations, which include mechanical and thermal strains, α is the thermal expansion coefficient and Qij are the elements of the stiffness matrix, which are functions of the plate thickness and temperature; their relations are as follows:

$$\begin{aligned} &Q_{11} = Q_{22} = \frac{E_f(z,T)}{1-\nu_f^{2}(T)} \quad , \qquad Q_{12} = \frac{\nu_f E_f(z,T)}{1-\nu_f^{2}(T)} \\ &Q_{66} = \frac{E_f(z,T)}{2(1+\nu_f(T))} \end{aligned} \tag{11}$$

### 2.2.3. The Force and moment resultants

The vector of forces N and moments M caused by stresses in unit length are expressed in terms of strain components as follows [21]:

$$\begin{Bmatrix} N_{xx} \\ N_{yy} \\ N_{xy} \end{Bmatrix} = \int_{-h/2}^{h/2} \begin{Bmatrix} \sigma_{xx} \\ \sigma_{yy} \\ \sigma_{xy} \end{Bmatrix} dz \quad , \qquad \begin{Bmatrix} M_{xx} \\ M_{yy} \\ M_{xy} \end{Bmatrix} = \int_{-h/2}^{h/2} \begin{Bmatrix} \sigma_{xx} \\ \sigma_{yy} \\ \sigma_{xy} \end{Bmatrix} .z.dz \tag{12}$$

By replacing stress relations from the above Equations, we can find the forces and moment resultants in terms of the following matrix strain:

$$\begin{Bmatrix} N - N^{T} \\ M - M^{T} \end{Bmatrix}_{6\times1} = \begin{bmatrix} [A] & [B] \\ [B] & [D] \end{bmatrix}_{6\times6} \begin{Bmatrix} \varepsilon^{0} \\ k \end{Bmatrix}_{6\times1} \tag{13}$$

In the above relations $N^T$ and $M^T$, are the thermal forces and moments resultants, matrices A, B, and D are the extensional, coupling, and bending stiffness matrices, respectively, and they are as follows:

$$\begin{aligned} &\left[(A_{11},A_{22}),(B_{11},B_{22}),(D_{11},D_{22})\right] = \frac{1}{1-\nu^{2}}(E_1,E_2,E_3) \\ &(A_{12},B_{12},D_{12}) = \frac{\nu}{1-\nu^{2}}(E_1,E_2,E_3) \\ &(A_{66},B_{66},D_{66}) = \frac{\nu}{2(1+\nu)}(E_1,E_2,E_3) \end{aligned} \tag{14}$$

In the above relations, the values of $E_1$, $E_2$, and $E_3$ are based on Young's modulus $E_m$, $E_{cm}$, the thickness of plate (h), and volumetric percentage index (N) for two cases of FGM plate (symmetric and asymmetric) as follows [5-6]:

**Asymmetric**

$$\begin{aligned} &E_1 = E_m h + \left(\frac{E_{cm} h}{N+1}\right) \\ &E_2 = E_{cm} h^{2}\left[\frac{1}{(N+2)} - \frac{1}{(2N+2)}\right] \\ &E_3 = \frac{E_m h^{3}}{12} + E_{cm} h^{3}\left[\frac{1}{(N+3)} - \frac{1}{(N+2)} + \frac{1}{(4N+4)}\right] \end{aligned} \tag{15}$$

**Symmetric**

$$\begin{aligned} &E_1 = E_{cm} h\left(1 + \frac{1}{N+1}\right) \quad , \qquad E_2 = 0 \\ &E_3 = E_{cm} h^{3}\left[\frac{1}{12} + \frac{1}{4(N+3)}\right] \end{aligned} \tag{16}$$

Therefore, by replacing the stresses (Equation. (10)) and the strains (Equation (8)) and the effective Young's modulus in Equations (12), the resultant forces and moments are obtained as follows:

$$N_{xx} = \frac{E_1}{1-v^{2}}\left(\varepsilon_{xx}^{0} + v\varepsilon_{yy}^{0}\right) + \frac{E_2}{1-v^{2}}\left(k_x + vk_y\right) - \frac{\phi_m}{1-v} \tag{17}$$

$$N_{yy} = \frac{E_1}{1-v^2}\left(\varepsilon_{yy}^0 + v\varepsilon_{xx}^0\right) + \frac{E_2}{1-v^2}\left(k_y + vk_x\right) - \frac{\phi_m}{1-v}$$

$$N_{xy} = \frac{E_1}{2(1+v)}\gamma_{xy}^0 + \frac{E_2}{1+v}k_{xy}$$

$$M_{xx} = \frac{E_2}{1-v^2}\left(\varepsilon_{xx}^0 + v\varepsilon_{yy}^0\right) + \frac{E_3}{1-v^2}\left(k_x + vk_y\right) - \frac{\phi_b}{1-v}$$

$$M_{yy} = \frac{E_2}{1-v^2}\left(\varepsilon_{yy}^0 + v\varepsilon_{xx}^0\right) + \frac{E_3}{1-v^2}\left(k_y + vk_x\right) - \frac{\phi_b}{1-v}$$

$$M_{xy} = \frac{E_2}{2(1+v)}\gamma_{xy}^0 + \frac{E_3}{1+v}k_{xy}$$

In the above relations, the parameters ϕm and ϕb are as follows:

$$(\phi_m, \phi_b) = \int_{-h/2}^{+h/2}\left[E_m + E_{cm}\left(\frac{2z+h}{2h}\right)^N\right]\left[\alpha_m + \alpha_{cm}\left(\frac{2z+h}{2h}\right)^N\right]\Delta T(1,z)dz \qquad (18)$$

Also, the thermal force and moment resultants ($N^T$ and $M^T$) are defined as follows:

$$\begin{bmatrix} N_{xx}^T & M_{xx}^T \\ N_{yy}^T & M_{yy}^T \\ N_{xy}^T & M_{xy}^T \end{bmatrix} = -\int_{-h/2}^{+h/2}\begin{bmatrix} Q_{11} & Q_{12} & 0 \\ Q_{12} & Q_{22} & 0 \\ 0 & 0 & Q_{66} \end{bmatrix}\begin{bmatrix} 1 & 0 \\ 0 & 1 \\ 0 & 0 \end{bmatrix}\begin{bmatrix} \alpha(z,T) \\ \alpha(z,T) \end{bmatrix}\Delta T(1,z)dz \qquad (19)$$

Where, ΔT is the increase of temperature relative to the reference temperature T0 (without thermal strain) is as follows:

$$\Delta T = T(z) - T_0 \qquad (20)$$

### 2.3. Equations of Motion of the Plate

The dynamic Equations of motion of the plate and its boundary conditions are extracted from Hamilton's principle, which are defined as four boundary conditions at the edges of the plate and three equilibrium Equations as follows [1], [6]:

$$\frac{\partial N_{xx}}{\partial x} + \frac{\partial N_{xy}}{\partial y} = 0 \quad , \quad \frac{\partial N_{yy}}{\partial y} + \frac{\partial N_{xy}}{\partial x} = 0$$

$$\frac{\partial^2 M_{xx}}{\partial x^2} + 2\frac{\partial^2 M_{xy}}{\partial x\,\partial y} + \frac{\partial^2 M_{yy}}{\partial y^2} + N_{xx}\frac{\partial^2 w_0}{\partial x^2} + \qquad (21)$$

$$2N_{xy}\frac{\partial^2 w_0}{\partial x\,\partial y} + N_{yy}\frac{\partial^2 w_0}{\partial y^2} + P - 2\mu\dot{w}_0 = I_0\ddot{w}_0$$

Where, *P* (x, y, t) is the distribution of external force on the upper surface of the plate (z = + h / 2) and μ is the coefficient of viscous damping per unit area of the plate. Also, $I_0$ is the inertial of the plate in the z-direction, and is defined as follows:

$$I_0 = \int_{-h/2}^{+h/2}\rho(z)dz \qquad (22)$$

Where $\rho(z)$ is the density of the plate.

### 2.4. Boundary Condition

The boundary condition of the plate is defined as follows:
At x=0 and x= L1:

$$w_0 = v_0 = M_{xx} = 0 \quad , \quad N_{xx} = N_{xx}^* = -N_{xx}^0 \qquad (23)$$

At y=0 and y= L2:

$$w_0 = v_0 = M_{yy} = 0 \quad , \quad N_{yy} = N_{yy}^* = -N_{yy}^0 \qquad (24)$$

### 2.5. Extraction of The Equation of FGM Plate Deflection

In order to establish the first two Equations of motion (Equations (21)), the function of the potential stress field ϕ is considered as follows [6]:

$$N_{xx} = \phi_{,yy} \quad , \quad N_{yy} = \phi_{,xx} \quad , \quad N_{xy} = -\phi_{,xy} \qquad (25)$$

Moreover, the third Equation (Equation (21)) can be obtained in terms of the two unknown parameters of the stress field (ϕ) and the transverse displacement ($w_0$). For this purpose, by applying inverse algebraic operations on Equation (13), it can be written as follows:

$$\begin{Bmatrix} \{\varepsilon^0\} \\ \{M\} - \{M^T\} \end{Bmatrix} = \begin{bmatrix} [A^*] & [B^*] \\ -[B^*]^T & [D^*] \end{bmatrix}\begin{Bmatrix} \{N\} - \{N^T\} \\ \kappa \end{Bmatrix} \qquad (26)$$

As shown in Equation 26, the matrices shown are as follows:

$$[A^*] = [A]^{-1} \quad , \quad [B^*] = -[A]^{-1}[B]$$
$$[B^*]^T = -[B][A]^{-1} \quad , \quad [D^*] = [D] - [B][A]^{-1}[B] \qquad (27)$$

By substituting the above relations, in the third Equation of motion of the plate and simplifying, the first fourth-order governing Equation is obtained with respect to two unknown parameters of the stress field (φ) and transverse displacement ($w_0$) [6]:

$$D\nabla^4 w_0 - \left(\phi_{,xx} w_{0,yy} - 2\phi_{,xy} w_{0,xy} + \phi_{,yy} w_{0,xx}\right) + I_0\ddot{w}_0 + 2c\dot{w}_0 = P - \left(\frac{E_2}{E_1}\right)\nabla^2 N^T + \nabla^2 M^T \tag{28}$$

Where, $D$ is a parameter defined as follows:

$$D = \frac{E_1E_3 - E_2^2}{E_1(1 - v^2)} \tag{29}$$

To solve the above Equation, we need another Equation including two unknown parameters mentioned above, which can be obtained from the compatibility conditions and simplification. The compatibility Equation is:

$$\begin{aligned} &\varepsilon\text{\_}(xx,yy)\text{\^{}}0 + \varepsilon\text{\_}(yy,xx)\text{\^{}}0 \\ &- \gamma\text{\_}(xy,xy)\text{\^{}}0 \\ &= w\text{\_}(0,xy)\text{\^{}}2 \\ &- w\text{\_}(0,xx)\ w\text{\_}(0,yy) \end{aligned} \tag{33}$$

By substituting the strains from relation 17 and the function field of stress potential (relations 25) in Equation (30), the second fourth-order governing Equation, including two unknown parameters of the stress field (φ) and the transverse displacement ($w_0$) is obtained as follows:

$$\nabla^4\phi = E_1\left(w_{0,xy} - w_{0,xx}w_{0,yy}\right) - (1 - v)\nabla^2 N^T \tag{31}$$

Thus, two Equations 28 and 31 are the basic governing Equations, including the terms of thermal force and moment resultants to obtain the general dynamic response of the FGM plates under the external excitation.

## 3 SOLVING EQUATION OF FGM PLATES BY CONSIDERING THERMAL TERMS

In order to solve the governing Equations in general, taking into account the boundary conditions, the unknown parameters of $w_0$ and $\phi$ are assumed to be in the form of sinusoid functions as follows [6]:

$$w_0(x, y, t) = w_{mn}(t).Sin\lambda_m x.Sin\mu_n y \tag{32}$$

$$\begin{aligned} \phi(x,y,t) &= A_{mn}(t)Cos\,2\lambda_{\mathrm{m}}\,\mathrm{x} + B_{mn}(t)Cos\,2\mu_n y + \\ &C_{mn}(t)Cos\,2\lambda_{\mathrm{m}}\,\mathrm{x}Cos\,2\mu_n y + D_{mn}(t)Sin\,\lambda_m xSin\,\mu_n y \\ &+\frac{1}{2}N_{xx}^{*}y^2 + \frac{1}{2}N_{yy}^{*}x^2 \end{aligned} \tag{33}$$

Where:

$$\mu_n = \frac{n\pi}{L_2} \quad , \quad \lambda_m = \frac{m\pi}{L_1} \tag{34}$$

In Equation (32), $w_{mn}(t)$ is the maximum deflection of the FGM plates, and m, n = 1, 2, 3, ..., represent the number of half waves along the axes x and y, respectively.

Also, thermal force and moment resultants are assumed to be in the form of the following functions:

$$\begin{aligned} N^T &= N_{mn}^T Sin\,\lambda_m x Sin\,\mu_n y \\ M^T &= M_{mn}^T Sin\,\lambda_m x Sin\,\mu_n y \end{aligned} \tag{35}$$

Where, $N_{mn}^T$ and $M_{mn}^T$ from relation 19 are obtained as follows:

$$\begin{aligned} N_{xx}^T &= N_{yy}^T \\ &= \frac{h\Delta T}{1 - v(T)}\left[\frac{E_{cm}(T)\alpha_{cm}(T)}{2N + 1}\right. \\ &+ \frac{E_{cm}(T)\alpha_m() + E_m(T)\alpha_{cm}(T)}{N + 1} \\ &\left.+ E_m(T)\alpha_m(T)\right] \end{aligned} \tag{36}$$

$$\begin{aligned} M_{xx}^T = M_{yy}^T = -\frac{h^2\Delta T}{1-v(T)}\Bigg\{&E_{cm}(T)\alpha_{cm}(T)\left(\frac{1}{2N+2} - \frac{1}{4N+2}\right) + E_{cm}(T)\alpha_m(T)\left(\frac{1}{N+2} - \frac{1}{2N+2}\right) \\ &+ E_m(T)\alpha_{cm}(T)\left(\frac{1}{N+1} - \frac{1}{2N+2}\right)\Bigg\} \end{aligned} \tag{37}$$

$$N_{xy}^T = M_{xy}^T = 0$$

By substituting Equation (32), (33) and (35) into (31), the coefficients of $A_{mn}$, $B_{mn}$, $C_{mn}$ and $D_{mn}$ are obtained as follows:

$$\begin{aligned} &A_{mn}(t) = \frac{E_1 w_{mn}^2(t)\mu_n^2}{32\lambda_m^2} \quad , \quad B_{mn}(t) = \frac{E_1 w_{mn}^2(t)\lambda_m^2}{32\mu_n^2} \\ &C_{mn}(t) = 0 \quad , \quad D_{mn}(t) = \frac{N_{mn}^T((1-v)}{(\lambda_m^2 + \mu_n^2)} \end{aligned} \tag{38}$$

Therefore, by replacing these coefficients in relation 33, the function ϕ is obtained as follows:

$$\phi(x,y,t)=\frac{E_1 w_{mn}^2(t)\mu_n^2}{32\lambda_m^2}Cos\,2\lambda_{\mathrm{m}}\,\mathrm{x}+\frac{E_1 w_{mn}^2(t)\lambda_m^2}{32\mu_n^2}.$$
$$Cos\,2\mu_n y+\frac{N_{mn}^T(1-\nu)}{\left(\lambda_m^2+\mu_n^2\right)}Sin\lambda_m x Sin\mu_n y+ \qquad (39)$$
$$\frac{1}{2}N_{xx}^* y^2+\frac{1}{2}N_{yy}^* x^2$$

The external excitation force on the plate is considered to be proportional to the transverse displacement as follows:

$$P_t(x,y,t)=P_{mn}(t)Sin\lambda_m x Sin\mu_n y \qquad (40)$$

In the above relation, the coefficient $P_{mn}$ (t) is obtained by the Fourier series expansion as follows:

$$P_{mn}(t)=\frac{4}{L_1L_2}\int_0^{L_1}\int_0^{L_2}P_t(x,y,t)Sin\lambda_m x Sin\mu_n y\,dxdy \qquad (41)$$

In this research, the external load applied on the FGM plate is explosive load and the type of the explosive loading is considered as a free in-air spherical air burst. Such an explosion creates a spherical shock wave that travels radially outward in all directions with diminishing velocity. The form of the incident blast wave from a spherical charge is shown in “Fig. 2”.

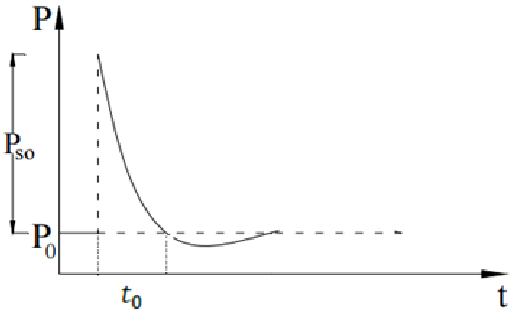

**Fig. 2** Incident pressure profile of a blast wave [23].

Where $P_{SO}$ is the peak overpressure above ambient pressure, $P_0$ is the ambient pressure, $t_a$ is the time of arrival, $t_p$ is the positive phase duration of the blast wave, t is the time and b is the coefficient of reduction of the amplitude wave of the explosion which is determined by adjustment to a pressure curve from a blast test. The waveform shown in “Fig. 2” is given by an expression known as the Friedlander Equation and is given as follows [6], [23]:

$$P_t(t)=\left(P_{So}-P_0\right)\left(1-\frac{(t-t_a)}{t_p}\right)\exp\left(-b\frac{(t-t_a)}{t_p}\right) \qquad (42)$$

Where

$$P_{so}=172/Z^3-114/Z^2+108/Z \quad , \quad Z=R/W^{\frac{1}{3}}$$

Where, *R* is the standoff distance in meters and *W* is the equivalent charge weight of TNT in kilograms. By substituting Equation (42) in (41), $P_{mn}(t)$ under the loading due to the explosion, it is obtained as follows:

$$P_{mn}(t)=\frac{16P_t(t)}{\pi^2} \quad , \quad (m,n)=(1,1) \qquad (43)$$

By replacing Equation (39) and (32) in (28), and using the Galerkin method, the following second-order Equation describing the nonlinear differential governing Equations of FGM plates under external exaction due to the explosion considering the expressions of the thermal force and moment resultants are obtained. The main unknown parameter of these Equations is the $W_{mn}(t)$ plate, which is the purpose of this research obtained as follows:

$$\ddot{w}_{mn}(t)+\frac{2c}{I_0}\dot{w}_{mn}(t)+\omega_{mn}^2 w_{mn}(t)+$$
$$\frac{E_1\left(\lambda_m^4L_2+\mu_n^4L_1\right)}{16I_0}w_{mn}^3(t)= \qquad (44)$$
$$\frac{1}{I_0}\left(P_{mn}(t)+\left(\lambda_m^2+\mu_n^2\right)\left(\frac{E_2}{E_1}N_{mn}^T-M_{mn}^T\right)\right)$$

In Equation (44), $w_{mn}(t)$ is the deflection of the FGM plate in terms of time, and the natural frequency $\omega_{mn}$ is obtained from the following Equation:

$$\omega_{mn}=\sqrt{\frac{K_{mn}}{I_0}} \qquad (45)$$

$I_0$ is the mass moment-of-inertia of the plate and the $K_{mn}$ is defined as follows:

$$K_{mn}=\frac{\left(E_1E_3-E_2^2\right)\pi^4}{E_1L_1^4\left(1-\nu^2\right)}\left(m^4+2m^2n^2\psi^2+n^4\psi^4\right)+ \qquad (46)$$
$$\left(N_{xx}^*\frac{m^2\pi^2}{L_1^2}+N_{yy}^*\frac{n^2\pi^2}{L_2^2}\right)$$

Where, ψ is the ratio of length to width of the plate (aspect ratio). Also, in Equation (44) the dimensionless damping coefficient $\Delta_{mn}$ could be defined as follows:

$$\frac{2}{I_0}\mu = 2\Delta_{mn}\omega_{mn} \rightarrow \Delta_{mn} = \frac{\mu}{I_0\omega_{mn}} \qquad (47)$$

In order to obtain a time response of FGM plate, the fourth-order Ronge-Kutta code with zero initial conditions in the MATLAB program is used to solve Equation (44) which is a second-order nonlinear non-homogeneous differential Equation.

## 4 RESULTS AND DISCUSSION

### 4.1. Validation

The considered FGM plate consists of Titanium alloy Ti-6Al-4V as a metal component and aluminum oxide as a ceramic component and has been restrained as simply supported on all edges. Its geometric and physical characteristics are selected in accordance with “Tables 1 and 2” [6]. Also, the number of half-waves considered along the axes x and y are m = n = 1, respectively.

**Table 1** Geometric parameters of FGM plate

| aspect ratio(ψ) | h (m) | $L_2$ (m) | $L_1$ (m) |
|---|---|---|---|
| 1 | 0.0254 | 1 | 1 |

**Table 2** Mechanical properties of FGM plate

| $E_m$ (GPa) | $E_c$ (GPa) | $\nu_m$ | $\nu_c$ |
|---|---|---|---|
| 105.7 | 320.24 | 0.2981 | 0.26 |
| $\alpha_m$ ($^0C^{-1}$) | $\alpha_c$ ($^0C^{-1}$) | $\rho_m(\frac{kg}{m^3})$ | $\rho_c(\frac{kg}{m^3})$ |
| $8.7*10^{-6}$ | $7.1*10^{-6}$ | 4429 | 3750 |

Also, the characteristics of the explosive loading wave in the air, the weight of the explosive, and distance of its center from the plate are shown in “Table 3”.

**Table 3** Characteristics of the explosive wave loading

| α | W (Kg) | R (m) | $t_a$ (s) | $T_p$ (s) |
|---|---|---|---|---|
| 0.5 | 0.7 | 0.766 | 0.000408 | 0.001372 |

In order to verify the results, using the above Tables, in similar geometric conditions and similar loading, the results of this study are compared with the results of Ref. [6]. Time response of the center point deflection of FGM plate in terms of the explosion time without consideration of temperature mode for asymmetric and symmetrical states with a volumetric percentage index of N = 0.5 are shown in “Figs. 3 and 4”, respectively. Comparison between the results of Ref. [6] and the present study have been presented in “Tables 4 and 5”. This comparison shows that the error percentage between them is negligible which confirms the accuracy of the present study.

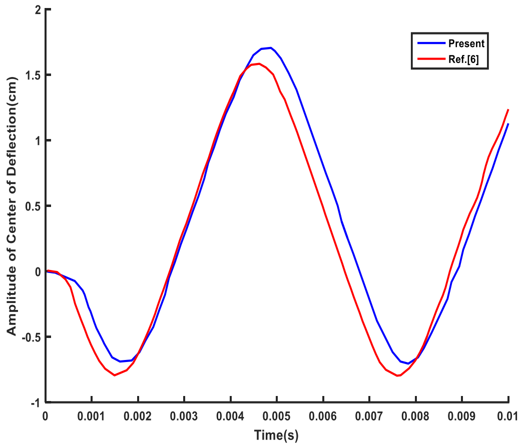

**Fig. 3** Time response of the center point deflection of asymmetric FGM plate with N=0.5 without thermal effects.

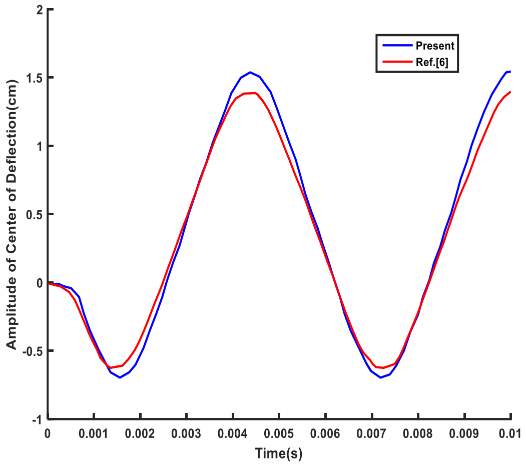

**Fig. 4** Time response of the center point deflection of symmetric FGM plate with N=0.5 without thermal effects.

**Table 4** Comparison between the results of Ref. [6] and the present study

| Asymmetric FGM plate | | | |
|---|---|---|---|
| | Ref.[6] | Present study | Error |
| Maximum deflection in the first period(cm) | 1.6 | 1.7 | %6.25 |
| Time of maximum deflection in the first period(s) | 0.0046 | 0.0049 | %6.5 |

**Table 5** Comparison between the results of Ref. [6] and the present study

| Symmetric FGM plate | | | |
|---|---|---|---|
| | Ref.[6] | Present study | Error |
| Maximum deflection in the first period(cm) | 1.39 | 1.53 | %10 |
| Time of maximum deflection in the first period(s) | 0.0043 | 0.0044 | %2.32 |

## 4.2. Effects of Different Parameters on The Dynamic Response

In this section, the results of the parametric study of the effect of different parameters on the time response of the center point deflection of the FGM plate have been investigated. The effect of temperatures ΔT(K) = (30,500,600, 700) on the nonlinear dynamic response of the asymmetric FGM plates with N = 0.5 is shown in “Fig. 5”. The geometrical and mechanical properties of the FGM plate and the characteristics of the explosive wave loading are similar to the previous ones. It can be seen that the dynamic response amplitude increases when the temperature ΔT increases since the flexibility of the plate increases. It means that the dynamic response amplitude is directly proportional to the temperature ΔT. The results of the first period in each temperature are given in “Table 6”.

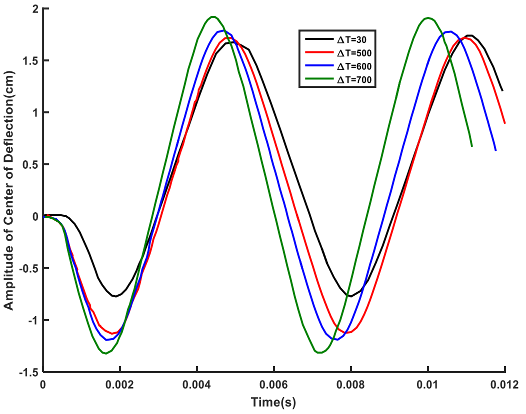

**Fig. 5** The effect of temperature on the nonlinear response of the FGM plates under blast load with N=0.5.

Figure 6 shows the effect of the volumetric percentage index N on the nonlinear dynamic response of the asymmetric FGM plates with N = 0, 5, 10, 50 and considering the effect of thermal forces and moments resultants. Obviously, the amplitude of the nonlinear dynamic response of the FGM plate is directly proportional to the power-law index N. At N = 0, the plate has a pure ceramic property and by increasing N, the metal property is added. In fact, by increasing N, the behavior of the plate becomes more flexible and the deflection is increased, as a result, the plate exhibits more geometric nonlinear effects.

**Table 6** The effect of temperature on the response FGM plate

| Results | Asymmetric FGM plate with N=0.5 | | | |
|---|---|---|---|---|
| | Difference temperature (℃) | | | |
| | 700 | 600 | 500 | 25 |
| Maximum deflection in the first period(cm) | 1.92 | 1.79 | 1.71 | 1.67 |
| The time of Maximum deflection in the first period(s) | 0.0043 | 0.0047 | 0.0049 | 0.005 |

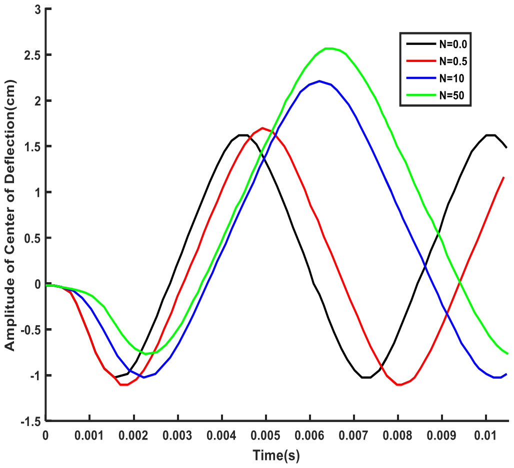

**Fig. 6** The effect of power-law index N on the time response of the center point deflection of asymmetric FGM plate with $\Delta T = +600$ ℃ and without damping effect under blast load.

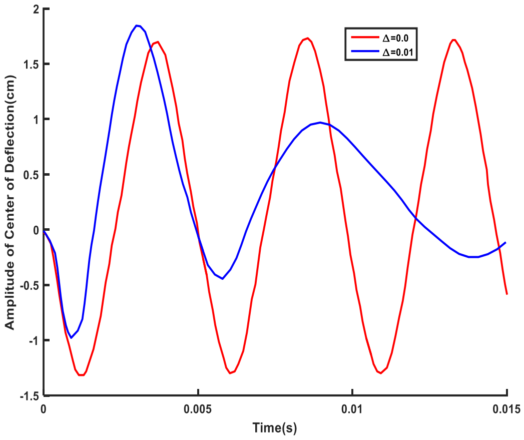

**Fig. 7** The effect of various amounts of damping on the time response of the center point deflection of asymmetric FGM plate with N=0.5.

Effects of various amounts of damping on the time response of the center point deflection of asymmetric FGM plate with N=0.5 and without temperature are shown in “Fig. 7”. It can be seen that central deflections vs. time attenuate faster as the amount of the damping coefficient is increased for a fixed volume fraction of the constituent materials. Because damping causes waste of energy and reduces the deflection amplitude.

The effect of damping with a value of $\Delta 11 = 0.1$ on the time response of the center point deflection of symmetric and asymmetric FGM plate with N=0.5 is also compared with temperature $(\Delta T = +600\ ^\circ\mathrm{C})$ and without temperature as shown in “Fig. 8”. As can be seen, regardless of the thermal effects, the smaller deflection amplitude corresponds to the symmetric FGM configuration.

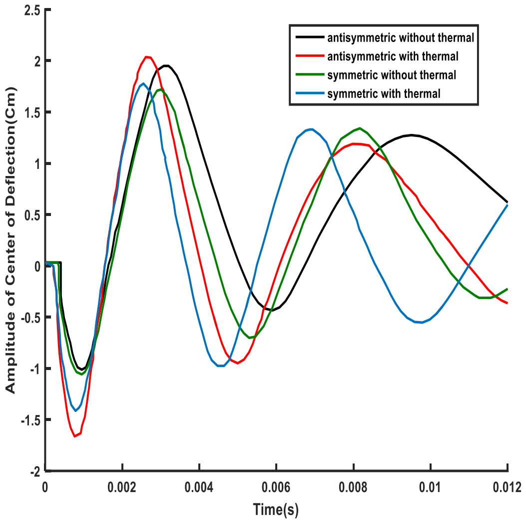

**Fig. 8** The effect of FGM configuration on the time response of the center point deflection of symmetric and asymmetric FGM plate with temperature $(\Delta T = +600\ ^\circ\mathrm{C})$ and without temperature.

Also, the effects of various amounts of damping on the time response of center point deflection of asymmetric FGM plate with N=0.5 and with temperature $\Delta T = +600\ ^\circ\mathrm{C}$ are shown in “Fig. 9”. It can be seen that by increasing the amount of the damping coefficient, the amplitude of the central deflections vs. time is decreased and damped. Because damping causes a waste of energy and reduces deflection in the presence of thermal effect.

Figure 10 illustrates the effect of the aspect ratio ($L_1/L_2$) of the plate on the time response of the center point deflection of the FGM plate under blast load with N=0.5. It is clear that the plate fluctuation amplitude decreases when increasing the aspect ratio of the plate. In conclusion, the plate fluctuation amplitude is in inverse proportion to the aspect ratio of the plate. So, in similar conditions, by doubling the ratio of length to width of the plate (ψ=2), the center deflection of the plate is decreased by about 70%. Therefore, for optimal design, the use of FGM plates with a high aspect ratio leads to smaller deflections against blast load and consequently leads to lower stress values.

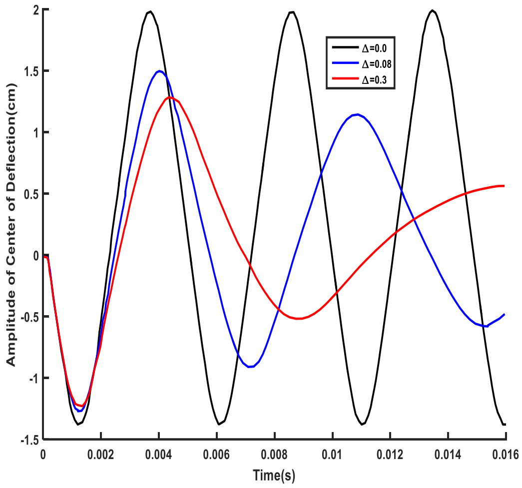

**Fig. 9** The effect of various amounts of damping on the time response of the center point deflection of asymmetric FGM plate with N=0.5 and temperature $(\Delta T = +600\ ^\circ\mathrm{C})$.

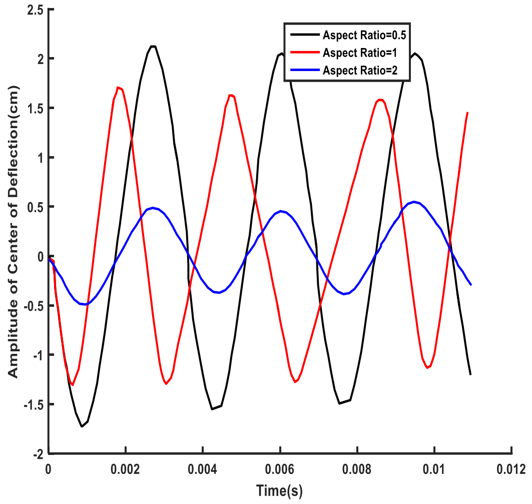

**Fig. 10** The effect of aspect ratio (L1/L2) of asymmetric FGM plate on the time response of the center point deflection under blast load.

Figure 11 shows the effect of explosive mass on the time response of the center point deflection of FGM plate under blast load. The physical and geometric characteristics of the plate and the characteristics of the explosive loading are the same as in the previous cases, and only the explosive mass is different. As can be seen, the center point deflection amplitude of FGM plate increases when explosive mass is increased. Amplitude of deflection is directly proportional to the explosive mass. For example, an increase in the mass of explosives from 0.4 to 0.7 kg leads to an increase in the central deflection of the plate at the peak of the first period from 1.41 cm to 1.69 cm, which is an increase of about 20%, as well as an increase the mass, reduces the occurrence time of the peak of the domain during the first period from 0.0056 seconds to 0.0044 seconds.

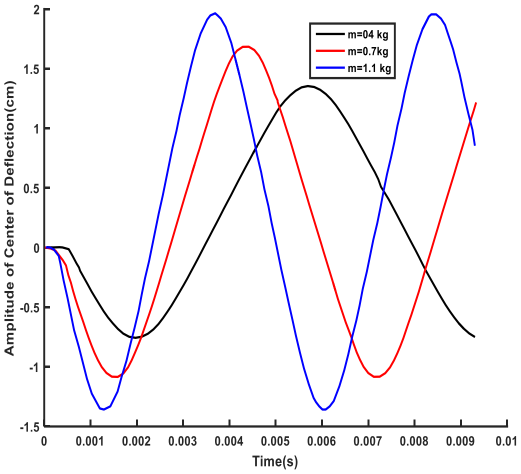

**Fig. 11** The effect of explosive mass on the time response of the center point deflection of FGM plate under blast load with N = 0.5.

## 5 CONCLUSIONS

In this paper, the behavior and dynamic response of FGM plates against blast load were investigated. The main purpose of the reduction of deflection and displacement is to reduce the stresses caused by the explosion waves in the plates. Various factors and parameters are effective in increasing or decreasing the deflection of the plate, including the FGM material percentage index (N), the aspect ratio of the plate, the geometric structure of the FGM plate (phase gradation) in terms of the symmetrical or asymmetric structure, weight of the explosive, the distance of the explosive from the plate, the damping, the effects of temperature, etc. In the present study, these parameters were investigated. Finally, the following results can be summarized:

A) The amplitude of the center point deflection of the FGM plate is less than the pure metal plates when exposed to the blast load and in the FGM plates, the deformation of symmetrical plates is smaller than the asymmetric plates.

B) By applying the damping coefficient of the FGM plates, the amplitude of the center point deflection is reduced and damped during the explosion.

C) By increasing the aspect ratio of the FGM plate, its center point deflection against explosion waves reduces. Therefore, the use of plates with a high aspect ratio leads to smaller deflection and lower stress values.

D) By increasing the volumetric index percentage of FGM, the center point deflection is increased.

E) By considering the effects of thermal resultant forces and moments, the center point deflection is increased and by increasing the temperature, the center point deflection of the plate is increased.

Finally, it should be noted that the theory presented in this study is based on the theory of elasticity, and no plastic deformation or fracture is considered, and it is assumed that the behavior of the plate remains elastic all the time.

## REFERENCES

[1] Shen, H. S., Functionally Graded Materials: Nonlinear Analysis of Plates and Shells, CRC Press, Tylor & Francis Group, London, New York, Published January 15, 2011, ISBN 9780367386016.

[2] Turkmen, H. S., Mecitoglu, Z., Dynamic Response of a Stiffened Laminated Composite Plate Subjected to Blast Load, Journal of Sound and Vibration, Vol. 221, No 3, 1999, pp. 371-389, DOI.org/10.1006/jsvi.1998.1976.

[3] Chi, S., Chung, U., Mechanical Behavior of Functionally Graded Material Plates Under Transverse Load, Int. J. Solids and Structures, Vol. 43, N0. 13, 2006, pp. 3657-3674, DOI.org/10.1016/j.ijsolstr.2005.04.011.

[4] Alibeigloo, A., Exact solution for Thermoelastic Response of Functionally Graded Rectangular Plates, Composite Structures, Vol. 92, No. 1, 2010, pp. 113-121, DOI.org/10.1016/j.compstruct.2009.07.003.

[5] Tung, H. V., Duc, N. D., Nonlinear Analysis of Stability for Functionally Graded Plates Under Mechanical and Thermal Loads, Composite Structures, Vol. 92, No. 5, 2010, pp. 1184-1191, DOI.org/10.1016/j.compstruct.2009.10.015.

[6] Hause, T., Advanced Functionally Graded Plate-Type Structures Impacted by Blast Loading, International Journal of Impact Engineering, Vol. 38, No. 5, 2011, pp. 314-321, DOI.org/10.1016/j.ijimpeng.2010.11.006.

[7] Aksoylar, C., Ömercikog˘lu, A., Mecitog˘lu, Z., and Omurtag, M. H., Nonlinear Transient Analysis of Fgm and FML Plates Under Blast Loads, Composite Structures, Vol. 94, No. 2, 2012, pp. 731-744, DOI.org/10.1016/j.compstruct.2011.09.008.

[8] Sreenivas, P., Siva Kumar, A., Pavuluri, S., and Kumari, A. A., Investigation on Transient Dynamic Response of Functionally Graded Materials, International Journal of Application or Innovation in Engineering & Management, Vol. 2, No. 9, 2013, pp. 214-218.

[9] Goudarzi, M., Zamani, J., Experimental and Numerical Investigation of the Maximum Deflection of Circular Aluminum Plate Subjected to Free Air Explosion, (In

Persian) Modares Mechanical Engineering, Vol. 15, No. 1, 2015, pp. 219-226.

[10] Duong, N. T., Duc, N. D., Evaluation of Elastic Properties and Thermal Expansion Coefficient of Composites Reinforced by Randomly Distributed Spherical Particles with Negative Poissons Ratio, Composite Structures, Vol. 153, 2016, pp. 569–577, DOI:10.1016/j.compstruct.2016.06.069.

[11] Duc, N. D., Duc, N., Tuan, N. D., Tran, P., and Quan, T. Q., Nonlinear Dynamic Response and Vibration of Imperfect Shear Deformable Functionally Graded Plates Subjected to Blast And Thermal Load, Journal of Mechanics of Advanced Materials and Structure, Vol. 24, No. 4, 2016, pp. 318-329, DOI:10.1080/15376494.2016.1142024.

[12] Duc, N. D., Quang, V. D., and Anh, V. T. T., The Nonlinear Dynamic and Vibration of the S-FGM Shallow Spherical Shells Resting On an Elastic Foundations Including Temperature Effects, International Journal of Mechanical Sciences, Vol. 123, 2017, pp. 54–63, DOI.org/10.1016/j.ijmecsci.2017.01.043.

[13] Cong, P. H., Anh, V. M., and Duc, N. D., Nonlinear Dynamic Response of Eccentrically Stiffened FGM Plate using Reddys TSDT in Thermal Environment, Journal of Thermal Stresses, Vol. 40, No. 6, 2017, pp. 704–732, DOI.org/10.1080/01495739.2016.1261614.

[14] Hajlaoui, A., Triki, E., Frikha, A., Wali, M., and Dammak, F., Nonlinear Dynamics Analysis of FGM Shell Structures with a Higher Order Shear Strain Enhanced Solid-Shell Element, Latin American Journal of Solids and Structure, Vol. 14, 2017, pp. 72-91, DOI.org/10.1590/1679-78253323.

[15] Thang, P. T., Duc, N. D., and Nguyen-Thoi, T., Thermomechanical Buckling And Post-Buckling of Cylindrical Shell with Functionally Graded Coatings and Reinforced by Stringers, Aerospace Science and Technology, Vol. 66, 2017, pp. 392-401, DOI.org/10.1016/j.ast.2017.03.023.

[16] Duc, N. D., Quang, V. D., Nguyen, P. D., and Chien, T. M., Nonlinear Dynamic Response of Functionally Graded Porous Plates on Elastic Foundation Subjected to Thermal and Mechanical Loads, J. Appl. Comput. Mech., Vol. 4. No. 4, 2018, pp. 245-259, DoI:10.22055/JACM.2018.23219.1151.

[17] Hong kong, P., Dinh Duc, N., Studied Analytical Solutions for The Nonlinear Dynamic Response of ES-FGM Plate Under Blast Load, Vietnam Journal of Mechanics, VAST, Vol. 40, No. 1, 2018, pp. 33 – 45, DOI:10.15625/0866-7136/9840.

[18] Kim, S. E., Duc, N. D., Nam, V. H. and Sy, N. V., Nonlinear Vibration and Dynamic Buckling of Eccentrically Oblique Stiffened FGM Plates Resting On Elastic Foundations in Thermal Environment, Thin-Walled Structures, Vol. 142, 2019, pp. 287-296, DOI.org/10.1016/j.tws.2019.05.013.

[19] Duc, N. D., Hadavinia, H., Quan, T. Q., and Khoa, N. D., Free Vibration and Nonlinear Dynamic Response of Imperfect Nanocomposite FG-CNTRC Double Curved Shallow Shells in Thermal Environment, European Journal of Mechanics - A/Solids, Vol. 75, 2019, pp. 355-366, DOI.org/10.1016/j.euromechsol.2019.01.024.

[20] Upadhyay, A., Shukla, K., Geometrically Nonlinear Static and Dynamic Analysis of Functionally Graded Skew Plates, Communication in Nonlinear Science and Numerical Simulation, Vol. 18, No. 8, 2013, pp. 2252-2279, DOI.org/10.1016/j.cnsns.2012.12.034.

[21] Soltani, M., Hatami, S., and Azhari, M., Free Vibration of Thin Functionally Graded Plates by Exact Finite Strip Method, Journal of computational Methods in Engineering, Vol. 32, No. 2, 2014, pp. 33-54.

[22] Thang, P. T., Nguyen-Thoi, T., and Lee, J., Closed-form Expression for Nonlinear Analysis of Imperfect Sigmoid-FGM Plates with Variable Thickness Resting On Elastic Medium, Composite Structures, Vol. 143, 2016, pp. 143-150, DOI.org/10.1016/j.compstruct.2016.02.002.

[23] Smith, P., Hetherington, J., Blast and Ballistic Loading of Structures, 1st Edition, CRC Press. Tylor & Francis GrouPublished August 15, 1994, ISBN 9780367866877.

*Int. J. Advanced Design and Manufacturing Technology, 2023, Vol. 16, No. 4, pp. 49-59*

*DOI: 10.30486/admt.2024.1958234.1370* *ISSN: 2252-0406* *https://admt.isfahan.iau.ir*

# Non-Destructive Assessment of Concrete Quality Produced with Riverbed Sand and Drainage Sand as Fine Aggregates

**Aderemi A. Alabi** *, **Ayobami E. Agboola**
Department of Physics,
Federal University of Agriculture, Abeokuta, Nigeria
E-mail: derylab@yahoo.com, enihayor4real@gmail.com
(Corresponding author)

**Joseph Olawale Akinyele**
Department of Civil Engineering,
Federal University of Agriculture, Abeokuta, Nigeria
E-mail:joakin777@yahoo.com

**Victor Makinde**
Department of Physics,
Federal University of Agriculture, Abeokuta, Nigeria
E-mail: makindev@funaab.edu.ng

**Received: 20 June 2023, Revised: 3 December 2023, Accepted: 10 December 2023**

**Abstract:** In this work, the effect of fine aggregates from two different sources on the quality and strength of concrete was determined using UPV measurements. The concrete samples were produced using a nominal mix ratio of 1: 1½: 3 and water-cement ratio of 0.55, with three different aggregate sizes (3/8, ½ and ¾ inches) of granite mixed separately with sand obtained from Ogun river and a local drainage in Abeokuta, Southwestern, Nigeria. UPV was measured through each sample on days 1, 7, 14, 21 and 28 after curing using Pundit lab+ equipment. Comparison of the actual compressive strength and estimated compressive strengths from equations generated for each sample type using the crushed samples on the 7th and 28th days respectively shows that most estimations were within the acceptable ±20% variation. Results show that there is no significant difference between the samples made from using either of the two fine aggregates.

**Keywords:** Concrete, Concrete Quality, Fine Aggregate, Non-Destructive Testing, Ultrasonic Pulse Velocity

**Biographical notes**: **Aderemi A. Alabi** obtained his PhD in Solid Earth Physics from the Department of Physics, Federal University of Agriculture, Abeokuta, Nigeria. He is currently Associate Professor in the same Department. **Ayobami E. Agboola** obtained MSc in Geophysics from the Department of Physics, Federal University of Agriculture, Abekuta, Nigeria in 2022. He is a lecturer in the Department of Science Laboratory Technology, Moshood Abiola Polytechnic, Abeokuta, Nigeria. **Joseph Olawale Akinyele** is a Professor of Structural Engineering in the Department of Civil Engineering, Federal University of Agriculture, Abeokuta, Nigeria. **Victor Makinde** is a professor of Solid Earth Physics, in the Department of Physics, Federal University of Agriculture, Abeokuta, Nigeria.

Research paper

## 1 INTRODUCTION

Destructive tests are often performed to assess the properties of in-situ concrete for the quality control and assurance of concrete. However, non-destructive test methods are more practical and cost-effective in material evaluation. Changes in concrete properties with time and external effects could also be studied using non-destructive techniques; thus, it is plausible to assess quality assurance and quality control using non-destructive testing [1].

Non-destructive method of testing concrete is used to obtain the compressive strength and other properties of concrete from existing structures and also provide immediate results for the strength of concrete structure [2]. Avoiding damage and disturbance to the performance of structural components of concrete are the main advantages of the non-destructive method, with quick and simple application, the test results can be achieved easily on the site [2-3]. Non-destructive tests provide an opportunity to assess many properties of concrete which include fundamental parameters such as density, elastic modulus, strength surface hardness, surface absorption, reinforcement location, size and distance from the surface. The test is also useful for inspecting the quality of workmanship and structural integrity by its ability to detect voids, cracking and delamination [4].

Since the quality of some materials can be sometimes related to their elastic stiffness, therefore a measurement of the ultrasonic pulse velocity of the materials can often be used to study their quality and determine their elastic properties [5].

The quality of concrete is usually specified in terms of strength it is therefore helpful to use ultrasonic pulse velocity measurements to give an estimate of concrete strength. The relationship between ultrasonic pulse velocity and strength is affected by several factors such as the age of the concrete, mix proportions, moisture condition, curing conditions, type of cement and type of aggregate [6]. The principle that a wave travels faster in denser media is applied to determine the quality of a material from the velocity of the wave which can be applied to several types of materials such as wood, and concrete, among others [7]. The velocity of an ultrasonic pulse travelling in a solid depends on some properties of the material such as its density and elastic properties. The ultrasonic wave measurement is a useful tool in evaluating the dynamic modulus of elasticity of concrete [8] and is an important factor when assessing the quality and performance of structural concrete [9-10]. The Ultrasonic Pulse Velocity (UPV) is a suitable parameter for estimating static modulus of elasticity, dynamic modulus of elasticity, static Poisson's ratio and dynamic Poisson's ratio [11]. The concrete quality, homogeneity and compressive strength of existing structures can also be evaluated by the UPV testing [12]. Therefore, empirical relationships may be established between the pulse velocity and both the dynamic and static elastic moduli and the strength of concrete. The strength relationship is influenced by several factors including the type of cement, cement quality, admixtures, type and size of the aggregate, curing conditions and age of concrete [4]. Concrete, as a material with a very heterogeneous composition owes its heterogeneity to the nature of its constituents (cement, sand, and gravel), their dimensions, geometry and/or distribution. Thus, it is highly possible that defects and damages could exist in the concretes [7], [13].

Fine aggregates for concrete construction purposes are normally sourced locally and are available in natural deposits at various locations and along the courses of rivers, on the shores of lakes and the sea, and in arid regions, the quality of fine aggregate can vary significantly due to the geographic location and environmental condition. Fine aggregates have a great influence on the workability and cost of concrete, very coarse sands produce harsh and unworkable concrete mixtures, and very fine sands increase the water requirement and are therefore uneconomical [14]. The coarse aggregates commonly used are granites, trap-rocks, gravels, limestones, sandstones, slags, and coal cinders. These materials differ greatly in strength, hardness, porosity, and available gradation of the size of particles [14].

Aggregates determine the quality and features of concrete and play an important role in concrete properties such as strength, stiffness, dimensional stability, durability, workability, and economy; therefore, the physical and chemical properties of aggregates are of interest [15]. Concrete is sensitive to the geological origin of natural aggregates, and its porosity plays an important role in affecting the elastic modulus of concrete because dense aggregates have better mechanical properties [15]. The modulus of elasticity used in concrete design computations is usually estimated from empirical expressions that assume direct dependence on the strength, unit weight and aggregate origin of the concrete [16].

Reported that the use of ultrasonic pulse velocity (UPV) as a non-destructive testing of concrete for assessment of concrete quality has been extensively investigated for decades and is more likely to assess the quality and characteristics of site concrete[17], [18] and described the development of pulse-echo techniques to permit the detection of defects and cracks from tests on one surface as well as the use of a vacuum coupling system, and the application of signal processing techniques to yield information about internal defects and features [19]. Another interesting development described by [20] involves the use of rolling transmitter and receiver scanners which do not need any coupling medium; giving room for a faster and effective way of measuring the pulse velocity. Reported the correlation between UPV and compressive strength of concrete for some typical mixes in simultaneous measurements of pulse velocity and compressive strength made on 150 mm cubes, at different ages from 1 day to 28 days, the result revealed a linear relationship between strength and velocity [21].

Studied the concrete setting time and concrete strength using the Impact-Echo method and found no difference in the correlation between ultrasonic velocity and concrete compressive strength when the water-cement ratio ranged from 0.57 – 0.5, whereas the aggregate content influenced their correlation [22]. A relationship between ultrasonic velocity and compressive strength of concrete was found [23] using different mineral admixtures such as high volume of fly ash (FA), Blast Furnace Slag (BFS) and combination of FA and BFS in replacement of Portland cement. The compressive strength and the ultrasonic pulse velocity values were determined at curing periods of the 3rd, 7th, 28th and 120th days. An exponential relationship between compressive strength and ultrasonic pulse velocity was reported.

Conducted an experimental investigation on the modulus of elasticity of concrete with a total of 60 mixtures and the effects of water/cement ratio, aggregate type, aggregate maximum size, and fly ash content were investigated [24]. The modulus of elasticity of the concretes was obtained besides compressive strength and ultrasound pulse velocities of the concrete. A model was also proposed to predict the dynamic modulus of concrete; the predicted model has a close association with experimental test results. Proposed an empirical equation between UPV and Cube Compressive strength of Concrete which revealed a strong correlation between the UPV and compressive strength [25].

Proposed a Non-destructive evaluation for Glass-Epoxy composite [26]. Impact-echo was used to investigate the thickness and integrity of composite plates. Four composite plates are made of epoxy and fibreglass with different thicknesses of which one comprises a predetermined internal flaw. The impact-Echo device was utilized to detect plate thickness and internal flaws. It was reported that the method is appropriate for thickness measurement and flaw detection of Epoxy-Glass composites within acceptable accuracy.

A warm accumulative roll bonding process (Warm-ARB) using Al-1060 and fine particles of Al2O3 was applied to produce Aluminum Metal Matrix Composite (AMMCs) [27]. The microstructure and mechanical properties of composites were studied after different Warm-ARB passes by tensile test, Vickers microhardness test and scanning electron microscopy. It was reported that as the ARB passes increase, the uniformity of clusters increases considerably and further submitted that the $Al_2O_3$ particles have an enhancing effect on the elongation after a certain number of passes and the tensile strength of the composites increases with ARB passes and enhances the tensile toughness of the composite with more passes. It was established that adding $Al_2O_3$ particles to AMMCs leads to an improvement of the hardness.

Aggregate is one of the major aspects of concrete that is generally more plentiful, rigid, and resistant part which influences the ultrasonic-compressive strength correlation and changes the elastic properties [28-29]. There have been different views on the impact of aggregate on compressive strength of concrete, studied the properties of normal-strength concrete as affected by coarse aggregate size and demonstrated that an increase in aggregate size from 10 mm (3/8 in.) to 64 mm (2½ in.) results in a decrease in the compressive strength of concrete, by as much as 10 per cent [30].

Investigated changes in concrete strength for mixes made with various aggregate sizes and different water-to-cement ratios and reported that an increase in maximum aggregate size from 19 mm (¾ in.) to 38 mm (1½in.) decreases the compressive strength by about 30 per cent for water-to-cement ratios (0.40 to 0.70) [31]. Compared the effect of four different coarse aggregate types on the behaviour of normal and high-strength concretes [32]. It was submitted that high-strength coarse aggregates typically yield higher compressive strengths in high-strength concretes, while coarse aggregate strength has little effect on compressive strength in normal-strength concretes. Showed that compressive strength increases with an increase in coarse aggregate size [33]. Studied the effect of coarse aggregate size on the compressive strength and flexural strength of concrete and reported that the compressive strength of concrete increases with an increase in coarse aggregate sizes [34].

Studied the effect of aggregate type on the compressive strength of concrete and reported that aggregate type affects the compressive strength of normal concrete [35]. The effect of aggregate mineralogy on the strength of concrete was assessed by [36] who reported that concrete with igneous aggregate performed better, followed by concrete with aggregate from sedimentary origin while concrete with metamorphic aggregate had the least compressive strength.

Aggregate sources are necessary for societal needs and cannot be obtained without causing environmental impacts. The environmental impacts can however be minimized by assessing different sources of aggregate and reducing the dependence of natural aggregate on a sole source of natural aggregate. Riverbed sand excavation has been one of the major sources of fine aggregates in Southwestern Nigeria because of the presence of many rivers in the region as well as because of recommendations of riverbed sands for use as fine aggregate [14]. Sand washes up into drainages which causes their blockage and thus flooding in most parts of the country can be another source of fine aggregate. By collecting this sand for use as fine aggregate, flooding which is a major problem in the region is greatly reduced.

The choice of fine aggregate in concrete production is crucial, as it influences the workability, strength, and durability of the resulting concrete. Riverbed sand is often preferred for its naturally rounded particles, while drainage sand, sourced locally, may offer economic advantages. However, the influence of these sand sources on the overall quality of concrete is not fully understood. By employing non-destructive assessment techniques, this study aims to investigate the qualities of concretes produced using riverbed sand and drainage channels as fine aggregate by providing a comprehensive analysis of concrete quality, considering factors such as compressive strength, ultrasonic pulse velocity, and other relevant parameters.

The knowledge provided by this study can be used as a prerequisite for selecting suitable sand to be used as fine aggregate for concrete production.

## 2 EXPERIMENTAL MATERIALS

Limestone Portland cement (LPC) (42.5N) was used as the binder for the concrete. The cement complies with the relevant Nigerian Industrial Standards, [37-42]. The coarse aggregate used was granite obtained from a quarry and crushed into three different sizes 9.5 mm (3/8 inch), 12.5 mm (½ inch) and 19 mm (¾ inch) respectively with sands obtained from local drainage and along the bank of Ogun river used as fine aggregate (all aggregates were obtained in Abeokuta). Impurities and larger aggregates were separated from the fine aggregates using a 5 mm sieve [43] and sieve analysis was carried out on all the aggregates [44]. “Table 1” shows the physical properties of the aggregate used and “Figs. 1 and 2” show the sieve analysis for the coarse and fine aggregates, respectively.

**Table 1** Physical properties of coarse aggregates

| Material | Density (g/cm$^3$) | Fineness Modulus |
|---|---|---|
| Granite | 2.67 | - |
| Drainage sand | 1.53 | 2.51 |
| Ogun riverbed sand | 1.65 | 2.58 |

The water of drinkable quality was used for mixing the concrete constituents with a mix ratio of 1: 1½: 3 [45] and a water-cement ratio of 0.55 for non-air entrained concretes for compressive strength of 30MPa. There were six sample types [1GO (3/8 inch granite and Ogun riverbed sand), 1GL (3/8 inch granite and local drainage sand), 2GO (½ inch granite and Ogun riverbed sand), 2GL (½ inch granite and local drainage sand), 3GO (¾ inch granite and Ogun riverbed sand) and 3GL (¾ inch granite and local drainage sand)]. Each sample was cast in a metal cube mould (150 mm) to produce ten standard concrete cubes (150 × 150 × 150 mm) for each sample type. The samples were initially cured in the air for 24 hours. The moulds were removed and concrete cubes were immersed in a curing tank containing clean water for 28 days [46].

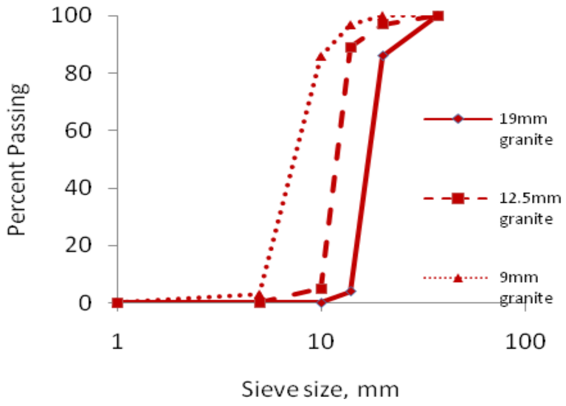

**Fig. 1** Coarse aggregate particle size distribution.

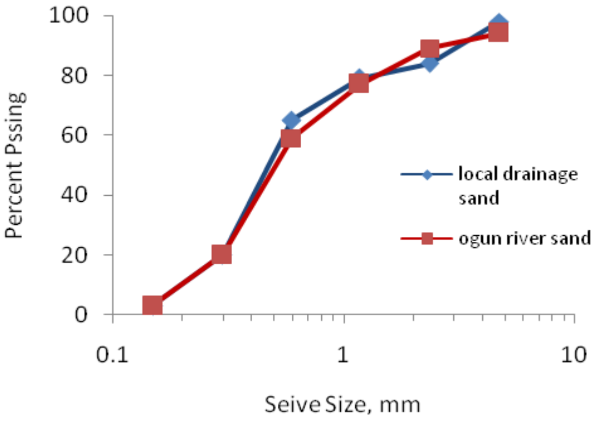

**Fig. 2** Fine aggregate particle size distribution.

## 3 EXPERIMENTAL METHOD

Ten similar sample specimens were made for each sample type to guarantee statistical validity. Statistical analysis was performed on the ultrasonic pulse velocity for each measurement day, the parameters calculated were; mean, standard deviation, coefficient of variation and p-value.

### 3.1. Ultrasonic Pulse Velocity (UPV)

UPV test, as one of the non-destructive tests, operates by sending high-frequency elastic waves into a medium and the travel time for the pulse to propagate through the medium is measured [47]. Pundit lab+ equipment was used to measure ultrasonic pulse velocities through the concrete samples, the pulse was generated by a transmitter and received by a receiver ("Fig. 3") using the direct transmission mode because the transfer of energy between transducers is at its maximum and the accuracy of the path length measurement is principally governed by the accuracy of velocity determination. The pulse velocity (v) can be calculated when the measured time (t) and the path length (L) are known as follows:

$$V=L/t \quad (1)$$

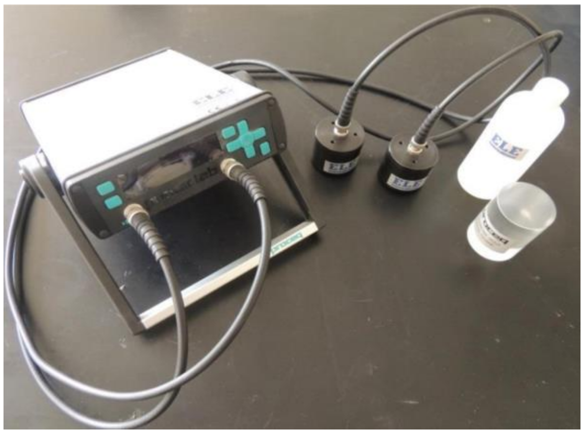

**Fig. 3** Pundit Lab+ Equipment.

"Table 2" shows the use of UPV to classify the quality of concrete. The ultrasonic wave velocity measurement was taken on each concrete cube five times at a weekly interval for 28 days. The concrete cube samples were removed from the curing tank; the water was allowed to drain before subjecting each cube to an ultrasonic pulse velocity test [48-49].

**Table 2** Quality of concrete as a function of the Ultrasonic Pulse Velocity (UPV)

| UPV (km/sec) | Above 4.5 | 3.5 to 4.5 | 3.0 to 3.5 | 2.0 to 3.0 | Below 2.0 |
|---|---|---|---|---|---|
| Concrete Quality | Excellent (E) | Good (G) | Medium (M) | Poor (P) | Very Poor (V.P) |

Source [25].

### 3.2. Compressive strength

The compressive strength of five concrete cubes from each sample type was determined on the 7th day while the compressive strength of another three concrete cubes from each sample type was determined on the 28th day using the hydraulic universal testing machine (WE 1000B).

### 3.3. Statistical Distribution

Kolmogorov-Smirnov and Shapiro-Wilk goodness-of-fit tests were applied to all the cases to check if the data can be modelled statistically following a normal distribution using the mean and standard deviation for the Kolmogorov-Smirnov test and distribution around the minimum and maximum values for the Shapiro-Wilk test. The proposed null hypothesis (H01) stated that "the means obtained from experimental observations data of Ultrasonic Pulse Velocity (UPV) behaved according to a normal distribution", and the Alternate Hypothesis (HA1) stated that "the means of the data does not behave according to a normal distribution". The p-value represented the probability of rejecting the null hypothesis, the smaller the p-value, the smaller the probability that there will be an error in the hypothesis. A recommended value often used is 0.05 which implies that the hypothesis should be rejected when the p-value is less than 0.05. The level of skewness and kurtosis of the distributions was also determined. A rule of thumb for interpreting skewness suggests that if the skewness is less than −1 or greater than +1, the distribution is highly skewed, if it is between −1 and −0.5, or between +0.5 and +1, the distribution is moderately skewed, however, the skewness is approximately symmetric if it is between −0.5 and +0.5. For the kurtosis, when the excess kurtosis is greater than 0, the distribution is platykurtic but leptokurtic when the excess kurtosis is less than 0 [50].

## 4 RESULTS AND DISCUSSION

### 4.1. Statistical Distribution

The statistical distribution analyses ("Table 3") revealed that all samples' UPV measurements behaved according to a normal distribution when subjected to the Kolmogorov-Smirnov normality test for all the measurement days. When subjected to the Shapiro-Wilk normality test, sample 1GL UPV behaved according to a normal distribution only on day 28 while that of 1GO deviated from a normal distribution only on day 28, sample 2GL's UPV deviated from normal distribution only on day 7 but 2GO behaved as a normal distribution throughout the measurement days, the UPV of sample 3GL deviated from normal distribution only on day 7 while sample 3GO's UPV also behaved according to a normal distribution throughout the measurement days.

Although some of the samples' p-value values were less than 0.05 (statistically significant) with the Shapiro-Wilk normality test, all sample distributions were however normally distributed when subjected to the Kolmogorov-Smirnov uniformity test.

**Table 3** Statistical distribution test for the UPV measurements

| Sample | Mean ± sd | Skewness | Kurtosis | Goodness-of-fit test (Normality) | | | | |
|---|---|---|---|---|---|---|---|---|
| | | | | **Sample size = 10** | **$D_{5\%}$ = 0.409** | | | |
| | | | | Kolmogorov-Smirnov | | | Shapiro-Wilk | |
| | | | | Dmax | P-value | Remark | P-value | Remark |
| Day 1 | | | | | | | | |
| 1GL | 3923±250 | 0.163 | -2.050 | 0.288 | 0.378 | Normal | 0.039 | Not Normal |
| 1GO | 3408±87 | 0.608 | -1.255 | 0.243 | 0.594 | Normal | 0.072 | Normal |
| 2GL | 3747±51 | -1.545 | 2.617 | 0.147 | 0.982 | Normal | 0.511 | Normal |
| 2GO | 3435±58 | -0.100 | -0.227 | 0.205 | 0.792 | Normal | 0.172 | Normal |
| 3GL | 3920±104 | -0.545 | -0.828 | 0.201 | 0.815 | Normal | 0.481 | Normal |
| 3GO | 3656±148 | 0.045 | -1.440 | 0.148 | 0.981 | Normal | 0.601 | Normal |
| Day 7 | | | | | | | | |
| 1GL | 4170±101 | -1.545 | 2.617 | 0.201 | 0.816 | Normal | 0.045 | Not Normal |
| 1GO | 4170±68 | -0.100 | -0.227 | 0.187 | 0.895 | Normal | 0.866 | Normal |
| 2GL | 4218±90 | -0.665 | -1.487 | 0.281 | 0.407 | Normal | 0.020 | Not Normal |
| 2GO | 4206±75 | -0.053 | -0.618 | 0.130 | 0.996 | Normal | 0.962 | Normal |
| 3GL | 4187±57 | -2.050 | 5.317 | 0.292 | 0.363 | Normal | 0.007 | Not Normal |
| 3GO | 4251±45 | -0.312 | -0.822 | 0.142 | 0.988 | Normal | 0.562 | Normal |
| Day 14 | | | | | | | | |
| 1GL | 4208±51 | 2.100 | 4.470 | 0.370 | 0.500 | Normal | 0.008 | Not Normal |
| 1GO | 4150±58 | 0.975 | 1.892 | 0.255 | 0.902 | Normal | 0.651 | Normal |
| 2GL | 4238±51 | 0.199 | -0.644 | 0.150 | 1.000 | Normal | 0.956 | Normal |
| 2GO | 4233±50 | -0.276 | -1.141 | 0.207 | 0.983 | Normal | 0.629 | Normal |
| 3GL | 4363±76 | 1.486 | 2.461 | 0.284 | 0.814 | Normal | 0.245 | Normal |
| 3GO | 4370±81 | 0.378 | -1.376 | 0.235 | 0.945 | Normal | 0.753 | Normal |
| Day 21 | | | | | | | | |
| 1GL | 4268±90 | 4.470 | 2.100 | 0.352 | 0.569 | Normal | 0.012 | Not Normal |
| 1GO | 4236±97 | 1.892 | 0.975 | 0.294 | 0.782 | Normal | 0.172 | Normal |
| 2GL | 4378±50 | -1.142 | 0.409 | 0.192 | 0.993 | Normal | 0.717 | Normal |
| 2GO | 4274±69 | -0.471 | -0.055 | 0.115 | 1.000 | Normal | 0.999 | Normal |
| 3GL | 4530±103 | 0.261 | 0.847 | 0.169 | 0.999 | Normal | 0.765 | Normal |
| 3GO | 4519±176 | 1.036 | -0.802 | 0.204 | 0.986 | Normal | 0.840 | Normal |
| Day 28 | | | | | | | | |
| 1GL | 4408±50 | -0.664 | 0.816 | 0.246 | 0.923 | Normal | 0.594 | Normal |
| 1GO | 4375±62 | 3.124 | 1.808 | 0.314 | 0.708 | Normal | 0.023 | Not Normal |
| 2GL | 4420±82 | -0.372 | 0.323 | 0.136 | 1.000 | Normal | 0.988 | Normal |
| 2GO | 4412±46 | 0.241 | 0.062 | 0.158 | 1.000 | Normal | 0.983 | Normal |
| 3GL | 4536±74 | -2.137 | 0.012 | 0.211 | 0.979 | Normal | 0.645 | Normal |
| 3GO | 4624±84 | -3.186 | -0.579 | 0.325 | 0.665 | Normal | 0.058 | Normal |

Also, when the strength of concrete does not exceed 70 MPa, the normal distribution is appropriate in most cases [51]. Therefore, from a general point of view, it is convenient to accept the initially proposed hypothesis that 'the experimental data follows a normal distribution'.

### 4.2. Quality Assessment of Concrete Samples

The samples' quality assessment result ("Table 4") shows that all samples made with local drainage fine aggregate were of good quality on the first day of measurement, samples made with Ogun riverbed sand were of medium quality except the sample which, was made with 19.5 mm aggregate size, the samples were all of the good quality on day 7 and remained good quality till day 28 but samples made with 19.5mm aggregate size achieved excellent quality on day 21. The samples' quality comparison revealed that all the concretes' quality increases with age, ANOVA was however used to determine if there were statistical differences between the samples' quality for each age ("Table 5").

**Table 4** Samples' quality assessment

| Sample | DAY 1 | | DAY 7 | | DAY 14 | | DAY 21 | | DAY 28 | |
|---|---|---|---|---|---|---|---|---|---|---|
| | UPV (m/s) | Quality | UPV (m/s) | Quality | UPV (m/s) | Quality | UPV (m/s) | Quality | UPV (m/s) | Quality |
| 1GL | 3923 | G | 4170 | G | 4208 | G | 4268 | G | 4408 | G |
| 1GO | 3408 | M | 4170 | G | 4150 | G | 4236 | G | 4375 | G |
| 2GL | 3747 | G | 4218 | G | 4238 | G | 4378 | G | 4420 | G |
| 2GO | 3435 | M | 4206 | G | 4233 | G | 4274 | G | 4412 | G |
| 3GL | 3920 | G | 4187 | G | 4363 | G | 4530 | E | 4536 | E |
| 3GO | 3656 | G | 4251 | G | 4370 | G | 4519 | E | 4624 | E |

**Table 5** ANOVA result of statistical comparison of samples' qualities

| Aggregate size | 9.5mm | 12.5mm size | 19mm size |
|---|---|---|---|
| Day 1 | SSD | SSD | SSD |
| | F(2,27) = 37.98,<br>p = 0.000 | F(2,27) = 162.71,<br>p = 0.000 | F(2,27) = 21.34,<br>p = 0.000 |
| Day 7 | NSSD | NSSD | SSD |
| | F(2,27) = 0.00,<br>p = 0.998 | F(2,27) = 0.11,<br>p = 0.741 | F(2,27) = 7.76,<br>p = 0.012 |
| Day 14 | NSSD | NSSD | NSSD |
| | F(2,12) = 2.78,<br>p = 0.134; | F(2,12) = 0.03,<br>p = 0.875 | F(2,12) = 0.02,<br>p = 0.891 |
| Day 21 | NSSD | SSD | NSSD |
| | F(2,12) = 0.31,<br>p = 0.592 | F(2,12) = 7.33,<br>p = 0.027 | F(2,12) = 0.01,<br>p = 0.909 |
| Day 28 | NSSD | NSSD | NSSD |
| | F(2,12) = 0.86,<br>p = 0.380; | F(2,12) = 0.04,<br>p = 0.843 | F(2,12) = 3.10,<br>p = 0.116 |

On day 1, the comparison revealed that there was a statistically significant difference between the quality of samples made with local drainage fine aggregate and Ogun riverbed fine aggregate for all aggregate sizes. Samples made with local drainage fine aggregate were statistically significantly of higher quality (3923±250, 3747±51 and 3920±104) than samples made with Ogun riverbed sand fine aggregate (3408±87, 3435±58 and 3656±148). On the 7th day, there was no statistically significant difference between the quality of samples for 9.5 mm size and 12.5 mm size granite coarse aggregates, however, samples made with local drainage fine aggregate were statistically significantly of lower quality (4187±57) than the samples made with Ogun riverbed fine aggregate (4251±45) for the 19 mm granite coarse aggregates size. No statistically significant difference was observed between the samples' qualities on the 14th day. On the 21st day, a statistically significant difference was only observed between the qualities of samples made with 12.5 mm aggregate size, the local drainage fine aggregate (4378±90) sample was statistically significantly of higher quality than the samples made with Ogun riverbed fine aggregate (4274±69). There was no statistically significant difference between the qualities of the samples on the 28th day.

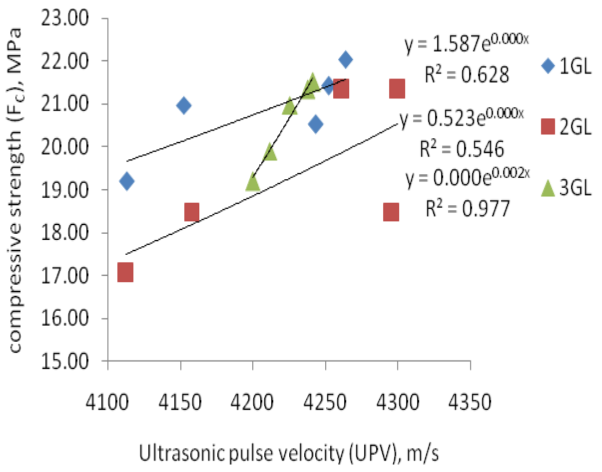

**Fig. 4** Relationship between UPV and $f_c$ for local drainage sand (Day 7).

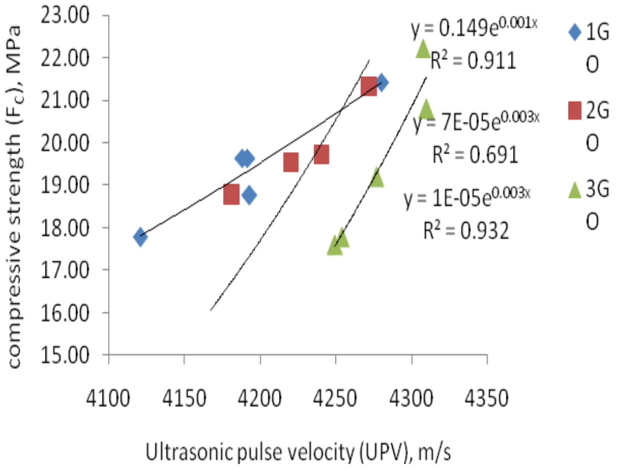

**Fig. 5** Relationship between UPV and $f_c$ for Ogun riverbed sand (Day 7).

## 4.3. Compressive Strength Determination

The results of the measured compressive tests ($f_c$) were determined by averaging the result of crushing five specimens on the 7th day and 3 specimens on the 28th day and used to obtain a relationship between UPV and compressive strength (Figs. 4-7), an exponential relationship was proposed for both day 7 and day 28 in "Table 6" which was used to determine the predicted compressive strength ($f_{cp}$) ("Table 7") of the samples. The predicted compressive strength was compared with the measured compressive strength and the percentage variations wase within the allowable ±20 per cent variation [52].

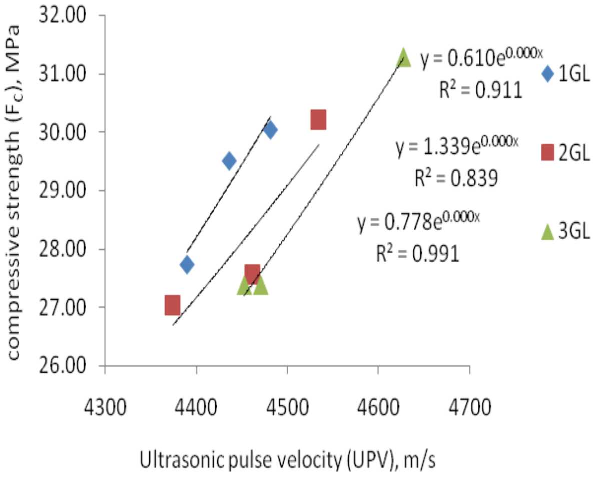

**Fig. 6** Relationship between UPV and $f_c$ for local drainage sand (Day 28).

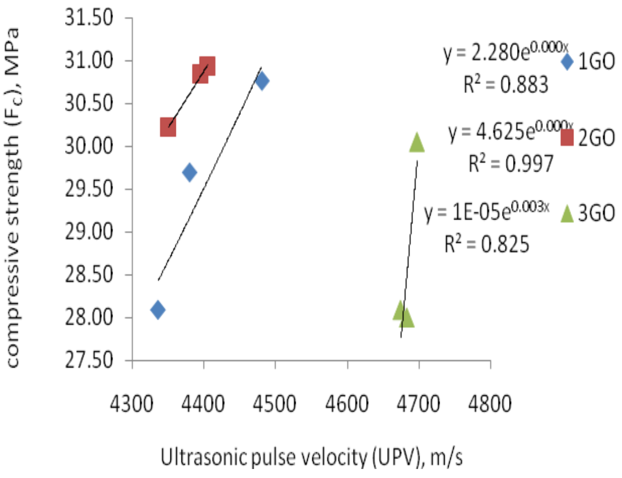

**Fig. 7** Relationship between UPV and $f_c$ for Ogun riverbed sand (Day 28).

**Table 6** The proposed exponential relationship between UPV and compressive strength

| | Day 7 | | Day 28 | |
|---|---|---|---|---|
| Sample | Equation | R$^2$ | Equation | R$^2$ |
| 1GL | $f_c = 1.5874e^{0.0006Vp}$ | 0.628 | $f_c = 0.6108e^{0.0009Vp}$ | 0.911 |
| 1GO | $f_c = 0.1492e^{0.0012Vp}$ | 0.911 | $f_c = 2.2803e^{0.0006Vp}$ | 0.883 |
| 2GL | $f_c=0.5231e^{0.0009Vp}$ | 0.546 | $f_c = 1.3394e^{0.0007Vp}$ | 0.839 |
| 2GO | $f_c = 7E\text{-}05e^{0.003Vp}$ | 0.691 | $f_c = 4.6251e^{0.0004Vp}$ | 0.997 |
| 3GL | $f_c = 0.0002e^{0.0028Vp}$ | 0.977 | $f_c = 0.7789e^{0.0008Vp}$ | 0.991 |
| 3GO | $f_c = 1E\text{-}05e^{0.0034Vp}$ | 0.932 | $f_c = 1E\text{-}05e^{0.0031Vp}$ | 0.825 |

**Table 7** Variation between measured compressive strengths and estimated compressive strengths

| | Day 7 | | | Day 28 | | |
|---|---|---|---|---|---|---|
| Sample | $f_c$ (MPa) | $f_{cp}$ (MPa) | % Var | $f_c$ (MPa) | $f_{cp}$ (MPa) | % Var |
| 1GL | 20.84±1.07 | 19.41±1.13 | -6.86 | 29.10±1.21 | 32.30±1.47 | 11.00 |
| 1GO | 19.45±1.35 | 22.29±1.82 | +14.60 | 29.51±1.34 | 31.5±1.19 | 6.74 |
| 2GL | 19.34±1.91 | 23.37±1.86 | +20.84 | 28.27±1.71 | 29.60±1.70 | 4.70 |
| 2GO | 18.74±2.65 | 21.61±4.85 | +15.31 | 30.67±0.39 | 27.07±0.50 | -11.74 |
| 3GL | 20.59±0.99 | 24.94±3.52 | +21.13 | 28.68±2.26 | 29.37±1.74 | 2.41 |
| 3GO | 19.52±1.99 | 19.10±2.84 | -2.15 | 28.71±1.16 | 23.17±4.21 | -19.30 |

## 5 CONCLUSIONS

In conclusion, the non-destructive assessment of concrete quality produced with riverbed sand and drainage sand using three different aggregate sizes yielded valuable insights into the performance of the concrete. The findings can be summarized as follows:

1. The study demonstrated the effectiveness of non-destructive assessment methods in evaluating the quality of concrete. Non-destructive techniques, such as ultrasonic pulse velocity, proved to be reliable tools for characterizing concrete properties without causing damage to the structure.
2. The quality of concrete samples was predominantly 'Good' at early ages, with a consistent improvement observed as the concrete aged. This suggests a positive correlation between concrete quality and curing time.
3. Concrete samples made with local drainage sand exhibited better quality compared to other sources. This indicates that the choice of fine aggregate source can significantly influence the overall quality of the concrete.
4. Despite variations in aggregate sources and sizes, there were generally no statistically significant differences detected in the quality of the concrete samples. This suggests that factors other than the ones investigated might be influencing concrete quality.
5. The study did not reveal a clear effect of both sand sources and aggregate size on the compressive strength of the concrete samples. This implies that factors beyond the chosen parameters might be more influential in determining compressive strength.
6. The relationship observed between compressive strength and ultrasonic pulse velocity suggests a potential method for estimating the compressive strength of similar concrete compositions. This finding could have practical applications in non-destructive testing.
7. The proposed equations for estimating compressive strength based on ultrasonic pulse velocity demonstrated reliability, with estimated values falling within the acceptable ±20% variation range. This strengthens the utility of these equations for practical applications.
8. The non-destructive assessments revealed that concrete produced with riverbed sand and drainage sand as fine aggregates exhibited comparable quality. This suggests that, at least within the parameters investigated, both sand sources can yield concrete of similar structural integrity, the choice between these two sand sources may not significantly impact concrete performance.

In summary, the non-destructive assessment of concrete quality with riverbed sand and drainage sand as fine aggregates demonstrates the reliability of these methods in evaluating structural properties. The study supports the notion that both sand sources can produce concrete of comparable quality, emphasizing the importance of considering non-destructive techniques for quality control and monitoring in concrete construction.

## REFERENCES

[1] Birgul, R., Hilbert Transformation of Waveforms to Determine Shear Wave Velocity in Concrete, Cement and Concrete Research, Vol. 39, 2009, pp. 696–700.

[2] Hamidian, M., Shariati, M., Arabnejad, M. M. K., and Sinaei, H., Assessment of High Strength and Light Weight Aggregate Concrete Properties Using Ultrasonic Pulse Velocity Technique, Int. J. Phys. Sci., Vol. 6, No. 22, 2011, pp. 5261–5266.

[3] Hobbs, B., Tchoketch, K., Nondestructive Testing Techniques for The Forensic Engineering Investigation of Reinforced Concrete Buildings, Forensic Science Inter-national, Vol. 167, No. 2-3, 2007, pp. 167-172, doi:10.1016/j.forsciint.2006.06.065.

[4] International Atomic Energy Agency, (IAEA), Training Course Series, Guide Book on Non-Destructive Testing of Concrete Structures, No. 17, 2002, pp. 100-127.

[5] Uday, B., Application of Ultra-Sonic Pulse Velocity Techniques for Concrete Quality Measurements, NBMCW, 2001, http://www.nbmcw.com/articles/concrete/23866-techniques-for-concrete-quality-measurements.html.

[6] Lorenzi, A., Reginato, L. A., Fávero, R. B., Carlos, L., and Filho, S., 3D Ultrasonic Tomography Technique as a tool to Evaluate Concrete Structures, EJ. Nondestr. Test., Vol. 21, 2016.

[7] Ali, B. A., Assessment of Concrete Compressive Strength by Ultrasonic Non-Destructive Test, University of Baghdad, 2008, pp. 3.

[8] Jones, R., Facaoaru, I., Recommendations for Testing Concrete by The Ultrasonic Pulse Method, Materials and Structures, Vol. 2, No. 10, 1969, pp. 275–284.

[9] Kar, A., Halabe, U. B., Ray, I., and Unnikrishnan, A., Nondestructive Characterizations of Alkali Activated Fly Ash And/Or Slag Concrete, Eur. Sci. J., Vol. 9, No. 24, 2013, <http://www.eujournal.org/index.php/esj/article/view/1695/1684>.

[10] Singh, G., Siddique, R., Effect of Waste Foundry Sand (WFS) as Partial Replacement of Sand on The Strength, Ultrasonic Pulse Velocity and Permeability of Concrete, Constr. Build. Mater, Vol. 26, No. 1, 2012, pp. 416–422. http://dx.doi.org/10.1016/j.conbuildmat.2011.06.041.

[11] Qixian, L., Bungey, J. H., Using Compression Wave Ultrasonic Transducers to Reassure the Velocity of Surface Waves and Hence Determine Dynamic Modulus of Elasticity for Concrete Construction and Building Materials, Elsevier, Construction and Building Materials, Vol. 10, No. 4, 1996, pp. 237-242.

[12] Breysse, D., Nondestructive Evaluation of Concrete Strength: An Historical Review and A New Perspective by Combining NDT Methods, Construction and Building Materials, Vol. 33, 2012, pp. 139-163, ISSN 0950-0618, https://doi.org/10.1016/j.conbuildmat.2011.12.103.

[13] Corneloup, G., Garnier, V., Etude D'uneméthodeultrasonoreadaptée À La Mesure De L'endommagement des Bétons: Étudebibliographiqueet Analyse des Solutions, Contrat IUT-EDF, 1995.

[14] Ajagbe, W. O., Tijani, M. A., and Oyediran, I. A., Engineering and Geological Evaluation of Rocks for Concrete Production, Lautech Journal of Engineering and Technology, Vol. 9, No. 2, 2017, pp. 67-79.

[15] Langer, W. H., Knepper, D. H., Geologic Characterization of Natural Aggregate: Afield Geologist Guide to Natural Aggregate Resource Assessment, Open File Report, 1995, pp. 95-582.

[16] Mehta, P. K., Monteiro, P. J. M., Concrete Microstructure, Properties and Materials, McGraw Hill, 2006.

[17] Solís-Carcaño, R., Moreno, E., Evaluation of Concrete Made with Crushed Limestone Aggregate Based on Ultrasonic Pulse Velocity, Construction and Building Materials, Vol. 22, No. 6, 2008, pp. 1225-1231.

[18] Hillger, W., Imaging of Defects in Concrete by Ultrasonic Pulse-Echo Technique, Proc. Struct. Faults and Repairs 93, Eng. Technics Press, Edinburgh, Vol. 3, 1993, pp. 59–65.

[19] Kroggel, O., Ultrasonic Examination of Crack Structures in Concrete Slabs, Proc. Struct. Faults and Repairs 93, Eng. Technics Press, Edinburgh, Vol. 3, 1993, pp. 67–70.

[20] Sack, D. A., Olson, L. D., Advanced NDT Methods For Evaluating Concrete Bridges and Other Structures, Proc. Struct. Faults and Repairs 93, Eng. Technics Press, Edinburgh, Vol. 1, 1993, pp.65–76.

[21] Rajagopalan, P. R., Prakash, J., and Naramimhan, V., Correlation Between Ultrasonic Pulse Velocity and Strength of Concrete, Indian Concrete J., Vol. 47, No. 11, 1973, pp. 416-418.

[22] Pessiki, S. P., Carino, N. J., Setting Time and Concrete Strength Using the Impact-Echo Method, ACI Mater. J., Vol. 85, 1989, pp. 389–399.

[23] Demirboga, R., Turkmen, I., and Karakoc, M. B., Relationship Between Ultrasonic Velocity and Compressive Strength for High-Volume Mineral-Admixture Concrete, Cem. Concr Res., Vol. 34, 2004, pp. 2329–2336.

[24] Yıldırım, H., Sengul, O., Modulus of Elasticity of Substandard and Normal Concretes, Constr. Build. Mater, Vol. 25, No. 4, 2011, pp. 1645–1652. http://dx.doi.org/10.1016/j.conbuildmat.2010.10.009.

[25] Qasrawi, H. Y., Concrete Strength by Combined Non-Destructive Methods Simply and Reliably Predicted, Cem. Concr. Res., Vol. 30, 2000, pp. 739–746.

[26] Amiri, M., Tabatabaee Ghomi, M., and Liaghat, Gh., Non-Destructive Evaluation of Glass-Epoxy Composite Using Impact-Echo Method, Int J of Advanced Design and Manufacturing Technology, Vol. 10, No. 1, 2017, pp. 85-91.

[27] Heydari Vini, M., Farhadipour, P., Fabrication of

AA1060/Al2O3 Composites by Warm Accumulative Roll Bonding Process and Investigation of Its Mechanical Properties, Int J of Advanced Design and Manufacturing Technology, Vol. 10, No. 4, 2017, pp. 91–98.

[28] Sturrup, V., Vecchio, F., and Caratin, H., Pulse Velocity as A Measure of Concrete Compressive Strength, Situ/Nondestructive Testing of Concrete, ACI SP-82, 1984, pp. 201-227.

[29] Ravari, A. K., Othman, I. B., and Ibrahim, Z. B., Finite Element Analysis of Bolted Column Base Connection Without and With Stiffeners. Int. J. Phys. Sci., Vol. 6, No. 1, 2011, pp. 1-7.

[30] Walker, S., Bloem, D. L., Effects of Aggregate Size on Properties of Concrete, ACI Journal, Proceedings, Vol. 57, No. 3, 1960, pp. 283-298.

[31] Cordon, W. A., Gillespie, H. A., Variables in Concrete Aggregates and Portland Cement Paste Which Influence the Strength of Concrete, ACI Journal, Proceedings, Vol. 60, No. 8, 1963, pp. 1029-1052.

[32] Ezeldin, A. S., Aitcin, P. C., Effect of Coarse Aggregate on The Behavior of Normal and High-Strength Concretes, Cement, Concrete, and Aggregates, CCAGDP, Vol. 13, No. 2, 1991, pp. 121-124.

[33] Zhou, F. P., Lydon, F. D., and Barr, B., Effect of Coarse Aggregate on Elastic Modulus and Compressive Strength of High-Performance Concrete, Cement and Concrete Research, Elsevier, 1995,

[34] Ajamu, S. O., Ige, J. A., Effect of Coarse Aggregate Size on The Compressive Strength and The Flexural Strength of Concrete Beam, Journal of Engineering Research and Applications, Vol. 5, No. 4, 2015, pp. 2248-2267.

[35] Abdullahi, M., Effect of Aggregate Type on Compressive Strength of Concrete, International Journal of Civil and Structural Engineering, Vol. 2, No. 3, 2012, pp. 791-800.

[36] Buertey, J. T., Atsrim, F., and Ofei, W. S., An Examination of the Physiomechanical Properties of Rock Lump and Aggregates in Three Leading Quarry Sites Near Accra, American Journal of Civil Engineering, Vol. 4, No. 6, 2018, pp. 264-275.

[37] NIS 11, Specification for Ordinary Portland Cement, Standards Organisation of Nigeria, 1974.

[38] NIS 444-1, Composition, Specification and Conformity Criteria for Common Cements, Standards Organization of Nigeria, 2003.

[39] NIS 447, Methods of Testing Cement-Determination of Setting Time and Soundness, Suite 1, 24 Greenville Estate Badore, Lekki-Ajah, Lagos Nigeria, 2003.

[40] NIS 455, Methods of Testing Cement-Taking or Preparing Samples of Cement, Suite 1, 24 Greenville Estate Badore, Lekki-Ajah, Lagos Nigeria, 2003.

[41] BS 12, British Specification for Portland Cement. British Standard Institution, London, 1996.

[42] EN 197-1, Standard Test Method for Ordinary Portland Cement, European Committee for Standardization (CEN). Brussels, 2000.

[43] BS 112., Determination of Properties of Fine Aggregate BSI, Linfordwood, MiltonKeynes MK14 6LE, U. K, 1971.

[44] BS 933: 1, Determination of Particle Size Distribution-Sieving Method, BSI, 1997.

[45] Anum, I., Williams, F. N., Adole, A. M., and Haruna, A. C., Properties of Different Grades of Concrete Using Mix Design Method, IJGAES., Vol. 2 No. 6, 2014.

[46] Aminur, M. R., Harunur, D., Teo, C., L. and Abu, Zakir, M. M., Effect of Aggregates and Curing Conditions on The Compressive Strength of Concrete with Age,UNIMAS E-Journal of Civil Engineering, Vol. 1, No. 2, 2010, pp. 1– 6.

[47] Ji-Hwan, A., Jeong-Hee, N., Soo-Ahn, K., and Sung-Ho, J., Estimation of the Compressive Strength of Concrete Using Shear Wave Velocity Geotechnical Special Publication. GeoHunan International Conference, No. 196, 2009, pp. 154-164.

[48] BS 1881, Testing Concrete: Recommendations for Measurement of Velocity of Ultrasonic Pulses in Concrete Part 203, 1986.

[49] ASTM-C597, Standard Test Method Pulse Velocity Through Concrete, American Society for Testing and Materials, 2009.

[50] Brown, 2011, http://www.tc3.edu/instruct/sbrown/stat/shape.htm.

[51] Lizarazo-Marriaga, J., LópezYépez, G. L., Effect of Sedimentary and Metamorphic Aggregate on Static Modulus of Elasticity of High-Strength Concrete-Dyna, Year 78, Nro., Vo. 170, 2011, pp. 235-242. Medellin. ISSN 0012-7353.

[52] IS: 13311 (Part-1), Non-Destructive Testing of Concrete – Methods of Tests, Bureau of Indian Standard, New Delhi, India, 1992.

*Int. J. Advanced Design and Manufacturing Technology, 2023, Vol. 16, No. 4, pp. 61-68*

*DOI: 10.30486/ADMT.2024.2001757.1426 ISSN: 2252-0406 https://admt.isfahan.iau.ir*

# A Study on The Effects of Different Pad Materials on Brake System Performance of a High-Capacity Elevator by FEM Simulation

**Mohammad Sajjad Mahdieh*, Farshad Nazari, Ali Riyadh Khairullah**
Department of Mechanical Engineering,
Shahid Chamran University of Ahvaz, Ahvaz, Iran
E-mail: s.mahdieh@scu.ac.ir, F.nazari@scu.ac.ir, alireyadh@scu.ac.ir
*Corresponding author

**Received: 19 November 2023, Revised: 20 December 2023, Accepted: 31 December 2023**

**Abstract:** The brake system must be reliable and display unchanging action throughout its use, as it guards the health and life of many people. Properly matched friction pair, a drum, and a brake pad have a great impact on these factors. The brake pads are far more complex components. New technologies make it possible to develop materials with various compositions and different proportions and connect them permanently in fully controllable processes. This elaboration shows that all these factors have a greater or lesser impact on the coefficient of friction, resistance to friction wear and high temperature, and the brake pad's operating life. The friction materials are required to provide a stable coefficient of friction and a low wear rate at various operating speeds, pressures, temperatures, and environmental conditions. The aim of this work is therefore to investigate the possibility of using a Finite Element Analysis (FEA) approach to evaluate the braking performance of a heavy-duty elevator with different non-conventional pad materials including Composite Carbon fiber reinforced, Composite Epoxy SMC and SiC (silicon carbide). The results show that the performance of SiC (silicon carbide) is better than two other materials. In the braking system with SiC, the required time for stoppage of the system is lower than two other materials.

**Keywords:** Braking System, Design Enhancement, Elevator, External Shoe Brake, FEM Simulation, Pad Materials

**Biographical notes: Mohammad Sajjad Mahdieh** received his PhD in Mechanical Engineering from the University of Tehran, Iran. He is currently an Assistant Professor at the Department of Mechanical Engineering, Shahid Chamran University of Ahvaz, Iran. His research areas are inverse engineering, 3D printing and metal forming. **Farshad Nazari** is currently an Assistant Professor at the Department of Mechanical Engineering, Shahid Chamran University of Ahvaz, Iran. His research areas are 3D printing and metal forming. **Ali Riyadh Khairullah** is an international MSc student at the Department of Mechanical Engineering, Shahid Chamran University of Ahvaz, Iran.

Research paper

## 1 INTRODUCTION

Brakes are one of the most important components of the elevators. The brake system must be reliable and display unchanging action throughout its use, as it guards the health and life of many people. The term drum brake usually means a brake in which shoes press on the inner/outer surface of the drum. When shoes press on the outside of the drum, it is usually called a clasp brake. Drum brake components include the backing plate, brake drum, shoe, wheel cylinder, and various springs and pins. In operation, the brake shoe of an external contracting brake is tightened around the rotating drum by moving the brake lever. The brake shoe carries the brake lining, which is riveted or glued to the shoe. When the brake is applied, the shoe moves and presses the lining against the inside of the drum. The friction between the lining and drum provides the braking effort. Energy is dissipated as heat. In most elevators (as in this project), the external shoe brake system is applied. Figure 1 shows some external shoe brakes and different pad linings.

In the past two decades, asbestos has become a popular ingredient used to produce brake pads, due to its strength, resistance to heat and fire-proof. Since the 1980s, asbestos has been known as a harmful content and was banned from being used as an ingredient to produce brake pads. Therefore, non-asbestos contents like Kevlar (aramid fiber), glass fiber, and graphite were used to replace the asbestos.

More than 10 different constituents are usually contained in a frictional brake pad. These constituents often contain binder resin, reinforcing fibers, solid lubricants, abrasives, wear resistance, and other friction modifiers. Binder resin and reinforcing fibers used in friction materials have a substantial influence in determining friction characteristics. For improved physical strength and friction performance, the friction materials usually contain two or three different fibers from metallic, ceramic, glass, acrylic, and other fiber. New technologies make it possible to develop materials with various compositions and different proportions and connect them permanently in fully controllable processes. The friction materials are required to provide a stable coefficient of friction and a low wear rate at various operating speeds, pressures, temperatures, and environmental conditions. Furthermore, these materials must also be compatible with the rotor material to reduce its extensive wear, vibration, and noise during braking. Therefore, improving the design of a brake system is a significant practical problem. Shoe brake devices are simple in design and have cost advantages. Ma et al. developed an elevator safety gear braking testing rig based on the disc-pad braking model in principles of energy equivalent and speed equivalent to evaluate the braking behavior of short carbon fiber (SCF) reinforced carbon/carbon (C/C) composite and Cu-based powder metallurgy (P/M) material [1].

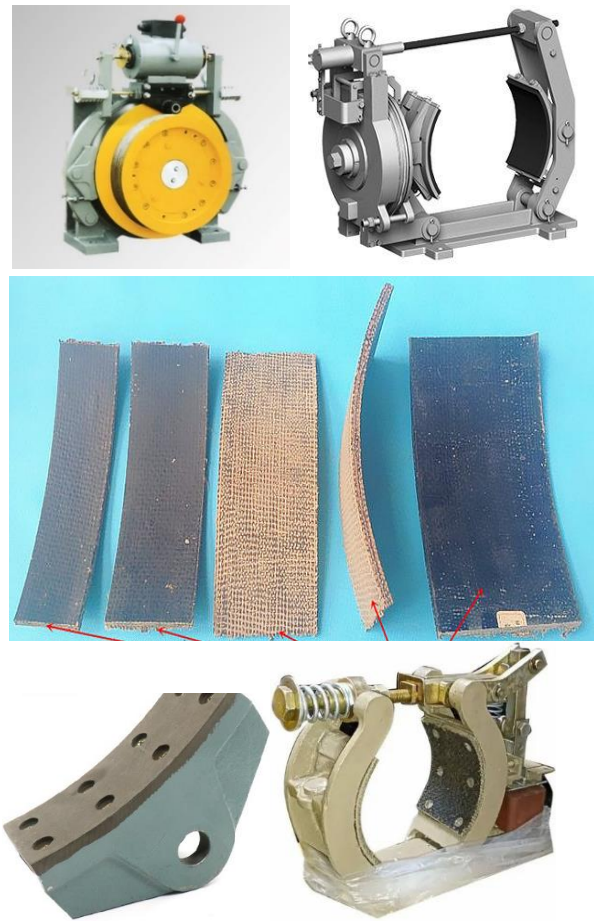

**Fig. 1** External shoe brakes and linings.

El-Hija et al. developed Novel C/C–SiC materials for their use as brake pads for high-speed elevators. Under dynamic and stationary conditions, these materials exhibit high thermal shock resistance, high coefficients of friction, and extremely low wear rates. In addition, it has been found that the SiC content of the C/C–SiC materials on the friction surface heavily influences the frictional behaviour [2]. Liew et al. studied the tribological properties difference of potentially newly designed non-commercial brake pad materials with and without asbestos under various speeds and nominal contact pressure. The two fabricated non-commercial asbestos brake pad (ABP) and non-asbestos brake pad (NABP) materials were tested and compared with a Selected Commercial Brake Pad (CMBP) material using a pin-on-disc tribo-test-rig under dry contact conditions. Results showed that friction coefficients for all materials were insensitive to increasing speed and pressure [3]. Borawski published a review article in which he mentioned and investigated the kinds of material for the braking system. His review collects the most important, and the most unconventional materials used in the production of brake pads, and characterizes their impact on the tribological properties of pads. According to his review, the brake system must be reliable and display unchanging action throughout its use, as it guards the health and life of many people. Properly matched friction pair, a disc and brake pad (in disc brakes), have a great impact on these factors [4]. Applying FEM methods has been very common among researchers [5-8], for example, Riva et al., investigated the possibility to use a Finite Element Analysis (FEA) approach combined with a COF pv-map to compute the global COF of a disc brake system. The local COF is determined from a pv-map for each local sliding velocity and contact pressure determined by the FEA. Results obtained by the simulation are compared with dyno bench test of the same brake system to investigate the validity of the simulation approach. Results show that the simulation is perfectly in line with the experimental measurements in terms of in-stop COF development, but slightly higher with a positive offset for every braking [9]. Günay et al., recommended research and development studies based on finite element modeling and prototype manufacturing in order to produce high-efficiency and safety brake systems compatible with rail system vehicles [10]. Verma et al. focused on the tribological behaviour of a commercial friction pad material dry sliding against a cast iron disc. Pin-on-disc tests were conducted at room temperature under mild wear conditions, as concerns load and rotating speed. The effect of some components of pad material, in particular copper, on the dynamic of formation of tribological layer and wear debris was presented [11]. By applying finishing methods, the surface integrity of manufactured pads can be improved [12-16]. Dmitriev et al. established a model typical for contact situations of automotive brakes based on the method of movable cellular automata [17]. Nouby et al. presented an FE model of the disc brake corner that includes the wheel hub and steering knuckle. Their model was an extension of earlier FE disc brake models. Experimental modal analysis of the disc brake system was initially used to validate the FE model [18]. By appearing advanced manufacturing methods such as modern machining, new pads with advanced materials have been manufactured [19-23]. Yevtushenko et al. carried out Finite Element Analysis (FEA) of a single braking process for the axisymmetric heat conduction problem of friction in a pad/disc brake system in the present article. Two materials of the pad FC-16L (retinax A) and FMC-11 (metal ceramic) and one material of the disc (cast iron) were analyzed in their study [24]. Talati et al. extracted the governing heat Equations for the disk and the pad in the form of transient heat Equations with heat generation that is dependent on time and space. The problem is solved analytically using Green's function approach [25]. Yevtushenko et al. studied the influence of nine various (experimental and theoretical) formulas for heat partition ratio on temperature in a pad/ disc tribosystem. The real dimensions, operating conditions, and thermophysical properties of materials of two different disc brake systems were adopted for the finite element analysis [26]. Shanker reviewed different braking methods and procedures used in the study of automotive braking system. It covers types of braking systems, material properties and different types of materials used in the manufacturing of especially disc brakes [27]. Lu et al. tested a brake pad material used in a popular, commercially available vehicle that consisted of steel wool, iron powder, graphite, coke, styrene–butadiene rubber, MgO, $BaSO_4$, and phenolic resin with the friction assessment and screening test. Their material exhibited an average friction coefficient of 0.419 and a low total wear of 6.25wt% [28].

In this study, the effects of the brake pad materials on the braking system performance are investigated via FEM simulation. In this case, some different materials of brake pads including modern materials including Composite Carbon fiber reinforced, Composite Epoxy SMC and SiC (silicon carbide) are selected, then, their properties are extracted from their manufacturer catalogues as well as related papers. The brake system is modelled in a CAD software (SolidWorks) and the FEM simulation is performed in Ansys software. The performance of the brake system is compared by different pad materials and the proper pad material is introduced.

## 2 MATERIALS AND METHODS

In this study, the simulations are performed in Ansys software 2022. The initial model was designed via SolidWorks software and then was imported in the Ansys software according to “Fig. 2”. The model contains braking system parts including brake pads, shaft, lever, pulley and link.

In this project, non-conventional (modern) materials were used for the brake pads including Composite Carbon fiber reinforced, Composite Epoxy SMC and SiC (silicon carbide). These materials were selected due to their growing applications in the braking pad. The properties of selected pads materials are demonstrated at the “Table 1”.

To analyze this problem in Ansys, three modules can be used: rigid dynamic, static structural and transient structural. In the present study, the third module - transient structural- has been applied. Transient structural module is proper for problems with high deflection as well as high velocity. This module also has a higher analysis rate. In the next step, the materials should be defined. The shaft material was defined as a structural steel with a yield stress equal to 25 MPa.

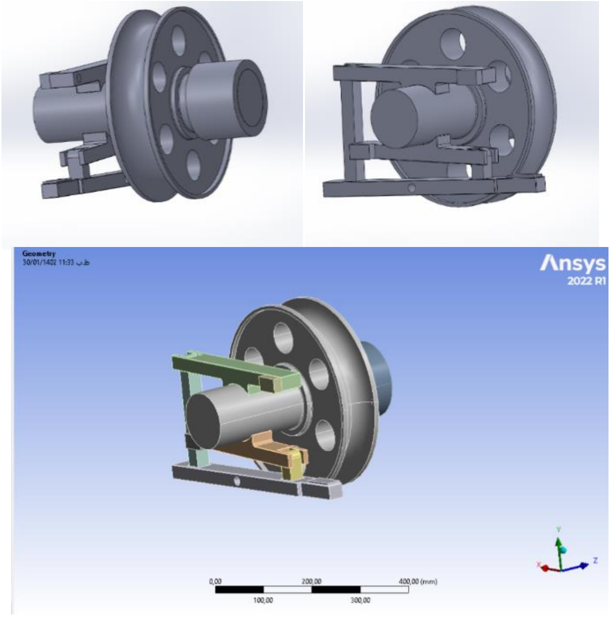

**Fig. 2** Initial model of braking system.

**Table 1** Properties of Composite Carbon fiber reinforced, Composite Epoxy SMC and SiC

| Materials<br>Properties | SMC | Carbon fiber | SiC |
|---|---|---|---|
| Denisty | 1.47e-6 kg/mm$^3$ | 1.7e-6 kg/mm$^3$ | 3.1 kg/mm$^3$ |
| Young's Modulus | 57810 MPa | 94870 MPa | 410000 Mpa |
| Poisson's Ratio | 0.303 | 0.319 | 0.14 |
| Bulk Modulus | 49033 MPa | 87745 MPa | 3900 Mpa |
| Shear Modulus | 22175 MPa | 35941 MPa | 55000 MPa |
| Ultimate Strength | 261 MPa | 503 MPa | 1020 MPa |
| Yield Strength | 249 MPa | 503 MPa | 1015 MPa |
| Thermal Conductivity | 0.00046 W/mm.C | 0.026 W/mm.C | 0.12 W/mm.C |

In the next step, connections among parts in the Connection module were defined. In the other world, the boundary conditions were set. According to "Fig. 3", the holder is fixed and the shaft can rotate in the centre of it. In addition, the motion of the pad is defined. In this way, when forces are imposed on the lever, the movement of the lever leads to the movement of the pad and contact of the pad to the shaft.

In the Contact module, the action and reaction of parts when colliding with each other are defined. In this section, if no contact is defined between two parts, these two parts pass through each other. Therefore, three kinds of contacts can be defined among parts: frictional, sticking, and no frictional. In the present project, the frictional contact between the shaft and pads was defined.

It is worth mentioning that the Coefficient of Friction CoF is not constant and depends on the velocity of the shaft and the temperature. Precisely defining the CoF is not easy, and many surveys have been conducted to measure it. For example, "Fig. 4" shows the results of a study in which the CoF was measured in different conditions [22]. Anyway, in the present study, the CoF is presumed constant for each material and independent of speed.

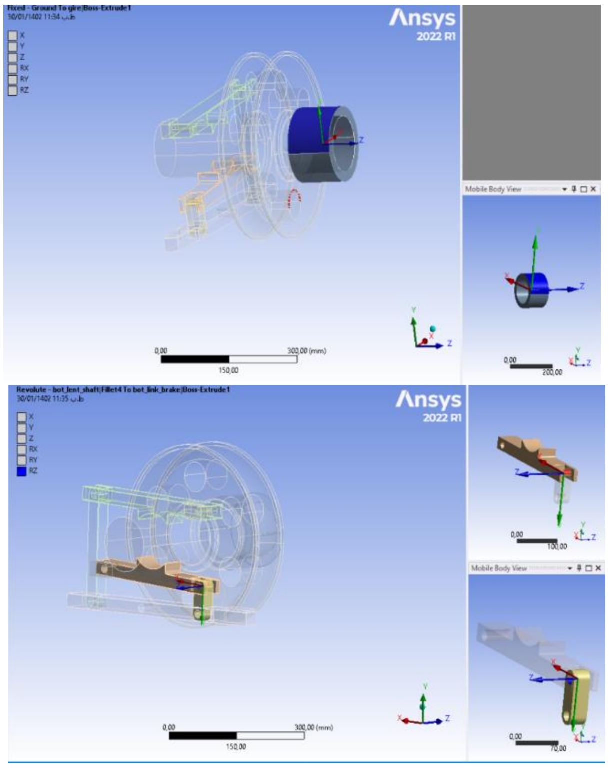

**Fig. 3** Boundary conditions.

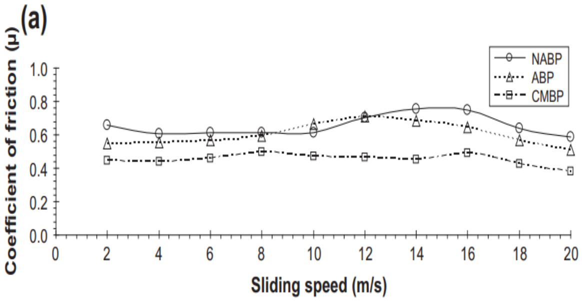

**Fig. 4** Coefficient of friction versus speed in some materials [22].

The Meshing is defined in the Mesh module. According to "Fig. 5", meshing was performed between the shaft and the pad's halves. Here, due to the significance of the shaft and pads, these parts have fine mesh sizes; despite the other parts such as the pulley and links which have larger mesh sizes. If the mesh size of the whole of the mechanism is identical, the run time increases dramatically. The mesh size is 15mm and it is a 2D (surface mesh) type. In addition, the mesh control was applied to investigate the convergence of the results.

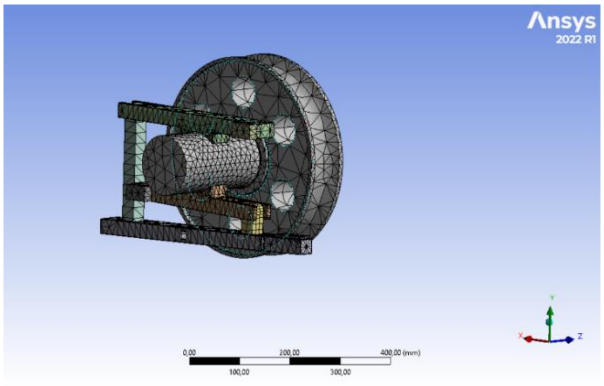

**Fig. 5** Meshed part.

## 3 RESULTS & DISCUSSIONS

In this study, the effects of the brake pad materials on the braking system performance were investigated via FEM. The results are as follows. According to "Fig. 6", the whole braking system was stress analyzed and, the maximum stress imposed on brake pads and the shaft was obtained.

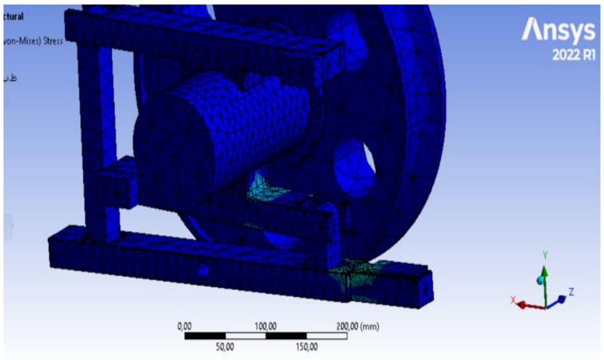

**Fig. 6** Stress analyzed of braking system

Figure 7 shows the stress on the shaft for the carbon fiber pad's material. As it is obvious, the maximum stress on the shaft with this pad's material is 84MPa. Figure 8 demonstrates the stress on the shaft for the SMC pad's material. As it is clear, the maximum stress on the shaft with this pad's material is 54MPa which is lower than carbon fiber. The maximum stress on the pads with carbon fiber pad material is about 455MPa which is shown in "Fig. 9". In addition, the maximum stress on the pads with SMC pad material is about 301MPa ("Fig. 10"). The stresses on pads are very high and result in an increase in the temperature of pads and consequently increase in their abrasion.

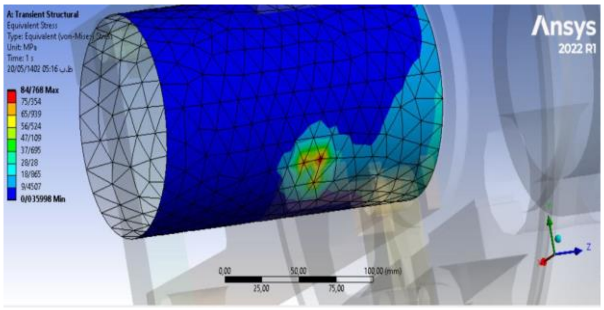

**Fig. 7** Stress on the shaft (carbon fiber pad).

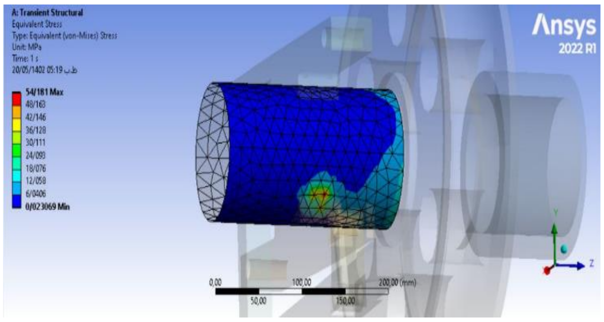

**Fig. 8** Stress on the shaft (SMC pad).

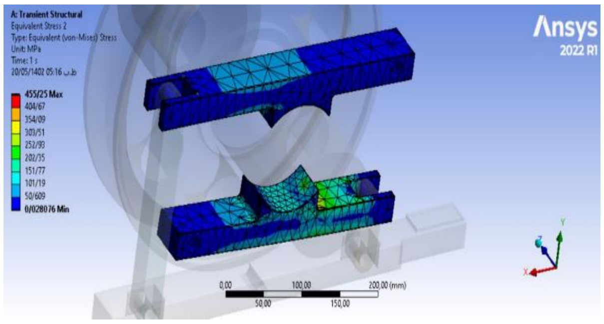

**Fig. 9** Stress on the pads (carbon fiber pad)

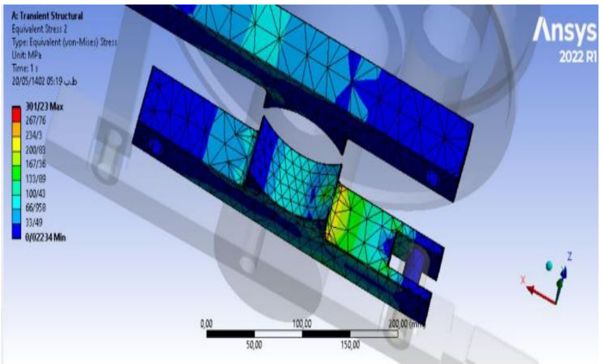

**Fig. 10** Stress on the pads (SMC pad).

The strain imposed on the braking system (pads, links and levers) was obtained as well and is shown in “Fig. 11” (for carbon fiber pad’s material) and in “Fig. 12” (SMC pad’s material). The maximum strain was 0.004 mm/mm for both materials which implies the stiffness of the braking system.

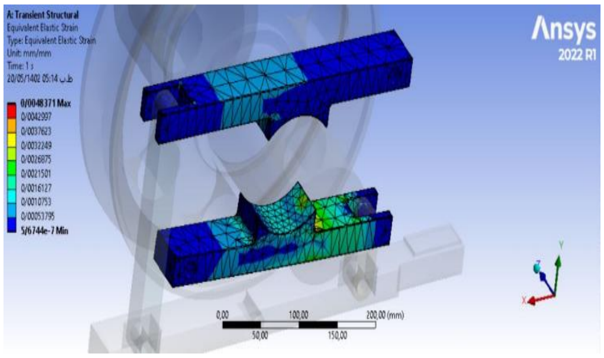

**Fig. 11** Strain of the pads and levers (carbon fiber pad).

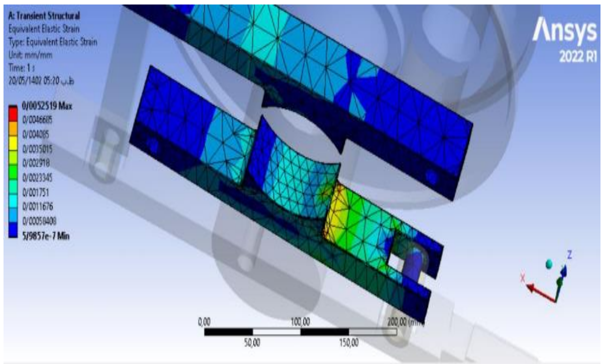

**Fig. 12** Strain of the pads and levers (SMC pad).

In “Fig. 13”, the velocity contour and in “Fig. 14”, the acceleration contour are demonstrated. The acceleration and velocity of the rotating elements further from the center are more than those located at the center of rotation. In addition, in “Fig. 15”, the total displacement of the elements that occurred during the braking action is shown. The total displacement of the external elements of the pulley is maximum and equals 30cm.

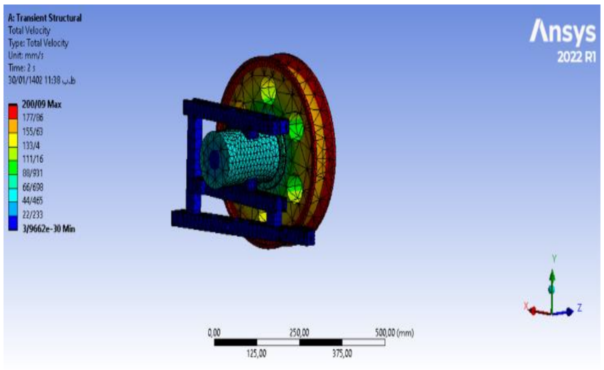

**Fig. 13** Velocity contour.

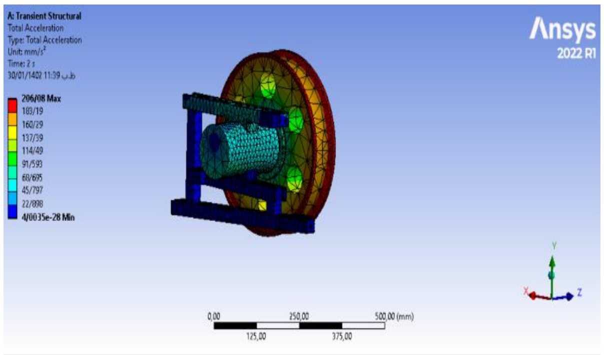

**Fig. 14** Acceleration contour.

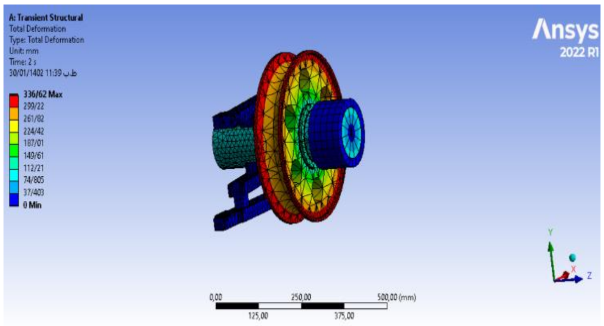

**Fig. 15** Total displacement.

In “Fig. 16”, the diagram of the negative acceleration of the braking system for fiber carbon pad material is shown. according to this diagram, the system stops after 0.5s, which is acceptable. As it was mentioned before, the initial rotary speed of the shaft was 10m/s. In addition, as “Fig. 17” shows, the stresses imposed on the system increase dramatically during the braking period.

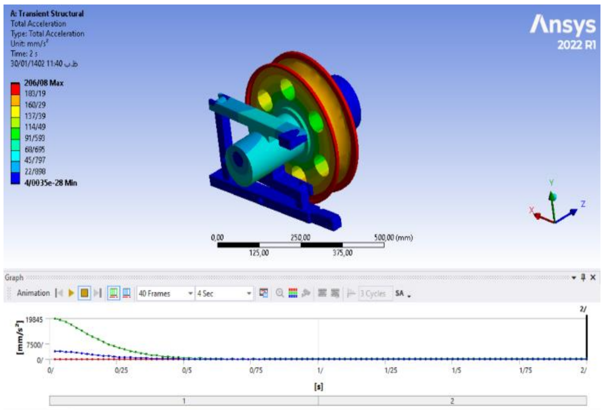

**Fig. 16** Negative acceleration of the braking system for fiber carbon pad.

In the “Fig. 18”, the performance of three pad materials is compared. To investigate the performance of the pad material, the negative acceleration, negative velocity, and the increase in stress during the braking period are analyzed.

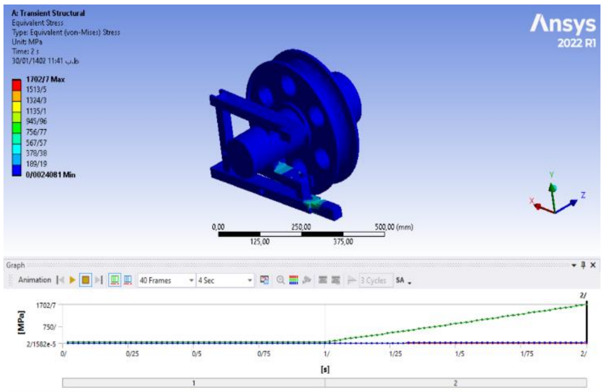

**Fig. 17** Stresses imposed on the system during braking period for fiber carbon pad.

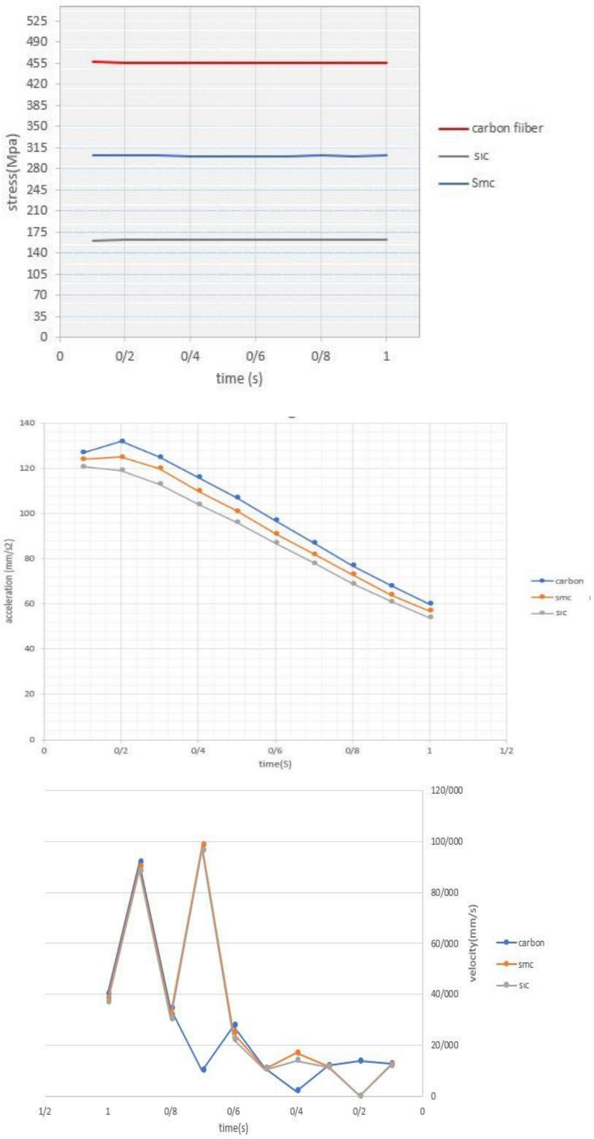

**Fig. 18** Comparison performance of three pad materials (Stress, Velocity and Acceleration).

Accordingly, the performance of SiC (silicon carbide) is better than two other materials. In the braking system with SiC, the required time for stoppage of the system is lower than two other materials. In addition, the performance of SMC is better than Composite Carbon fiber reinforced.

## 4 CONCLUSIONS

In this study, the effects of the brake pad materials on the braking system performance were investigated via FEM simulation. The following conclusions can be drawn from the present work:

- The maximum stress on the shaft with carbon fiber pad material was 84MPa.
- The maximum stress on the shaft with the SMC pad material was 54MPa which was lower than carbon fiber.
- The maximum stress on the pads with carbon fiber pad material was about 455MPa.
- The maximum stress on the pads with SMC pad material was about 301MPa.
- The stresses on pads were very high resulting in an increase in the temperature of pads and consequently increase in their abrasion.
- The strain imposed on the braking system (pads, links, and levers) was obtained as well.
- The maximum strain was approximately 0.004 mm/mm for both materials which implies the stiffness of the braking system.

## 5 ACKNOWLEDGEMENTS

We are grateful to the Research Council of Shahid Chamran University of Ahvaz for financial support (SCU.EM1402.39184).

## REFERENCES

[1] Ma, X., et al., Experimental Evaluation of Braking Pad Materials Used for High-Speed Elevator, Wear, Vol. 477, 2021, pp. 203872.

[2] El-Hija, H. A., Krenkel, W., and Hugel, S., Development of C/C–SiC Brake Pads for High-Performance Elevators. International Journal of Applied Ceramic Technology, Vol. 2, 2005, pp. 105-113.

[3] Liew, K., Nirmal, U., Frictional Performance Evaluation of Newly Designed Brake Pad Materials, Materials & Design, Vol. 48, 2013, pp. 25-33.

[4] Borawski, A., Conventional and Unconventional Materials Used in The Production of Brake Pads–Review, Science and Engineering of Composite Materials, Vol. 27, No. 1, 2020, pp. 374-396.

[5] Mahdieh, M. S., et al., A Study on Stamping of Airliner's Tail Connector Part Through FEM Simulation, Journal of Simulation and Analysis of Novel Technologies in Mechanical Engineering, Vol. 15, No. 3, 2023, pp. 5-13.

[6] Mahdieh, M. S., Esteki, M. R., Feasibility Investigation of Hydroforming of Dental Drill Body by FEM Simulation, Journal of Modern Processes in Manufacturing and Production, Vol. 11, No. 2, 2022, pp. 71-83.

[7] Mahdieh, M. S., Monjezi, A., Investigation of an Innovative Cleaning Method for the Vertical Oil Storage Tank by FEM Simulation, Iranian Journal of Materials Forming, 2022.

[8] Mahdieh, M. S., Bakhshi Zadeh, M., and Zare Reisabadi, A., Improving Surface Roughness in Barrel Finishing Process Using Supervised Machine Learning, Journal of Simulation and Analysis of Novel Technologies in Mechanical Engineering, Vol. 15, No. 2, 2023, pp. 5-15.

[9] Riva, G., Varriale, F., and Wahlström, J., A Finite Element Analysis (FEA) Approach to Simulate the Coefficient of Friction of A Brake System Starting from Material Friction Characterization, Friction, Vol. 9, No. 1, 2021, pp. 191-200.

[10] Günay, M., Korkmaz, M. E., and Özmen, R., An Investigation on Braking Systems Used in Railway Vehicles, Engineering Science and Technology, An International Journal, Vol. 23, No. 2, 2020, pp. 421-431.

[11] Verma, P. C., et al., Braking Pad-Disc System: Wear Mechanisms and Formation of Wear Fragments, Wear, Vol. 322, 2015, pp. 251-258.

[12] Saraeian, P., et al., Influence of Vibratory Finishing Process by Incorporating Abrasive Ceramics and Glassy Materials on Surface Roughness of CK45 Steel, ADMT Journal, Vol. 9, No. 4, 2016, pp. 1-6.

[13] Vakili Sohrforozani, A., et al., A Study of Abrasive Media Effect on Deburring in Barrel Finishing Process, Journal of Modern Processes in Manufacturing and Production, Vol. 8, No 3, 2019, pp. 27-39.

[14] Mahdieh, M. S., The Surface Integrity of Ultra-Fine Grain Steel, Electrical Discharge Machined Using Iso-Pulse and Resistance–Capacitance-Type Generator, Proceedings of the Institution of Mechanical Engineers, Part L: Journal of Materials: Design and Applications, Vol. 234, No, 4, 2020, pp. 564-573.

[15] Vakili Sohrforozani, A., et al., Effects of Abrasive Media on Surface Roughness in Barrel Finishing Process, ADMT Journal, Vol. 13, No. 3, 2020, pp. 75-82.

[16] Mahdieh, M. S., Improving Surface Integrity of Electrical Discharge Machined Ultra-Fined Grain Al-2017 by Applying RC-Type Generator, Proceedings of the Institution of Mechanical Engineers, Part E: Journal of Process Mechanical Engineering, 2023, pp. 09544089231202329.

[17] Dmitriev, A., Österle, W., and Kloβ, H., Numerical Simulation of Typical Contact Situations of Brake Friction Materials, Tribology International, Vol. 41, No. 1, 2008, pp. 1-8.

[18] Nouby, M., Srinivasan, K., Simulation of the Structural Modifications of A Disc Brake System to Reduce Brake Squeal, Proceedings of the Institution of Mechanical Engineers, Part D: Journal of Automobile Engineering, Vol. 225, No. 5, 2011, pp. 653-672.

[19] Mahdieh, M. S., Mahdavinejad, R., Comparative Study on Electrical Discharge Machining of Ultrafine-Grain Al, Cu, and Steel, Metallurgical and Materials Transactions A, Vol. 47, No. 12, 2016, pp. 6237-6247.

[20] Mahdieh, M. S., Mahdavinejad, R. A., A Study of Stored Energy in Ultra-Fined Grained Aluminum Machined by Electrical Discharge Machining, Proceedings of the Institution of Mechanical Engineers, Part C: Journal of Mechanical Engineering Science, Vol. 231, No. 23, 2017, pp. 4470-4478.

[21] Mahdieh, M. S., Mahdavinejad, R., Recast Layer and Micro-Cracks in Electrical Discharge Machining of Ultra-Fine-Grained Aluminum, Proceedings of the Institution of Mechanical Engineers, Part B: Journal of Engineering Manufacture, Vol. 232, No. 3, 2018, pp. 428-437.

[22] Mahdieh, M. S., Zare-Reisabadi, S., Effects of Electro-Discharge Machining Process on Ultra-Fined Grain Copper, Proceedings of the Institution of Mechanical Engineers, Part C: Journal of Mechanical Engineering Science, Vol. 233, No. 15, 2019, pp. 5341-5349.

[23] Mahdieh, M. S., Recast Layer and Heat-Affected Zone Structure of Ultra-Fined Grained Low-Carbon Steel Machined by Electrical Discharge Machining, Proceedings of the Institution of Mechanical Engineers, Part B: Journal of Engineering Manufacture, Vol. 234, No. 5, 2020, pp. 933-944.

[24] Yevtushenko, A., Grzes, P., Axisymmetric FEA of Temperature in A Pad/Disc Brake System at Temperature-Dependent Coefficients of Friction and Wear, International Communications in Heat and Mass Transfer, Vol. 39, No. 8, 2012, pp. 1045-1053.

[25] Talati, F., Jalalifar, S., Analysis of Heat Conduction in A Disk Brake System, Heat and Mass Transfer, Vol. 45, No. 8, 2009, pp. 1047-1059.

[26] Yevtushenko, A., Grzes, P., Finite Element Analysis of Heat Partition in A Pad/Disc Brake System, Numerical Heat Transfer, Part A: Applications, Vol. 59, No. 7, 2011, pp. 521-542.

[27] Shanker, P. S., A Review on Properties of Conventional and Metal Matrix Composite Materials in Manufacturing of Disc Brake, Materials Today: Proceedings, Vol. 5, No. 2, 2018, pp. 5864-5869.

[28] Lu, Y., Tang, C. F., and Wright, M. A., Optimization of a Commercial Brake Pad Formulation, Journal of Applied Polymer Science, Vol. 84, No. 13, 2002, pp. 2498-2504.

*Int. J. Advanced Design and Manufacturing Technology, 2023, Vol. 16, No. 4, pp. 69-77*

*DOI: 10.30486/admt.2024.1994136.1418 ISSN: 2252-0406 https://admt.isfahan.iau.ir*

# Effect of Post-Weld Heat Treatment on Microstructure and Mechanical Properties of AA7075 Welds

**Alireza Jalil, Nasrollah Bani Mostafa Arab ***
Faculty of Mechanical Engineering,
Shahid Rajaee Teacher Training University, Tehran, Iran
E-mail: ar.jalil@sru.ac.ir, n.arab@sru.ac.ir
*Corresponding author

**Malek Naderi**
Department of Materials and Metallurgical Engineering,
Amirkabir University of Technology, Tehran, Iran
E-mail: mnaderi@aut.ac.ir

**Yaghoub Dadgar Asl**
Department of Mechanical Engineering,
Technical and Vocational University, Tehran, Iran
E-mail: ydadgar@tvu.ac.ir

**Received: 17 August 2023, Revised: 28 November 2023, Accepted: 30 November 2023**

**Abstract:** The attractive mechanical properties of 7075 alloy, such as its high strength-to-weight ratio and fracture toughness, have received special attention in the automotive and aerospace industries. However, welding as a fabrication process has a detrimental effect on this alloy's properties which affects its mechanical performance. In this work, to compensate for the loss in mechanical properties caused by welding, proper heat treatment operations are adopted. To this end, 1.5 mm AA7075 sheets were first preheated and butt welded using the gas tungsten arc welding process. The welded sample was solution heat treated, quenched, and then artificially aged. Microhardness tests showed an increase of hardness in all zones of the aged specimen compared to those of the original welded blank before heat treatment. A maximum microhardness value of 180 HV was recorded in the heat-affected zone of the aged specimen. In addition, elongation at break, and strength (yield, tensile, and fracture) of the original welded blank increased by about 50% after the artificial aging operation.

**Keywords:** AA7075, Mechanical Properties, Post-Weld Heat Treatment, TIG Welding

**Biographical notes: Alireza Jalil** is a PhD student in the field of manufacturing engineering at Shahid Rajaee Teacher Training University, Tehran, Iran. He received his MSc from Shahid Rajaee Teacher Training University in 2014. **Nasrollah Bani Mostafa Arab** is an Associate professor of Mechanical Engineering at Shahid Rajaee Teacher Training University, Iran. He received his PhD from IIT Delhi, India, in 1993. **Malek Naderi** is a Professor in the Department of Mining and Metallurgical Engineering, at Amirkabir University of Technology, Tehran, Iran. He received his PhD from RWTH Aachen University in Germany, in 2007. **Yaqoub Dadgar Asl** is an assistant professor in the Department of Mechanical Engineering at Technical and Vocational University, Iran. He received his PostDoc in mechanical engineering from Pusan National University, South Korea, in 2019.

Research paper

## 1 INTRODUCTION

The environmental concerns and requirements of greenhouse gas emissions have led transportation industries to lightweight products. Aluminum alloys as a subset of lightweight materials are abundantly used in automotive and aircraft structures due to their low density, high strength-to-weight ratio, and good corrosion resistance [1]. Among aluminum alloys, the AA7075 alloy with precipitates of $Mg_2Zn$ and $Al_2CuMg$ phases presents the strength and stiffness required for the body in white (BIW) in aerospace and automotive industries [2]. This alloy is a precipitate-strengthened alloy with the additions of zinc, magnesium, and copper alloying elements.

The Solution Heat Treatment (SHT) process on 7075 Al alloy as a heat-treatable Al−Zn−Mg−Cu alloy, influences the content and distribution of the coarse secondary phases and the evolution of the microstructure, thus leading to a change in the mechanical properties of the alloy. The distribution and size of precipitates mainly depend on the SHT process. Hence, a suitable SHT condition is important to gain proper mechanical properties. It has also been reported that aging is the most preferred method to improve the hardness and strength of AA7075 [3]. During aging, precipitation occurs in a super-saturated aluminum solid solution, and then the alloy's hardness and strength increase [4]. Aging is the precipitation strengthening that provides by far the strongest contribution to the strength of aged Al-Zn-Mg-Cu alloys.

The precipitation mechanism of aging or precipitate hardening in most commercially 7xxx alloys such as AA7075 is $\alpha \rightarrow$ Guinier Preston (GP) zones $\rightarrow \eta' \rightarrow \eta$. Here $\alpha$ represents supersaturated solid solution (SSS) and is obtained by rapid cooling to room temperature after taking it into solution. The $\eta$ phase is the equilibrium phase with a hexagonal structure containing Al, Zn, Mg, and Cu, which can be considered to be based on a solid solution of $MgZn_2$ with AlCuMg components (i.e., Mg $(Zn, Al, Mg)_2$ or Mg $(Zn_2, AlMg)$). However, $\eta'$ phase (fine precipitates of Zn and Mg-rich metastable $MgZn_2$ phase) is a metastable hexagonal phase. GP zones can form as progenitors of the metastable $\eta'$ phase. The age-strengthening factor of AA7075 is more related to fine-scale precipitation of the metastable $\eta'$ phase and has a very important role in the mechanical properties of the 7075 alloy. $\eta'$ phase occurs after aging at 120 ◦C for 4 h, and phases form after 24 h aging time. The size, shape, concentration, and distribution of precipitates are effective parameters for the mechanical properties of this alloy [5-8]. XU et al. [9] observed that $MgZn_2$ particles completely dissolved at a heat treatment of 475°C for 5 minutes. The $Al_2CuMg$ phase gradually disappeared and finally dissolved into the matrix completely at 490 °C, and the $Al_7Cu_2Fe$ phase exhibited no change during the SHT [10].

Welding is one of the most common joining methods for aluminum alloys and tungsten inert gas (TIG) is one of the most used welding processes [11]. As an efficient metal joining process, the welding process makes the joint's strength equal to or sometimes greater than the strength of the base metal and has been widely used in almost all branches of industry [12-13]. In spite of advantages, welding Al-Zn-Mg-Cu aluminum alloys is difficult because of the weld metal zone's porosity, slag inclusion, and cracks. Welding as a production process has a negative impact on the mechanical properties of AA7075 alloy which significantly decreases these properties compared to the base material [14]. Significant strength reduction after the gas tungsten arc welding process (GTAW) and thus considerably lower hardness in the fusion zone (FZ) and heat affected zones (HAZs) are the result of significant precipitate dissolution and coarsening of heat-treatable alloys undergoing high welding temperatures [15]. AA 7075 alloy also exhibits hot cracking and porosity defects via fusion-based additive manufacturing methods. Appropriate post-weld heat treatment can be used to overcome the loss in mechanical properties caused by welding.

To improve the mechanical performance of welded joints, an appropriate post-weld heat treatment is required for the 7xxx aluminum alloy joints [8]. The post-weld heat treatment has shown a practical option to recover the strength of the joints by modifying the graining and distribution of the secondary strengthening particles, therefore it can be an effective method of improving the mechanical properties of welded joints [8], [11].

Liu Xiao et al. [16] carried out TIG butt welding of 7075 aluminum alloy by a self-made 7075 wire before and after heat treatment. They reported that after heat treatment, the mechanical properties of the joint greatly improved. The maximum elongation and tensile strength reached 16.9% and 94% of the base metal (BM). Before heat treatment, $\eta(MgZn_2)$, $S(CuMgAl_2)$, T(AlZnMgCu), and other precipitates distributed continuously at the grain boundary, reduced the mechanical properties of the joint and weakened the influence of grain size. After heat treatment, most of the precipitated phases dissolved into the matrix, and the grain size became the main factor affecting the mechanical properties of the joint. Using TIG AA7075 welding, Tusk et al. [17] found the formation of hot cracks in welded joints and studied the effect of heat treatment and cooling rate on mechanical and microstructural properties. The filler metal type has an important effect on the properties of the welded joint. Welding with dissimilar filler materials aims to dilute the crack-sensitive BM with less crack-sensitive filler material. By diluting the melting zone with dissimilar filler, the concentration of alloy elements of AA7075 decreases. This leads to a decrease in weld strength and an increase in the likelihood of liquation cracking [18]. Kou et al. [19] found aluminum filler alloys such as ER5356 cause the melting zone to solidify earlier than the partially melted zone abutting the melt pool (pure AA7075), creating tension towards the center of the melt pool leading to liquation cracks.

For some authors, the loss of hardness in the boundary between the BM and the HAZ is the major reason for the failure in aluminum alloys. The hardening phase dissolution operation in the matrix during the welding causes a reduction in the mechanical properties of the HAZ. Also, the increased grain size near the molten pool applies greater softening [20]. One way to control solidification cracking is to correct the FZ grain structure with fine-grained coaxial grains. Coarse columnar grains are more prone to solidification cracks than fine coaxial grains while fine-grained coaxial grains deform more easily with contractile strains [21].

Few studies have reported GTAW welding of AA7075 with features of SHT and aging on the mechanical properties of the welded joints. In the present study, preheated 1.5 mm thick AA7075 sheets were initially butt joined using the GTAW welding process. The welded sample was subjected to SHT, then rapidly quenched in a cooling die to form a supersaturated solid solution, and finally artificially aged (AA). Investigations were carried out to study the effect of welding, and artificial aging on microstructure, elongation, strength, and Vickers microhardness of TIG welded AA7075.

## 2 EXPERIMENTAL PROCEDURES

### 2.1. Materials

In the present study, AA7075-T6 sheets with 140*120 mm dimensions with a thickness of 1.5 mm were cut and prepared. Also, sub-size tensile test specimens were cut following the ASTM E08 standard [22] in the rolling direction using a wire cut machine. Uniaxial tensile tests were carried out on a SANTAM universal testing machine at a speed of 1 mm/min using an extensometer with a 50 mm gauge length to measure exact displacements. The 0.2% offset yield strength, ultimate tensile strength, and elongation at break were evaluated for tensile specimens. The Chemical composition of the base material in the as-received condition and filler rod are shown in “Table 1”. Vickers microhardness (HV) test was also performed using a Vickers indenter with 300gf load and 10s dwell time according to ASTM E384-16 standard [23].

**Table 1** Chemical composition (wt. %) of base metal (AA 7075) and filler metal (5356)

| Material | Zn | Mg | Cu | Cr | Fe | Si | Ti | Mn | Zr | Al |
|---|---|---|---|---|---|---|---|---|---|---|
| AA7075 | 5.70 | 2.02 | 1.35 | 0.18 | 0.15 | 0.07 | 0.047 | 0.02 | 0.01 | Remaining |
| Filler metal (5356) | 0.10 | 5.50 | 0.10 | 0.12 | 0.40 | 0.25 | 0.13 | 0.10 | - | Remaining |

### 2.2. Preheating

Preheating builds up additional heat which decreases the cooling rate of a welded joint. Preheating does not affect the final outlook of the weld zone cross-section but may improve the weld joint properties. The extra heat of preheating increases the temperature of the material around the weld zone to facilitate welding. In this work, AA7075 sheets were first cleaned and deoxidized with a wire brush and acetone solution. The sheets were then subjected to 80 ° C for a period of 4 minutes in a furnace to obtain a homogeneous microstructure throughout the sheets [24]. By preheating, the sheets are prepared for welding with a moderate thermal gradient.

### 2.3. Welding Operation

The GTAW process was selected for welding as this process produces high-quality welds [11] at a reasonable cost. One of the most critical factors to consider for GTAW is the filler metal. The ER5356 (Mg-rich) plays an important role in the strength of the weldment joint due to its good penetration depth [25]. The filler metal ER5356 of 1.6 mm diameter was therefore used for butt welding the sheets under the conditions given in “Table 2”.

**Table 2** GTAW welding process parameters

| | |
|---|---|
| Tungsten electrode diameter (mm) | 2.4 |
| Filler rod diameter (mm) | 1.6 |
| Alternating Current (AC) (A) | 90-110 |
| Welding speed (mm /min) | 16 |
| Gas flow rate (l /min) | 10 |
| Pre-heat temperature (°C) | 80 |
| Shielding gas | Argon |
| Gas pressure (bar) | 100 |
| Gas purity | 99.99 % |

In this work, a thick plate with a V-shaped groove was used as a fixture to fix the sheets with a root gap of 1mm during the welding process as shown in “Fig. 1(a)”. Before welding, the parts and fixture surfaces were cleaned with a soft wire brush and acetone solution to remove oxides and other contaminants. The welding direction was chosen perpendicular to the sheet's rolling direction. GTAW welding process parameters were set according to “Table 2”. The welding process was performed manually as shown in “Fig. 1(a)”. Figure 1. (b) shows the welded blank with the designed set-up.

Welded samples were prepared for tensile, microhardness, and metallographic tests to evaluate the mechanical properties (“Fig. 2”). The specimens were prepared perpendicular to the weld line (“Fig. 2 (b)”).

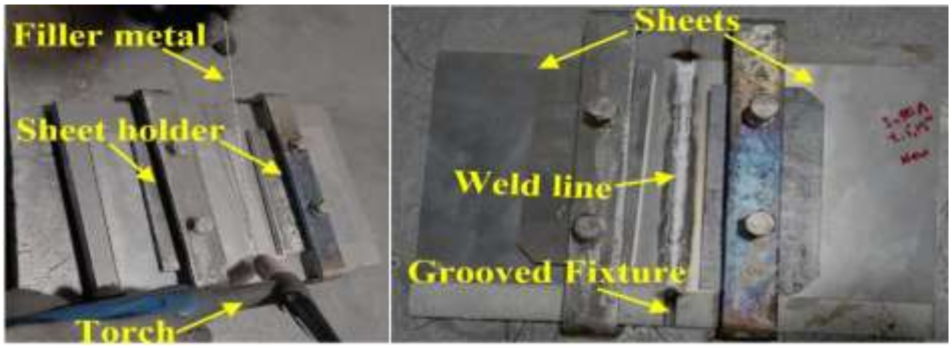

(a) (b)

**Fig. 1** The welding set-up: (a): Fixture for welding the sheets, and (b): The final welded blank.

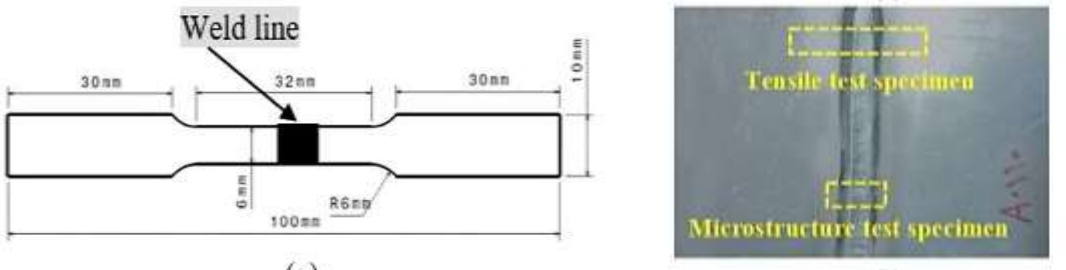

(a) (b)

**Fig. 2** Test specimens: (a): The tensile specimen geometry and dimensions, and (b): Positions of the test specimens.

### 2.4. Post-Weld Heat Treatment

For post-weld heat treatment of the welded blank, the solution heat treatment was first performed at 480 °C for a soaking time of 10 min using a controlled temperature furnace. The solution heat treated samples were then quenched to ambient temperature as quickly as possible using a flat water-cooling die. Finally, an artificial aging operation was carried out at 120°C for a soaking time of 24 h in a heat treatment furnace to complete the post-weld heat treatment.

### 2.5. Uniaxial Tensile and Hardness Tests

To obtain tensile properties (tensile strength $\sigma_U$, yield strength $\sigma_Y$, percentage of elongation El%, and fracture strength $\sigma_F$), uniaxial tensile tests with a constant strain rate of 1 mm/min were carried out. The tensile specimens for the welded blank (WB) and the AA specimen were prepared perpendicular to the welding direction using a wire cutting machine as explained in section 2.1, according to ASTM E8 [22].

Vickers microhardness (HV) test was also performed (as explained in section 2.1) to measure the hardness values of the BM, the WB, and the AA specimen. The hardness profiles were obtained over the joint cross-section using ASTM E384-16 standard [23].

### 2.6. Metallography

Metallographic samples were prepared as ASTM E3-11 standard [26] technique using sandpaper and alumina powder for polishing. After polishing, the etching solution of nitric acid, hydrochloric acid, hydrofluoric acid, and distilled water was first used and the final etching was done with a modified chlorine solution, according to ASTM E883-11 [27] to reveal the microstructure. The microstructural analysis was performed using an optical microscope. Also, An X-ray diffraction (XRD) test was performed to identify the phases in the as-received AA7075.

## 3 RESULTS AND DISCUSSION

### 3.1. Microstructure Studies

To describe the characteristics of the weldment joint, a cross-sectional macrograph of FZ, HAZ, and BM zones of WB is shown in “Fig. 3”. Figur 4” shows that the microstructure morphology of the BM has a typical rolled structure, and the grains are banded or fibrous along the deformation direction. The base metal microstructure consisting of coarse and elongated Al grains with a dispersion of fine and coarse precipitates diffused in the field of α matrix of the alloy is shown in “Fig. 4”.

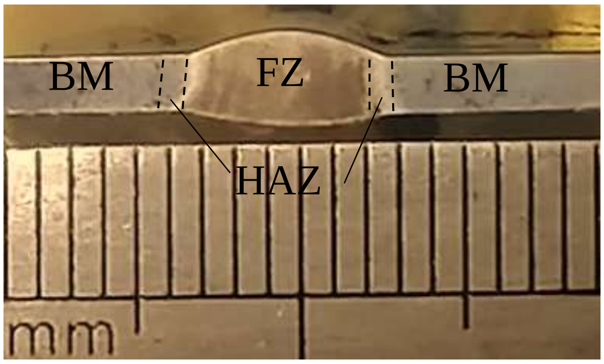

**Fig. 3** Cross-section macrograph of FZ, HAZ and BM zones in the WB.

**Fig. 4** Optical micrograph of the AA7075 base metal.

The XRD graph for the as-received AA7075 is shown in "Fig. 5".

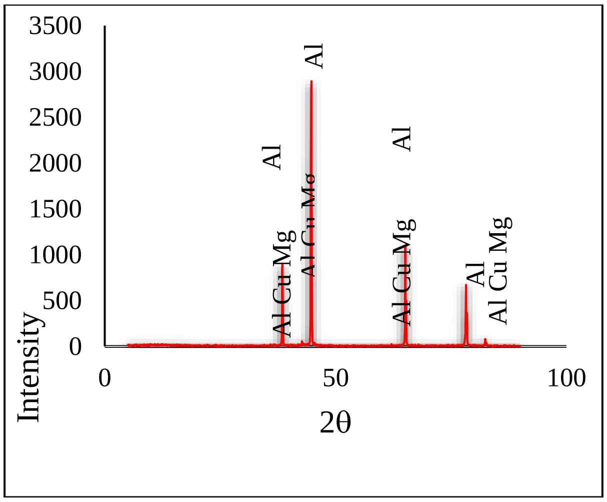

**Fig. 5** X-ray diffraction of the as-received AA7075.

This XRD reveals the different contents of phase compositions of the alloy. Based on the peaks of the graph, it is observed that the microstructure consists of Al, AlCuMg, and $Al_2CuMg$ particles. The very small precipitates of $MgZn_2$ also act as a strengthening phase of aluminum alloy 7075 as reported by other researchers [28-29]. However, the presence of $MgZn_2$ was not detected, which may be due to the XRD technique that was not sensitive enough to study the low content of $MgZn_2$ intermetallic phases or the dissolving of some Zn and Mg atoms in the Al matrix.

As observed in the optical micrograph of HAZ and FZ of the WB in "Fig. 6", the precipitates are dispersed inside the grains and at the grain boundaries. The overaging caused by the welding heat input that leads to the formation of coarse precipitates inside the FZ spherical grains reduces the strength and hardness. In contrast to the base metal's microstructure, the microstructure of the FZ consisted of equiaxed grains. The dispersion of precipitates into the matrix of the FZ is due to the incidence of dynamic recrystallization. The hardening phase dissolution operation in the matrix during the welding process and the increased grain size near the molten pool cause greater softening and a reduction in the mechanical properties of the HAZ as reported by Gomez et al. [20].

**Fig. 6** Optical micrograph of HAZ and FZ of the WB.

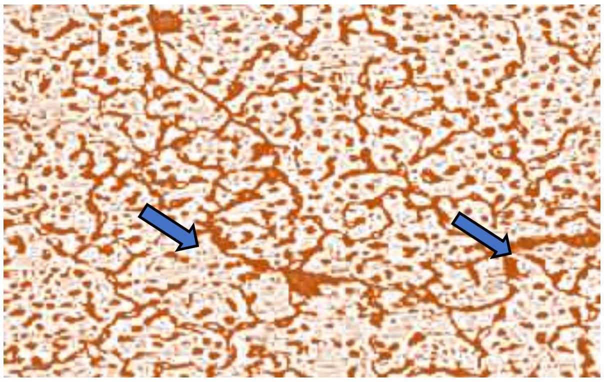

**Fig. 7** Optical micrograph of a microcrack in the FZ (200X).

The properties of the FZ of the WB are also affected by the filler metal type. As mentioned earlier in the introduction section, welding with dissimilar filler metal ER5356 dilutes the melting zone and the concentration of the alloying elements of AA7075 decreases resulting in a decrease in weld strength and an increase in the likelihood of liquation cracking [18-19]. This type of crack was observed in the FZ of the WB as shown in “Fig. 7”. Microcracks of this nature usually originate from grain boundaries where intergranular cracks developed.

Figure 8 presents the microstructure of the BM of the WB after artificial aging (AA) at 120°C for 24 h. Artificial age hardening of the 7075-type alloys is considered the main source of alloy strength [28]. During the AA process, several structural transformations such as precipitation hardening, solid solution strengthening, and grain refinement occur within the aluminum alloy 7075.

**Fig. 8** Optical micrograph of the BM of AA specimen.

These mechanisms offer improved strength, hardness, and fatigue resistance. The fine precipitates within the microstructure of the alloy are composed of strengthening elements such as Cu, Zinc, and Mg. These precipitates act as obstacles to the movement of dislocations, leading to increased strength and hardness. The solid solutions formed during solid solution strengthening, and the fine-grain structures also contribute to better mechanical properties after the AA process. Comparison of micrographs of “Fig. 4” (initial material) and “Fig. 8” (AA specimen)” indicates the recovery of the microstructure and hence improvement in the mechanical properties after the AA operation. It is seen that after the AA process, the morphology of irregular coarse particles is changed into almost globular shapes, as also reported previously by Ding et al. [11].

Figure 9 reveals the changes and modification of the WB joint microstructure in three regions (BM, HAZ, and FZ) of the AA sample. Examining the microstructure of Fig. 9, the almost uniform distribution and fineness of precipitates in the HAZ matrix of the AA specimen due to proper aging operation tend to improve this zone's hardness and strength compared to those of the WB. After the aging process, the microstructure consisted of very fine and dense precipitates inside the grains, while precipitation density at the grain boundaries almost disappeared. The grain shape and morphology of FZ also showed the coaxial and regular grains. The smaller and more uniformly distributed precipitates inside the grains can lead to higher strength and hardness of the FZ of the AA sample.

**Fig. 9** Optical micrograph of different zones of artificially aged joint.

### 3.2. Tensile Properties

The tensile properties of the BM, the WB, and the AA specimens are presented in “Table 3” and “Fig. 10”. The harmful effect of welding caused an almost 38% reduction in the tensile properties ($\boldsymbol{\sigma}_U$, $\boldsymbol{\sigma}_Y$, and $\boldsymbol{\sigma}_F$) of the WB compared to those of the BM. A 65% decrease in elongation was also observed. As stated earlier in section 3.1, these reductions are mainly due to the microstructural changes in the WB. However, post-weld heat treatment of the WB was found to be beneficial to enhance the tensile properties. Variations of mechanical properties indicate that the strength values of the AA specimen are very close to those of the BM. Despite a 65% loss of ductility of the WB, the aging operation caused improvements of 50% in elongation at break and 54% in fracture strength. Therefore, a noticeable improvement in mechanical properties can be achieved after proper post-weld heat treatment of the specimens.

**Table 3** Mechanical properties ratios (%) of the BM, the WB, and the AA specimens

| specimen | $\boldsymbol{\sigma}_U$ (MPa) | $\boldsymbol{\sigma}_Y$ (MPa) | $\boldsymbol{\sigma}_F$ (MPa) | El% |
|---|---|---|---|---|
| AA | 546 (96 %) | 445(90 %) | 520 (100.4 %) | 9 (69%) |
| WB | 352 (62 %) | 295 (60 %) | 337 (65 %) | 4.5 (35%) |
| AA7075 | 569 (100%) | 495 (100%) | 518 (100%) | 13 (100%) |

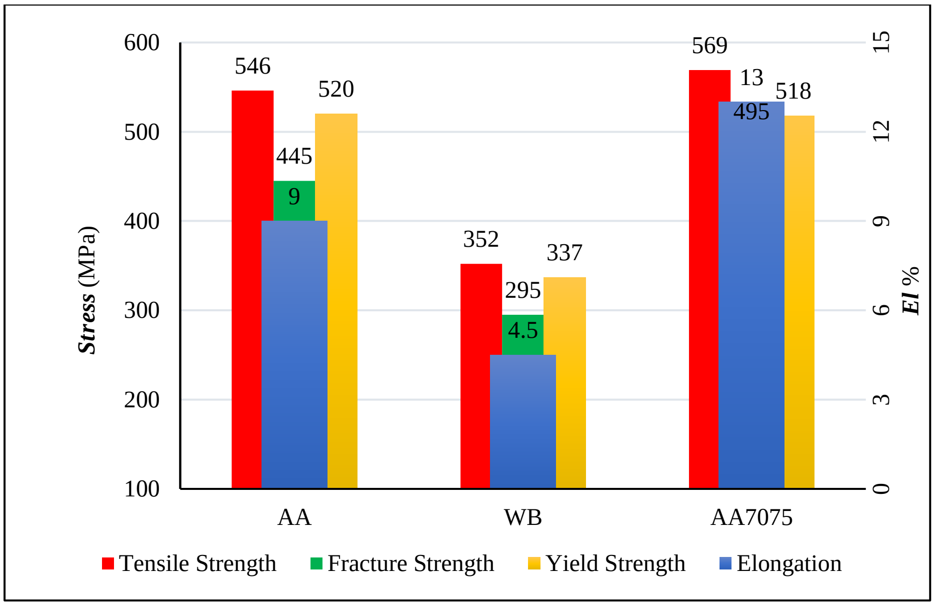

**Fig. 10** Variation of strength and elongation at break of the BM, the WB, and the AA specimens.

### 3.3. Microhardness Measurement

The distribution of Vickers microhardness across the cross-section of the BM, the WB, and the AA specimens is presented in “Fig. 11”. The detrimental effect of welding has resulted in the lowest hardness in the FZ and the HAZ of the WB, compared to those of the BM and the AA sample. The AA process performed on the WB caused an increase in the hardness level of different zones of the AA sample due to the mechanisms of precipitation hardening, solid solution strengthening, and grain refinement explained earlier. Figures 10 and 11 show that the fusion zones in the WB and the AA specimens have the lowest strength and hardness where the fracture occurs in the tensile test (“Fig. 12”).

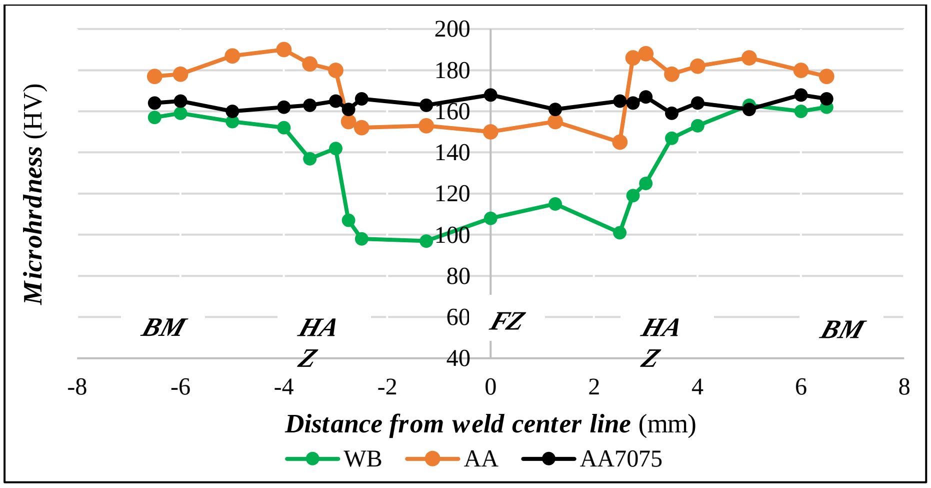

**Fig. 11** Distribution of microhardness across the cross-section of the BM, the WB, and the AA specimens.

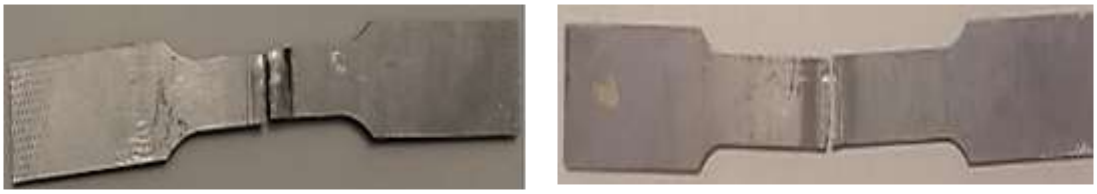
(a) (b)

**Fig. 12** Fractures in the weld zone of: (a): The WB, and (b): The AA specimens.

## 4 CONCLUSIONS

In this article, 1.5 mm thick sheets of AA7075 were first preheated and welded using the gas tungsten arc welding process. The effect of post-weld heat treatment on the microstructure and mechanical properties of the welded parts was investigated. The results of this study demonstrate that:

1- The tensile properties and microhardness of the welded part decreased compared to those of the original sheet due to microstructural changes caused by welding.

2- The lowest Vickers microhardness of about 110 was observed in the fusion zone of the welded part compared to 170 of the base metal.

3- Welding caused an almost 40% reduction in yield, tensile, and fracture strengths and a 65% decrease in elongation.

4- The post-weld heat treatment performed on the welded part changed the microstructure and significantly improved the mechanical properties in such a way that the tensile properties and microhardness of the aged specimen were close to those of the base metal.

5- Tensile tests caused fractures in the fusion zones (weakest zone) of both the welded part and the artificially aged specimens.

## REFERENCES

[1] Zheng, K., Politis, D. J., Wang, L., and Lin, J., A Review on Forming Techniques for Manufacturing Lightweight Complex-Shaped aluminum Panel Components, International Journal of Lightweight Materials and Manufacture, Vol. 1, No. 2, 2018, pp. 55-8. https://linkinghub.elsevier.com/retrieve/pii/S258884041830012X.

[2] Peter, I., Rosso, M., Study of 7075 Aluminum Alloy Joints, Scientific Bulletin of 'Valahia' University, Materials & Mechanics, Vol. 15, No. 13, 2017, pp. 7-11, Doi 10.1515/bsmm-2017-0011.

[3] Yildirim, M., Özyürek, D., and Gürü, M., The Effects of Precipitate Size on the Hardness and Wear Behaviors of Aged 7075 Aluminum Alloys Produced by Powder Metallurgy Route, Arabian Journal for Science and Engineering, Vol. 15, No. 41, 2016, pp. 4273–4281.

[4] Chen, R., Iwabuchi, A., and Shimizu, T., The Effect of a T6 Heat Treatment on The Fretting Wear of a Sic Particle-Reinforced A356 Aluminum Alloy Matrix Composite, Wear, Vol. 238, No. 2, 2000, pp. 110–119, DOI:10.1016/S0043-1648(99)00328-2.

[5] Li, Z., Xiong, B., Zhang, Y., Zhu, B., Wang, F., and Liu, H., Investigation of Microstructural Evolution and Mechanical Properties During Two-Step Aging Treatment at 115 and 160 ◦C in an Al–Zn–Mg–Cu Alloy Pre-Stretched Thick Plate, Materials Characterization, Vol. 59, No. 3, 2008, pp. 278–282, https://doi.org/10.1016/j.matchar.2007.01.006.

[6] Isadere, A. D., Aremo, B., Adeoye, M. O., Olawale, O. J., and Shittu, M. D., Effect of Heat Treatment on Some Mechanical Properties of 7075 aluminum Alloy, Materials Research, Vol. 16, No. 1, 2013, pp. 190–194, https://doi.org/10.1590/S1516-14392012005000167.

[7] Fakioglu, A., Özyürek, D., Effects of Re-Aging on the Fatigue Properties of aluminum Alloy AA7075, Materials Testing, Vol. 56, No. 7–8, 2014, pp. 575–582, https://doi.org/10.3139/120.110598.

[8] Wang, Z., Wang, S., Zhang, C., and Wang, Z., Effect of Post-Weld Heat Treatment on Microstructure and Mechanical Properties of 7055 Aluminum Alloy Electron Beam Welded Joint, Material Research Express, Vol. 7, 2020, 066528, https://doi.org/10.1088/2053-1591/ab9cea.

[9] Xu, D. K., Rometsch P. A., and Birbilis, N., Improved Solution Treatment for an As-Rolled Al−Zn−Mg−Cu Alloy, Part I. Characterisation of Constituent Particles and Overheating, Materials Science and Engineering A, Vol. 534, No. 2, 2012, pp. 234−243, https://doi.org/10.1016/j.msea.2011.11.065.

[10] Liu, J., Li, H., Li, D., and Yue, W., Application of Novel Physical Picture Based on Artificial Neural Networks to Predict Microstructure Evolution of Al−Zn−Mg−Cu Alloy During the Solid Solution Process, Transactions of Nonferrous Metals Society of China, Vol. 25, No. 3, 2015, pp. 944−953, https://doi.org/10.1016/S1003-6326(15)63683-4.

[11] Ding, J., Wang, D., Wang, Y., and Du, H., Effect of Post Weld Heat Treatment on Properties of Variable Polarity TIG Welded AA2219 Aluminium Alloy Joints, Transactions of Nonferrous Metals Society of China, Vol. 24, No. 5, 2014, pp. 1307-1316, doi.org/10.1016/S1003-6326(14)63193-9.

[12] Asadi, P., Alimohammadi, S., Kohantorabi, O., Soleymani, A., and Fazli, A., Numerical Investigation on The Effect of Welding Speed And Heat Input on The Residual Stress of Multi-Pass TIG Welded Stainless Steel Pipe, Proceedings of the Institution of Mechanical Engineers, Part B: Journal of Engineering Manufacture, 2021, Vol. 235, No. 6-7, pp. 1007–1021, doi.org/10.1177/0954405420981335.

[13] Asadi, P., Alimohammadi, S., Kohantorabi, O., Fazli, A., and Akbari, M., Effects of Material Type, Preheating and Weld Liang, Improving Mechanical Properties of PVPPA Welded Joints of 7075 Aluminum Alloy by PWHT, Materials, Vol. 11, No. 3, 2018, pp. 379, https://doi.org/10.3390/ma11030379.

[14] Miles, M. P., Decker, B. J., and Nelson, T. W., Formability and Strength of Friction stir-welded

Aluminum Sheets, Metallurgical and Materials Transactions A, Vol.35, 2004, pp. 3461–3468.

[15] Xiao, L., Chenyang, W., Xiaoping, L., Bin, Z., and Runzhou, L., Investigation of 7075 Aluminum Alloy TIG Welding Joint Using 7075 Aluminum Alloy Wire Before and After Heat Treatment, Materials Research Express, Vol. 10, No. 4, 2023, https://doi.org/10.1088/2053-1591/accac4.

[16] Tušek, J., Klobčar, D., Tungsten inert gas (TIG) welding of aluminum alloy EN AW-AlZn5.5MgCu, Metalurgija Vol. 55, No. 4, 2016, pp. 737–40.

[17] Sokoluk, M., Cao, C., Pan, S., and Li, X., Nanoparticle-Enabled Phase Control for Arc Welding of Unweldable Aluminum Alloy 7075, Nature Communications, Vol. 10, 2019, pp. 98, https://doi.org/10.1038/s41467-018-07989-y.

[18] Kou, S., Solidification and Liquation Cracking Issues in Welding, Vol. 55, No. 6, 2003, pp. 37–42, http://dx.doi.org/10.1007/s11837-003-0137-4.

[19] Gomez, J. M., Salazar, D. E., Urena, A., Villauriz, E., Manzanedo, S., and Barrenaa, I., TIG, and MIG Welding of 6061 and 7020 aluminum Alloys, Microstructural Studies and Mechanical Properties, Welding International, Vol. 13, No. 4, 2010, pp. 293-295, https://doi.org/10.1080/09507119909447381.

[20] Janaki Ram, G. D., Mitra, T. K., Shankar, V., and Sundaresan, S., Microstructural Refinement Through Inoculation of Type 7020 Al–Zn–Mg Alloy Welds and Its Effects on Hot Cracking and Tensile Property, Journal of Materials Processing Technology, Vol. 142, No. 1, 2003, pp. 174–81, https://doi.org/10.1016/S0924-0136(03)00574-0.

[21] E28 Committee, Test Methods for Tension Testing of Metallic Materials, ASTM International, DOI: 10.1520/E0008_E0008M-13A.

[22] E04 Committee, Standard Test Method for Microindentation Hardness of Materials, ASTM International, DOI: 10.1520/E0384-16.

[23] Yeni, C., Sayer, S., Pakdil, M., Comparison of Mechanical and Microstructural Behavior of TIG, MIG, and Friction Stir Welded 7075 Aluminum Alloy, Vol. 47, No. 5, 2009, pp. 341–347.

[24] Mabuwa, S., Msomi, V., Review on Friction Stir Processed TIG and Friction Stir Welded Dissimilar Alloy Joints, Metals, Vol. 10, No. 1, 2020, pp. 142, doi:10.3390/met10010142.

[25] E04 Committee, Standard Guide for Preparation of Metallographic Specimens, E3–11. DOI:10.1520/E0003-11R17.

[26] E04 Committee, Standard Guide for Reflected–Light Photomicrography, E883 – 11. DOI: 10.1520/E0883-11R17.

[27] Tahmasbi, A., Samuel, A. M., Zedan, Y., Songmene, V., and Samuel, F. H., Effect of Aging Treatment on the Strength and Microstructure of 7075-Based Alloys Containing 2% Li and/or 0.12% Sc, Materials, Vol. 16, No. 23, 2023, pp. 7375, https://doi.org/10.3390/ma16237375.

[28] Ghosh, A., Ghosh, M., Microstructure and Texture Development of 7075 Alloy During Homogenization, Philoso Phical Magazine, 2018, https://doi.org/10.1080/14786435.2018.1439596.

[29] Li, G., Chen, F., and Han, Y., Pass Number on Residual Stress of Welded Steel Pipes by Multi-Pass TIG Welding (C-Mn, SUS304, SUS316), Asadi, Thermal Science and Engineering Progress, Vol. 16, 2020, 100462, https://doi.org/10.1016/j.tsep.2019.100462.

*Int. J. Advanced Design and Manufacturing Technology, 2023, Vol. 16, No. 4, pp. 79-85*

*DOI: 10.30486/admt.2024.1997251.1421 ISSN: 2252-0406 https://admt.isfahan.iau.ir*

# Experimentally Designed of PVC/NiAl$_2$O$_3$/AlF$_3$ Nanocomposite by Sol-Gel Method

**Elinaz Ahmadian, Maryam Kargar Razi ***
Department of Chemistry, Islamic Azad University,
North Tehran Branch, Tehran, Iran
Email: elina2964@yahoo.com, mkargarrazi@yahoo.com
*Corresponding author

**Babak Sadeghi**
Department of Chemistry, Islamic Azad University,
Tonekabon Branch, Tonekabon, Iran
Email: bsadeghi1177@gmail.com

**Mahbobeh Nakhaei**
Department of Chemistry, Islamic Azad University,
North Tehran Branch, Tehran, Iran
Email: mnakhaeia@gmail.com

**Received: 24 September 2023, Revised: 28 November 2023, Accepted: 30 November 2023**

**Abstract:** In this study, we have synthesized nano Aluminum Fluoride (nAF) nanoparticles by the sol-gel method and studied the nano-sized morphology of crystals. In the other section, the PVC/NiAl$_2$O$_3$/AlF$_3$ (nPNA) nanocomposite was successfully prepared and characterized by FT-IR, and HRTEM techniques. FTIR peaks of the PVC and nPNA have been shown spherical shape of PVC and also spherical shapes nanoparticles of nPNA loaded on PVC. A solvothermal method has been successfully introduced and applied for catalyst efficiency. This nanocomposite was used for the removal of Congo red dye. For this purpose, the morphology and the structure of crystals have been changed by modification on precursor gel. Meanwhile, precursor gel preparation and the interaction on the nano-sized area have been studied. This study exhibited that PVC/NiAl$_2$O$_3$/AlF$_3$ (nPNA) nanocomposite is an effective catalyst for the synthesis of some organic derivatives. The results show that the as-prepared nanocomposite is an efficient catalyst and that PVC/NiAl$_2$O$_4$/AlF$_3$ nanocomposite can be used in the next-generation of some organic reactions and faster production of various materials.

**Keywords:** Nano Catalytic activity, Nano-Size, Morphology, Sol-gel, TEM

**Biographical notes: Maryam Kargar Razi** received her Postdoc in Inorganic Chemistry and Glass University of Friedrich Schiller University in Germany, and PhD in Inorganic Chemistry University of IAU Science and Research Branch in 2000. She is currently an Assistant Professor at the Department of Chemistry, North Tehran University, and Tehran, Iran. **Babak Sadeghi** is Associate Professor of Inorganic Chemistry at the University of Tonekabon, Iran. He received her PhD in Inorganic Chemistry from IAU Science and Research Branch, Iran in 2004. His current research focuses on the Synthesis of Nano Materials. **Elinaz Ahmadian** is PhD student at the Department of Chemistry, North Tehran University, and Tehran, Iran. **Mahbobeh Nakhaei** is Assistant Professor at the Department of Chemistry, North Tehran University, and Tehran, Iran.

Research paper

## 1 INTRODUCTION

Synthesis of the sol-gel method has been so widely developed that nano-metal oxides, either pure or organic-inorganic hybrid materials, are applied and available now [1-8]. One of the most common applications of $Al_2O_3$ and $nAlF_3$ (and their derivatives) is as a catalyst support. Many physical properties of the catalyst support, such as temperature, pH, aging time, raw materials and preparation technique, have a major impact on the performance of the catalyst in sol-gel processes [9-11]. Ono et al. [12] were the first to report this procedure and they managed to study the effectiveness of the pH and number of pH-swing frequencies on the Aluminium Oxide formation. Maity et al. [13] prepared the catalyst supported by alumina via various techniques, such as pH-swing, and determined that this method improved the pore size distribution (PSD). [14].

Aluminum fluoride has a number of current and potential applications as an additive to the molten electrolyte of the aluminum production cell in order to lower the melting point and increase the electrical conductivity. Moreover, among metal fluoride catalysts and catalyst supports for halogen exchange reactions, $AlF_3$ is one of the most important catalysts [15-18]. We have recently developed a reduction method of converting Ag nanospheres into nanorods [19], nanoplates [20], their antibacterial activity [21-22], an improved and easy synthetic route for silver nanoparticles in poly (diallyldimethylammonium chloride) (PDDA) [23], synthesis of Gold/HPC hybrid nanocomposite [24], preparation of Ag/ZnO nanocomposite [25-26] and comparison nanosilver particles and nanosilver plates for the oxidation of ascorbic acid [27].

As part of our efforts to investigate the usefulness of nanocomposite catalysts for the synthesis of organic and heterocyclic compounds [28-30], we report an efficient process for the synthesis of arylidende barbituric acid derivatives from the cyclo-condensation reaction between barbituric acid, various aldehydes by using 1 mol% ammonia mediated at room temperature. In the present paper, nPNA composite was successfully prepared (from nAF) and then, catalytic activity of nPNA has been considered in the synthesis of two organic derivatives.

## 2 EXPERIMENTAL

### 2.1. Characterization

Transmission electron microscopy (TEM, Model Hitachi 4500-M) was used to study morphology and particle size. It was performed using Bruker AXS diffractometer D8 ADVANCE with Cu-Kα radiation in the range $2\theta=10^{\circ}\text{–}80^{\circ}$. FT-IR spectra of the samples were done using a spectrometer (Model Perkin–Elmer) in the wavelength range 400-4000 $cm^{-1}$.

### 2.2. Materials and Methods

Baribituric acid (BBA) and various aldehydes were purchased from Aldrich company and used as received without further purification. Solution pH ranged between 7 and 10. The resulting gel nAF was kept at 50 ºC for 20 h. Then, obtained gel were filtered and rinsed with a $NH_3$.

### 2.3. Catalytic Activity

The catalytic activity of the $PVC/NiAl_2O_4/AlF_3$ (nPNA) was shown as below optimization procedure. BBA, nPNA, and methanolic solution of various benzaldehydes were added to hot water and stirred until the color precipitate of the products has been prepared. The precipitate of solid was filtered. A solvothermal method has been successfully introduced and applied for catalyst efficiency. The ABBA derivatives have been characterized by FT-IR spectroscopy.

### 2.4. Result and Discussion

During the preparation, the chemical reactions (reaction 1) that occurred are highlighted as changes in the various crystalline phases observed in the XRD pattern. It can therefore be said that Nano Aluminum fluoride (nAF) was utilized in this sample as precipitant [15-16].

$$Al\,(CH_3COO)_3 + Al_2O_2F_4 + 5HF \xrightarrow{\underline{\text{alkaline regions}}} 3nanoAlF_3 + 3\,CH_3COOH + H_2 + O_2 \qquad (NH_3\ \text{Solvent}) \qquad (1)$$

In glass reactor (nAF)

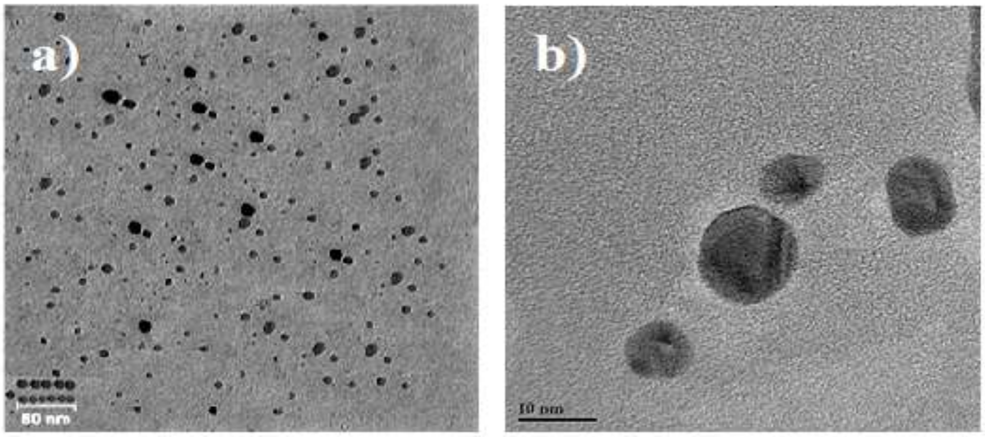

**Fig. 2** HR TEM images of the nAlF$_3$ sample.

Figure 1 (a, b) represents the HRTEM direct image of nAlF$_3$ sample. The size of the particle is spherical in shape and has a size in the range of 10-18 nm which was a good similarity to the size obtained in the optical model. TEM images were prepared to determine the produced nanoparticles' size, morphology, and uniformity. The results showed the production of hexagonal nAlF$_3$ nanoparticles, and it matches the XRD patterns.

The FTIR spectrum of nAlF$_3$ is shown in “Fig. 2”. In this sample, there is not broad absorption bands at 3300-3500 cm$^{-1}$ associated with O-H stretching of adsorbed water. The sharp peak at 1645 cm$^{-1}$ belongs to the bending vibration of H-OH in (a small amount of water) $H_2O$ molecules. The band at 1075 cm$^{-1}$ is related to symmetrical Al-F bending modes. The adsorption peak at 1635 cm$^{-1}$ belongs to the bending vibration of O-H group in the adsorbed water [31-35].

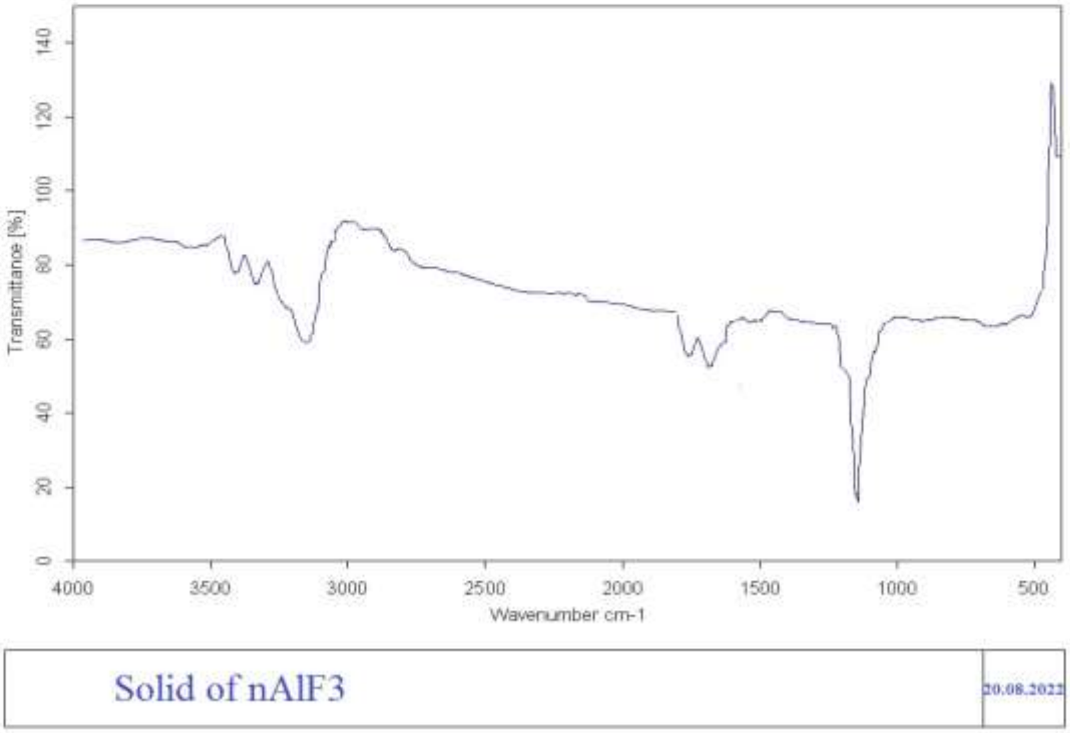

**Fig. 2** FTIR spectrum of the nano AlF$_3$.

PVC/$NiAl_2O_4$/$AlF_3$ (nPNA) nanocomposite was prepared using the reaction of PVC, $AlCl_3$, and $NiCl_2$ in the presence of NaOH. The chemical structure of PVC and PVC/$NiAl_2O_4$/$AlF_3$ was studied by FT-IR spectroscopy and the results are presented in “Fig. 3”.

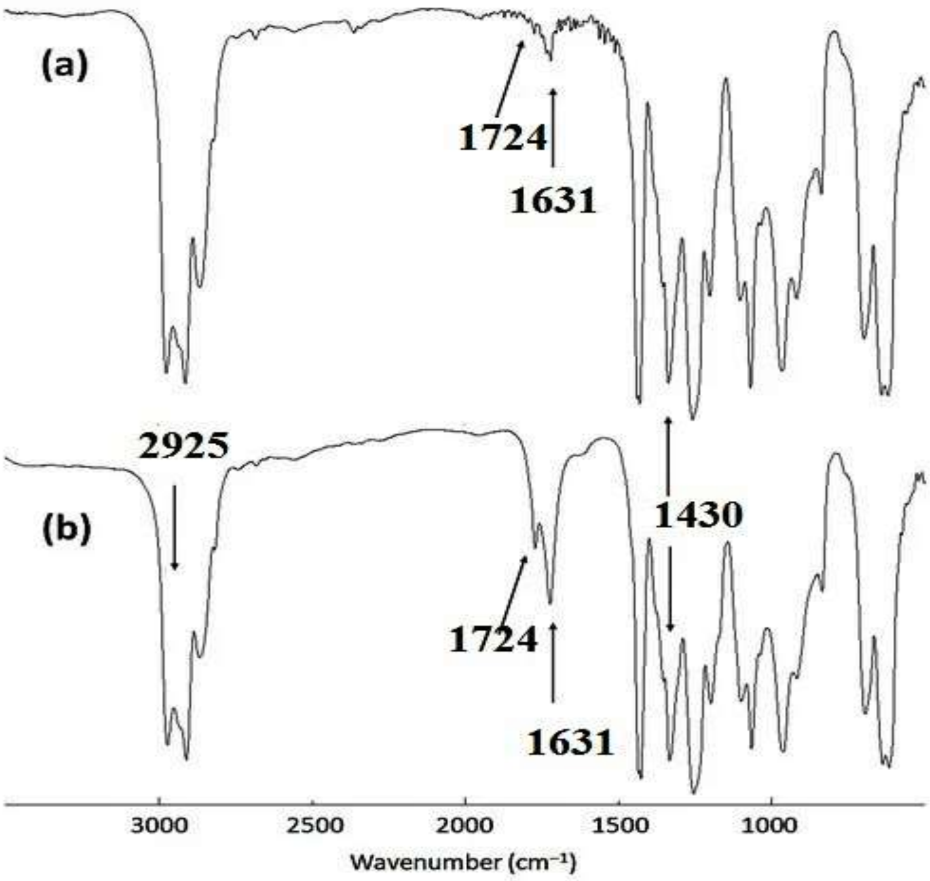

**Fig. 3** FT-IR spectra of: (a): PVC, and (b): PVC/$NiAl_2O_4$/$AlF_3$ composite.

The absorption bands in the infrared spectrum of polyvinyl chloride at 503, and 650 $cm^{-1}$ are assigned to the amorphous absorption band of C–Cl stretching, and C–Cl crystalline absorption band, respectively. The υ(C–C) stretching vibrations band has been showed around 845. The bands at 1100 and 1175 cm-1 correspond to perpendicular chain stretch and parallel chain stretch [36]. The absorption band at 1359 $cm^{-1}$ corresponds to $CH_2$ wag and the other band at 1430 $cm^{-1}$ is due to the bending mode of $CH_2$. The absorption band at 1631 $cm^{-1}$ is assigned to the carbon=carbon double bond stretching vibration for conjugated bonds, or either aromatic or aliphatic or both. The band at 1724 $cm^{-1}$ is probably from the carbonyl stretching vibration. The wideband at 2925 $cm^{-1}$ corresponds to the $CH_2$ asymmetric stretching mode, the peak broadening is due to the intermolecular and intra-molecular hydrogen bonds [37]. However, the small shift in 650, 845, and 1724 $cm^{-1}$ band positions confirmed the formation of PVC/$NiAl_2O_4$/$AlF_3$ nanocomposite in the PVC polymer matrix. The peaks at 689, 614, and 427 cm-1 concerning Metal-O (Al-O and Ni-O) stretching [38-40].

## 2.5. Catalytic Activity of Arylidene Barbituric Acid Derivatives

The color of barbituric acid is white, while the color of FCG-1 (R=COOH) is pale-brown and FCG-2 (R=$NH_2$) is orange. The melting point of FCG-1 is about 293 ºC and is more than the melting point of FCG-2 (223 ºC), due to the COOH group that causes increasing hydrogen bond strength in FCG-2.

“Table 1” shows the conditions for the synthesis of ABBA, under various derivatives. The yield of the products is very low in acetonitrile, dichloromethane and is a medium in methanol and water, while the yield increased to ≥ 97% using a water-methanol (l: 1 v/v) mixture. Preparation of FCG-2 (40 sec) is faster than FCG-1 (210 sec) because $NH_2$ is an electron donor while COOH is an electron acceptor. The results presented in this article are a continuation of previous works [41]. For example, the yield and time for the preparation of FCG-2 (entry 2 in "Table 1") are higher than this compound prepared by Rajput and Kaur [41]. By increasing the catalyst, the yield of FCG-1 and FCG-2 increased from 82 to 92 and 90 to 97%. Also, by changing the solvent from methanol to methanol-water, the yield of FCG-1 and FCG-2 increased. In the absence of the PVC/$NiAl_2O_4$/$AlF_3$, only a trace (< 50%) of FCG-1 and FCG-2 was obtained which is in agreement with previous reports [42]. This reaction has been monitored by the formation of colored precipitate product and is simple, and clean. The purified compounds have been recrystallized and characterized by FT-IR and UV-vis spectroscopies. Until now, there have been many reports on the preparation of arylidene barbituric acid by various catalysts [41], [43-46].

**Table 1** Optimization of the preparation of arylidene barbituric acid derivatives

| Entry | R | Time (min) | Yield (%) | Catalyst amount (g) | Solvent |
|---|---|---|---|---|---|
| | | Arylidene | Barbituric | Acid Derivatives | |
| 1 | COOH | 4 | 92 | 0.03 | Methanol-Water (1: 1) |
| 2 | $NH_2$ | 1 | 97 | 0.03 | Methanol-Water (1: 1) |
| 3 | COOH | 6 | 82 | 0.02 | Methanol-Water (1: 1) |
| 4 | $NH_2$ | 2 | 90 | 0.02 | Methanol-Water (1: 1) |
| 5 | COOH | 17 | 80 | 0.03 | Methanol |
| 6 | $NH_2$ | 6 | 89 | 0.03 | Methanol |
| 7 | COOH | 27 | 77 | 0.02 | Methanol |
| 8 | $NH_2$ | 9 | 80 | 0.02 | Methanol |

## 3 CONCLUSIONS

In conclusion, a multi-step precipitation method with the sol-gel technique was implemented. The TEM images and FT-IR spectroscopy indicated that the prepared $nAlF_3$ had low crystallinity and images showed that particle size is nanometer scale. Using the TEM images, the crystal size of the sample was 19.5 nm. The FT-IR spectroscopy confirmed the formation of $nAlF_3$ and PVC/$NiAl_2O_4$/$AlF_3$ nanocomposite in PVC polymer matrix. nPNA has been prepared and used as a new catalyst for the preparation of ABBA. The result confirmed that the nPNA composite is a good catalyst. This catalyst produces the FCG-1 and FCG-2 compounds in a very short time and with high yields. FTIR peaks of the PVC and nPNA have been shown spherical shape of PVC and also spherical shapes of nanoparticles of nPNA loaded on PVC. The main information from this study can be fixed or altered to optimize responses at more levels for future studies. These results show that PVC/$NiAl_2O_4$/$AlF_3$ nanocomposite can be used in next-generation of some organic reactions and faster production of various materials.

## 4 ACKNOWLEDGMENTS

The financial and encouragement support was provided by the Research vice Presidency of North Tehran & Tonekabon Branch, Islamic Azad University, and Executive Director of Iran-Nanotechnology Organization (Govt. of Iran).

## 5 CONFLICTS OF INTEREST

The authors declare that there are no conflicts of interest regarding the publication of this manuscript.

## REFERENCES

[1] Turner, M. E., Trentler, T. J., and Colvin, V. L., Thin Films of Macroporous Metal Oxides, Adv. Mater., Vol. 13, 2001, pp. 180-183.

[2] Aguado, J., Serrano, D. P., Escola, J. M., Garagorri, E., and Fernandez, J. A., Catalytic Cracking of a Polyolefin Mixture Over Different Acid Solid Catalysts, Polym. Degrad. Stabil., Vol. 69, 2000, pp. 11-16.

[3] Gronchi, P., Kaddouri, A., Centola, P., and Del Rosso, R., Synthesis of Nickel Supported Catalysts for Hydrogen Production by Sol-Gel Method, J. Sol-Gel Sci. Tech., Vol. 26, 2003, pp. 843-846.

[4] L. Khelifi, L., Ghorbel, A., Effect of Preparation Conditions on the Stability of Pt/$Al_2O_3$ Catalysts in Methane Combustion, J. Sol-Gel Sci Tech., Vol. 19, 2000, pp. 643-646.

[5] Meixner, H., Lampe, U., Gerblinger, J., and Fleische, M., Chemosensors for Motor Management Systems of The Future, Fresenius J. Anal. Chem., Vol. 348, 1994, pp. 536-541.

[6] Bennett, R. A., McCavish, N. D., Non-Stoichiometric Oxide Surfaces and Ultra-Thin Films: Characterisation of $TiO_2$, Topics in Catalysis. Vol. 36, 2005, pp. 11-19.

[7] Chemistry of Advanced Materials: An Overview, Wiely-VCH, Inc, Canada, 1998, Chapt. 9, Molecular Precursor Routes to Inorganic Solids, pp. 389–448.

[8] Righini, G. C., Pelli, S., Nonlinear Properties of Semiconductor-Doped Silica Solgel Films, J. Sol-Gel Sci. Tech., Vol. 8, 1997, pp. 991–997.

[9] Maryani, E., Abdullah, M., Dayamanti, H., and Septawendar, R., Effect of Ultrasonic Irradiation on The Characteristic of $\gamma$-$Al_2O_3$ Nanorods Synthesized from Nitrate Salt-Starch Precursors Trough a Facile Precipitation Method, J. Ceram. Soc. Japan., Vol. 124, 2016, pp. 1205-1210.

[10] Amirsalari, Farjami, S., Effect of pH and Calcinations Temperature on Structural and Optical Properties of Alumina Nanoparticles, J. Superlatt. Microstruct. Vol. 82, 2015, pp. 507-524.

[11] Da-Ros, S., Barbosa-Coutinho, E., Schwaab, M., Calsavara, V., and Fernandes-Machado, N. R. C., Modeling the Effects of Calcination Conditions on The Physical and Chemical Properties of Transition Alumina Catalysts, J. Mater. Character., Vol. 80, 2013, pp. 50-61.

[12] Tayseir Mohammed, E., Saikat, M., Some Studies on The Surface Modification of Sol-Gel Derived Hydrophilic Silica Nanoparticles, Int. J. Nano Dimens., Vol. 8, 2017, pp. 97-106.

[13] Maity, S. K., Ancheyta, J., and Rana, M. S., Support Effects on Hydroprocessing of Maya Heavy Crude, J. Energy and Fuel., Vol. 19, 2005, pp. 343-347.

[14] Fernandez., V. C., Ramrez, J., Alejandre, A. G., Sanchez-Minero, F., Cuevas-Garcıa, R., and Torres-Mancera, P., Synthesis, Characterization and Evaluation of NiMo/$SiO_2$–$Al_2O_3$ Catalysts Prepared by the pH-Swing Method, J. Catal. Today., Vol. 130, 2008, pp. 337–344.

[15] Dao Quan, H., Yang, H., Tamura, M., and Sekiya., A., $SbF_5$/PAF—a Novel Fluorinating Reagent in Preparing Fluorine Compounds, J. Fluorine Chem., Vol. 125, 2004, pp. 1169-1172.

[16] Sekiya, dao Quan, H., Tamura, M., Gao, R. X., and Murata, J., Sol-Gel Synthesis and Catalytic Properties of PVC/$NiAl_2O_3$/$AlF_3$ Nanocomposite", J. Fluorine Chem., Vol. 112, 2001, pp. 145-148.

[17] Dao Quan, H., Tamura, M., Takagi, T., and Sekiya, A., Fluorination of N-Dodecane Adsorbed on Porous Aluminium Fluoride by Gaseous Fluorine, J. Fluorine Chem., Vol. 99, 1999, pp. 167-170.

[18] Krespan, C. G., Dixon, D. A., Fluoroolefin Condensation Catalyzed by Aluminum Chlorofluoride, J. Fluorine Chem., Vol. 77, 1996, pp. 117-126.

[19] Sadjadi, M. A. S., Sadeghi, B., Meskinfam, M., Zare, K., and Azizian, J., Synthesis and Characterization of Ag/PVA Nanorods By Chemical Reduction Method, Physica E: Low-Dimensional Systems and Nanostructures, Vol. 40, 2008, pp. 3183-3186.

[20] Sadeghi, B., Sadjadi, M. A. S., and Vahdati, R. A. R., Nanoplates Controlled Synthesis and Catalytic Activities of Silver Nanocrystals, Superlattices and Microstructures, Vol. 46, 2009, pp. 858-863.

[21] Sadeghi, B., Jamali, M., Kia, Sh., Amini Nia, A., and Ghafari., S., Synthesis and Characterization of Silver Nanoparticles for Antibacterial Activity, Int. J. Nano Dimens., Vol. 1, 2010, pp. 119-124.

[22] Sadeghi, B., Garmaroudi, F. S., Hashemi, M., Nezhad, H. R., Nasrollahi, A., Ardalan, S., and Ardalan, S., Comparison of the Anti-Bacterial Activity on The Nanosilver Shapes: Nanoparticles, Nanorods and Nanoplates, Adv. Powder Technol., Vol. 23, 2012, pp. 22-26.

[23] Sadeghi, B., Pourahmad, A., Synthesis of Silver/Poly (Diallyl Dimethyl Ammonium Chloride) Hybride Nanocomposite, Adv. Powder Tech., Vol. 22, 2012, pp. 669-673.

[24] Sadeghi, B., Ghammamy, Sh., Gholipour, Z., and Amini Nia, A., Gold/Hydroxypropyl Cellulose Hybrid Nanocomposite Constructed with More Complete Coverage of Gold Nano-Shell, Mic & Nano Lett., Vol. 6, 2011, pp. 209-213.

[25] Sadeghi, B., Preparation of ZnO/Ag Nanocomposite and Coating on Polymers for Anti-Infection Biomaterial Application, Spectrochimica Acta Part A: Molecular and Biomolecular Spectroscopy., Vol. 118, 2014, pp. 787-792.

[26] Sadeghi, B., Controlled Growth and Characterization Ag/ZnO Nanotetrapods for Humidity Sensing, Comb. Chem. & High throughput Screening., Vol. 21, 2018, pp. 1-6.

[27] Sadeghi, B., Meskinfam, M., A Direct Comparison of Nanosilver Particles and Nanosilver Plates for The Oxidation of Ascorbic Acid, Spectrochim. Acta Part A: Molec. Biomolec. Spectros., Vol. 97, 2012, pp. 326-328.

[28] Vahdat, S. M., Ghafouri Raz, Sh., and Baghery, S., Application of nano $SnO_2$ as a Green and Recyclable Catalyst for The Synthesis of 2-aryl or Alkylbenzoxazole Derivatives Under Ambient Temperature, J. Chem. Sci., Vol. 126, 2014, pp. 579-585.

[29] Vahdat, S. M., Chekin, F., Hatami, M., Khavarpour,

M., Baghery, S., and Roshan-Kouhi, Z., Synthesis of Polyhydroquinoline Derivatives Via a Four-Compone, Chin. J. Catal., Vol. 34, 2013, pp. 758-763.

[30] Zolfigol, M. A., Baghery, S., Moosavi-Zare, A. R., Vahdat, S. M., Alinezhad, H., and Norouzi, M., Design of 1-Methylimidazolium Tricyanomethanide as The First Nanostructured Molten Salt and Its Catalytic Application in The Condensation Reaction of Various Aromatic Aldehydes, Amides And β-Naphthol Compared with Tin Dioxide Nanoparticles, RSC Adv., Vol. 5, 2015, pp. 45027-45037.

[31] Liu, Ch., Li, J., Liew, K., Zhu, J., and Bin Nordin, M. R., An Environmentally Friendly Method for The Synthesis of Nano-Alumina with Controllable Morphologies, J. RSC Adv., Vol. 2, 2015, pp. 8352–8358.

[32] Wuy, Y. S., Ma, J., Hu, F., and Li, M. C., Synthesis and Characterization of Mesoporous Alumina Via a Reverse Precipitation Method, J. Mater. Sci. Technol., Vol. 28, 2011, pp. 572-576.

[33] Sun, X., Li, J., Zhang, F., Qin, X., Xiu, Zh., and H. Ru, H., Synthesis of Nanocrystalline γ-$Al_2O_3$ Powders from Nanometric Ammonium Aluminum Carbonate Hydroxide, J. Am. Ceram. Soc., Vol. 86, 2003, pp. 1321-1325.

[34] Xiuhong, M., Linhai, D., Xiaohua, X., Qiang, W., and Haiyan, W., Synthesis of Macro Mesostructured γ-$Al_2O_3$ with Large Pore Volume and High Surface Area by A Facile Secondary Reforming Method, J. China Petrol. Process. Petrochem. Technol., Vol. 16, 2014, pp. 20-28.

[35] Zhu, Zh., Sun, H., Liu, H., and Yang, D., PEG-Direct Hydrothermal Synthesis of Alumina Nanorods with Mesoporous Structure via AACH Nanorod Precursors, J. Mater. Sci., Vol. 45, 2010, pp. 46-54.

[36] Gerrard, D. L., Maddams, W. F., The Resonance Raman Spectrum of Degraded Poly (Vinyl Chloride), 2. γ-Irradiated Samples, Macromolecules, Vol. 10, 1977, pp. 1221-1224.

[37] Ganesan, D., Samikanno, A., Muthaiah, Ch., and Ramasamy, K. M., Synthesis and Characterization of CdS Nanoparticle Anchored Silica-Titania Mixed Oxide Mesoporous Particles: Efficient Photocatalyst for Discoloration of Textile Effluent, Int. J. Nano Dimens., Vol. 10, 2019, pp. 272-280.

[38] Rajesh Krishnan, G., Sreeraj, M. K., and Sreekumar, K., Modification of Poly (Vinyl Chloride) With Pendant Metal Complex for Catalytic Applications, C. R. Chimie., Vol. 16, 2013, pp. 736-741.

[39] Huang, G., He, E., Wang, Z., Fan, H., Shangguan, J., Croiset, E., and Chen, Z., Synthesis and Characterization ofγ-Fe2O3for H2S Removal at Low Temperature, Ind. Eng. Chem. Res., Vol. 54, 2015, pp. 8469-8478.

[40] Mehdizadeh, R., Saghatforoush, L. A., and Sanati, S., Solvothermal Synthesis and Characterization of α-Fe2O3 Nanodiscs and Mn3O4 Nanoparticles with 1,10-Phenanthroline, Superlatt. Microstruct., Vol. 52, 2012, pp. 92-98.

[41] Rajput, J, K., Kaur, G., CoFe2O4 Nanoparticles: An Efficient Heterogeneous Magnetically Separable Catalyst For "Click" Synthesis of Arylidene Barbituric Acid Derivatives at Room Temperature, Chin. J. Catal., Vol. 34, 2013, pp. 1697-1704.

[42] Schafer, H., Milow, B., and Ratke, L., Synthesis of Inorganic Aerogels Via Rapid Gelation Using Chloride Precursors, RSC Adv., Vol. 3, 2013, pp. 15263-15272.

[43] Khan, K. M., Ali, M., Farooqui, T. A., Khan, M., Taha, M., and Perveen, S., An Improved Method for The Synthesis of 5-Arylidene Barbiturates Using BiCl3, J. Chem. Soc. Pak., Vol. 31, 2009, pp. 823-828.

[44] Alcerreca, G., Sanabria, R., Miranda, R., Arroyo, G., Tamariz, J., and Delgado, F., Preparation of Benzylidene Barbituric Acids Promoted by Infrared Irradiation in Absence of Solvent, Synth. Commun., Vol. 30, 2000, pp. 1295-1301.

[45] Quinonero, D., Ferontera, A., Benzen, An Unexpected Binding Unit in Anion-π Recognition: The Critical Role of CH/π Interactions, Sci. Vol. 4, 2022, pp. 32-36.

[46] Katarzyna**,** O., Katarzyna, M. S., Marlena, G., Oskar, K., Mateusz, Z. B., Piotr, G., Michał, L., Rosław, G., and Agnieszka, W., Influence of Hydrogen Bonds and π–π Interactions on the Fluorescence of Crystalline (N-Alkylpyridyl) enamino-pyrrolo [2,3-b] Quinoxalin-2-One Derivatives, Crys. Growth Des., Vol. 22, 2022, pp. 1571-1582.

*Int. J. Advanced Design and Manufacturing Technology, 2023, Vol. 16, No. 4, pp. 87-97*

*DOI: 10.30495/ADMT.2022.1949929.1334* *ISSN: 2252-0406* *https://admt.isfahan.iau.ir*

# Investigation of Pressure Distribution on Slippers of a Monorail Sled with Vibration Damper

**Mohammad Reza Najafi**
Department of Mechanical Engineering,
University of Imam Hossein Comprehensive, Iran
E-mail: drmrnajafi@ihu.ac.ir

**Saeed Mahjoub Moghadas ***
Department of Mechanical Engineering,
University of Imam Hossein Comprehensive, Iran
E-mail: smahjoubmoghadas@ihu.ac.ir
*Corresponding author

**Received: 15 January 2022, Revised: 3 April 2022, Accepted: 15 April 2022**

**Abstract:** In this paper, the pressure distribution on the slippers of a mono-rail sled with vibration damping is investigated. Due to the many applications of sled testing in the aerospace industry, the study of system vibrations is highly noticeable. In this research, first, by mathematical modelling of the sled, the governing Equations are extracted and natural frequencies and vibration modes are obtained from the analytical method using the mass and stiffness matrix of the system. Then, using numerical simulation and validation methods with experimental results performed in wind tunnels, the modal analysis of the designed sled sample is performed. A difference of less than eight percent in both numerical and analytical methods proves the accuracy of the results. The results show that the role of the slipper in the vibrations created in the sled is very important due to the large torsional and transverse oscillations in different positions, and the highest static pressure occurs in the inner layer of the slipper.

**Keywords:** Modal Analysis, Natural Frequency, Pressure Distribution, Sled Test, Slipper

**Biographical notes: Mohammad Reza Najafi** received his PhD in Mechanical Engineering from Imam Hossein Comprehensive University in Tehran, Iran. His current research interests include vibration and dynamics. **Saeed Mahjoub Moghadas** is an Associate Professor of Mechanical engineering at the University of Imam Hossein Comprehensive, Iran, since 1986. He received his PhD with the thesis subject “Internal Combustion Engines Control and Diagnostics through Instantaneous Speed of Rotation Analysis” at L'ensam University, Paris, France, in 1985. He has authored 20 books and translated 15 others in the field of dynamic, vibration, and control.

Research paper

## 1 INTRODUCTION

Sled testing technology is now limited to a few countries. Experimental facilities of this technology include long rails, chassis, carriage, propulsion engines, and sled or projectile body. Slippers are used to connect this system to the rails. The slippers slide on the rails to allow the sled to move. Fig. **1** shows how to connect rail and slipper.

**Fig. 1** Sled and rail connection.

The sled technology is used to achieve supersonic speeds up to 8 Mach and to provide experimental conditions in the field of space equipment [1], projectile penetration [2], parachute [3], pilot seat [4], anti-penetration structures [5], propulsion tests [6], and ultrasonic aerodynamic tests [7]. Real examples of sleds are also shown in “Fig. 2”.

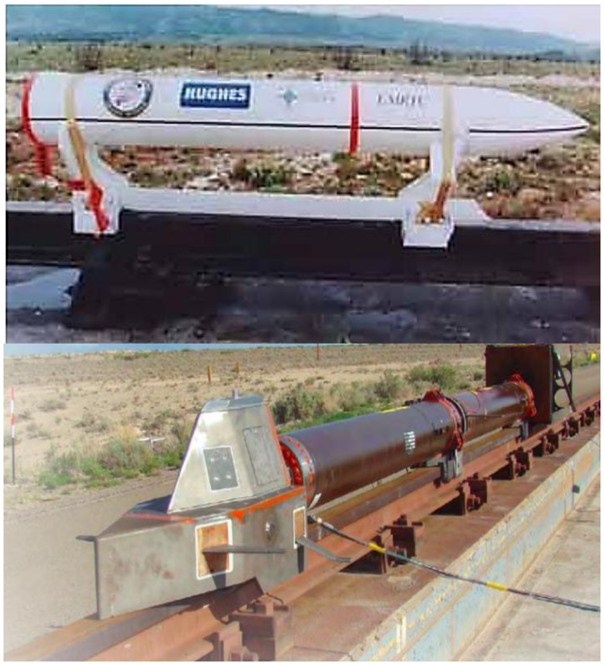

**Fig. 2** Real example of mono-rail sled system [8].

Sled testing technology has attracted the attention of researchers in recent years [9–13]. Due to the high speed of this technology, the vibrations on the sled are one of the main bottlenecks of this system, which has been noticed by many researchers [14–17]. Minto discussed a sled capacity development program to achieve high supersonic speeds. The results of their research show that the generated vibrational loads due to the impact of the slipper on the rail at speeds more than 6000 ft/sec lead to the failure of the sled body [18]. Bosmajian et al. studied the magnetic rail system of the sled. The aim of this study was to increase the sled capability for reduction of the vibrational environment at a final speed of 3000 m/s [19], and in the continuation of this research, Gurol et al. investigated the condition of the magnetic rail track in sled test at a higher speed. They showed that using a magnetic suspension system could significantly reduce sled vibrations [20]. Chen et al. investigated the amplitude of rocket sled vibrations and the time and frequency measurements of irregularity characteristics using statistical methods [21]. Turnbull et al. investigated the dynamic analysis of a sled system using narrow-gauge rails. The aerodynamic parameters of drag and lift, and pitch and yaw torques have been studied as a function of the angle of attack and acceleration has been obtained at four points on the sled [22]. Dunshee has modeled the mono-rail sled system as a two-degree-of-freedom beam with the capability to twist slightly in addition to moving in a vertical direction, using dynamic and vibrational analysis, and also has assumed the dynamic movement and a harmonic stimulation of a slipper [23]. Researchers have used mathematical models such as beams to analyze the behavior of dynamic systems such as high-speed trains, bridges, and automobiles [24–27]. Afshar et al. modelled the train bridge as a beam and investigated the use of linear and nonlinear vibration dampers for nonlinear beams at transient loads. The results show that for normal forces and short beams, linear and nonlinear models have similar behaviors [28].

Despite the research that has been done on sled testing, vibration analysis and modal analysis of sleds considering study of the role and the pressure distribution on slipper, which are the main outstanding of the present paper, have not been carried out by researchers so far. In the present paper, using the analytical method, first the vibrational Equations of the system are extracted and the natural frequencies are obtained. Then, the numerical simulation method is used to validate the obtained results and the modal analysis of a mono-rail sled with dampers is performed and the shape of its modes is clarified. Finally, the pressure and velocity distributions in the computational domain and the body of the sled and the slippers are also examined.

## 2 MATHEMATICAL MODELING

Most of the sled vibrations are caused by the impact of the slippers on the rails. Since the materials used in sleds and slippers are stiff, considerable vibrations are transmitted from the slippers and the rails to the body due to the impact of the rails [29], most of which occur in the upper parts of the slipper [30]. Thus, the use of dampers at the junction of the sled body to the slipper can greatly prevent the transmission of vertical vibrations from the rail surface to the sled. In this case, the sled can be modeled as a system that is excited transversely from the slipper. An overview of this type of sled modeling is shown in “Fig. 3”.

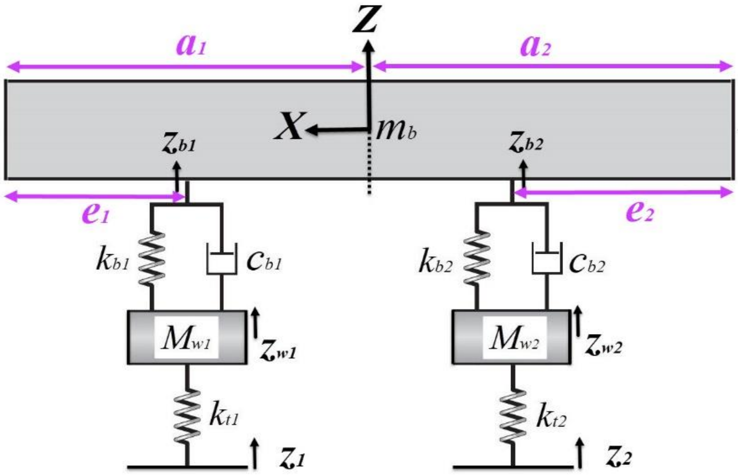

**Fig. 3** Sled mathematical model.

The parameters of present modeling describe $m_b$ as sled body mass, $m_{w1}$ as front slipper mass, $m_{w2}$ as rear slipper mass, $z_b$ as vertical sled body displacement, $z_{b1}$ as rear slipper displacement, $z_{b2}$ as rear slipper displacement, $\theta_b$ as a rotation of sled body around Y-axis (pitch motion) and $I_{yy}$ as inertia moment.

## 3 EXTRACTIONS OF GOVERNING EQUATIONS

Considering the displacement of the slippers due to the transverse motion of the center of mass as well as the twisting motion around the Y-axis ($\theta_b$), there is:

$$z_{b1} = z_b - (a_1 - e_1)\ \theta_b \tag{1}$$

$$\dot{z}_{b1} = \dot{z}_b - (a_1 - e_1)\ \dot{\theta}_b \tag{2}$$

$$z_{b2} = z_b + (a_2 - e_2)\ \theta_b \tag{3}$$

$$\dot{z}_{b2} = \dot{z}_b + (a_2 - e_2)\ \dot{\theta}_b \tag{4}$$

So, the vibrational Equations of the various components of the sled are now being extracted. To move the front slipper, there is $m_{w1}$ in the Z direction as obtained in relation (5):

$$\begin{aligned} & m_{w1}\ddot{z}_{w1} - k_{b1}\left(z_b - (a_1 - e_1)\theta_b - z_{w1}\right) \\ & -c_{b1}\left(\dot{z}_b - (a_1 - e_1)\dot{\theta}_b - \dot{z}_{w1}\right) \\ & -k_{t1}\left(z_{w1} - z_1\right) = 0 \end{aligned} \tag{5}$$

For the rear slipper motions, there is $m_{w2}$ in the Z direction as discussed in the relation (6):

$$\begin{aligned} & m_{w2}\ddot{z}_{w2} - k_{b2}\left(z_b + (a_2 - e_2)\ \theta_b - z_{w2}\right) \\ & -c_{b2}\left(\dot{z}_b + (a_2 - e_2)\ \dot{\theta}_b - \dot{z}_{w2}\right) \\ & -k_{t2}\left(z_{w2} - z_2\right) = 0 \end{aligned} \tag{6}$$

For the sled body motion ($m_b$) in the Z direction, there is:

$$\begin{aligned} & m_b\ddot{z}_b + k_{b1}\left(z_b - (a_1 - e_1)\ \theta_b - z_{w1}\right) + \\ & c_{b1}\left(\dot{z}_b - (a_1 - e_1)\ \dot{\theta}_b - \dot{z}_{w1}\right) + \\ & k_{b2}\left(z_b + (a_2 - e_2)\ \theta_b - z_{w2}\right) + \\ & c_{b2}\left(\dot{z}_b + (a_2 - e_2)\ \dot{\theta}_b - \dot{z}_{w2}\right) = 0 \end{aligned} \tag{7}$$

For the sled body rotation around the Y-axis, there is:

$$\begin{aligned}&\mathrm{I_{yy}}\,\ddot{\theta}_b - k_{b1}\left(z_b - (a_1 - e_1)\,\theta_b - z_{w1}\right)(a_1 - e_1)\\ &- c_{b1}\left(\dot{z}_b - (a_1 - e_1)\,\dot{\theta}_b - \dot{z}_{w1}\right)(a_1 - e_1)\\ &+ k_{b2}\left(z_b + (a_2 - e_2)\,\theta_b - z_{w2}\right)(a_2 - e_2)\\ &+ c_{b2}\left(\dot{z}_b + (a_2 - e_2)\,\dot{\theta}_b - \dot{z}_{w2}\right)(a_2 - e_2) = 0\end{aligned} \tag{8}$$

By multiplying the above values as indicated in relation (8), and simplifying them, the vibrational Equations of the four-degree-of-freedom system are obtained.

$$\begin{aligned}&m_{w1}\,\ddot{z}_{w1} + c_{b1}\,\dot{z}_{w1} - c_{b1}\,\dot{z}_b + \acute{S}_{13}\,\dot{\theta}_b +\\ &k_{b1}\,z_{w1} - k_{b1}\,z_b + S_{12}\,\theta_b = 0\end{aligned} \tag{9}$$

$$\begin{aligned}&m_{w2}\,\ddot{z}_{w2} + c_{b2}\,\dot{z}_{w2} - c_{b2}\,\dot{z}_b - \acute{S}_{15}\,\dot{\theta}_b +\\ &k_{b2}\,z_{w2} - k_{b2}\,z_b - S_{14}\,\theta_b = 0\end{aligned} \tag{10}$$

$$\begin{aligned}&m_b\,\ddot{z}_b - c_{b1}\,\dot{z}_{w1} - c_{b2}\,\dot{z}_{w2} + \acute{S}_{23}\,\dot{z}_b -\\ &\acute{S}_{25}\,\dot{\theta}_b - k_{b1}\,z_{w1} - k_{b2}\,z_{w2} + S_{22}\,z_b -\\ &S_{24}\,\theta_b = 0\end{aligned} \tag{11}$$

$$\begin{aligned}&\mathrm{I_{yy}}\,\ddot{\theta}_b + \acute{S}_{13}\,\dot{z}_{w1} - \acute{S}_{15}\,\dot{z}_{w2} - \acute{S}_{25}\,\dot{z}_b +\\ &\acute{S}_{27}\,\dot{\theta}_b + S_{12}\,z_{w1} - S_{14}\,z_{w2} - S_{24}\,z_b +\\ &S_{26}\,\theta_b = 0\end{aligned} \tag{12}$$

In the above Equations, the parameters are introduced as follows:

$$k_{b1}\left(a_1 - e_1\right) = S_{12} \tag{13}$$

$$c_{b1}\left(a_1 - e_1\right) = \dot{S}_{13} \tag{14}$$

$$k_{b2}\left(a_2 - e_2\right) = S_{14} \tag{15}$$

$$c_{b2}\left(a_2 - e_2\right) = \dot{S}_{15} \tag{16}$$

$$k_{b1}\left(a_1 - e_1\right)^2 = S_{12}\left(a_1 - e_1\right) = S_{16} \tag{17}$$

$$c_{b1}\left(a_2 - e_2\right)^2 = \dot{S}_{13}\left(a_1 - e_1\right) = \dot{S}_{17} \tag{18}$$

$$k_{b2}(a_1 - e_1)^2 = S_{14}(a_2 - e_2) = S_{18} \tag{19}$$

$$c_{b2}\left(a_2 - e_2\right)^2 = \dot{S}_{15}\left(a_2 - e_2\right) = \dot{S}_{19} \tag{20}$$

$$k_{b1} + k_{b2} = S_{22} \tag{21}$$

$$c_{b1} + c_{b2} = \dot{S}_{23} \tag{22}$$

$$S_{12} - S_{14} = S_{24} \tag{23}$$

$$\dot{S}_{13} - \dot{S}_{15} = \dot{S}_{25} \tag{24}$$

$$S_{16} + S_{18} = S_{26} \tag{25}$$

$$\dot{S}_{17} + \dot{S}_{19} = \dot{S}_{27} \tag{26}$$

$$k_{t1}\left(z_{w1} - z_1\right) = f_{w1} \tag{27}$$

$$k_{t2}\left(z_{w2} - z_2\right) = f_{w2} \tag{28}$$

That Equation of system motions is obtained as relation (29):

$$\left[\mathrm{M}\right]\ddot{z} + \left[\mathrm{C}\right]\dot{z} + \left[\mathrm{K}\right]z = \mathrm{F} \tag{29}$$

Thus, the Equations of vibrational motion of the system are obtained as relation (30):

$$\begin{aligned}&\begin{bmatrix} m_b & 0 & 0 & 0\\ 0 & \mathrm{I_{yy}} & 0 & 0\\ 0 & 0 & m_{w1} & 0\\ 0 & 0 & 0 & m_{w2}\end{bmatrix}\begin{bmatrix}\ddot{z}_b\\ \ddot{\theta}_b\\ \ddot{z}_{w1}\\ \ddot{z}_{w2}\end{bmatrix}\\ &+\begin{bmatrix}\dot{S}_{23} & -\dot{S}_{25} & -c_{b1} & -c_{b2}\\ -\dot{S}_{25} & \dot{S}_{27} & \dot{S}_{13} & -\dot{S}_{15}\\ -c_{b1} & \dot{S}_{13} & c_{b1} & 0\\ -c_{b2} & -\dot{S}_{15} & 0 & c_{b2}\end{bmatrix}\begin{bmatrix}\dot{z}_b\\ \dot{\theta}_b\\ \dot{z}_{w1}\\ \dot{z}_{w2}\end{bmatrix}\\ &+\begin{bmatrix}S_{22} & -S_{24} & -k_{b1} & -k_{b2}\\ -S_{24} & S_{26} & S_{12} & -S_{14}\\ -k_{b1} & S_{12} & k_{b1} & 0\\ -k_{b2} & -S_{14} & 0 & k_{b2}\end{bmatrix}\begin{bmatrix}z_b\\ \theta_b\\ z_{w1}\\ z_{w2}\end{bmatrix}=\begin{bmatrix}0\\ 0\\ f_{w1}\\ f_{w2}\end{bmatrix}\end{aligned} \tag{30}$$

According to the modeling of a mono-rail sled, mass values and geometry of different components were extracted. The amount of elastomer stiffness used on top of the slipper was also obtained experimentally. “Table 1” shows the values of the various parameters of the designed sled.

**Table 1** The values of the various parameters of the designed sled [31]

| Parameter | Values | Unit |
|---|---|---|
| $m_b$ | 14.69 | kg |
| $m_{w1} = m_{w2}$ | 0.79 | kg |
| $k_{b1} = k_{b2}$ | 370 | kN/m |
| $C_{b1} = C_{b2}$ | 29.94 | N.s/m |
| $a_1$ | 450 | mm |
| $a_2$ | 393 | mm |
| $e_1$ | 285 | mm |
| $e_2$ | 195 | mm |

## 4 RESULTS

Vibrational analysis and sled modal analysis need to be carried out numerically and the numerical simulation results must be verified before numerical simulation of the sled is done.

### 4.1. Validation of Numerical Results

In terms of the aerodynamic geometry of the sleds, a study is done in which the drag force of an Ogive body is obtained experimentally in the NASA wind tunnel of the United States. In addition to the advantage of presenting experimental results, the model has no wings and is geometrically similar to the sled in this study.

For validation, an Ogive cylinder body is simulated according to the test conditions using computational fluid dynamics methods and the drag force is calculated. To extract the values related to the Ogive nose in the experimental work, first, according to “Fig. 4”, the following relations were used.

$$y = \sqrt{\rho^2 - (L - x)^2} + R - \rho \tag{31}$$

$$\rho = \frac{R^2 + L^2}{2R} \tag{32}$$

For the nose profile relations, the following values are placed and the y parameter is calculated for different x parameters.

$$L = 14\text{ in.}, R = 2\text{ in.} \quad \Rightarrow \quad \rho = 50\text{ in.} \tag{33}$$

$$y = \sqrt{2500 - (14 - x)^2} - 48 [in.] \tag{34}$$

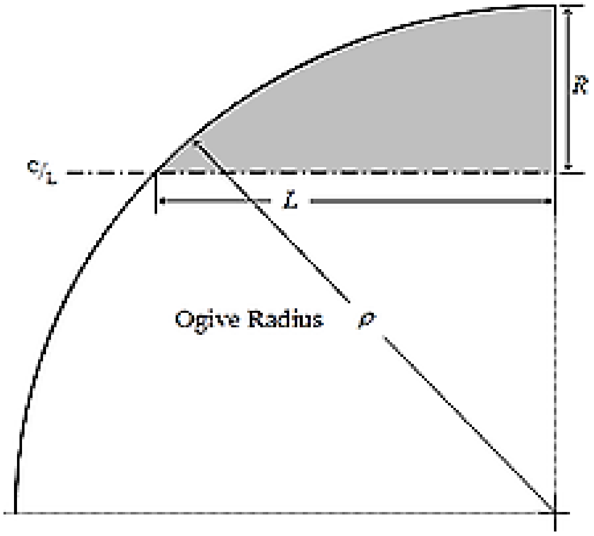

**Fig. 4** Measurement with parameters of Ogive nose.

Considering the obtained values, “Fig. 5” is represented.

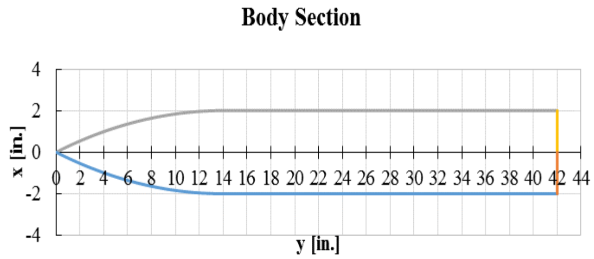

**Fig. 5** Measurement of the sled nose section.

Then, the Ogive nose is designed, which is shown in “Fig. 6”.

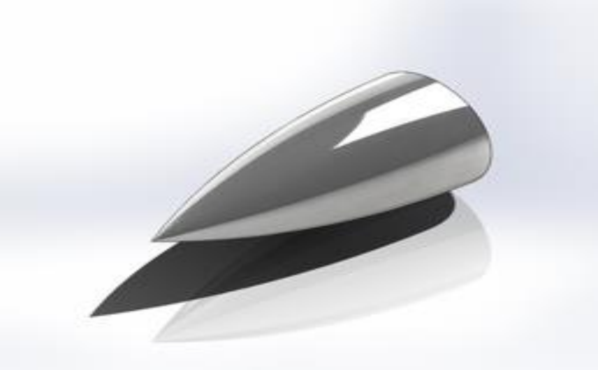

**Fig. 6** Design of the sled nose section.

The body geometry is designed using the model specifications shown in “Fig. 7”.

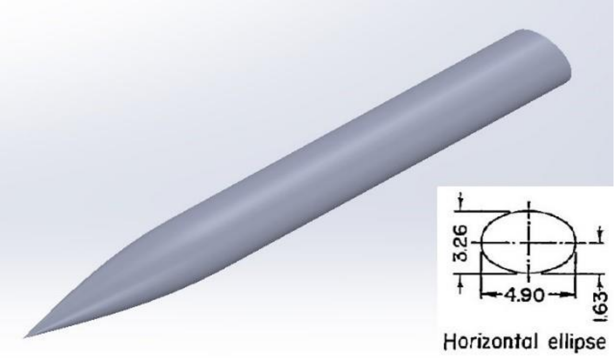

**Fig. 7** Geometry of model regarding [32].

The computational field and the network around the model are taken into consideration using the software and the range of fluid flow is analyzed. The dimensions of the domain should be considered large enough that it does not affect the results. (“Fig. 8”).

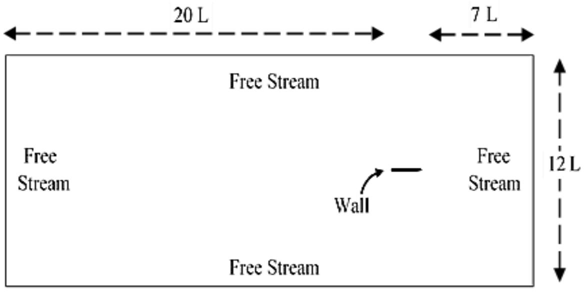

**Fig. 8** Boundary condition and computational domain.

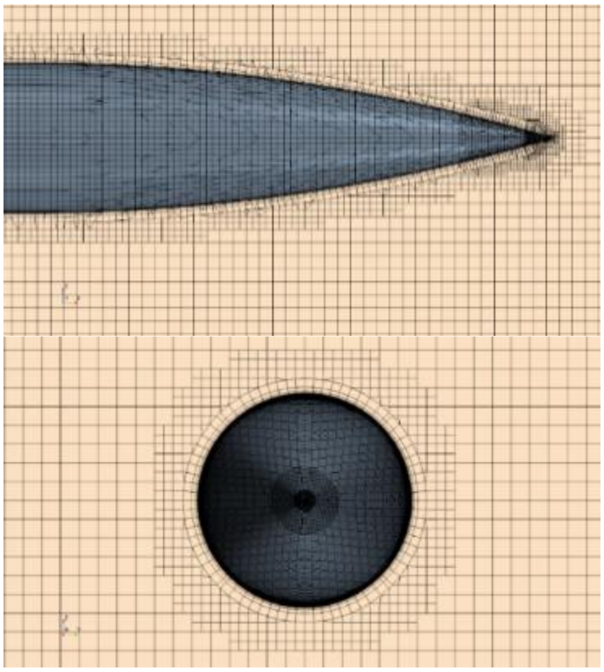

**Fig. 9** Networking model of reference [32].

In this study, the length of the calculated range is 28 times more than the length of the body, so the distance from the beginning of the domain range to the nose portion is 7 times more than the length, and the distance from the end of the body to the end of the domain is 20 times more than it. The width and height of the domain are also 12 times more than the length. In all cases, for all boundaries around the domain, a freestream boundary condition was applied. The mesh networking of the model is produced using the trimmer method, which has four rows of boundary layers, the number of cells is 2707757 and the total thickness of the boundary layer network is 0.0072 m. Fig. **9** shows the research networking of the aforementioned reference. The side view and the front view of the meshing in the whole computational range are also shown in “Fig. 10”.

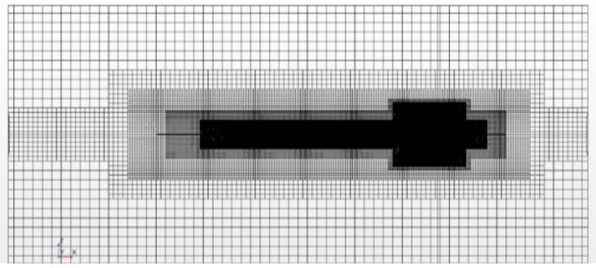

**Fig. 10** Side view and front view of meshing in the whole computational range.

In all simulations, the k-ε model is selected, which is suitable for engineering problems with high Reynolds numbers. In the k-ε model, the $Y^+$ boundary layer network must be greater than 30 and less than 300, as “Fig. 11” confirms.

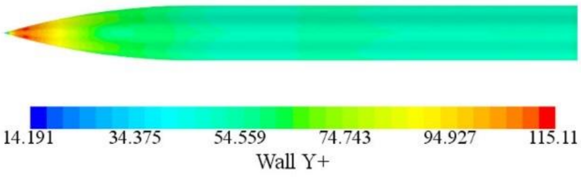

**Fig. 11** $Y^+$ values.

The amount of drag force in the present numerical method in comparison with the amount of drag force obtained from the experimental test at two different cross-sectional levels and pressures is given in “Table 2”.

**Table 2** Comparison of numerical and experimental simulation results

| $P_0$ [psi] | Experimental results [N] | Present working [N] | Error percent |
|---|---|---|---|
| 7.5 | 64.76 | 59.23 | 8.54 |
| 4.5 | 40.39 | 36.8 | 8.88 |

The results show that the error of the numerical method is less than 10% of the experimental test results, so the results of the numerical simulation method in the present study are confirmed.

### 4.2. Numerical Simulation

Considering the accuracy of the numerical solution methods, the numerical analysis of the sled is carried out. The studied sled in the present study is integrated and due to the mono-rail option, it lacks chassis and carriage. Dimensions and computational domain meshing, coordinate system and boundary conditions were carried out regarding the validation model of [32]. The computational domain and meshing network around the body are shown in “Fig. 12” from the front view. The mesh number in the computational domain is 2846662.

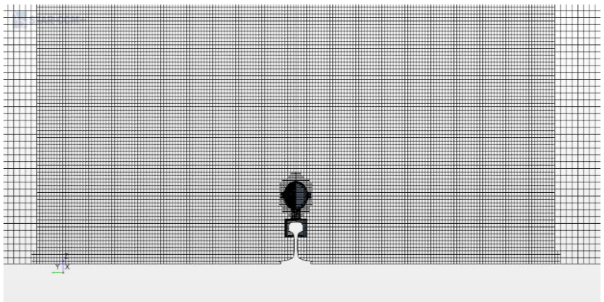

**Fig. 12** Front view of the complete computational domain meshing.

The simulation settings were considered to be the same as the validation. The properties of the working fluid are shown in “Table 3”.

**Table 3** Working fluid properties and environmental conditions [33].

| Parameter | Values | Unit |
|---|---|---|
| $P_0$ | 101325 | Pa |
| $T_0$ | 288.15 | K |
| c | 340.3 | $\frac{m}{s}$ |
| $\mu$ | $1.789\times10^{-5}$ | $\frac{\text{kg}}{m.s}$ |
| $\rho$ | 1.225 | $\frac{\text{kg}}{m^3}$ |

The sled model of the present study is finally shown in “Fig. 13”.

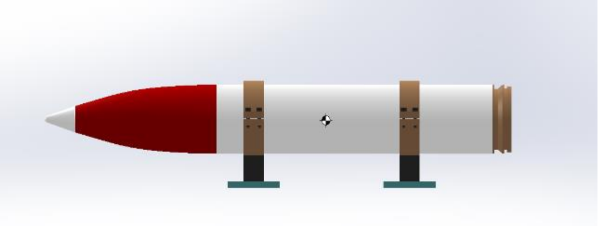

**Fig. 13** Side view of sled model.

### 4.3. Modal analysis

For multi-degree-of-freedom systems, matrices and vectors are used to determine modal properties, and to extract natural frequencies. The Equation of motion of the system is considered as relation (35):

$$[\mathrm{M}]\left\{\ddot{\mathrm{z}}(\mathrm{t})\right\}+[\mathrm{C}]\left\{\dot{\mathrm{z}}(\mathrm{t})\right\}+[\mathrm{K}]\left\{\mathrm{z}(\mathrm{t})\right\}=\{\mathrm{F}\} \tag{35}$$

Also, there is:

$$\{\Psi\}_r=\{z(t)\}=\{Z\}e^{i\omega t} \tag{36}$$

Considering Equation (36), to investigate the motion of free vibrations of the sled system, there is relation (37):

$$\left([K]-\boldsymbol{\omega}^2[M]\right)\{\boldsymbol{\Psi}\}=\{0\} \tag{37}$$

Considering orthogonality of modes, there is:

$$\omega_r{}^2=\frac{k_r}{m_r}\ ,\ (r=1,2,\ldots,n) \tag{38}$$

In the above relations, $m_r$ and $k_r$ are related to the mass and stiffness of the modal or the generalized mass and stiffness of the r<sup>th</sup> mode. [Kr] and [Mr] are considered as the mass and stiffness matrices for the rth mode respectively, so the natural frequency and the mode shape matrices can be written as (39) and (40):

$$\left[\omega_r^2\right]=\begin{bmatrix}\omega_1^2 & 0 & \ldots & 0\\ 0 & \omega_2^2 & \ldots & 0\\ \ldots & \ldots & \ldots & \ldots\\ 0 & 0 & \ldots & \omega_n^2\end{bmatrix} \tag{39}$$

$$[\Psi]=\left[\{\Psi\}_1,\{\Psi\}_2,\ldots,\{\Psi\}_n\right] \tag{40}$$

The Equation of motion of a multi-degree-of-freedom system with disproportionate structural damping is expressed as relation (41):

$$[M]\left\{\ddot{x}\right\}+[K]\{x\}+i\left[C^*\right]\{x\}=\{0\} \tag{41}$$

The damping structure matrix can be considered as an imaginary part of a complex stiffness matrix, defined as relation (42):

$$\left[K^*\right]_c=[K]+i\left[C^*\right] \tag{42}$$

To solve the above Equation, relation (43) is obtained:

$$\{x(t)\} = \{X\}\ e^{j\lambda t} \tag{43}$$

In this relation, λ is a complex frequency and includes both vibration and damping terms, and {X} indicates the complex vector of displacement domains. By substituting the value, the following problem of complex eigenvalue is obtained as the following relation.

$$\left(\left[K^*\right]_c - \lambda^2 [M]\right)\{X\} = \{0\} \tag{44}$$

The solution of Equation (44) includes the diametric matrix of the eigenvalue [λr] and the eigenvector matrix [Ψ]. The relation of the eigenvalue $\lambda r^2$ with the natural frequency $\omega_r$ and the damping dissipation coefficient of the system ηr is obtained as relation (45):

$$\lambda_r^2 = \omega_r^2 \left(1 + i\eta_r\right)\ \ ,\left(r = 1, 2, \ldots, n\right) \tag{45}$$

λr is known as the complex natural frequency of the system. [$\lambda r^2$] is the natural frequency matrix of the system. The corresponding eigenvector, $\{\Psi\}_r$, is a complex vector. All eigenvectors, corresponding eigenvalues of $\omega_r$ in ascending order, are placed next to each other and these values result in the mixed matrix as the mode shape matrix of [Ψ]. Considering the orthogonal properties of the system, there is:

$$\left[\lambda_r^2\right] = \left[m_r\right]^{-1}\left[k_r\right] \tag{46}$$

In this case, the modal mass of $m_r$ and the modality stiffness of $k_r$ are complex values. To obtain natural frequencies, given the four degrees of freedom of the system, [$\lambda r^2$] value for the four modes of the system is considered equal to the matrix of [B].

$$[\mathrm{B}] = [\mathrm{M}]^{-1}\ [\mathrm{K}] \tag{47}$$

By placing the value of $[m_r]^{-1}$ in Equation (46) and obtaining the root mean square of the eigenvalues, the natural frequencies of the system will be in the form of a matrix of [λr].

$$\lambda_r = \begin{cases} 84.7 & rad/s \\ 129.9 & rad/s \\ 866.5 & rad/s \\ 855.1 & rad/s \end{cases} \cong \begin{cases} 13.48 & Hz \\ 20.68 & Hz \\ 137.9 & Hz \\ 136.1 & Hz \end{cases} \tag{48}$$

Finally, the system modes are obtained as follows:

$$\mathrm{u}_1 = \begin{bmatrix} 0 \\ 0.99 \\ -0.11 \\ 0.11 \end{bmatrix},\ \mathrm{u}_2 = \begin{bmatrix} -0.73 \\ 0 \\ -0.48 \\ -0.48 \end{bmatrix}$$
$$\mathrm{u}_3 = \begin{bmatrix} 0.05 \\ 0 \\ -0.71 \\ -0.71 \end{bmatrix},\ \mathrm{u}_4 = \begin{bmatrix} 0 \\ 0.12 \\ 0.7 \\ -0.7 \end{bmatrix} \tag{49}$$

Where, the first and second modes indicate torsional and transverse vibrations of the system, respectively. The third and fourth modes show the vertical vibrations of both slippers and the vibrational motion due to torsion, respectively. The transverse and torsional vibrations of all modes demonstrate the importance of the slipper role in the sled system.

To validate the values of the natural frequencies of the system analytically and to obtain the shape of the modes, a modal analysis of the designed sled is carried out numerically. The mesh model of the designed sled is shown in “Fig. 14”.

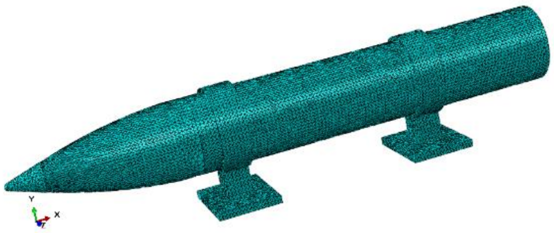

**Fig. 14** Meshing of designed sled model.

Fig. **15** shows the sled modal analysis for the first mode of the system which is related to the torsional vibration around the center of mass of the sled. Due to the rigidity of the sled body, the amount of torsional vibration is low.

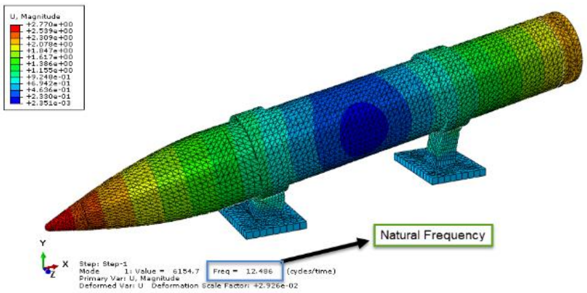

**Fig. 15** First (torsional) mode of sled.

Fig. **16** shows the second mode, which shows the transverse vibrations of the sled. In this case, the sled vibrates vertically without torsional motion, and the vibration rate of the two slippers is equal to each other.

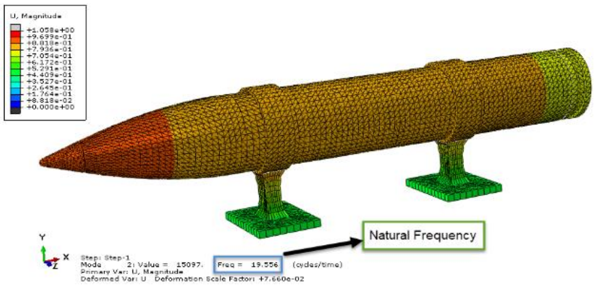

**Fig. 16** Second (transverse) mode of the sled.

In the third mode, both slippers vibrate in one direction (transverse) and there is no torsional movement in the sled as shown in "Fig. 17". The vibrations are much greater than the first and second vibrations modes which implies the importance of the slipper role in the sled system.

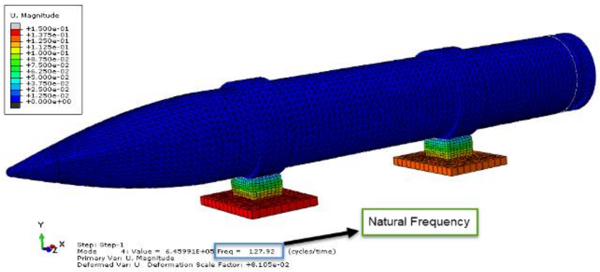

**Fig. 17** Third mode of the sled.

The fourth mode is similar to the third mode, except that the displacement of slippers is in opposite directions due to torsional vibrations. Fig. **18** represents the fourth mode.

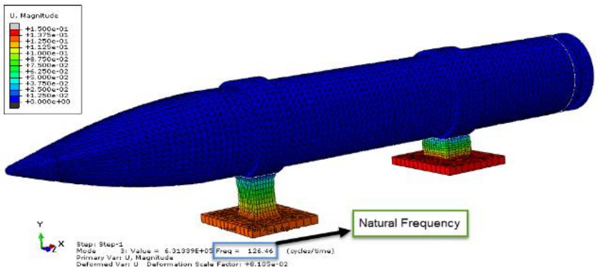

**Fig. 18** Fourth mode of the sled.

"Table 4" describes the values of the natural frequencies of the system in both analytical and numerical methods. The results error is less than 8%, and both results are confirmed. The difference in results can be attributed to the distribution of mass and geometry of the sled. On the other hand, the obvious difference between the frequencies of the first and second modes from the frequencies of the third and fourth modes shows the significant role of the slipper in the sled system.

**Table 4** Comparison of natural frequencies in numerical simulation method with analytical method

| Natural frequency | Numerical result (Hz) | Analytical result (Hz) | Error percentage |
|---|---|---|---|
| First mode | 12.49 | 13.48 | 7.34 |
| Second mode | 19.56 | 20.68 | 5.41 |
| Third mode | 127.9 | 137.9 | 7.25 |
| Forth mode | 126.5 | 136.1 | 7.42 |

### 4.4. Pressure and Velocity Distribution

Fig. **19** shows the contour of the Mach number in the computational domain. According to the velocity distribution, it is assumed that a vortex is formed due to the pressure difference in the back of the sled body. Also, the highest pressure after the front slipper is applied on the distance part between the two slippers.

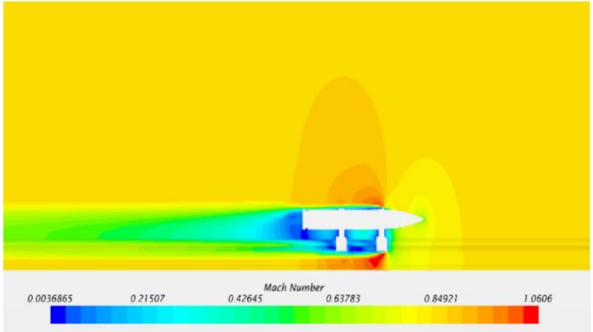

**Fig. 19** Contour of the Mach number in the computational domain.

Fig. **20** shows the high-pressure areas of the fluid around the sled. As can be seen, the highest pressure, except the front slipper, is in the distance between the two slippers.

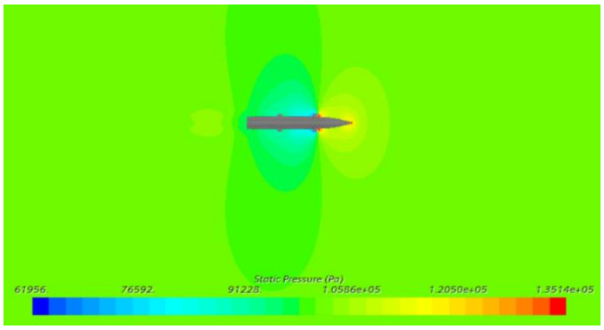

**Fig. 20** Static pressure contour in the computational domain.

## 5 CONCLUSIONS

In this paper, the pressure distribution on the slippers of a mono-rail sled has been investigated, and the vibrational and modal analyses are also investigated with an emphasis on the role of slippers. First, the governing vibration Equations, natural frequencies of the system, and vibration modes were extracted in the analytical method. Then, by validating the numerical method with the experimental results performed in the wind tunnel, modal analysis of sled system was carried out, and the modes shapes were designed. The torsional and transverse vibrations created in the slippers as well as the static pressure distribution of the slippers show that this part of the sled, which has more risk of damage due to applied stresses, is very important.

## REFERENCES

[1] Gragossian, A., Pierrottet, D. F., Estes, J., Barnes, B. W., Amzajerdian, F., and Hines, G. D., Navigation Doppler Lidar Performance Analysis at High Speed and Long Range, AIAA Scitech 2020 Forum 1 PartF(January), 2020, pp. 1–6. Doi: 10.2514/6.2020-0369.

[2] Deleon, A., Baker, W. P., and Palazotto, A. N., Evaluation of a Nonlinear Melt Region Produced Within a High Speed Environment, AIAA/ASCE/AHS/ASC Struct Struct Dyn Mater Conf 2018 (210049), 2018, pp. 1–17. Doi: 10.2514/6.2018-0187.

[3] Meacham, M. B., Gallon, J. C., Johnson, M. R., Natzic, D. B., Thompson, N., Aguilar, D., Marti, B., Hennings, E., and Rivellini, T., Rocket Sled Strength Testing of Large, Supersonic Parachutes, Aerodyn Decelerator Syst Technol Conf1–28, 2015. Doi: 10.2514/6.2015-2163.

[4] Guan, H., Zhu, Y., and Zhang, S. J., Aerodynamic characteristics of Ejection Seat and Occupant, 51st AIAA Aerosp Sci Meet Incl New Horizons Forum Aerosp Expo 2013 (January), 2013, pp. 1–20, Doi: 10.2514/6.2013-386.

[5] Cinnamon, J. D., Palazotto, A. N., Further Validation of A General Approximation for Impact Penetration Depth Considering Hypervelocity Gouging Data, Int J Impact Eng, Vol. 34, No. 8, 2007, pp. 1307–1326. Doi: 10.1016/j.ijimpeng.2006.08.005.

[6] Nakata, D., Kozu, A., Yajima, J., Nishine, K., Higashino, K., and Tanatsugu, N., Predicted and Experimented Acceleration Profile of the Rocket Sled, Trans Japan Soc Aeronaut Sp Sci Aerosp Technol Japan 10(ists28):Ta_1-Ta_5, 2012. Doi: 10.2322/tastj.10.ta_1.

[7] Xiao, J., Zhang, W. W., Xue, Q., Zhang, L. R., and Zhou, X. B., Reliability Analysis of Engine Shell Strength under Rocket Sledge Vibration Environment, J Phys Conf Ser, Vol. 1176, No. 6, 2019, pp. 4–9, Doi: 10.1088/1742-6596/1176/6/062047.

[8] Butova, S. V., Gerasimov, S. I., Erofeev, V. I., and Kamchatnyi, V. G., Stability of High-Speed Objects Moving Along a Rocket Track Guide. J Mach Manuf Reliab, Vol. 44, No. 1, 2015, pp. 1–5. Doi: 10.3103/S1052618815010021.

[9] Hooser, C., Afb, H., and Beach, H., AIAA 2002-3037 AIAA 2002-3037 Proposed Hypersonic Air-Breathing Test Capability At The Holloman High Speed Test Track Usaf-Holloman High Speed Test Track Neil Bosmajian The Boeing Company-Reusable Space Systems, Test (June), 2002, pp. 1–12.

[10] Nakata, D., Yajima, J., Nishine, K., Higashino, K., Tanatsugu, N., and Kozu, A., Research and Development of High Speed Test Track Facility in Japan. 50th AIAA Aerosp Sci Meet Incl New Horizons Forum Aerosp Expo (January), 2012, pp. 1–11. Doi: 10.2514/6.2012-928.

[11] Hsu, Y. H., Langhorn, A., Ketchen, D., Holland, L., Minto, D., and Doll, D., Magnetic Levitation Upgrade to the Holloman High Speed Test Track, IEEE Trans Appl Supercond, Vol. 19, No. 3, 2009, pp. 2074–7. Doi: 10.1109/TASC.2009.2019558.

[12] Kumar, V., Terrazas, J., Edmonds, R., and Kotteda, V. M. K., Multiphase CFD Modeling of The Braking Phenomena for The Holloman High-Speed Test Track, 23rd AIAA Int Sp Planes Hypersonic Syst Technol Conf 2020, 2020, pp. 1–10. Doi: 10.2514/6.2020-2446.

[13] Wang, B., Zheng, J., Yu, Y., Lv, R., and Xu, C., Shock-Wave/Rail-Fasteners Interaction for Two Rocket Sleds in The Supersonic Flow Regime, Fluid Dyn Mater Process, 2020. Doi: 10.32604/FDMP.2020.09681.

[14] Guangqi, H., Yin, A. I., R., and Zhenzhen, J., Simulation Analysis of Rocket Sled Vibration Reduction Platform, J Exp Test, Vol. 2, 2006, pp. 10–3.

[15] Xiao, J., Zhang, W. W., Xue, Q., Gao, W. B., and Deng, B., Analysis of Rocket Sled Vibration Signal Transmission Based on Zigbee Application, J Phys Conf Ser, Vol. 1176, No. 6, 2019, pp. 8–13. Doi: 10.1088/1742-6596/1176/6/062006.

[16] Tong, D. C., Mechanical Simulation of Rocket Sled Test Damping System, Nav Electron Eng, Vol. 8, 2012, pp. 87–9.

[17] Compilation, D. W., Theory of Vibration Reduction, Tsinghua Univ Press, 2014, pp. 69–91.

[18] Minto, D. W., Recent Increases in Hypersonic Test Capabilities at the Holloman High Speed Test Track, 38th Aerosp Sci Meet Exhib (January), 2000. Doi: 10.2514/6.2000-154.

[19] Bosmajian, N., Minto, D., and Holland, L., Status of the Magnetic Levitation Upgrade to the Holloman High Speed Test Track, 21st Aerodynamic Measurement Technology and Ground Testing Conference, 2000, pp. 2289.

[20] Gurol, H., Ketchen, D., Holland, L., Minto, D., Hooser, M., and Bosmajian, N., Status of the Holloman High

Speed Maglev Test Track (HHSMTT), AIAA Aviat 2014 - 30th AIAA Aerodyn Meas Technol Gr Test Conf (June), 2014, pp. 1–15. Doi: 10.2514/6.2014-2655.

[21] Chen, S., He, Y., and Li, Z., Analysis of the Rocket Sled Track Irregularity in Time and Frequency Domains, CICTP 2014: Safe, Smart, and Sustainable Multimodal Transportation Systems, 2014, pp. 111–8.

[22] Turnbull, D., Hooser, C., Hooser, M., and Myers, J., Soft Sled Test Capability at the Holloman High Speed Test Track. US Air Force T&E Days, 2010.

[23] Kevin Dunshee Holloman High-Speed Test Track Design Manual. vol. 1.

[24] Bashash, S., Salehi-Khojin, A., and Jalili, N., Forced Vibration Analysis of Flexible Euler-Bernoulli Beams with Geometrical Discontinuities, Proceedings of the American Control Conference, 2008.

[25] Xiang, J., He, D., and Zeng, Q. Y., Analysis Theory of Spatial Vibration of High-Speed Train and Slab Track System, J Cent South Univ Technol (English Ed, 2008. Doi: 10.1007/s11771-008-0024-9.

[26] Gao, F., Wu, Z., Li, F., and Zhang, C., Numerical and Experimental Analysis of The Vibration and Band-Gap Properties of Elastic Beams with Periodically Variable Cross Sections. Waves in Random and Complex Media, 2019. Doi: 10.1080/17455030.2018.1430918.

[27] Mosavi, A., Benkreif, R., and Varkonyi-Koczy, A. R., Comparison of Euler-Bernoulli and Timoshenko beam Equations for Railway System Dynamics, Advances in Intelligent Systems and Computing, 2018.

[28] Afshar, N. P., Samani, F. S., and Molaie, M., Application of Linear And Nonlinear Vibration Absorbers For The Nonlinear Beam Under Moving Load, J Comput Appl Res Mech Eng, 2015. Doi: 10.22061/jcarme.2015.344.

[29] Jin, L., Zhang, Q., Lei, B., and Li, Z., Simulation and Research on 3D Gouging Model Based on Abaqus/Explicit, 2012 16th International Symposium on Electromagnetic Launch Technology, 2012, pp. 1–5.

[30] Buentello Hernandez, R. G., Palazotto, A. N., and Le, K. H., 3D Finite Element Modeling of High-Speed Sliding Wear, Collect Tech Pap - AIAA/ASME/ASCE/AHS/ASC Struct Struct Dyn Mater Conf1–20, 2013.

[31] Greenwood, D. T., Advanced Dynamics Najafi MR, Moghadas SM Investigation Effect of Adding a SBR Damper to A Sled Sample and Extraction of Its Equivalent Stiffness and Damping. ADMT J, 2022.

[32] Carlson, H. W., Gapcynski, J. P., An Experimental Investigation at a Mach Number of 2.01 of the Effects of Body Cross-Section Shape on the Aerodynamic Characteristics of Bodies and Wing-Body Combinations, 1955.

[33] Cengel, Y. A., Fluid Mechanics, Tata McGraw-Hill Education.

*Int. J. Advanced Design and Manufacturing Technology, 2023, Vol. 16, No. 4, pp. 99-108*

***DOI: 10.30486/admt.2024.1968460.1383*** ***ISSN: 2252-0406*** ***https://admt.isfahan.iau.ir***

# Simulation of a Freight Train and The Effect of Wheel Flat Defect on The Wheel/Rail Dynamic Forces

**Sajjad Sattari**
Department of Mechanical Engineering,
Najafabad Branch, Islamic Azad University, Najafabad, Iran
E-mail: sajjad.sattari@gmail.com

**Mohammad Saadat*, Sayed Hasan Mirtalaie,**
**Mehdi Salehi, Ali Soleimani**
Department of Mechanical Engineering,
Najafabad Branch, Islamic Azad University, Najafabad, Iran
E-mail: saadat@pmc.iaun.ac.ir, mirtalaie@pmc.iaun.ac.ir,
mehdi.salehi@pmc.iaun.ac.ir, soleimani@pmc.iaun.ac.ir
*Corresponding author

**Received: 27 September 2022, Revised: 23 April 2023, Accepted: 28 April 2023**

**Abstract:** Wheel/rail interaction is one of the most important research topics in railway engineering and generally includes impact response, vibrations, and track safety. Track structure failures caused by wheel/rail impact dynamic forces can lead to significant economic loss through damage to rails, ballast, fastening system, etc. Wheel/rail impact forces occur due to defects in wheels and/or rails such as wheel flats, irregular wheel profiles, rail corrugation, etc. A wheel flat can cause a large dynamic impact force as well as high frequency forced vibrations, which will eventually lead to damage to the train and track structure. In the present work, a freight train (3D model) was used to analyze the dynamic impact caused by the wheel flat using UM software. The effects of wheel flat depth and length (0, 0.2, 0.5, 1, 1.5, 2, and 3 mm) at two speeds of 50 and 80 km/h on wheel/rail dynamic forces have been investigated. The results showed that the presence of a wheel flat defect significantly increases the wheel/rail dynamic impact. For example, by increasing the wheel flat depth to 3 mm, the values of maximum force at speeds of 50 and 80 km/h have changed by about 235% and 400%, respectively.

**Keywords:** Freight Train, Railway Vehicles, Simulation, Wheel Flat Depth, Wheel Flat, Wheel/Rail Force

**Biographical notes: Sajjad Sattari** is a PhD candidate in Mechanical Engineering at the Islamic Azad University of Najafabad (IAUN), Iran. His current research focuses on railway engineering and solid mechanics. He received his MSc in mechanical engineering from IAUN in 2016. **Mohammad Saadat** is an Assistant Professor of Mechanical Engineering at IAUN. His current research interests include control, mechatronics, and hybrid electric vehicles. He received his PhD in Mechanical Engineering from IUT in 2016. **Sayed Hasan Mirtalaie** is an Assistant Professor of Mechanical Engineering at IAUN. His current research interest includes dynamics and vibration. He received his PhD in Mechanical Engineering from UK in 2017. **Mehdi Salehi** is an Assistant Professor of Mechanical Engineering at IAUN. He received his PhD in Mechanical Engineering from IUT in 2011. **Ali Soleimani** is an Assistant Professor of Mechanical Engineering at IAUN. He received his PhD in Mechanical Engineering from TMU in 2016.

Research paper

## 1 INTRODUCTION

The existence of a geometric defect in the interaction between the rail and the wheel is one of the sources of the dynamic interaction of the train. Wheel profiles have a significant effect on the safety and dynamic performance of the vehicle; For example, in terms of the dynamic stability of the vehicle, the magnitude of the wheel/rail contact forces, and/or ride comfort. Wheel tread defects are usually divided into two main categories: (i) defects along a portion of the wheel circumference and (ii) defects around the entire wheel. Both mentioned defects are considered types of wheel out-of-roundness (OOR) phenomena. The first group includes wheel flat, shelling, spalling, etc., and is mainly caused by braking damage and rolling contact fatigue cracking. The second category includes corrugation of the wheel and polygonal wheel (due to non-uniform wear), which are periodic irregularities around the wheel that can be caused by unbalanced loads. The non-roundness of the railway wheels has an undesirable effect on the components of the track and the railway vehicle. In recent decades, some researchers have focused on the methods of diagnosing and analyzing the dynamic behaviour of the train due to wheel flat [1-12]. When the wheel-set is locked and slides along the rails as a result of improper or defective brakes, wheel flat occurs. Therefore, the surface of the wheels becomes flat instead of round due to the friction between the wheels and the rails. Wheel flats create high dynamic impact loads on railway substructure, which cause significant damage to rail and track vehicles. Among these damages, we can mention broken axles, hot axle-boxes, damaged rolling bearings, and cracks in wheels, rails, and ballasts. In addition, this type of wheel defect causes excessive noise and vibration. These large vibrations are transmitted to the rolling stock and by applying and inducing excessive forces (more than the permissible values), they cause damage to the suspension systems, bogie frame, and body of rail vehicles. In addition, wheel and track irregularities can lead to improper performance of the train and overhead track interaction. Therefore, in order to deal with this issue, railway centers generally carry out the necessary measures and monitoring. As a precaution, most passenger trains are now equipped with advanced anti-slip systems that slightly reduce wheel/rail slip. However, with increasing operating speeds and axle loads, wheel flatting cannot be completely avoided. In addition, since freight trains do not have anti-slip systems, the condition of the wheels is usually worse and has a significant impact on the useful life of the trains and substructure [13-29].

In recent years, various researchers have studied the field of wheel flat defects (causes, solutions to reduce defects, maintenance, and railway vehicles monitoring), among which can be referred to Bosso et al. [17], Mishra et al. [18], Chen et al. [19], Ng et al. [20], Wang et al. [21], Sattari et al. [22], etc. Bosso et al. [17] used an algorithm in the time domain to detect wheel flat defects (early stage and to estimate the severity) by measuring the vertical acceleration on the axle-box. Mishra et al. [18] presented the real-time implementation of fiber Bragg grating sensors on rail tracks and investigated the train's wheel flat status (passenger train running at a speed 70 kmph). Chen et al. [19] assessed wheel conditions in high-speed trains under various operational conditions. Ng et al. [20] studied the association between wheel flat, wheel/rail impact responses, and vibration signals (a 3D finite element model). Wang et al. [21] investigated the axle-box vertical vibration caused by wheel flat in the conventional time and frequency domain by modeling a high-speed railway system (94 degrees of freedom with wheel flat defect). Sattari et al. [22] studied the dynamic and safety of a freight train with wheel flat when passing through turnouts. Their results showed that the depth of the wheel flat, as well as the train speed, strongly affect the dynamic forces and derailment coefficient at the turnout.

Train wheels, among other components, are critical for the safety and ride comfort of railway systems. Various methods have been used to assess the wheel health conditions. In this paper, dynamic simulation is used to determine the effect of two basic parameters of wheel flat depth and train speed on wheel/rail dynamic forces, which is rarely presented in other research. In the current paper, first, the modeling of a freight train is done in the Universal Mechanism (UM) multi-body software, and then the effect of the depth and length of the wheel flat on the vertical force of the wheel/rail is evaluated. Investigations were carried out from the depth of the wheel flat from 0 to 3 mm (up to a length of 168 mm) at two speeds of 50 and 80 km/h and on a straight route.

## 2 RAILWAY SYSTEMS

The structural structure of the railway can be considered as consisting of two main parts: superstructure and substructure. What is generally referred to as the superstructure of railway tracks consists of the sleeper, fastening system, ballast, and sub-ballast layers (or other alternative components in different types of slab tracks), which provide a suitable platform for the train to pass. In general, and in terms of structure, the types of the superstructure in railway tracks can be classified into two general groups: ballasted and slab track. According to the conditions of the route and technical and economic studies, both types of these tracks can be used. In “Fig. 1”, a sample of ballasted tracks in Iran and Gaduk railway station (Tehran-Mazandaran route) can be seen. The use of ballasted tracks is widely used in Iran's railway tracks and due to their lower construction cost and taking into account all their advantages and disadvantages, it has an acceptable performance overall [30-36].

**Fig. 1** Train-track system and considered bogie.

## 3 MODELING (TRAIN AND WHEEL FLAT)

To simulate a freight train, a three-piece bogie type 18-100 used in the countries of America, Russia, China, Canada, India, Australia, Brazil, and Iran has been used. Generally, simulations of three-piece bogies are based on models of a wedge friction system. The inertial properties of the wedges have been ignored and the linear model of tangential contact forces has been used. Some researchers used this train model for dynamic simulations. After completing the simulation of the dynamic characteristics of the train in the UM input section, the UM simulation section has been used to simulate the dynamic behavior of the system. Figure 2 shows a diagram of the simulated model, including the body, bogie, and its components, as well as the wheel/rail force. Generally, 3-piece bogies simulations are based on models of a wedge frictional system. The inertia properties of wedges are ignored and the linear model of tangential contact forces is used. The bogie has rigid contacts between the side frame and axle-boxes, car-body and bolsters in the center plate and side bearings including clearances, between frictional wedges and bolster or side frame. Hertzian solution and FASTSIM algorithm by Kalker as well as a modified non-elliptic multipoint contact model are used. To provide more details about the simulation, refer to references [22-24], [29-31], [37-38].

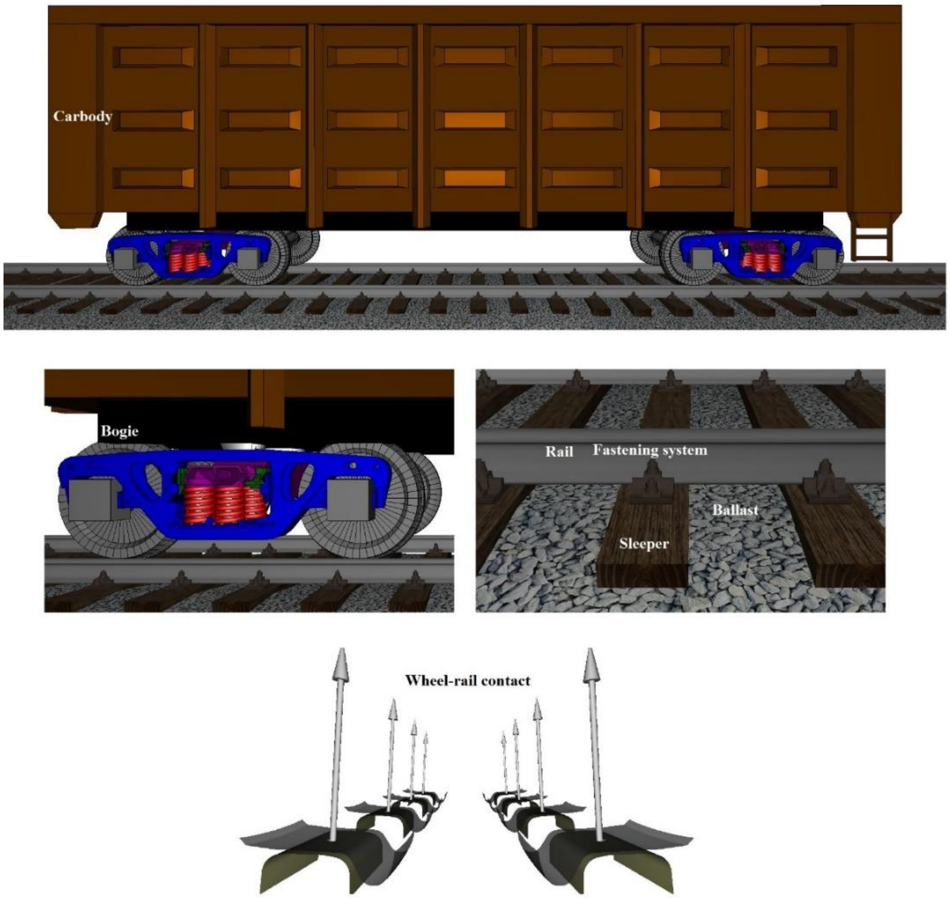

**Fig. 2** Freight train modeled in UM software and its component.

The wheel flat defect generally occurs in two ways and a schematic of these two can be seen in “Fig. 3”. In “Fig. 3 (a)”, the wheel flat is rounded and in “Fig. 3 (b)” the wheel flat is deformed with smooth areas and sharp points (newly formed) [22-23], [39-44]. In this research, dynamic forces have been extracted from the wheel flat defect in the rounded state (“Fig. 3(a)”) and at different depths.

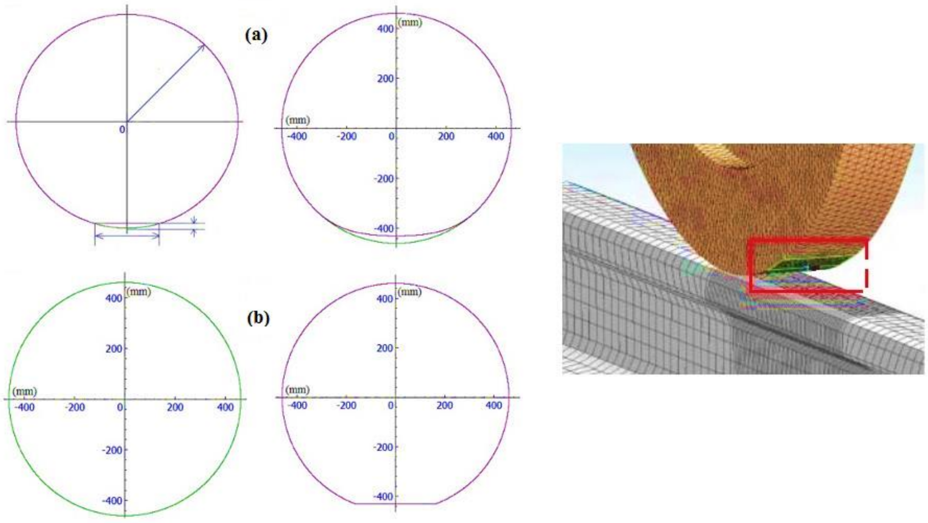

**Fig. 3** Wheel flat defects in the form of: (a) rounded and (b) newly formed.

## 4 RESULTS AND DISCUSSION

Researchers with a field study of vibrations and train-track interaction have a great desire to obtain the values of wheel/rail forces considering different conditions of track and train. Today, the available methods for calculating wheel/rail dynamic forces are divided into two direct and indirect methods. In direct methods, the internal reactions of the wheel or train (including shear and bending moments, acceleration or displacement) are measured, which are directly related to the dynamic force of the wheel/rail.

There are many indirect methods, and among them, it is possible to measure the response of the train on the wagon body, bogie frame and axle-box of the train passing the track to calculate the dynamic force of the wheel/rail. These methods are more flexible, as trains can be equipped at stop times. Also, the use of software such as MATLAB, ABAQUS, UM, ANSYS, etc. to simulate railway systems and extract wheel/rail dynamic forces is interesting for researchers (indirect method). Today, with the increasing speed of trains, the growth of freight train loading and the variety of working conditions, the comprehensive study of wheel and rail dynamics is becoming more and more important [22-24], [30-33].

The bogie of the freight wagon has three main components, namely the wheelset, the bolster, and the side frame. In Iran, the widely used wagon bogie is shown in “Figs. 1 and 2”. The single-section freight wagon is mainly composed of one car-body and two bogies. Each group of bogies includes two wheelsets (including axle-boxes), two side frames, one bolster, and two suspension systems (114 DOFs). The car-body and bogie are rigid bodies with mass and they are assumed to move at a uniform speed along a straight railway line. The dynamic balance equation of a freight car can be expressed by the following formula (“Eq. (1)”):

$$\ddot{U}_{fw} + C_{fw}\dot{U}_{fw} + K_{fw}U_{fw} = f_{wr} \tag{1}$$

Where, $M_{fw}$ is the mass matrix of the freight wagon, $C_{fw}$ and $K_{fw}$ are the damping and stiffness matrices of the freight wagon, respectively, $\ddot{U}_{fw}$, $\dot{U}_{fw}$, $U_{fw}$ are the acceleration, velocity, and displacement vectors of the freight wagon, $f_{wr}$ is the vector of the wheel/rail contact force [29].

The wheel flat is mainly characterized by the wheel flat length (L) and the flat depth (D), calculated according to Equation (2):

$$D = \frac{L^2}{16r_w} \tag{2}$$

In which, $r_w$ is the radius of the wheel. Also, the wheel flat vertical profile deviation (Z) is defined as (“Eq. (3)”):

$$Z = -\frac{D}{2}\left(1 - cos\frac{2\pi x}{L}\right)H(x - (2\pi r_w - L)), \quad 0 \le x \le 2\pi r_w \tag{3}$$

In which, H is the Heaviside periodic function, and x is the coordinate aligned with the track longitudinal direction. When a defective wheel rotates, the flat of the wheel causes a periodic impulse to the track with a particular frequency. The frequency of the periodic impulse corresponding to the flat impact frequency ($f_f$) can be determined as follows (“Eq. (4)”):

$$f_f = \frac{V}{2\pi r_w} \tag{4}$$

In which, V is the train speed [22-23], [27-28].

Figures 4 and 5 show the effect of wheel flat depth on wheel/rail vertical dynamic forces in a freight train with a speed of 50 and 80 km/h, respectively. The results show that with the increase in the depth of the wheel flat, the wheel/rail forces have increased significantly and it is consistent with the results of other researchers [39-44]. As can be seen in “Figs. 4 and 5”, the wheel/rail vertical force fluctuates in the range of 115 kN in all wheels of the train in the state without wheel flat defects (“Figs. 4 and 5 (a)”). However, by applying the defect and increasing the wheel flat depth and the speed of the train, these values show a significant increase. The results of the studies by Masilo et al. [39], Pringer et al. [40], Mosleh et al. [41], Spiro et al. [42], Bayan et al. [43], and Newton et al. [44] also show that with increasing the wheel flat depth, dynamic forces have increased.

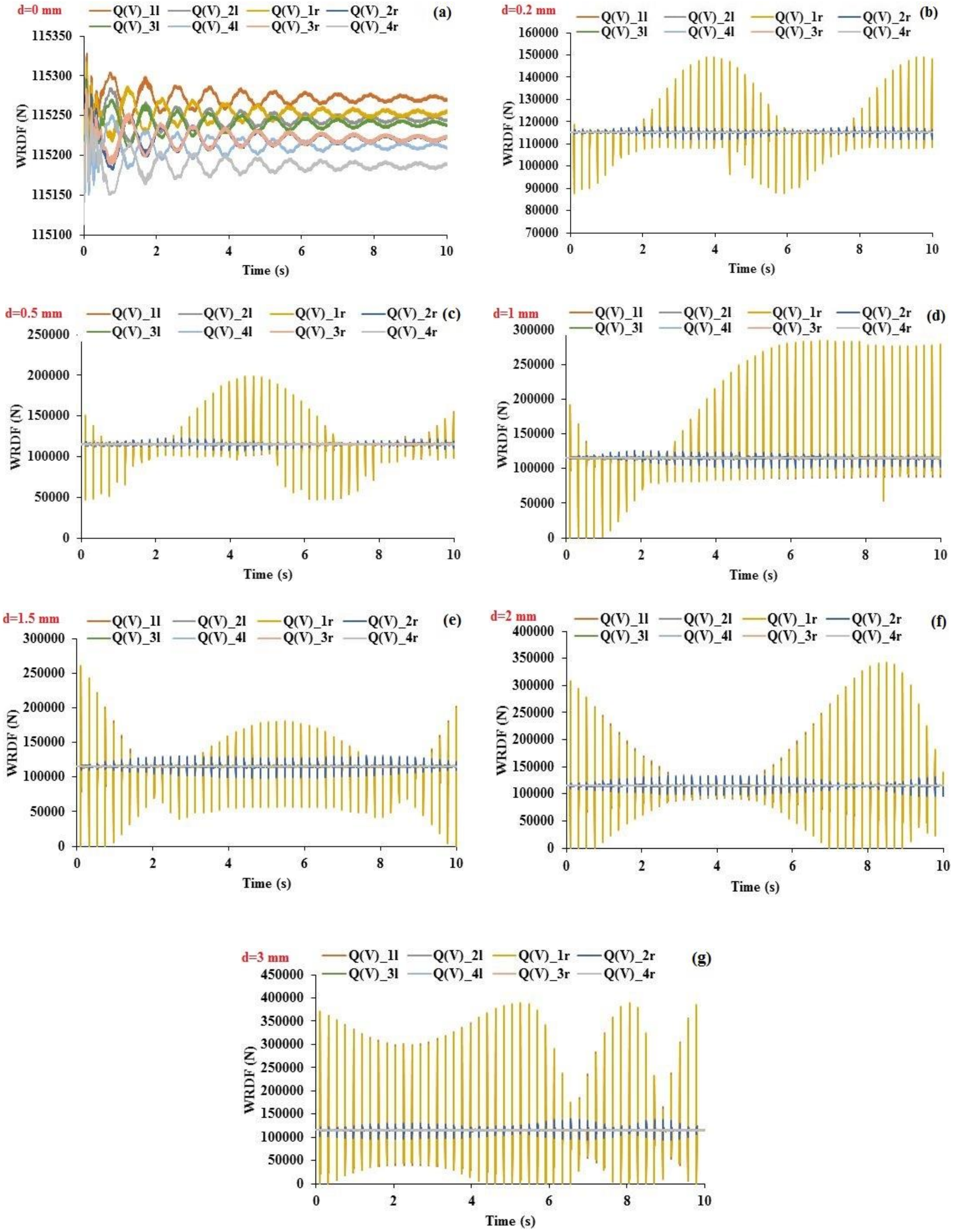

**Fig. 4** Wheel/rail dynamic force at a speed of 50 km/h and in the wheel flat with different depths: (a): 0, (b): 0.2, (c): 0.5, (d): 1, (e): 1.5, (f): 2, and (g): 3 mm.

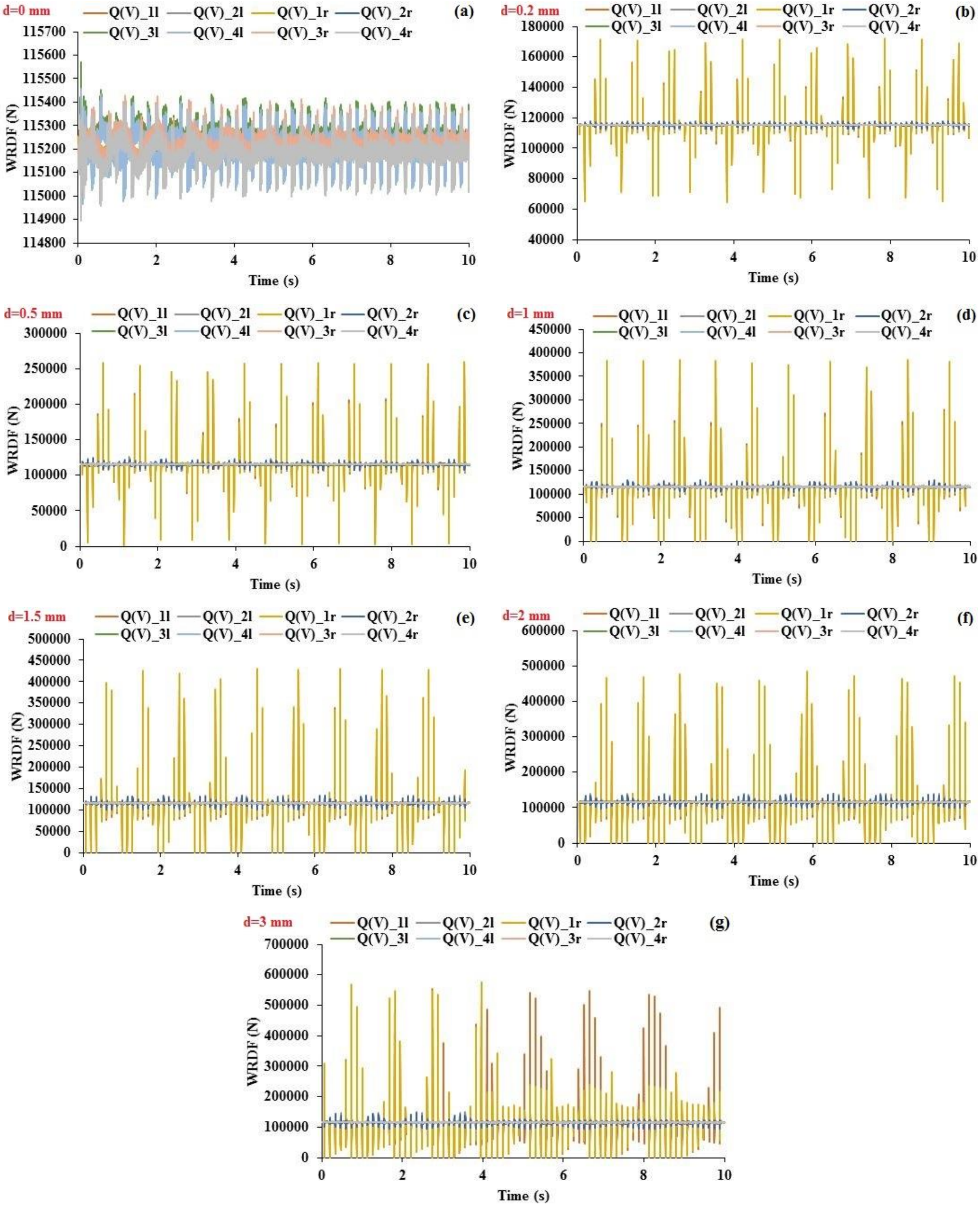

**Fig. 5** Wheel/rail dynamic force at a speed of 80 km/h and in the wheel flat with different depths: (a): 0, (b): 0.2, (c): 0.5, (d): 1, (e): 1.5, (f): 2 and (g): 3 mm.

Figure 6 compares the wheel/rail dynamic forces (maximum and minimum values) at different depths of the wheel flat and different speeds. The results show that the wheel flat depth and train speed are two important factors in estimating the wheel/rail dynamic forces. The results of the studies by Spiro et al. [42] and Wall et al. [45] also showed that with the increase in train speed, the wheel/rail dynamic forces increased and it is in accordance with the current research. By increasing the wheel flat depth at a constant speed, the dynamic force is increased. For example, by increasing the wheel flat depth to 3 mm, the values of maximum force at speeds of 50 and 80 km/h have changed by about 235% and 400%, respectively. Also, by increasing the speed of the train at a wheel flat depth, the dynamic forces have increased. For example, at speeds of 50 and 80 km/h and a wheel flat depth of 1 mm, the maximum force values change by about 37%.

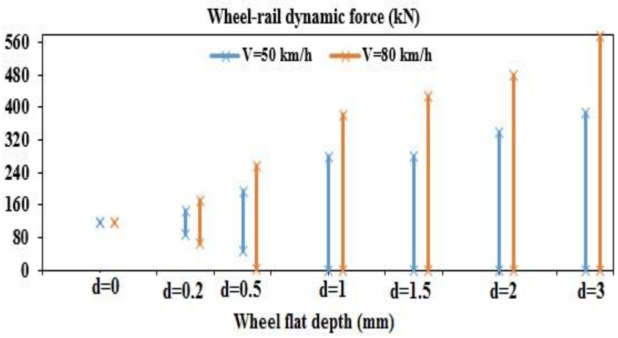

**Fig. 6** Effect of train speed and wheel flat depth on wheel/rail dynamic force.

## 5 CONCLUSIONS

Calculation and estimation of wheel/rail dynamic forces can be done directly and indirectly. In this research, UM multi-body dynamics software was used for modeling, simulating, and extracting dynamic forces (indirect method). A common freight train in many countries was modeled with an 18-100 3-piece bogie, and then the effects of two parameters of train speed and wheel flat depth on wheel/rail dynamic forces were evaluated. Wheel flats are a key source of issues in railway systems, as they generate significant wear on both the infrastructure and the train carriages.

They can cause serious damage to the train and accidents, so identifying worn wheels is critical for human safety and rail transit. The results showed that both mentioned parameters are highly effective in estimating the forces and influencing them. By increasing the wheel flat depth at a constant speed, the dynamic forces of the wheel/rail have increased dramatically. Also, by comparing the changes in the train speed in a certain wheel flat depth, an increase in dynamic forces has occurred. For example, in the wheel flat depth of 0.2 mm, with the change of train speed from 50 to 80 km/h, the maximum value of vertical wheel/rail forces has changed by about 16% from about 147 to 171 kN.

## REFERENCES

[1] Nielsen, J. C. O., Johansson, A., Out-of-Round Railway Wheels-A Literature Survey, Proc. Inst. Mech. Eng. Part F, J. Rail Rapid Transit, Vol. 214, 2000, pp. 79–91.

[2] Barke, D. W., Chiu, W. K., A Review of the Effects of Out-Of-Round Wheels on Track and Vehicle Components, Proc. Inst. Mech. Eng. Part F, J. Rail Rapid Transit, Vol. 219, 2005, pp. 151–175.

[3] Johansson, A., Andersson, C., Out-of-Round Railway Wheels—A Study of Wheel Polygonalization Through Simulation of Three-Dimensional Wheel–Rail Interaction and Wear, Veh. Syst. Dyn., Vol. 43, 2005, pp. 539–559.

[4] Nielsen, J., Out-of-Round Railway Wheels, Chalmers University of Technology: Göteborg, Sweden, 2009.

[5] Fesharakifard, R., Dequidt, A., Tison, T., and Coste, O., Dynamics of Railway Track Subjected to Distributed and Local Out-Of-Round Wheels, Mech. Ind., Vol. 14, 2013, pp. 347–359.

[6] Lan, Q., Dhanasekar, M., and Handoko, Y. A., Wear Damage of Out-Of-Round Wheels in Rail Wagons Under Braking, Eng. Fail. Anal., Vol. 102, 2019, pp. 170–186.

[7] Dukkipati, R. V., Dong, R., Impact Loads due to Wheel Flats and Shells, Veh. Syst. Dyn., Vol. 31, 1999, pp. 1–22.

[8] Wu, T., Thompson, D., A Hybrid Model for The Noise Generation Due to Railway Wheel Flats, J. Sound Vib., Vol. 51, 2002, pp. 115–139.

[9] Uzzal, R. U. A., Ahmed, W., and Rakheja, S., Dynamic Analysis of Railway Vehicle-Track Interactions Due to Wheel Flat with A Pitch-Plane Vehicle Model, J. Mech. Eng., Vol. 39, 2008, pp. 86–94.

[10] Vale, C., Influência da Qualidade dos Sistemas Ferroviários no Comportamento Dinâmico e no Planeamento da Manutenção Preventiva de Vias de Alta Velocidade. Ph.D. Thesis, Faculty of Engineering of the University of Porto, Porto, Portugal, 2010 (In Portuguese).

[11] Li, Y., Liu, J., and Wang, Y., Railway Wheel Flat Detection Based on Improved Empirical Mode Decomposition, Shock. Vib., 2016, pp. 1–14.

[12] Alemi, A., Corman, F., Pang, Y., and Lodewijks, G., Reconstruction of an Informative Railway Wheel Defect Signal from Wheel–Rail Contact Signals Measured by Multiple Wayside Sensors, Proc. Inst. Mech. Eng. Part F, J. Rail Rapid Transit, Vol. 233, 2018, pp. 49–62.

[13] Palo, M., Condition Monitoring of Railway Vehicles, A Study on Wheel Condition for Heavy Haul Rolling Stock, Operation and Maintenance Engineering Luleå University of Technology: Luleå, Sweden, 2012.

[14] Baasch, B., Heusel, J., Roth, M., and Neumann, T., Train Wheel Condition Monitoring via Cepstral Analysis of Axle Box Accelerations, Appl. Sci., Vol. 11, 2021, pp. 1432.

[15] Song, Y., Wang, Z., Liu, Z., and Wang, R., A Spatial Coupling Model to Study Dynamic Performance of Pantograph-Catenary with Vehicle-Track Excitation, Mech. Syst. Signal Process., Vol. 151, 2021, pp. 107336.

[16] Luo, R., Anti-Sliding Control Simulation of Railway Vehicle Braking, Chin. J. Mech. Eng., Vol. 44, 2008, pp. 35–40.

[17] Bosso, N., Gugliotta, A., and Zampieri, N., Wheel Flat Detection Algorithm for Onboard Diagnostic, Measurement, Vol. 123, 2018, pp. 193-202.

[18] Mishra, S., Sharan, P., and Saara, K., Real Time Implementation of Fiber Bragg Grating Sensor in Monitoring Flat Wheel Detection for Railways, Engineering Failure Analysis, Vol. 138, 2022, 106376.

[19] Chen, Si-Xin., Zhou, L., and Ni, Yi-Qing, Wheel Condition Assessment of High-Speed Trains Under Various Operational Conditions Using Semi-Supervised Adversarial Domain Adaptation, Mechanical Systems and Signal Processing, Vol. 170, 2022, 108853.

[20] Ng, A., Yap, T., Railway Wheel Flat Modeling and Vibration Signal Analysis for Improved Wheel Condition Monitoring and Predictive Maintenance, 6th International Conference on Intelligent Transportation Engineering (ICITE), 2021, pp 548–557.

[21] Wang, R., Crosbee, D., Beven, A., Wang, Z., and Zhen, D., Vibration-Based Detection of Wheel Flat on a High-Speed Train, Advances in Asset Management and Condition Monitoring, 2020, pp. 159–169.

[22] Sattari, S., Saadat, M., Mirtalaie, SH., Salehi, M., and Soleimani, A., Parametric Study of Wheel Flats Effects on Dynamic Forces and Derailment Coefficient in Turnouts, Int. J. of Heavy Vehicle Systems, 2023 (In production).

[23] Sattari, S., Saadat, M., Mirtalaie, SH., Salehi, M., and Soleimani, A., Effects of Train Speed, Track Irregularities, And Wheel Flat on Wheel-Rail Dynamic Forces, Int. J. of Heavy Vehicle Systems, 2023 (In production).

[24] Sattari, S., Saadat, M., Mirtalaie, SH., Salehi, M., and Soleimani, A., Modeling and Simulation of a Freight Train Brake System, International Journal of Railway Research, Vol. 9, No. 1, 2022, pp. 57-70.

[25] Xing, Z., Zhang, Z., Yao, X., Qin, Y., and Jia, L., Rail Wheel Tread Defect Detection Using Improved YOLOv3, Measurement, Vol. 203, 2022, 111959.

[26] Yang, J., Zhao, Y., Wang, J., Liu, C., and Bai, Y., Influence of Wheel Flat on Railway Vehicle Helical Gear System Under Traction/Braking Conditions, Engineering Failure Analysis, Vol. 134, 2022, 106022.

[27] Mohammadi, M., Mosleh, A., Vale, C., Ribeiro, D., Montenegro, P., and Meixedo, A., An Unsupervised Learning Approach for Wayside Train Wheel Flat Detection, Sensors, Vol. 23, No. 4, 2023, 1910, https://doi.org/10.3390/s23041910.

[28] Gonçalves, V., Mosleh, A., Vale, C., and Montenegro, P. A., Wheel Out-of-Roundness Detection Using an Envelope Spectrum Analysis, Sensors, Vol. 23, No. 4, 2023, 2138, https://doi.org/10.3390/s23042138.

[29] Gao, M., Cong, J., Xiao, J., He, Q., Li, S., Wang, Y., Yao, Y., Chen, R., and Wang, P., Dynamic Modeling and Experimental Investigation of Self-Powered Sensor Nodes for Freight Rail Transport, Applied Energy, Vol. 257, 2020, 113969, https://doi.org/10.1016/j.apenergy.2019.113969.

[30] Sattari, S., Saadat, M., Mirtalaie, SH., Salehi, M., and Soleimani, A., Modeling a Passenger Train and Analyzing the Ride Comfort in Different Conditions with The Sperling Index, 2nd International Conference on Computer Engineering and Science (CCES), 2022.

[31] Sattari, S., Saadat, M., Mirtalaie, SH., Salehi, M., and Soleimani, A., Evaluation of Sperling's Index in Passenger and Freight Trains Under Different Speeds and Track Irregularities, International Journal of Advanced Design and Manufacturing Technology (ADMT), Vol. 15, No. 4, 2022, pp. 87-96, DOI: 10.30486/admt.2023.1963242.1367.

[32] Sattari, S., Saadat, M., Mirtalaie, SH., Salehi, M., and Soleimani, A., Modeling of a Rail Suspension System to Investigate Vertical Vibration and Effective Parameters on It, International Journal of Railway Research, Vol. 9, No. 2, 2022, pp. 1-20, DOI: 10.22068/ijrare.299.

[33] Sattari, S., Saadat, M., Mirtalaie, SH., Salehi, M., and Soleimani, A., Comparison of Vibration Amplitude in Isfahan Subway Due to Track Structure- An Experimental Study, International Journal of Advanced Design and Manufacturing Technology (ADMT), 2023 (In production).

[34] Sadeghi, J., Ballasted Railway Tracks: Fundamentals of Analysis and Design, ed. 3, Iran University of Science and Technology, 2019.

[35] Sadeghi, J., Khajehdezfuly, A., and Moghadasnejad, F., Railway Concrete Slab Track: Fundamentals of Analysis and Design, ed. 1, Iran University of Science and Technology, 2018.

[36] Esmaeili, M., Heydari Noghabi, H., and Mosayebi, A., Principle and Foundation of Railway Ballastless Tracks, ed. 1, Iran University of Science and Technology, 2016.

[37] Kovalev, R., et al., Freight Car Models and Their Computer-Aided Dynamic Analysis, Multibody System Dynamics, Vol. 22, 2009, pp. 399-423.

[38] Bernal, E., Spiryagin, M., and Cole, C., Onboard Condition Monitoring Sensors, Systems and Techniques for Freight Railway Vehicles: A Review, IEEE Sensors Journal, Vol. 19, No. 1, 2019, pp. 4-24.

[39] Mazilu, T., A Dynamic Model for The Impact Between the Wheel Flat and Rail, UPB Scientific Bulletin, Series D: Mechanical Engineering, Vol. 69, 2007.

[40] Pieringer, A., Kropp, W., and Nielsen, J. C. O., The Influence of Contact Modelling on Simulated Wheel/Rail Interaction Due to Wheel Flats, Wear, Vol. 314, No. 1, 2014, pp. 273-281.

[41] Mosleh, A., Railway Vehicle Wheel Flat Detection with Multiple Records Using Spectral Kurtosis Analysis, Applied Sciences, Vol. 11, No. 9, 2021, pp. 4002.

[42] Spiroiu, M. A., Crăciun, C. I., Wheel Flat Effect on Wheel-Rail Dynamic Interaction, IOP Conference Series: Materials Science and Engineering, Vol. 444, 2018, pp. 042002.

[43] Bian, J., Gu, Y., and Murray, M. H., A Dynamic Wheel–Rail Impact Analysis of Railway Track Under Wheel Flat by Finite Element Analysis, Vehicle System Dynamics, Vol. 51, No. 6, 2013, pp. 784-797.

[44] Newton, S. G., Clark, R. A., An Investigation into the Dynamic Effects on the Track of Wheel flats on Railway Vehicles, Journal of Mechanical Engineering Science, Vol. 21, No. 4, 1979, pp. 287-297.

[45] Vale, C., Wheel Flats in the Dynamic Behavior of Ballasted and Slab Railway Tracks, Appl. Sci., Vol. 11, No. 15, 2021, pp. 7127.